ABSTRACT

Title of dissertation: CALCULATION OF REALISTIC CHARGED-PARTICLE TRANSFER MAPS

Chad Mitchell
Doctor of Philosophy, 2007

Dissertation directed by: Professor Alexander J. Dragt
Department of Physics

The study and computation of nonlinear charged-particle transfer maps is fundamental to understanding single-particle beam dynamics in accelerator devices. Transfer maps for individual elements of the beamline can in general depend sensitively on nonlinear fringe-field and high-multipole effects. The inclusion of these effects requires a detailed and realistic model of the interior and fringe magnetic fields, including knowledge of high spatial derivatives. Current methods for computing such maps often rely on idealized models of beamline elements. This Dissertation describes the development and implementation of a collection of techniques for computing realistic (as opposed to idealized) charged-particle transfer maps for general beamline elements, together with corresponding estimates of numerical error.

Each of these techniques makes use of 3-dimensional measured or numerical field data on a grid as provided, for example, by various 3-dimensional finite element field codes. The required high derivatives of the corresponding vector potential $\mathbf{A}$, required to compute transfer maps, cannot be reliably computed directly from this data by numerical differentiation due to numerical noise whose effect becomes progressively worse with the order of derivative desired. The effect of this noise, and its

amplification by numerical differentiation, can be overcome by fitting on a bounding surface far from the axis and then interpolating inward using the Maxwell equations. The key ingredients are the use of surface data and the smoothing property of the inverse Laplacian operator.

We explore the advantages of map computation using realistic field data on surfaces of various geometry. Maps obtained using these techniques can then be used to compute realistically all derived linear and nonlinear properties of both single pass and circular machines. Although the methods of this Dissertation have been applied primarily to magnetic beamline elements, they can also be applied to electric and radio-frequency beamline elements.

CALCULATION OF REALISTIC CHARGED-PARTICLE TRANSFER MAPS

by

Chad Mitchell

Dissertation submitted to the Faculty of the Graduate School of the
University of Maryland, College Park in partial fulfillment
of the requirements for the degree of
Doctor of Philosophy
2007

Advisory Committee:
Professor Alex Dragt, Chair/Advisor
Professor William Dorland
Professor Robert Gluckstern
Professor John Osborn
Professor Edward Ott

Preface

The layout of this Dissertation is as follows. Chapter 1 serves as a general introduction to the problem of computing charged-particle symplectic transfer maps using Lie algebra techniques. The motivation for using surface methods is discussed. In Chapters 2-5, we outline a number of techniques for computing such transfer maps for realistic magnetic elements of accelerator devices using measured or numerical magnetic field data. These methods make use of data provided on surfaces of various geometry, in order to avoid problems caused by the amplification of numerical noise. Of particular interest will be the relationship between the geometry of the fitting surface and the smoothing properties of the resulting integral operator. The optimum surface in each case will depend on the characteristics of the individual beamline element. Chapters 2-4 discuss the use of cylinders of various cross-section. In Chapter 5, we introduce a technique for general (piecewise-smooth) surface geometries. Finally, Chapter 6 describes a proposed application of these techniques to the Damping Rings of the future International Linear Collider.

Many of these techniques build on the work of previous students of the University of Maryland and others, in particular the technique described in Chapter 2. The primary original contributions are described in Chapters 3, 4, and 5. A fair amount of supplementary material in the Appendices will be referred to as needed.

Acknowledgements

I would like to thank my advisor, Professor Alex Dragt, for his patient guidance and support throughout this project. My experience working with him has been wonderfully rewarding, and I find it difficult to imagine a better advisor. I am also thankful to Professors Robert Gluckstern, Ed Ott, John Osborn, and Bill Dorland for agreeing to serve on my Dissertation Committee.

Thanks to Drs. Marco Venturini, Dan Abell, and Rob Ryne for many helpful conversations. This thesis rests on the contributions of these and many other former members of the Dynamical Systems and Accelerator Theory group at the University of Maryland. In addition, I thank Dr. Peter Walstrom for his ideas and correspondence regarding rectangular cylinder and bent box fitting routines.

Thanks also to Drs. Mark Palmer, David Sagan, Jim Crittenden, and Jeremy Urban at Cornell for providing field tables for their design of the ILC wiggler prototype, as well as several helpful conversations.

I am deeply grateful to Dr. Andy Wolski and others for allowing me to participate in several workshops regarding the design of the International Linear Collider Damping Rings.

Support of this research by the U.S. Department of Energy under Grant DEFG02-96ER40949 is gratefully acknowledged.

Most of all, I would like to thank my friends and family for all the support they have given me over the past few years. My parents have never spared a word of encouragement, and this never would have happened without their care and support.

Table of Contents

List of Tables

List of Figures

Chapter 1

Statement of Problem

This Dissertation describes the development of a collection of techniques for computing realistic nonlinear charged-particle transfer maps through general beamline elements of accelerator storage rings and other devices. Such methods use accurate, three-dimensional field data provided by finite element modeling to incorporate all fringe fields and nonlinear multipoles into a map description of the beam dynamics. The key ingredients are the use of surface data and the smoothing property of the inverse Laplacian operator.

In the present Chapter we provide the motivation for such an enterprise, and discuss the challenges associated with computing and representing transfer maps from realistic field data. In Section 1.1, we introduce the concept of a symplectic transfer map and describe the role that such maps play in characterizing the dynamics of nonlinear Hamiltonian systems. Section 1.2 discusses the need for a representation of the vector potential within the region of interest that is analytic in each spatial variable. Finally, in Section 1.3 we describe how such a representation can be accurately determined by fitting magnetic field data onto a surface bounding the region of interest and extrapolating into the interior with the aid of the Maxwell equations.

1.1 Transfer Maps and Lie Algebraic Tools

1.1.1 Maps and nonlinear dynamics

The ultimate goal of studying any nonlinear dynamical system is to obtain a complete characterization of the geometry of the set of possible orbits for the system. Of particular interest are the asymptotic properties of the orbits: the existence of constants of the motion, the classification of orbit families (fixed points, period-k orbits and quasiperiodic orbits, etc.) and the asymptotic distribution and statistical behavior of orbits [1]. In the study of accelerator beam dynamics, we are especially interested in the long-term stability of relativistic charged-particle orbits in configurations of electric and magnetic fields. Synchrotrons often require the storage of such charged-particle beams for a large number of turns [2]. At the Large Hadron Collider (LHC), for example, counter-rotating beams of protons are intended to be stored for approximately 4×10^8 turns while colliding at a center-of-mass energy of 14 TeV. "The presence of nonlinear components of the guiding fields of the machine can render the motion slightly chaotic, so that after a large number of turns the particles may be lost, colliding with the beam-pipe and degrading the luminosity of the machine."[3] Similar considerations apply to synchrotron light sources and damping rings.

The use of maps in the study of nonlinear dynamical systems has proven fruitful since their introduction by Poincaré (1899). In the context of accelerator physics, the use of maps provides a natural way to characterize the dynamical effect of individual beam-line elements. A transfer map is a function that maps a particle's initial

phase-space coordinates at entry of the beam-line element to its corresponding coordinates at exit. While numerical integration can be used to determine individual particle orbits through the beam-line, the use of maps is both conceptually clearer and computationally far more efficient. Once accurate transfer maps have been found for individual beam-line elements, one can determine all single-particle properties of the ring, including tunes, chromaticities, anharmonicities, and linear and nonlinear lattice functions using the theory of normal forms [4],[5]. In addition, the iteration of the single resulting one-turn map allows us to accurately track a large ensemble of particles for millions of turns without the need to numerically integrate a large number of initial conditions, and thereby to estimate the dynamic aperture of the device.

The classical state of each particle is given by its coordinates denoted $\mathbf{z} = (q_1, p_1, q_2, p_2, q_3, p_3)$ in the 6D phase space $\mathbb{R}^6$. The dynamics of a given particle are described by a Hamiltonian $H(\mathbf{z}, t)$, defined on some open subset U of the phase space over some time interval T. The system is then described by the canonical equations:

$$\dot{q}_k = \frac{\partial H}{\partial p_k}, \qquad \dot{p}_k = -\frac{\partial H}{\partial q_k} \tag{1.1}$$

where derivatives on the left are taken with respect to the independent variable t. In more compact notation, we write

$$\dot{\mathbf{z}} = J\nabla_{\mathbf{z}} H \tag{1.2}$$

where the matrix J is given by

$$J = \begin{pmatrix} 0 & 1 & 0 & 0 & 0 & 0 \\ -1 & 0 & 0 & 0 & 0 & 0 \\ 0 & 0 & 0 & 1 & 0 & 0 \\ 0 & 0 & -1 & 0 & 0 & 0 \\ 0 & 0 & 0 & 0 & 0 & 1 \\ 0 & 0 & 0 & 0 & -1 & 0 \end{pmatrix}. \tag{1.3}$$

These equations together define a *Hamiltonian flow* [1]. We assume H is analytic in the region of interest. Given an *initial* condition $\mathbf{z}^i \in U$ at $t = t_i \in T$, equations (1.1) are guaranteed to have a unique solution that exists for some nonvanishing interval $(t_i - \delta, t_i + \delta)$ in T. We now define a map $\mathcal{M}_{t_i \to t}$ for each t in $(t_i - \delta, t_i + \delta)$ from the phase space onto itself such that

$$\mathbf{z}(t) = \mathcal{M}_{t_i \to t}(\mathbf{z}^i). \tag{1.4}$$

Suppose we let t_i and t_f denote the entrance and exit from a given beam-line element. (Here the subscript f stands for *final*.) The map $\mathcal{M}_{t_i \to t_f}$ then fully characterizes the dynamics of that element. Maps for neighboring beam-line elements may be composed or *concatenated* by the rule

$$\mathcal{M}_{t_a \to t_c} = \mathcal{M}_{t_b \to t_c} \mathcal{M}_{t_a \to t_b}. \tag{1.5}$$

Furthermore, maps resulting from the Hamiltonian system (1.1) have an important defining property. It can be shown from (1.1) that the Jacobian matrix M, defined by

$$M_{jk} = \frac{\partial z_j^f}{\partial z_k^i}, \tag{1.6}$$

must satisfy the condition

$$M^T J M = J \tag{1.7}$$

for any t_i and t_f and all $\mathbf{z}^i$ [6]. The set of such matrices forms a group under multiplication, the *symplectic group*. Similarly, the set of all Hamiltonian mappings $\mathcal{M}$ of the phase space onto itself forms the group of *symplectic transformations* (maps). In this way, the study of Hamiltonian dynamical systems is equivalent to the study of symplectic mappings. For more details, the reader is referred to ([4],[5]).

1.1.2 Hamiltonian for a charged particle

The Hamiltonian for a charged particle in electric and magnetic fields is given by [7]:

$$H = \sqrt{m^2c^4 + (\mathbf{p} - q\mathbf{A})^2c^2} - q\Phi. \tag{1.8}$$

The times t_i and t_f of entry and exit from a given element will vary between particles in the beam. If we suppose that $dz/dt = \partial H/\partial p_z \neq 0$, we may introduce the longitudinal coordinate z as the independent variable in place of the time t. We begin by introducing the variable p_t as the momentum canonically conjugate to the variable t, defined by the relation

$$p_t = -H(x, p_x, y, p_y, z, p_z, t). \tag{1.9}$$

By the implicit function theorem, we may invert this relation locally for p_z to obtain an expression of the form

$$p_z = -K(x, p_x, y, p_y, t, p_t, z) \tag{1.10}$$

where K becomes the new Hamiltonian. We then verify using (1.1) that Hamilton's equations are satisfied:

$$\frac{\partial K}{\partial p_t} = \left(\frac{\partial H}{\partial p_z}\right)^{-1} = \dot{t}, \tag{1.11a}$$

$$\frac{\partial K}{\partial p_i} = \left(\frac{\partial H}{\partial p_i}\right)\left(\frac{\partial H}{\partial p_z}\right)^{-1} = \dot{q}_i, \tag{1.11b}$$

$$\frac{\partial K}{\partial t} = \left(\frac{\partial H}{\partial t}\right)\left(\frac{\partial H}{\partial p_z}\right)^{-1} = -\dot{p}_t, \tag{1.11c}$$

$$\frac{\partial K}{\partial q_i} = \left(\frac{\partial H}{\partial q_i}\right)\left(\frac{\partial H}{\partial p_z}\right)^{-1} = -\dot{p}_i, \tag{1.11d}$$

where the dot now indicates a derivative with respect to z, the new independent variable.

The dynamics of the particle in the phase space described by the canonical variables (x, p_x, y, p_y, t, p_t) are given by the Hamiltonian K. In the case of a charged particle we find, using (1.8),

$$K = -\sqrt{(p_t + q\Phi)^2/c^2 - m^2c^2 - (p_x - qA_x)^2 - (p_y - qA_y)^2} - qA_z. \tag{1.12}$$

The design orbit through the beamline element is the solution of (1.11) for a reference particle entering the element on-axis with design momentum p^0, corresponding to the initial condition $\mathbf{z}^i = (0, 0, 0, 0, t_i, -p^0c/\beta)$. We let $x^r(z)$, $p_x^r(z)$, etc. denote the values of the reference coordinates at a given length z along the element. We will be interested in motion relative to this design orbit. Let l denote a desired length scale (eg., $l = 1$ cm). Introducing the dimensionless deviation variables

$$X = (x - x^r)/l, \qquad P_x = (p_x - p_x^r)/p^0, \tag{1.13a}$$

$$Y = (y - y^r)/l, \qquad P_y = (p_y - p_y^r)/p^0, \tag{1.13b}$$

$$\tau = c(t - t^r)/l, \qquad P_\tau = (p_t - p_t^r)/(p^0c), \tag{1.13c}$$

we may write a scaled Hamiltonian $H = K/(p^0 c)$ in terms of the deviation variables (1.13) as [8]:

$$\begin{aligned} H = -\frac{1}{l}\Bigg[& \left(P_\tau + \bar{p}_\tau^r + \frac{q\Phi}{p^0 c}\right)^2 - \left(\frac{mc}{p^0}\right)^2 \\ & - \left(P_x + \bar{p}_x^r - \frac{q}{p^0}A_x\right)^2 - \left(P_y + \bar{p}_y^r - \frac{q}{p^0}A_y\right)^2 \Bigg]^{1/2} \\ & - \frac{q}{p^0}A_z - \dot{\bar{x}}^r p_x + \dot{\bar{p}}_x^r x - \dot{\bar{y}}^r p_y + \dot{\bar{p}}_y^r y - \dot{\bar{\tau}}^r p_\tau + \dot{\bar{p}}_\tau^r \tau. \end{aligned} \tag{1.14}$$

In a neighborhood of the design orbit, the deviation variable Hamiltonian H has the (truncated) polynomial expansion

$$H = H^2 + H^3 + \cdots + H^n = \sum_{s=1}^{S} h_s(z) P_s(6; x, p_x, y, p_y, \tau, p_\tau). \tag{1.15}$$

We retain terms in the deviation variable Hamiltonian through terms of degree n. Here the $P_s(6;\cdots)$ are the various monomials homogeneous of degree $m(s)$ in the six phase-space deviation variables, and the H^m denote the sum of all such terms that are homogeneous of degree m.

1.1.3 Lie algebraic methods

We have seen that charged-particle motion through any beam-line element is described by a symplectic transfer map $\mathcal{M}$. We briefly discuss how such maps can be computed and stored using Lie algebraic techniques.

Let $\boldsymbol{\zeta} = (X, P_x, Y, P_y, \tau, P_\tau)$ denote the vector of deviation variables in (1.13). Given a function f of the phase space variables ζ_i, we define the Lie operator $: f :$ by

$$: f : g = [f, g] \tag{1.16}$$

where

$$[f,g] = \sum_i \frac{\partial f}{\partial q_i}\frac{\partial g}{\partial p_i} - \frac{\partial f}{\partial p_i}\frac{\partial g}{\partial q_i} \tag{1.17}$$

is the usual Poisson bracket. In this notation the canonical equations (1.11) can be written in the form

$$\dot{\zeta}_i = - : H : \zeta_i. \tag{1.18}$$

We define the Lie transformation associated with f to be the operator

$$\exp(: f :) = \sum_{n=0}^{\infty} \frac{1}{n!} : f :^n . \tag{1.19}$$

Given any analytic symplectic mapping which maps the origin into itself, the Dragt-Finn factorization theorem [9] states that the map can be written in the factorized form:

$$\mathcal{M} = \exp(: f_2^c :)\exp(: f_2^a :)\exp(: f_3 :)\exp(: f_4 :)... \tag{1.20}$$

where each generator f_m is a homogeneous polynomial of degree m. The quadratic polynomials f_2^c and f_2^a are related to symmetric matrices S^c and S^a that *commute* and *anticommute* with J, respectively. Through aberrations of order $(n-1)$ such a map has the symplectic approximation

$$\mathcal{M} = \mathcal{R}_2\exp(: f_3 :)\exp(: f_4 :)\cdots\exp(: f_n :) \tag{1.21}$$

where $\mathcal{R}_2 = \exp(: f_2^c :)\exp(: f_2^a :)$ describes the linear part of the map.

The linear map $\mathcal{R}_2$ and the Lie generators f_m are determined by solving the map equation of motion

$$\dot{\mathcal{M}} = \mathcal{M} : -H : . \tag{1.22}$$

In particular the map $\mathcal{R}_2$ acts as a linear transformation:

$$(\mathcal{R}_2\boldsymbol{\zeta})_j = \sum_{k=1}^{6} R_{jk}\zeta_k \tag{1.23}$$

and may be represented by the matrix R whose components are R_{jk}. Similarly, the second-degree Hamiltonian H^2 may be written as the quadratic form

$$H^2(\boldsymbol{\zeta}, z) = \frac{1}{2}\sum_{j,k=1}^{6} S_{jk}(z)\zeta_j\zeta_k \tag{1.24}$$

represented by the matrix S. Using (1.22) together with (1.21,1.23), we find that the matrix R for the linear map obeys the equation

$$\dot{R} = JSR, \qquad \text{with } R(z_i) = I. \tag{1.25}$$

We next introduce the interaction Hamiltonian $H^{int} = H_3^{int} + H_4^{int} + ...$ by

$$H_m^{int}(\boldsymbol{\zeta}^i, z) = H_m(\mathcal{R}_2\boldsymbol{\zeta}^i, z). \tag{1.26}$$

The generators f_m then obey equations governed by the H_m^{int}. Through $m = 6$ they are given by the relations

$$\dot{f}_3 = -H_3^{int}, \tag{1.27a}$$

$$\dot{f}_4 = -H_4^{int} + (:f_3:/2)(-H_3^{int}), \tag{1.27b}$$

$$\dot{f}_5 = -H_5^{int} + :f_3:(-H_4^{int}) + (1/3):f_3:^2(-H_3^{int}), \tag{1.27c}$$

$$\begin{aligned}\dot{f}_6 = &- H_6^{int} + :f_3:(-H_5^{int}) + (1/2):f_4:(-H_4^{int}) \\ &+ (1/4):f_4::f_3:(-H_3^{int}) + (1/2):f_3:^2(-H_4^{int}) \\ &+ (1/8):f_3:^3(-H_3^{int}),\end{aligned} \tag{1.27d}$$

subject to the initial conditions

$$f_m(z_i) = 0. \tag{1.28}$$

These equations must be integrated together with the 36 equations for the elements of the matrix R, and the 6 canonical equations for the reference orbit. This requires (through $m = 6$) the integration and storage of 938 variables. (Note that this is a significant savings in storage over that required by representing the motion in the form of a Taylor map in the initial variables $\boldsymbol{\zeta}^i$.)

1.2 Need for Analytic Representation of the Vector Potential

Determining the generators appearing in (1.21) requires that we have available the Taylor coefficients $h_s(z)$ along the full length of the beam-line element. These are determined according to (1.12) from the vector potential $\mathbf{A}$. Expanding about a design orbit through the beam-line element at a longitudinal location z yields representations for the components of $\mathbf{A}$ of the (truncated) form

$$A_w(x, y, z) = \sum_{l=1}^{L} a_l^w(z) P_l(2; x, y). \tag{1.29}$$

Here $w = x, y$, or z and the $P_l(2; x, y)$ are the various homogeneous monomials in the two transverse deviation variables (x, y). The upper limits L and S in the sums (1.15) and (1.29) are determined by n. For example, if $n = 6$ then $L = 27$ and $S = 923$. We conclude that what we need is a Taylor expansion for the vector potential components A_w in the deviation variables x and y. Their z-dependent coefficients $a_l^w(z)$ must be accurately determined from a knowledge of $\mathbf{B}$.

Linear approximations to the equations of motion (1.1) are obtained by considering only the second-degree part of the Hamiltonian H^2. In particular, for linear models of solenoids, dipoles, and quadrupoles it is sufficient to include terms up to second degree in the vector potential $\mathbf{A}$. The inclusion of fringe-field and high-multipole effects, however, requires a detailed and realistic model of the interior magnetic field, including knowledge of high spatial derivatives. A map in Lie form (1.21) possessing generators through f_m represents a map whose Taylor series possesses terms through degree $m-1$ in the initial variables $\boldsymbol{\zeta}^i$.

In general we have available measured or numerical three-dimensional magnetic field data on a discrete mesh of points available throughout the region of interest. Measured field values may be available at select interior points from a 3d magnetic Hall sensor. (Such a magnetic sensor, recently patented by CERN, claims an accuracy of 1.5×10^{-4} T for the range 0-1.5 T.) Alternatively, numerical field values may be available at select interior points from electromagnetic simulations, which are obtained using PDE solvers of various types for producing interior field values from a given magnet design. Because of the importance of these sources of numerical data, we briefly discuss the primary methods used by such electromagnetic solvers.

1.2.1 Finite difference methods

Finite difference methods approximate the differential equation $Lu = f$ by considering values at a finite set of points (nodes) within the domain of interest [10].

1. The domain is partitioned into a uniformly spaced grid.

2. At a given node, each derivative in L is approximated by an algebraic expression which references the values of u at adjacent nodes (a difference quotient).

3. The resulting finite system of coupled linear equations is inverted to obtain the solution values at the set of nodes.

1.2.2 Finite element methods

Finite element methods can be adapted to problems of great complexity and unusual geometry [11],[12],[13].

1. The differential equation is formulated as a variational problem in weak (integral) form. The problem $Lu = f$ is rewritten as: Find $v = u$ which minimizes the quadratic linear functional $I(v) = (Lv, v) - 2(f, v)$. In the usual case of Poisson's equation, for example, this amounts to minimizing the electrostatic potential energy.

2. The domain is partitioned into a (possibly irregular) mesh.

3. We search for an approximate solution u among the trial functions $u = \sum_{j=1}^{N} q_j \phi_j$ which minimizes the linear functional $I(v)$. The basis functions ϕ_j are taken to be piecewise polynomials in x, y, and z which vanish outside a local region of the mesh.

4. The integrals appearing in the functional $I(v)$ can be evaluated explicitly, producing a finite system of coupled linear equations for the coefficients $\{q_j\}$ that must be inverted to obtain the finite-element solution u.

1.2.3 Boundary element methods

The advantage of the boundary element method is that only the boundary (or boundaries) of the domain of the PDE requires sub-division. A discussion of this method may be found in [14],[15].

1. The differential equation $Lu = f$ is reformulated as an integral equation involving values of u and its derivative on the boundary of the domain.

2. A mesh is constructed over the boundary surface.

3. The boundary values for u and $\partial u/\partial n$ required in 1. are each approximated using some set of piecewise-polynomial basis functions on the boundary. That is, the solution of the boundary-integral equation is sought among functions of the form $u = \sum_{j=1}^{N} p_j \psi_j$, where each basis function ψ_j is a piecewise polynomial in the local coordinates on the boundary which vanishes outside a local region of the boundary mesh.

4. The integral equation is used together with the surface values obtained in 3. to calculate numerically the solution directly at any desired point in the interior of the domain. The integral of the boundary values may be done exactly, producing a linear functional of the coefficients p_j, which must be evaluated at each interior point.

Boundary element methods are especially useful for situations in which Green's functions can be calculated, in which case the integral equation in 1. reduces to a single integral of the surface values (in the form of some piecewise polynomial) against the Green's function for the domain.

Regardless of the method used, the net result typically consists of simulated values of the field components on some interior mesh. The required high derivatives of **A** cannot be reliably computed directly from this data by numerical differentiation due to numerical noise whose effect becomes progressively worse with the order of derivative desired. The differentiation of noisy data is a long-standing computational problem. One straightforward method of computing these derivatives involves fitting an interpolating function to data near the axis of the magnetic element and approximating derivatives using derivatives of this interpolant. Hildebrand [10] states:

> *Once an interpolating polynomial $y(x)$ has been determined so that it satisfactorily approximates a given function $f(x)$ over a certain interval I, it may be hoped that the result of differentiating $y(x), \cdots$, will also satisfactorily approximate the corresponding derivative...of $f(x)$. However ... we may anticipate the fact that, even though the deviation between $y(x)$ and $f(x)$ be small throughout the interval, still the slopes of the two curves representing them may differ quite appreciably. Further, it is seen that roundoff errors (or errors of observation) of alternating sign in consecutive ordinates could affect the calculation of the derivative quite strongly if those ordinates were fairly closely spaced $\cdots$. In particular, numerical differentiation should be avoided whenever possible, particularly when the data are empirical and subject to appreciable errors of observation.*

A discussion of numerical differentiation and the resulting amplification of noise is provided in Appendix A. For a simple three-point formula, for example, random errors of rms value σ contribute to an error in the derivative with rms value

$$\sigma_R = \frac{1}{\sqrt{2}h}\sigma, \tag{1.30}$$

where h is the distance between equally spaced mesh points. These concerns apply to both finite-differencing techniques and FFT techniques. The process of providing imperfect data on a finite mesh inevitably results in the loss of information about high-order derivatives.

A major goal of this thesis is to describe how such information can be extracted reliably from 3-dimensional magnetic field data $\mathbf{B}(\mathbf{r})$ on a grid as provided by various 3-dimensional finite element field codes, for example OPERA-3d available from Vector Fields. The key ingredients are the use of surface data and the smoothing property of the inverse Laplacian operator. We develop a collection of boundary-element type methods designed to produce, with high accuracy, Taylor series for each component of the vector potential in the interior of the solution domain. The effect of numerical noise, and its amplification by numerical differentiation, is overcome by fitting on a bounding surface far from the axis and exploiting the smoothing properties of the inverse Laplacian operator.

1.3 Inherent Analyticity and Use of Surface Data

We have discussed the difficulty of obtaining the derivatives of $\mathbf{A}$ appearing as the Taylor coefficients of the series (1.29). In addition, note that these derivatives

are not independent. By construction, we have chosen the potentials to be specified by the interior electric and magnetic fields:

$$\mathbf{B} = \nabla \times \mathbf{A}, \tag{1.31}$$

$$\mathbf{E} = -\nabla\phi - \frac{\partial \mathbf{A}}{\partial t}. \tag{1.32}$$

In addition, derivatives of the fields themselves are related through the Maxwell equations [7]:

$$\begin{aligned} \nabla \cdot \mathbf{E} &= \rho/\epsilon_0, & \nabla \times \mathbf{E} + \frac{\partial \mathbf{B}}{\partial t} &= 0, \\ \nabla \times \mathbf{B} - \frac{1}{c^2}\frac{\partial \mathbf{E}}{\partial t} &= \mu_0 \mathbf{J}, & \nabla \cdot \mathbf{B} &= 0. \end{aligned} \tag{1.33}$$

In the absence of electric and magnetic sources, these take the form

$$\begin{aligned} \nabla \cdot \mathbf{E} &= 0, & \nabla \times \mathbf{E} + \frac{\partial \mathbf{B}}{\partial t} &= 0, \\ \nabla \times \mathbf{B} - \frac{1}{c^2}\frac{\partial \mathbf{E}}{\partial t} &= 0, & \nabla \cdot \mathbf{B} &= 0. \end{aligned} \tag{1.34}$$

The existence of a well-behaved solution to (1.33) clearly requires that partial derivatives of the potentials through second-order exist and are related. In addition, we will see that (1.34) implies, under certain assumptions, that *all* partial derivatives exist, and the Maxwell equations contain information about relationships between derivatives at all orders. This information may be used to constrain the coefficients $a_j(z)$ of the series (1.29). Formulating (1.34) in the form of boundary-value potential problem will suggest a solution.

We are first interested in the smoothness properties of the solutions of (1.34). Given an open, bounded domain Ω, we define $C^k(\Omega)$ as the set of functions which

have continuous partial derivatives of all orders through order k inside Ω. We use the term "smooth" to refer to functions which lie in $C^k(\Omega)$ for all k. The set of such functions we denote $C^\infty(\Omega)$. Consider fields $\mathbf{E}$ and $\mathbf{B}$ in a source-free domain Ω. To study the smoothness properties of the fields $\mathbf{E}$ and $\mathbf{B}$, suppose that the fields are excited at some fundamental frequency and its first few harmonics. That is, we consider periodic solutions of the form

$$\mathbf{E}(\mathbf{r},t) = \sum_{n=0}^{m} \mathbf{E}^{(n)}(\mathbf{r}) \cos(\omega_n t + \phi_n), \tag{1.35a}$$

$$\mathbf{B}(\mathbf{r},t) = \sum_{n=0}^{m} \mathbf{B}^{(n)}(\mathbf{r}) \cos(\omega_n t + \phi_n), \tag{1.35b}$$

where $\omega_n = n\omega_0$ and $\mathbf{r} \in \Omega$. Static fields are contained as the special case $m = 0$ and $\omega_0 = 0$. Then it follows from (1.34) that each mode $\mathbf{E}^{(n)}$ and $\mathbf{B}^{(n)}$ for $n = 1, \cdots, m$ obeys a Helmholtz equation of the form

$$\left(\nabla^2 + \frac{\omega_n^2}{c^2}\right) \mathbf{E}^{(n)} = 0, \tag{1.36a}$$

$$\left(\nabla^2 + \frac{\omega_n^2}{c^2}\right) \mathbf{B}^{(n)} = 0. \tag{1.36b}$$

Solutions of (1.36) have many properties in common with harmonic functions (see Appendix H). In particular, any solution $\mathbf{E}^{(n)}$, $\mathbf{B}^{(n)}$ on Ω will possess Cartesian components $E_\alpha^{(n)}$, $B_\alpha^{(n)}$ for $\alpha = x, y, z$ that lie in $C^\infty(\Omega)$. Since differentiability in the variables x, y, z is required for every mode of (1.35), the same conclusion applies to $\mathbf{B}(\mathbf{r},t)$ and $\mathbf{E}(\mathbf{r},t)$. *In a source-free region, each component of a periodic solution* $\mathbf{E}$, $\mathbf{B}$ *of Maxwell's equations is a smooth function.* Furthermore, limiting arguments may be used to weaken the condition (1.35).

A stronger claim also holds. The field components of any solution (1.35) of

Maxwell's equations on the domain Ω are real-analytic in Ω. That is, at each point $\mathbf{r}_d$ in the domain the components of $\mathbf{E}$, $\mathbf{B}$, $\mathbf{A}$ and the function Φ may be expanded in convergent power series

$$E_\alpha(\mathbf{r}_d + \delta\mathbf{r}) = \sum_{a,b,c=0}^{\infty} \epsilon_{a,b,c}(\delta x)^a(\delta y)^b(\delta z)^c, \tag{1.37}$$

$$B_\alpha(\mathbf{r}_d + \delta\mathbf{r}) = \sum_{a,b,c=0}^{\infty} \beta_{a,b,c}(\delta x)^a(\delta y)^b(\delta z)^c, \tag{1.38}$$

in some neighborhood of $\mathbf{r}_d$. Grouping terms of like degree, we may obtain homogeneous polynomial series for each of the fields and potentials. This fact allows us to write series of the form (1.29). These properties do not generally hold in a region containing irregular (non-smooth) source currents or boundaries between media.

1.3.1 Surface Fitting

Consider an open, connected domain Ω within the interior of the beamline element in which there are no electric or magnetic sources. The fields $\mathbf{E}$, $\mathbf{B}$ are uniquely specified by their values on the boundary $\partial\Omega$. The treatment of time-dependent electric fields in rf cavities has been treated in detail in [18], when Ω is the interior of a circular cylinder. In the present work, we focus on configurations of static magnetic fields. We may then write $\mathbf{B}$ in terms of a magnetic scalar potential $\mathbf{B} = \nabla\Psi$ satisfying $\nabla^2\Psi = 0$. A solution for Ψ is then determined entirely by $\mathbf{n}\cdot\mathbf{B}$, the component of the field normal to the surface. We may write the solution as

$$\Psi(\mathbf{r}) = \langle\Psi(\mathbf{r}')\rangle_{\partial\Omega} - \int_{\partial\Omega} G(\mathbf{r},\mathbf{r}')\frac{\partial\Psi}{\partial n}(\mathbf{r}')dS', \tag{1.39}$$

where G is the Green's function for the domain Ω. In principle, (1.39) may be expanded in a Taylor series in the variables (x, y), leading to a boundary-integral formula for the interior Taylor coefficients. By solving $\nabla \times \mathbf{A} = \nabla \Psi$, we may obtain a power series for $\mathbf{A}$.

Surface fitting techniques utilizing (1.39) have several advantages over on-axis or midplane fitting, which we discuss throughout.

- The Maxwell equations are satisfied by construction.
- The numerical error in the interior is globally controlled. Due to the properties of harmonic functions, the error must take its extrema on the boundary, where we have done a controlled fit to the field data.
- Such techniques have been benchmarked against analytic results for fields due to arrays of magnetic monopoles.
- Results are relatively insensitive to surface errors due to the smoothing property of the inverse Laplacian operator. As a result, high frequency noise in the boundary data has little effect on the coefficients $a_j(z)$ appearing in (1.29).

In the remainder of this thesis, we explore the advantages of map computation using realistic field data on surfaces of various geometry. Of particular interest will be the relationship between the geometry of the fitting surface and the smoothing properties of the integral operator which is used to produce the interior coefficients. A proposed application to the damping rings of the International Linear Collider will follow.

1.4 Conclusion

Current approaches for computing charged-particle transfer maps for a given lattice often rely on idealized analytical models of the electric and magnetic fields of the component beamline elements, or approximate the effects of individual elements using matrix-kick methods or integrators (see Section 6.3.2).

The use of surface-fitting routines such as those described in this dissertation allows one, for the first time, to compute high-order nonlinear transfer maps for every element of a beamline using realistic field data. These maps include, by construction, the effect of fringe fields and nonlinear multipoles present in each beamline element, through the order of symplectic approximation. The appropriate surface-fitting procedure may be determined by the geometry of the element under consideration. (Note that multiple techniques may be used in many cases, allowing independent verification of results.)

- Solenoids and multipole magnets - Fitted using circular cylinders [16], Chapter 2.
- Wigglers and undulators - Fitted using elliptical or rectangular cylinders, Chapters 3-4.
- R-F cavities - Fitted using circular cylinders [18].
- Bending magnets - Fitted using bent boxes [19], Chapter 5.

Thus, it is now possible to compute accurate high-order transfer maps for all real (as opposed to idealized) beamline elements. These maps can then be used to

compute realistically all derived linear and nonlinear properties of both single pass and circular machines.

Chapter 2

Use of Circular Cylinder Surface

The first geometry we consider is that associated with an infinite circular cylinder. The use of a circular cylinder surface for boundary-value fitting in the context of computing transfer maps has been explored in detail elsewhere [16],[8]. A closely related approach can be found in [17]. Cylinder surface fitting is ideally suited for computing transfer maps for straight-axis magnetic elements such as nonlinear multipoles and wiggler magnets, and similar techniques for fitting time-dependent electric fields have been developed for computing transfer maps for RF-cavities [18].

In the present chapter, we review the results for static magnetic elements and discuss numerical benchmarks, as well as providing error estimates and a general discussion of smoothing in the circular cylinder case. The development of Section 2.1 will set the stage for similar developments in the chapters to follow.

2.1 Analytic Formulation

2.1.1 Determination of the Vector Potential

In a current-free region we may work with a scalar potential ψ satisfying $\mathbf{B} = \nabla\psi$. Because $\nabla \cdot \mathbf{B} = 0$, the potential must satisfy

$$\nabla^2\psi = 0 \tag{2.1}$$

everywhere within this region. Consider a coordinate system in which the z-axis lies along the axis of the beamline element. It follows from (2.1) that ψ is real-analytic in the variables x, y, and z. In addition, the potential ψ will behave along the axis in the fringe-field region far outside the element as

$$\psi \sim \frac{\mu_0}{4\pi}\frac{m_z}{z^2}, \tag{2.2}$$

where $\mathbf{m}$ is the magnetic moment of the element. It follows that ψ is absolutely integrable along the z-axis, and we may write its Fourier transform as

$$\tilde{\psi}(\rho,\phi,k) = \frac{1}{\sqrt{2\pi}}\int_{-\infty}^{\infty} dz e^{-ikz}\psi(\rho,\phi,z). \tag{2.3}$$

The resulting function $\tilde{\psi}$ must satisfy

$$(\nabla_\perp^2 - k^2)\tilde{\psi} = 0. \tag{2.4}$$

We now work in cylindrical coordinates (ρ,ϕ,z) defined by

$$x = \rho\cos(\phi), \tag{2.5}$$

$$y = \rho\sin(\phi), \tag{2.6}$$

$$z = z, \tag{2.7}$$

where the z-axis $\rho = 0$ lies along the length of the beam-line element near the design trajectory. In cylindrical coordinates, the general solution of (2.4) is given by

$$\tilde{\psi}(\rho,\phi,k) = \sum_{m=0}^{\infty} I_m(k\rho)\left[a_m(k)\sin(m\phi) + b_m(k)\cos(m\phi)\right]. \tag{2.8}$$

Therefore we have

$$\psi(\rho,\phi,z) = \sum_{m=0}^{\infty} \psi_{m,s}(\rho,z)\sin m\phi + \psi_{m,c}(\rho,z)\cos m\phi, \tag{2.9}$$

where

$$\psi_{m,s}(\rho, z) = \frac{1}{\sqrt{2\pi}} \int_{-\infty}^{\infty} dk e^{ikz} a_m(k) I_m(k\rho), \tag{2.10}$$

$$\psi_{m,c}(\rho, z) = \frac{1}{\sqrt{2\pi}} \int_{-\infty}^{\infty} dk e^{ikz} b_m(k) I_m(k\rho). \tag{2.11}$$

We refer to $\psi_{m,s}$ and $\psi_{m,c}$ as upright and skew multipole coefficients, respectively.

Suppose that we fit a circular cylinder of radius R along the axis of the beamline, lying within all iron or other magnetic sources. We let Ω denote the domain interior to the cylinder. Suppose that the component of the magnetic field normal to the surface B_ρ is known at all points on the surface. This defines a boundary-value problem for ψ in the domain Ω with Neumann boundary conditions. In particular, a solution for ψ exists and is uniquely determined by these boundary conditions, provided that

$$\oint_{\partial\Omega} B_\rho(\rho = R, \phi, z) dS = 0. \tag{2.12}$$

This condition is automatically satisfied when B_ρ is known exactly on the surface, since $\nabla \cdot \mathbf{B} = 0$ on Ω. The magnetic field in the interior is therefore determined by its values on the surface of the cylinder. We may write B_ρ on the surface in terms of its Fourier series as

$$B_\rho(\rho = R, \phi, z) = \left.\frac{\partial \psi(\rho, \phi, z)}{\partial \rho}\right|_{\rho=R} = \sum_{m=0}^{\infty} B_m(R, z) \sin(m\phi) + A_m(R, z) \cos(m\phi). \tag{2.13}$$

It follows from (2.2) and the analyticity of ψ that the coefficients B_m and A_m are analytic and absolutely integrable in z. Defining $\tilde{B}_m(R, k)$ and $\tilde{A}_m(R, k)$ according

to

$$\tilde{B}_m(R,k) = \frac{1}{\sqrt{2\pi}}\int_{-\infty}^{\infty} dz e^{-ikz} B_m(R,z), \tag{2.14}$$

$$\tilde{A}_m(R,k) = \frac{1}{\sqrt{2\pi}}\int_{-\infty}^{\infty} dz e^{-ikz} A_m(R,z), \tag{2.15}$$

we find the boundary-value solution for (2.9) is given in terms of the multipole coefficients:

$$\psi_{m,s}(\rho,z) = \frac{1}{\sqrt{2\pi}}\int_{-\infty}^{\infty} dk e^{ikz} \frac{I_m(k\rho)}{kI'_m(kR)}\tilde{B}_m(R,k), \tag{2.16}$$

$$\psi_{m,c}(\rho,z) = \frac{1}{\sqrt{2\pi}}\int_{-\infty}^{\infty} dk e^{ikz} \frac{I_m(k\rho)}{kI'_m(kR)}\tilde{A}_m(R,k). \tag{2.17}$$

We may now construct a power-series representation for the vector potential $\mathbf{A}$ using ψ as an intermediate quantity. Using the expansion

$$I_m(x) = \sum_{l=0}^{\infty} \frac{1}{l!(l+m)!}\left(\frac{x}{2}\right)^{2l+m} \tag{2.18}$$

in (2.17) we find that ψ can be represented as a Taylor series in ρ about the axis of the cylinder. Indeed,

$$\psi_{m,\alpha}(\rho,z) = \sum_{l=0}^{\infty} \frac{(-1)^l m!}{2^{2l} l!(l+m)!} C^{[2l]}_{m,\alpha}(z)\rho^{2l+m}, \tag{2.19}$$

where

$$C^{[2l]}_{m,s}(z) = \frac{1}{2^m m!}\frac{(-1)^l}{\sqrt{2\pi}}\int_{-\infty}^{\infty} dk e^{ikz}\frac{k^{2l+m-1}}{I'_m(kR)}\tilde{B}_m(R,k), \tag{2.20a}$$

$$C^{[2l]}_{m,c}(z) = \frac{1}{2^m m!}\frac{(-1)^l}{\sqrt{2\pi}}\int_{-\infty}^{\infty} dk e^{ikz}\frac{k^{2l+m-1}}{I'_m(kR)}\tilde{A}_m(R,k). \tag{2.20b}$$

The functions $C^{[0]}_{m,\alpha}$ are known as generalized on-axis gradients, determined by integration of one component of the field against a suitably determined kernel. The

on-axis gradients uniquely characterize the field of the beam-line element in the domain where (2.19) converges.

Given these on-axis gradients, Taylor expansions for the vector potential components A_x, A_y, and A_z may be found by solving $\nabla \times \mathbf{A} = \nabla\psi$. We consider the terms of (2.9) with $m \neq 0$. In the gauge with $A_\phi = 0$, we find that the remaining components of $\mathbf{A}$ are given by

$$A_\rho = \sum_{m=1}^{\infty} \frac{\cos(m\phi)}{m}\rho\frac{\partial\psi_{m,s}}{\partial z} - \frac{\sin(m\phi)}{m}\rho\frac{\partial\psi_{m,c}}{\partial z}, \tag{2.21a}$$

$$A_z = \sum_{m=1}^{\infty} -\frac{\cos(m\phi)}{m}\rho\frac{\partial\psi_{m,s}}{\partial \rho} + \frac{\sin(m\phi)}{m}\rho\frac{\partial\psi_{m,c}}{\partial \rho}. \tag{2.21b}$$

The term $m = 0$, corresponding to the field of a solenoid, is best treated separately using other techniques [8]. It may be verified directly that the above solution satisfies $\nabla \times \mathbf{A} = \nabla\psi = \mathbf{B}$. Therefore $\mathbf{B} = \nabla \times \mathbf{A}$ represents the unique interior solution for the field associated with the boundary values B_ρ. By construction, $\mathbf{B}$ then satisfies $\nabla \cdot \mathbf{B} = 0$ and $\nabla \times \mathbf{B} = 0$.

To make use of this result in (1.29), the solution must be expressed in cartesian coordinates fixed relative to the body of the beam-line element. The transformation from polar coordinates (ρ, ϕ) to the usual transverse cartesian coordinates (x, y) can be written as

$$\rho e^{i\phi} = x + iy. \tag{2.22}$$

Using the above expression together with (2.19,2.21) we may expand each component of the vector potential $\mathbf{A}$ about the axis of the cylinder in the form of a polynomial

series as:

$$A_{\{x,y\}} = \sum_{m=1}^{\infty}\sum_{l=0}^{\infty} \kappa_{lm}\{x,y\}(x^2+y^2)^l(\mathcal{R}e(x+iy)^m C_{m,s}^{[2l+1]}(z) - \mathcal{I}m(x+iy)^m C_{m,c}^{[2l+1]}(z)), \tag{2.23}$$

$$A_z = \sum_{m=1}^{\infty}\sum_{l=0}^{\infty} \kappa_{lm}(2l+m)(x^2+y^2)^l(-\mathcal{R}e(x+iy)^m C_{m,s}^{[2l]}(z) + \mathcal{I}m(x+iy)^m C_{m,c}^{[2l]}(z)), \tag{2.24}$$

where the constant coefficients are given by

$$\kappa_{lm} = \frac{(-1)^l(m-1)!}{2^{2l}l!(l+m)!}. \tag{2.25}$$

The degree of a given term is given by $d = 2l + m + 1$ (transverse components) or $d = 2l + m$ (longitudinal component). Summing all polynomials through a fixed degree d, we find that the truncated approximation $\mathbf{A}^d$ to the vector potential satisfies $\nabla \times \nabla \times \mathbf{A}^d = \mathcal{O}(x,y)^{d-1}$, provided the on-axis gradients exactly satisfy the condition

$$C_{m,\alpha}^{[r]}(z) = \frac{d^r C_{m,\alpha}^{[0]}(z)}{dz^r}. \tag{2.26}$$

for each integer $r > 0$, as expected from (2.20). The curl $\nabla \times \mathbf{B}$ therefore vanishes through the desired degree $(d-2)$ with an accuracy that depends only on the Fourier transform used in computing (2.20).

2.2 Numerical Implementation

The method described in the previous section has been implemented by others [16],[4] in the code MaryLie. The Taylor coefficients appearing in (2.21) are used

in the routine GENMAP to compute the map by integrating the map equations (1.25,1.27). We refer the reader to [4] for details. In the present work, we construct a Mathematica routine to produce the on-axis gradients $C_{n,\alpha}(z)$ from surface data as a numerical illustration.

2.3 Benchmarks of Numerical Accuracy

2.3.1 Monopole-Pair Benchmark

It is required that the surface fitting procedure just described be capable of reproducing high derivatives of fields that are rapidly varying and have nontrivial fringe-field behavior. As a numerical benchmark, we require a soluble model magnetic field for which these quantities can be analytically determined. For this purpose, we treat the case of the field due to a pair of magnetic monopoles with charges $+g$ and $-g$ where $|g| = 0.3$ Tcm^2. The monopoles are chosen to lie outside the domain of interest at the locations $y = a = 2d$ and $y = -a = -2d$, respectively, where $d = 2.3504$ cm. (Fig 2.1) Parameters were chosen to generate an on-axis peak field strength of 27.15G, comparable to that of the CESR 8-pole wiggler 21.5G. In this case the various $C^{[n]}_{m,\alpha}$ can be determined analytically to all orders as follows.

The magnetic field is given in this case by $\mathbf{B} = \nabla\Psi$, where

$$\Psi(x,y,z) = \frac{g}{\sqrt{z^2+x^2+(y-a)^2}} - \frac{g}{\sqrt{z^2+x^2+(y+a)^2}} = \Psi_-(x,y,z) - \Psi_+(x,y,z). \tag{2.27}$$

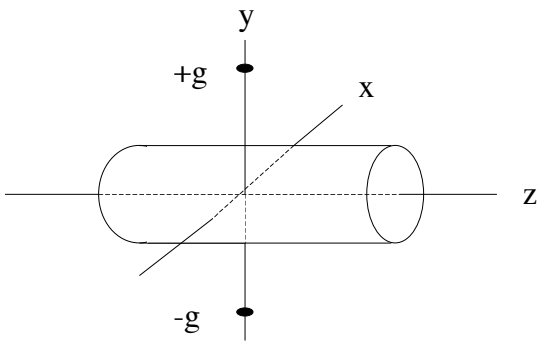

Figure 2.1: Fitting a monopole-pair field.

It is instructive to introduce the quantities

$$A = \frac{ay}{z^2 + a^2}, \quad B = \frac{x^2 + y^2}{z^2 + a^2} \tag{2.28}$$

so that

$$\Psi_-(x, y, z) = g(z^2 + a^2)^{-1/2} \frac{1}{\sqrt{1 - 2A + B}}, \tag{2.29}$$

and Ψ_+ is obtained under $a \to -a$. Noting the appearance of the generating function for the Legendre polynomials [23]

$$\frac{1}{\sqrt{1 - 2tu + t^2}} = \sum_{k=0}^{\infty} P_k(u) t^k, \tag{2.30}$$

it can be shown that Ψ is represented by the series

$$\Psi(x, y, z) = g(z^2 + a^2)^{-1/2} \sum_{n=0}^{\infty} Q_{2n+1}(x, y, z), \tag{2.31}$$

where each Q_n is a homogeneous polynomial of degree n in the variables (x, y) whose coefficients depend on z. The Q_n for odd n are given by

$$Q_n(x, y, z) = 2B^{n/2} P_n\left(\frac{A}{\sqrt{B}}\right), \tag{2.32}$$

where $Q_n(x, y, z)$ is odd in the variable y and even in the variable x. For example,

$$Q_1 = \frac{2ay}{z^2 + a^2}, \tag{2.33}$$

$$Q_3 = \frac{-3a^3x^2y + 2a^3y^3 - 3ax^2yz^2 - 3ay^3z^2}{(z^2 + a^2)^3}, \tag{2.34}$$

$$\begin{aligned} Q_5 = \frac{1}{4(z^2 + a^2)^5}(&15a^5x^4y - 40a^5x^2y^3 + 8a^5y^5 + 30a^3x^4yz^2 - 10a^3x^2y^3z^2 \\ &- 10a^3x^2y^3z^2 - 40a^3y^5z^2 - 40a^3y^5z^2 + 15ax^4yz^4 + 30ax^2y^3z^4 + 15ay^5z^4), \end{aligned} \tag{2.35}$$

etc. This expression (2.31) is to be compared with (2.9,2.19), written in terms of on-axis gradients. In cylindrical coordinates the functions Q_n become

$$Q_n(\rho, \phi, z) = 2\beta^n(z) \left(\frac{\rho}{a}\right)^n P_n(\beta \sin \phi), \tag{2.36}$$

where

$$\beta(z) = \frac{a}{\sqrt{z^2 + a^2}}. \tag{2.37}$$

Equating terms of degree n, for odd n, we have

$$2\frac{g}{a}\beta^{n+1}(z) \left(\frac{\rho}{a}\right)^n P_n(\beta \sin \phi) = \sum_{(l,m)\in S} (-1)^l \frac{m!}{2^{2l} l!(l + m)!} \rho^{2l+m} C_{m,s}^{[2l]}(z) \sin(m\phi) \tag{2.38}$$

where $S = \{(l, m) : 2l + m = n\}$. Due to the symmetry of the field, we find $C_{m,c}(z) = 0$ for all m. It can be seen from expansions of the form of (2.38) that we have nonvanishing contributions only for odd multipoles m, and

$$C_{n,s}(z) = \frac{2g\beta^{n+1}(z)}{\pi a^{n+1}} \int_0^{2\pi} P_n(\beta \sin \phi) \sin(n\phi) d\phi. \tag{2.39}$$

Evaluating the above integral, it can be shown that the nonvanishing on-axis gradients are given by:

$$C_{n,s}(z) \;=\; (-1)^{(n-1)/2} \frac{g}{a^{n+1}} \frac{(2n)!}{2^{2n-2}(n!)^2} \beta^{2n+1}(z) \tag{2.40}$$

where

$$\beta(z) = \frac{a}{\sqrt{z^2 + a^2}}. \tag{2.41}$$

It remains to discuss the domain of convergence for the homogeneous polynomial series (2.31). For fixed real u, the series for the generating function (2.30) converges in the domain $|t| < \min\{|u+\sqrt{u^2-1}|, |u-\sqrt{u^2-1}|\}$. In particular, for $-1 < u < 1$ the series converges for all $|t| < 1$. This corresponds to the domain defined by the condition $\sqrt{B} < 1$, where B is given in (2.28). We see that, for fixed z, the domain of convergence for the homogeneous series representing the field in terms of on-axis gradients is given by $\rho < \sqrt{z^2 + a^2}$, where $\rho = \sqrt{x^2 + y^2}$. In particular, the domain of convergence is a region of circular cross-section whose radius increases as we move longitudinally away from the location of the poles at $z = 0$. In Fig 2.2, we have provided a plot of the partial sum of the first 10 nonvanishing terms, corresponding to the sum of all polynomials through degree 19 in x and y. The sum is evaluated at $z = 0$, illustrating the region of convergence $\rho < a$.

Of interest is the fact that the radius of convergence for the gradient expansion is determined solely by the location of the sources of the field, and is independent of the boundary used to produce this series. Thus, the present result will also apply in the following two chapters on elliptical and rectangular cylinders.

We now apply these results as a numerical benchmark of the procedure described in the previous section. After a longitudinal Fourier transform, the trans-

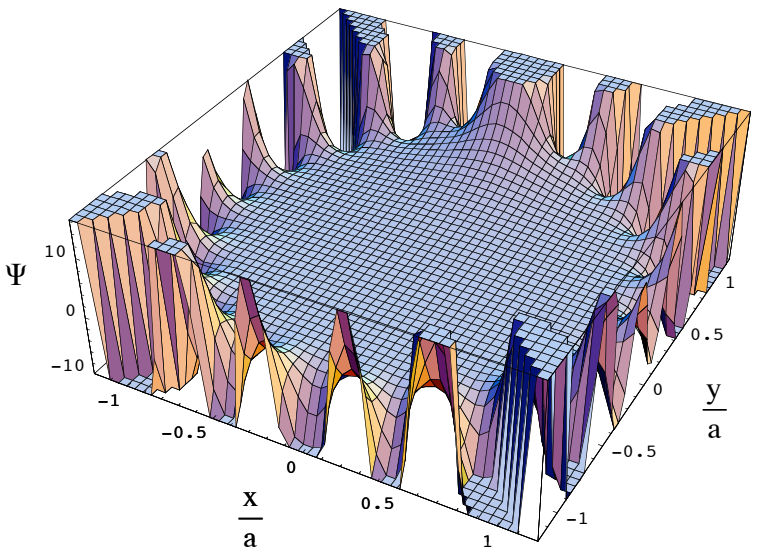

Figure 2.2: Plot of the partial sum of all terms through degree 19 of the homogeneous polynomial series (2.31), illustrating the disk of convergence $x^2 + y^2 < a^2$ at $z = 0$.

verse components of the field $\mathbf{B} = \nabla\psi$ given by (2.27) are

$$\tilde{B}_x = \left(\frac{2g}{\sqrt{2\pi}}\right) x|k| \left[\frac{K_1(a_1|k|)}{a_1} - \frac{K_1(a_2|k|)}{a_2}\right], \tag{2.42a}$$

$$\tilde{B}_y = \left(\frac{2g}{\sqrt{2\pi}}\right) |k| \left[(y-a)|k|\frac{K_1(a_1|k|)}{a_1} - (y+a)|k|\frac{K_1(a_2|k|)}{a_2}\right]. \tag{2.42b}$$

We use (2.42) to compute the normal component of the field $\tilde{B}$ at each point on the surface of a circular cylinder of radius $R = 1$. The coefficients $A_n(k_j)$ and $B_n(k_j)$ are then computed for an array of values n and $k_j = -k_{max} + (j-1)(\delta k)$ for $j = 1, 2, \cdots$. We use the cutoff value $k_{max} = 3$, sufficiently large to include the bulk of the spectral weight. Due to the symmetry of the field, the only nonvanishing coefficients are the $B_n(k_j)$ for n odd. These quantities may be used to construct the on-axis gradients from (2.20). The Fourier integral in (2.20) is computed using

Mathematica's "ListIntegrate" feature, which outputs the exact value of the integral of an interpolating polynomial of degree 3. This must be repeated for each z_i in some set $z_j = -L + jh$ for $j = 0, 1, \cdots$ extending sufficiently far to investigate the decay of the field away from its maximum at $z = 0$. These on-axis gradients, computed only from data on the surface of a cylinder, are then compared with the known analytic result (2.40). In Fig. 2.3 we have illustrated the functions $C_1(z)$, $C_3(z)$, $C_5(z)$, and $C_3^{[2]}(z)$, and the corresponding numerical results. Figure 2.4 illustrates the error relative to peak in the computed on-axis gradient functions, which results from approximating the Fourier integrals appearing in (2.20). Errors are on the order of 10^{-6} for the gradient C_1, and increase to 10^{-3} for the gradient $C_3^{[2]}$.

2.4 Insensitivity to Numerical Noise

2.4.1 Theory of Smoothing

By the mean value property of harmonic functions H on a domain Ω, at each $x_0 \in \Omega$ we have

$$H(x_0) = \frac{1}{4\pi\mathcal{R}^2} \int_S H(x) dS \tag{2.43}$$

where $S = S(x_0, \mathcal{R}) \subseteq \Omega$ is a sphere of radius $\mathcal{R}$ centered at the point $x = x_0$. If errors over the surface S are assumed to be randomly distributed with a mean near zero, we expect these errors to contribute little to the value $H(x_0)$ obtained by averaging over the surface of the sphere S. This straightforward averaging is a unique property of a spherical boundary geometry, but similar smoothing behavior occurs for other geometries, with the appearance of a more complex integration

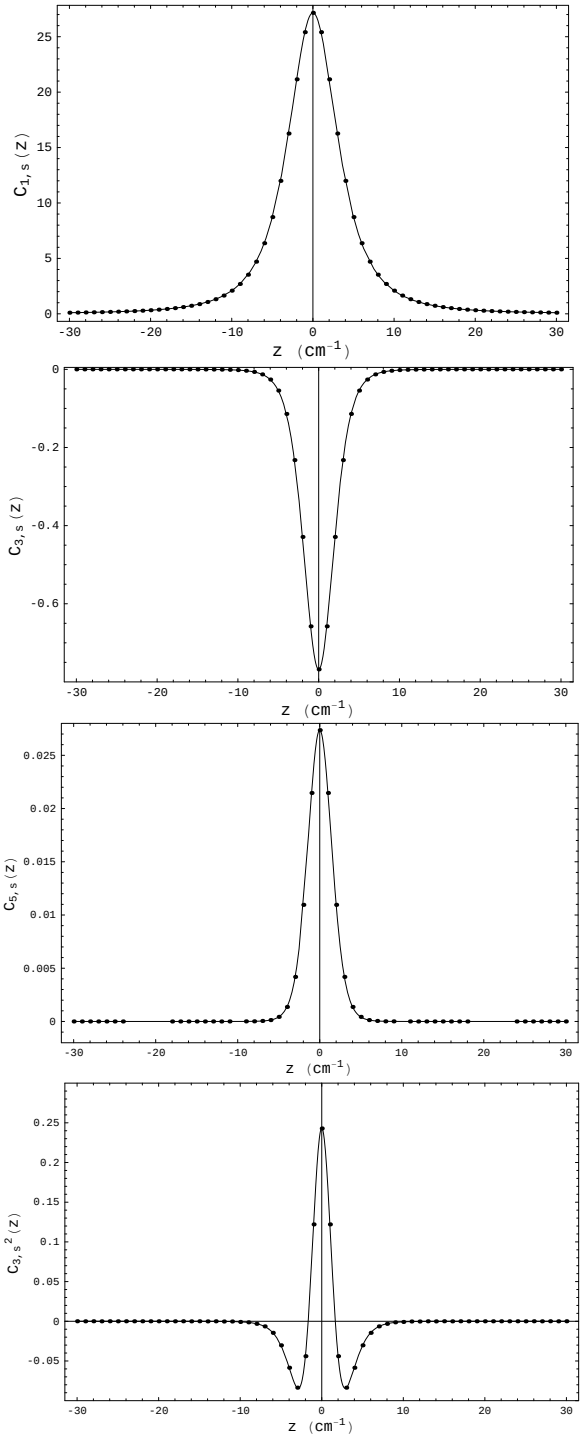

Figure 2.3: On-axis gradient functions $C_{1,s}$, $C_{3,s}$, $C_{5,s}$, and $C^{[2]}_{3,s}$ for the monopole-pair field. Solid lines denote the exact results of (2.40). Dots denote values computed by fitting onto the surface of a circular cylinder.

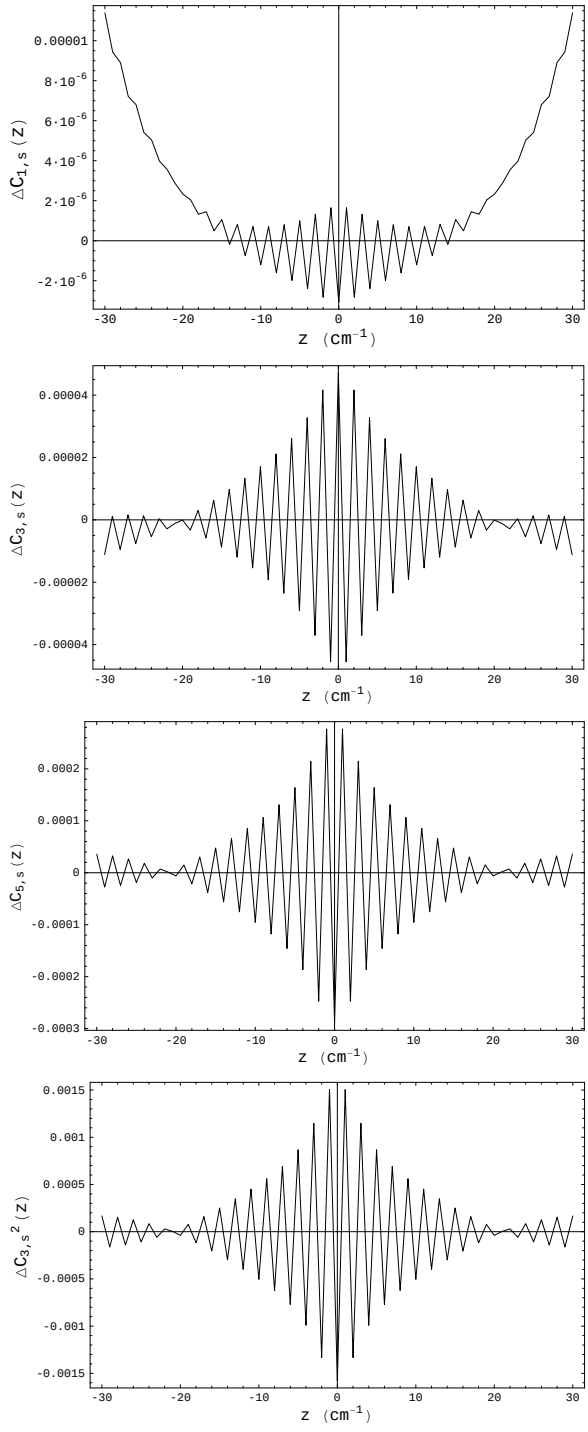

Figure 2.4: Error in the computed on-axis gradient functions $C_{1,s}$, $C_{3,s}$, $C_{5,s}$, and $C_{3,s}^{[2]}$, measured relative to peak values.

kernel corresponding to the Green's function for the domain Ω. We illustrate this smoothing mechanism for the geometry of a circular cylinder as follows.

Suppose data are provided on a lattice of regularly spaced mesh points separated by a characteristic distance h. The fitted field on the surface (including numerical errors) may be represented in terms of its Fourier components as

$$B_\rho^{fit}(R,\phi,z) = \sum_{m=0}^{\infty} \frac{1}{\sqrt{2\pi}} \int_{-\infty}^{\infty} dk e^{ikz} \left[\tilde{B}_m(R,k)\sin(m\phi) + \tilde{A}_m(R,k)\cos(m\phi) \right], \tag{2.44}$$

where k characterizes the frequency of variations in z, while the order of the multipole m characterizes the frequency of variations in ϕ. As illustrated in Appendix A, the presence of noise in the values B_ρ on the cylinder surface in the form of random measurement/numerical errors will introduce error in the high-frequency tails of the Fourier coefficients $\tilde{B}_m(k)$ and $\tilde{A}_m(k)$, adding weight to these coefficients for large k and m that is not present in the true solution. We will see that the integration of the surface coefficients $\tilde{B}_m$ and $\tilde{A}_m$ against the kernel of the inverse Laplacian will lead to an attenuation of these high-frequency Fourier components, leaving interior values insensitive to variations in the surface data.

To motivate the following discussion, we illustrate this phenomenon with a simpler example. Consider solving the Dirichlet problem for ψ in the domain Ω given the values $\psi|_{\partial\Omega}$ on the surface $\partial\Omega$ of the cylinder. The value ψ^{fit} on the cylinder surface may be represented in terms of its Fourier components as:

$$\psi^{fit}(R,\phi,z) = \sum_{m=0}^{\infty} \frac{1}{\sqrt{2\pi}} \int_{-\infty}^{\infty} dk e^{ikz} \left[\tilde{C}_m(R,k)\sin(m\phi) + \tilde{D}_m(R,k)\cos(m\phi) \right]. \tag{2.45}$$

Using (2.8) we see that the interior solution for ψ is given by

$$\psi^{fit}(\rho,\phi,z) = \sum_{m=0}^{\infty} \frac{1}{\sqrt{2\pi}} \int_{-\infty}^{\infty} dk e^{ikz} \frac{I_m(k\rho)}{I_m(kR)} \left[\tilde{C}_m(R,k)\sin(m\phi) + \tilde{D}_m(R,k)\cos(m\phi)\right]. \tag{2.46}$$

Now consider a smaller co-axial cylinder of fixed radius $\rho < R$, interior to Ω. The solution ψ^{fit} may be represented in terms of its Fourier components on the surface of the smaller cylinder as

$$\psi^{fit}(\rho,\phi,z) = \sum_{m=0}^{\infty} \frac{1}{\sqrt{2\pi}} \int_{-\infty}^{\infty} dk e^{ikz} \left[\tilde{C}_m(\rho,k)\sin(m\phi) + \tilde{D}_m(\rho,k)\cos(m\phi)\right] \tag{2.47}$$

where

$$\tilde{C}_m(\rho,z) = \eta_m(k)\tilde{C}_m(R,k), \qquad \tilde{D}_m(\rho,k) = \eta_m(k)\tilde{D}_m(R,k) \tag{2.48}$$

and

$$\eta_m(k) = \frac{I_m(k\rho)}{I_m(kR)}. \tag{2.49}$$

Each Fourier coefficient has now been multiplied by an associated *attenuation factor* $\eta_m(k)$. Using the asymptotic behavior of the modified Bessel functions I_m [22], it can be shown that $\eta_m(k)$ behaves for fixed m and large k as

$$\eta_m(k) \sim e^{-k(R-\rho)}\sqrt{\frac{R}{\rho}}, \tag{2.50}$$

provided $\rho \neq 0$. The coefficients $\tilde{C}_m(\rho,k)$, $\tilde{D}_m(\rho,k)$ at large k are therefore exponentially suppressed relative to their values on the cylinder of radius R. Similarly, for fixed k and large m we have

$$\eta_m(k) \sim e^{-m\tau} \tag{2.51}$$

where $\tau = \log(R/\rho) > 0$, and the coefficients for high-order multipoles m are exponentially suppressed relative to their values on the cylinder of radius R. Furthermore, this rate of suppression increases as we move farther inward from the surface (as ρ decreases). In the limiting case $\rho = 0$, along the axis, we have $I_m(k\rho) = 0$ for all $m \neq 0$ and

$$\eta_0(k) = \frac{1}{I_0(kR)}, \qquad \eta_m(k) = 0 \quad \text{for } m \neq 0. \tag{2.52}$$

We now return to expression (2.44). Given surface values B_ρ, the solution of the Neumann problem for ψ in the interior was obtained in (2.9,2.17). A similar attenuation of Fourier coefficients occurs in this case, with

$$\tilde{B}_m(\rho, z) = \nu_m(k)\tilde{B}_m(R, k), \qquad \tilde{A}_m(\rho, k) = \nu_m(k)\tilde{A}_m(R, k), \tag{2.53}$$

where the attenuation coefficients are now given by:

$$\nu_m(k) = \frac{I_m(k\rho)}{kI'_m(kR)} \tag{2.54}$$

with behavior for large k and large m given by

$$\nu_m(k) \sim \frac{e^{-k(R-\rho)}}{k}\sqrt{\frac{R}{\rho}} \quad \text{and} \tag{2.55}$$

$$\nu_m(k) \sim e^{-n\tau}\frac{R}{n} \tag{2.56}$$

respectively. Note that the units of the boundary values B_ρ and the interior solution ψ are different in this case, so the various $\nu_m(k)$ have units of distance. In addition, $\nu_m(k) \neq 1$ when $\rho = R$.

Finally, we consider the effect of smoothing on the on-axis gradient functions $C_n^{[m]}(z)$, which characterize various derivatives of the vector potential. Note that we

may write

$$C_{m,s}(z) = \frac{1}{\sqrt{2\pi}} \int_{-\infty}^{\infty} dk e^{ikz} \Lambda_{cir}^{m}(k) \tilde{B}_m(R,k), \tag{2.57a}$$

$$C_{m,c}(z) = \frac{1}{\sqrt{2\pi}} \int_{-\infty}^{\infty} dk e^{ikz} \Lambda_{cir}^{m}(k) \tilde{A}_m(R,k), \tag{2.57b}$$

where the integration kernels Λ_{cir}^{m} are given by:

$$\Lambda_{cir}^{m}(k) = \frac{1}{2^m m!} \frac{k^{m-1}}{I'_m(kR)}. \tag{2.58}$$

A plot of the first 6 kernels with $m = 1 \cdots 6$ is provided in Fig 2.5. Each kernel is of constant sign, and attains its maximum at $k = 0$ of value $1/mR^{m-1}$, with the exception of Λ^0, which diverges as $\Lambda^0 \sim 2/k^2 R$ near $k \approx 0$. The kernels decrease monotonically as $|k| \to \infty$.

Using the asymptotic series for large $\zeta >> 1$ and fixed order m [22],

$$I'_m(\zeta) \sim \frac{e^{\zeta}}{\sqrt{2\pi\zeta}} \{1 - \frac{4m^2+3}{8\zeta} + O(\frac{1}{\zeta^2})\}, \tag{2.59}$$

we see that the kernels decay for large frequencies as

$$\Lambda_{cir}^{n}(k) \sim \frac{1}{2^n n!} \sqrt{2\pi R} k^{m-1/2} e^{-kR} (1 + O((kR)^{-1})). \tag{2.60}$$

The kernel Λ_{cir}^{m} therefore serves as a low-pass filter in (2.57) to minimize the weight that the coefficients $\tilde{B}_m(R,k)$, $\tilde{A}_m(R,k)$ contribute to the functions $C_{m,s}$ and $C_{m,c}$ for large k. For this reason, the behavior of noise on the boundary has little influence on the interior solution in terms of the $C_{r,\alpha}^{[m]}$. Furthermore, we see from (2.60) that the amount of smoothing attenuation at a fixed k increases exponentially with the radius R of the bounding cylinder.

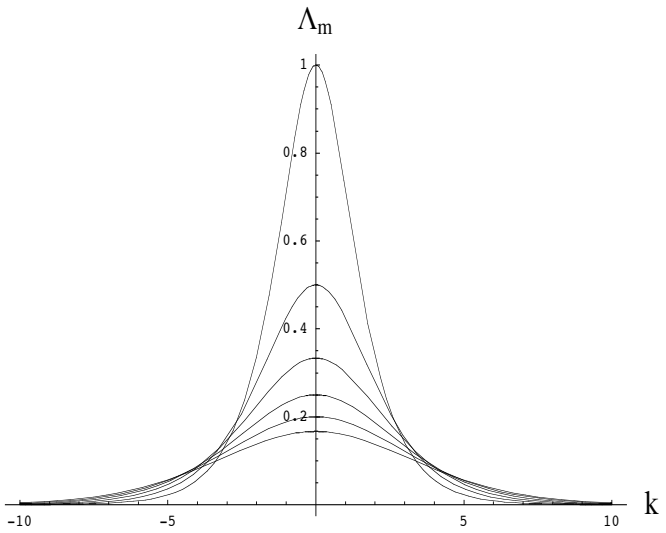

Figure 2.5: Illustration of the first 10 kernels Λ_{cir}^m for a cylinder with $R = 1$. Peak values decrease with increasing index m.

2.4.2 Error Estimates

In this section we obtain estimates for the error in the computed interior field and its derivatives. We will see that the error in the field and each of its Taylor coefficients is globally bounded by a factor that is set by errors in the surface data. Let $\psi^{(bv)}$ denote the interior solution (2.19,2.20) obtained from boundary-value data, which may contain numerical errors. By construction, $\nabla^2\psi^{(bv)} = 0$ and the error function $E = \psi^{(bv)} - \psi$ is harmonic on the interior of the cylinder Ω. By the maximum principle (Appendix H), we know that the error must attain its extrema on the boundary of the cylinder. That is,

$$|E(x)| \leq \sup_{\partial\Omega} E \tag{2.61}$$

at all points x in Ω. Since we have done a controlled fit of data onto the circular cylindrical boundary, it follows that the interior error is globally controlled.

We are also interested in derivatives of ψ. While derivatives of the interpolated field on the boundary need not exist, the interior solution is smooth by construction. A bound on each derivative is provided as follows [93],[96]. Suppose we let $M = \sup_{\partial\Omega} E$. Given any point $x \in \Omega$ in the interior of the cylinder, suppose we surround x with an open ball $B(x, r)$. We choose the largest radius r such that $B(x, r) \subseteq \Omega$, so that r represents the distance from x to the cylindrical boundary. Then for each derivative D^α, there is a constant C such that

$$|D^\alpha E(x)| \leq CMr^{-|\alpha|} \tag{2.62}$$

where C depends only on the order $|\alpha|$ of the derivative. (In fact $C = (3|\alpha|)^{|\alpha|}$. See Section H.3.1.). It follows that the fit improves as we move inward from the bounding surface.

We now wish to establish careful error estimates for the on-axis gradients appearing in (2.20). We estimate the rms error of each function $C_n^{[m]}(z)$ as follows. Let the fitted normal component of the field on the surface be given by $B_\rho^{(bv)}$. Defining the surface error

$$\tilde{E}(\phi, k) = \tilde{B}_\rho^{(bv)}(\phi, k) - \tilde{B}_\rho(\phi, k), \tag{2.63}$$

let

$$f_n(k) = B_n^{(bv)}(R, k) - B_n(R, k) \text{ and} \tag{2.64}$$

$$g_n(k) = A_n^{(bv)}(R, k) - A_n(R, k) \tag{2.65}$$

be the resulting errors in the upright and skew multipole coefficients, respectively. We may then write the error on the boundary as

$$\tilde{E}(\phi, k) = \sum_{n=0}^{\infty} [f_n(k) \sin(n\phi) + g_n(k) \cos(n\phi)]. \tag{2.66}$$

The error in a given on-axis gradient in this case is given by

$$\begin{aligned} \Delta\tilde{C}_{n,s}^{[m]}(z) &= \int_{-\infty}^{\infty} dk e^{ikz} (ik)^m \Lambda_{cir}^n(k) f_n(k), & (2.67) \\ \Delta\tilde{C}_{n,c}^{[m]}(z) &= \int_{-\infty}^{\infty} dk e^{ikz} (ik)^m \Lambda_{cir}^n(k) g_n(k). & (2.68) \end{aligned}$$

Using Parseval's theorem,

$$\int_{-\infty}^{\infty} |\Delta C_{n,s}(z)|^2 dz = \int_{-\infty}^{\infty} |\Delta\tilde{C}_{n,s}(k)|^2 dk. \tag{2.69}$$

Due to the rapid decay of the kernel Λ_{cir}^n, the norm of the absolute difference $\Delta C_{n,s}$ over all z is finite and strictly bounded above (for $n \neq 0$) by

$$\begin{aligned} ||\Delta C_{n,s}||^2 &= \int_{-\infty}^{\infty} |\Lambda_{cir}^n(k) f_n(k)|^2 dk < \max_k |\Lambda_{cir}^n|^2 \int_{-\infty}^{\infty} |f_n(k)|^2 dk \\ &= \frac{||f_n||^2}{(nR^{n-1})^2} \leq \left(\frac{1}{nR^{n-1}}\right)^2 ||E||_\Gamma^2, & (2.70) \end{aligned}$$

where $||E||_\Gamma$ is the norm of the error over the surface of the cylinder, given by

$$||E||_\Gamma = \left[\int_{-\infty}^{\infty} dz \int_{-\pi}^{\pi} d\phi |E(\phi, z)|^2\right]^{1/2}. \tag{2.71}$$

In order to obtain a reasonable estimate of this error, we assume that the surface errors are described by the model of noise described in Appendix A. Note that each error coefficient $f_j(k)$ for fixed k is a normal random variable dependent on the realization of the error over the surface of the cylinder. In this case, we may

estimate rms error by averaging over an ensemble of surface values as follows. For fixed k,

$$\langle|\Delta\tilde{C}_{n,s}(k)|^2\rangle = \langle|\Lambda^n_{cir}(k)f_n(k)|^2\rangle = \langle|f_j(k)|^2\rangle|\Lambda^n_{cir}(k)|^2. \tag{2.72}$$

Using the known k dependence of $\langle|f_j(k)|^2\rangle$ we estimate the error by averaging:

$$\overline{\langle||\Delta C_{n,s}||^2\rangle} = \overline{\int_{-\infty}^{\infty}\langle|f_j(k)|^2\rangle|\Lambda^n_{cir}(k)|^2dk} = \overline{\langle|f_j(k_p)|^2\rangle}\int_{-\kappa}^{\kappa}|\Lambda^n_{cir}|^2dk, \tag{2.73}$$

where the cutoff $k = \kappa$ is placed at the inverse scale of the correlation length of the noise E, which we take to be the longitudinal mesh spacing h such that $\kappa = \pi/h$.

Assuming the model of white noise described in Appendix A, and letting $\sigma^2 = \langle|B_\rho(R, \phi_j, z_k)|^2\rangle$ denote the size of the errors on the surface, we have

$$\langle|f_j(k)|^2\rangle = \frac{hL}{\pi^2}(\delta v)\sigma^2 \tag{2.74}$$

where L is the length of the domain, and h, δv are the longitudinal and azimuthal stepsizes, respectively. Therefore, using (2.73) we find

$$\overline{\langle||\Delta C_{n,s}||^2\rangle} = \frac{L}{\pi^2}(h\delta v)\sigma^2\int_{-\kappa}^{\kappa}|\Lambda^n_{cir}|^2dk, \tag{2.75}$$

where the integral on the right is of order 1 for the kernels of interest. In particular, fitting to a cylinder of radius $R = 1$ with a stepsize of $h = 0.1$cm and $\delta v = \pi/40$ yields an expected error

$$(\Delta C_{5,s}(z))_{rms} = \sqrt{\frac{1}{\pi^2}(h\delta v)\sigma^2\int_{-\kappa}^{\kappa}|\Lambda^n_{cir}|^2dk} = 0.025\sigma. \tag{2.76}$$

Finally, assume that we have fit field values onto a circular cylinder from a rectangular mesh with coordinates uniformly spaced in x and y with spacing

$\Delta x = \Delta y$, and uniformly spaced in z with spacing h. We determine the scale of azimuthal variation $\delta\phi$ corresponding to the mesh spacing Δx by writing

$$\Delta x \approx \left(\frac{\partial x}{\partial y}\right)\delta\phi + \left(\frac{\partial x}{\partial \rho}\right)\delta\rho = -y(\delta\phi) \tag{2.77}$$

for fixed $\rho = R$. Averaging over the cylinder,

$$\langle \Delta x^2 \rangle = \frac{\delta\phi}{2\pi}\int_{-\pi}^{\pi} y^2 d\phi = \rho^2(\delta\phi)^2/2 \text{ gives} \tag{2.78}$$

$$\delta\phi \approx \frac{\Delta x\sqrt{2}}{R}. \tag{2.79}$$

We may then define the scaled smoothing envelope

$$g_s(k) = \frac{1}{R}\sum_{p=0}^{N} |\Lambda_p^n(k)|^2 \tag{2.80}$$

so that

$$\langle ||\Delta C_{n,s}||^2 \rangle = \frac{hL\Delta x\sqrt{2}}{\pi^2}\sigma^2 \int_{-\kappa}^{\kappa} g_s(k)dk. \tag{2.81}$$

This quantity will reappear in the study of smoothing in Chapters 3-4. The smoothing envelope illustrates the suppression of high-frequency noise.

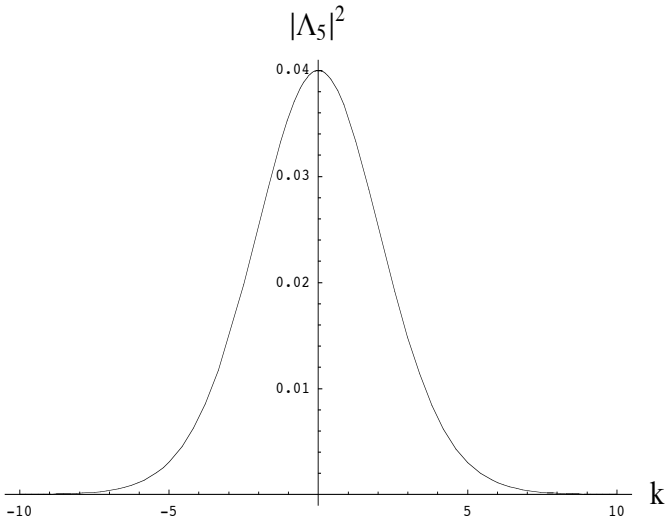

Figure 2.6: Illustration of the smoothing envelope for the gradient $C_5(z)$ due to fitting using a circular cylinder of radius $R = 1$.

Chapter 3

Use of Elliptic Cylinder Surface

The high accuracy and insensitivity to noise claimed for the method described in Chapter 2 are improved by choosing the radius R of the bounding circular cylinder to be as large as possible. In some cases, however, the domain of interest is restricted in one dimension, limiting both the size of the available domain and the number of data points available on the bounding surface. We consider, in particular, field data supplied in the domain between pole faces of wiggler or undulator magnets with small gap and wide poles (Fig. 3.1).

Simulations indicate that the dynamic aperture of damping rings and light sources is critically dependent on the nonlinear properties of their wiggler/undulator transfer maps, due to the strong nonlinearity of the wiggler field [60]. The computation of single-particle transfer maps through wigglers and undulators has often employed idealized wiggler models (Appendix E). However, wiggler transfer maps can in general depend sensitively on fringe-field and high-multipole effects. The inclusion of these effects requires a detailed and realistic model of the interior and fringe magnetic fields, including knowledge of high spatial derivatives. In the present chapter we explore the advantages of computing these transfer maps using data on the surface of a cylinder with *elliptical* cross-section. This approach preserves the desirable features of the approach described in Chapter 2, using circular cylinder

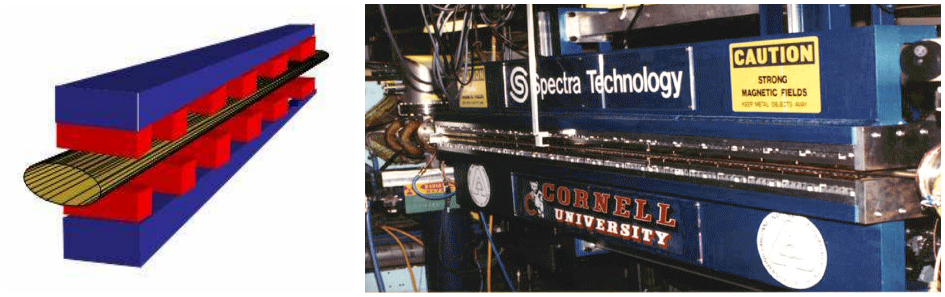

Figure 3.1: (Left) An elliptical cylinder fitting between the pole faces, having large major axis, and extending beyond the fringe-field region. (Right) Photo of the CHESS-APS 3.3 cm period, 123-pole undulator. The undulator is part of a synchrotron x-ray source planned for use at the Argonne Advanced Photon Source. Courtesy of Cornell University.

surfaces, while it improves insensitivity to errors in the boundary data by exploiting the wide pole-face geometry.

As an application, we have produced a transfer map for the proposed ILC (CESR-c type) wiggler using data provided by finite element computations [55]. Cornell, by utilizing the Vector Fields 3-d code OPERA, provided values of $\mathbf{B}$ on a rectangular mesh along the full length of the wiggler including the fringe-field regions. The normal component of $\mathbf{B}$ on the surface of the elliptical cylinder was obtained by interpolation using polynomial splines. This normal component on the surface was then used to compute the desired interior expansion for $\mathbf{A}$ using the scalar potential as an intermediate quantity.

3.1 Analytic Formulation

3.1.1 Determination of the Vector Potential

In a current-free region we work with a scalar potential ψ satisfying $\mathbf{B} = \nabla\psi$. We work in elliptic cylindrical coordinates, defined by the intersection of confocal ellipses with confocal hyperbolae (Fig. 3.2). Such coordinates are defined as follows:

$$x = f\cosh(u)\cos(v), \tag{3.1}$$

$$y = f\sinh(u)\sin(v), \tag{3.2}$$

$$z = z, \tag{3.3}$$

where f is the distance from the origin to the two foci at $(-f, 0)$ and $(f, 0)$. Here $u \in [0, \infty)$ plays the role of a radial coordinate, and $v \in [0, 2\pi)$ plays the role of an angular coordinate. Letting $\zeta = x+iy$ and $\eta = u+iv$, the coordinate transformation can be written as $\zeta = \mathcal{F}(\eta) = f\cosh\eta$. We denote the corresponding Jacobian as $J(u, v) = |\mathcal{F}'(\eta)|^2 = f^2(\cosh 2u - \cos 2v)/2$.

The scalar potential must satisfy $\nabla^2\psi = \nabla\cdot\mathbf{B} = 0$. Therefore, we may write $(\nabla_\perp^2 - k^2)\tilde{\psi}(u, v, k) = 0$ where

$$\tilde{\psi}(u, v, k) = \frac{1}{\sqrt{2\pi}}\int_{-\infty}^{\infty}\psi(u, v, z)e^{-ikz}dz, \tag{3.4}$$

and search for product solutions of the form $\tilde{\psi}(u, v, k) \propto U(u)V(v)$ in terms of orthogonal functions. As shown in Appendix D, the general solution of Laplace's equation in elliptic cylindrical coordinates takes the form [20]:

$$\psi = \sum_{m=0}^{\infty}\int_{-\infty}^{\infty}dke^{ikz}\left[\alpha(k)Ce_m(u, q)\,ce_m(v, q) + \beta(k)Se_m(u, q)\,se_m(v, q)\right] \tag{3.5}$$

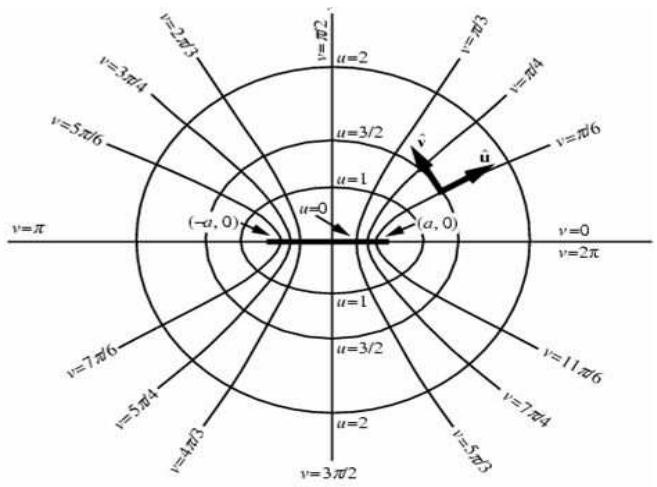

Figure 3.2: Illustration of elliptic cylindrical coordinates (u, v, z) in a plane $z =$ constant.

where we let $q = -\frac{k^2 f^2}{4}$. Here $ce_m(v, q)$ and $se_m(v, q)$ are Mathieu functions, while $Ce_m(u, q)$ and $Se_m(u, q)$ are modified Mathieu functions. Properties of these functions are described in detail in Appendix D. We refer to (3.5) as an"elliptic multipole" expansion, in analogy with the cylindrical case. In Chapter 2 it was shown that finding Taylor expansions for the vector potential components A_x, A_y, and A_z is equivalent to finding Taylor expansions for the coefficients $\psi_{m,s}$, $\psi_{m,c}$ in the cylindrical multipole expansion. A similar technique applies in this case, using the above expansion. In the remainder of this Chapter we show the following: how coefficients in the elliptic multipole expansion are related to coefficients in the cylindrical multipole expansion, how on-axis generalized gradients can be obtained from field data on the surface of a bounding elliptic cylinder, and how accuracy and insensitivity to noise are affected by the choice of boundary geometry. A numerical test and application to wiggler-magnet design follows.

3.1.2 Computation of Generalized Gradients from Field Data

Consider an infinite cylinder of elliptical cross-section with axis along the z-axis defined by the equation $u = U$, where U is a constant. The cylinder is characterized by the pair of parameters (U, f). We let Ω denote the domain interior to the elliptic cylinder. Suppose that B_u, the component of the magnetic field normal to the surface, is known at all points on the surface. This defines a boundary-value problem for ψ in the domain Ω with Neumann boundary conditions, and the magnetic field in the interior is determined by its values on the surface of the cylinder. As noted in Appendix D, the Mathieu functions $se_m(v, q)$ and $ce_m(v, q)$ form a complete orthogonal set on the interval $[-\pi, \pi]$. It follows that we may write, after performing a Fourier transform in the variable z,

$$\tilde{B}_u(u = U, v, k) = [\sqrt{J(U, v)}]^{-1} \partial_u \psi(u, v, k)\Big|_{u=U}, \tag{3.6}$$

$$\partial_u \psi(u, v, k)|_{u=U} = \sum_{m=1}^{\infty} [F_m(U, k) se_m(v, q) + G_m(U, k) ce_m(v, q)], \tag{3.7}$$

where we refer to F_m and G_m as odd and even angular Mathieu coefficients, respectively. Again we have defined $q = -\frac{k^2 f^2}{4}$. Orthogonality allows us to write

$$F_m(U, k) = \frac{1}{\pi} \int_0^{2\pi} \sqrt{J(U, v)} \tilde{B}_u(u = U, v, k) se_m(v, q) dv, \tag{3.8}$$

$$G_m(U, k) = \frac{1}{\pi} \int_0^{2\pi} \sqrt{J(U, v)} \tilde{B}_u(u = U, v, k) ce_m(v, q) dv. \tag{3.9}$$

Given the functions F_m and G_m on the boundary, we may construct the Fourier transform of the interior solution as follows:

$$\tilde{\psi}(u, v, k) = \sum_{m=0}^{\infty} \left[\frac{F_m(U, k)}{Se'_m(U, q)} \right] Se_m(u, q) se_m(v, q) + \left[\frac{G_m(U, k)}{Ce'_m(U, q)} \right] Ce_m(u, q) ce_m(v, q). \tag{3.10}$$

Since ψ is a harmonic function, we know that $\psi(x,y,z)$ is a real-analytic function of the variables x and y, and so is $\tilde{\psi}(x,y,k)$. It remains to construct a power series in the variables x, y. Through use of the Mathieu-Bessel relations described in Appendix D.2, we have the result

$$\begin{aligned}\tilde{\psi}(u,v,k) &= \sum_{m=0}^{\infty}\sum_{r=0}^{\infty}\left[\frac{F_m(U,k)}{Se'_m(U,q)}\right] g_s^m(k)B_r^{(m)}(k)I_r(k\rho)\sin(r\phi) \\ &+ \left[\frac{G_m(U,k)}{Ce'_m(U,q)}\right] g_c^m(k)A_r^{(m)}(k)I_r(k\rho)\cos(r\phi), \end{aligned} \tag{3.11}$$

where the coefficients g_s^m, g_c^m are given in (D.72). The quantities $A_r^{(m)}$ and $B_r^{(m)}$ are Fourier coefficients of the Mathieu functions ce_m and se_m, as defined in (D.10). It is important to note that $A_r^{(m)}$ and $B_r^{(m)}$ are nonzero only if the indices r, m are both even or the indices r, m are both odd. (That is, $r \bmod 2 = m \bmod 2$). All other terms appearing in (3.11) must vanish. Interchanging the order of the sums appearing in (3.11) we obtain

$$\tilde{\psi}(u,v,k) = \sum_{r=0}^{\infty}\{\beta_{\bar{r}}(U,k)I_r(k\rho)\sin(r\phi) + \alpha_r(U,k)I_r(k\rho)\cos(r\phi)\}, \tag{3.12}$$

where

$$\beta_r(U,k) = \sum_{m=0}^{\infty} g_s^m(k)B_r^{(m)}(k)\left[\frac{F_m(U,k)}{Se'_m(U,q)}\right], \tag{3.13}$$

$$\alpha_r(U,k) = \sum_{m=0}^{\infty} g_c^m(k)A_r^{(m)}(k)\left[\frac{G_m(U,k)}{Ce'_m(U,q)}\right]. \tag{3.14}$$

Nonvanishing contributions to the above sums occur for even m, if r is even, or odd m, if r is odd.

Using the Taylor expansion for $I_m(w)$ gives a power series in the variable ρ as in (2.19),

$$\psi_{m,\alpha}(\rho,z) = \sum_{l=0}^{\infty}(-1)^l\frac{m!}{2^{2l}l!(l+m)!}C_{m,\alpha}^{[2l]}(z)\rho^{2l+m}, \tag{3.15}$$

where the on-axis gradients are given by

$$C_{r,s}^{[m]}(z) = \frac{i^m}{2^r r!}\frac{1}{\sqrt{2\pi}}\int_{-\infty}^{\infty} k^{r+m} e^{ikz}\beta_r(U,k)dk, \tag{3.16a}$$

$$C_{r,c}^{[m]}(z) = \frac{i^m}{2^r r!}\frac{1}{\sqrt{2\pi}}\int_{-\infty}^{\infty} k^{r+m} e^{ikz}\alpha_r(U,k)dk. \tag{3.16b}$$

We may now obtain Taylor series in x and y for the scalar potential ψ and its derivatives. Using relations identical to those in the cylindrical case discussed in Section 2.1.1, we may obtain a power series for $\mathbf{A}$ with z-dependent coefficients determined by the generalized on-axis gradients. In the gauge $A_\phi = 0$,

$$A_z = \sum_{m=1}^{\infty}\sum_{l=0}^{\infty}\frac{(-1)^l(2l+m)(m-l)!}{2^{2l}l!(l+m)!}(x^2+y^2)(-\mathcal{R}e(x+iy)^m C_{m,s}^{[2l]}(z) + \mathcal{I}m(x+iy)^m C_{m,c}^{[2l]}(z)), \tag{3.17}$$

$$A_\rho = \sum_{m=1}^{\infty}\sum_{l=0}^{\infty}\frac{(-1)^l(2l+m)(m-l)!}{2^{2l}l!(l+m)!}(x^2+y^2)^{\frac{3}{2}}(-\mathcal{R}e(x+iy)^m C_{m,s}^{[2l]}(z) + \mathcal{I}m(x+iy)^m C_{m,c}^{[2l]}(z)). \tag{3.18}$$

From (3.17) and (3.18) we may in turn obtain expansions for $\mathbf{B}$ in terms of on-axis gradients. For example, in the case of midplane symmetry, the vertical field takes the form:

$$\begin{aligned} B_y = C_1(z) + 3C_3(z)(x^2-y^2) - \frac{1}{8}C_1^{[2]}(x^2+3y^2) \\ +\frac{1}{192}C_1^{[4]}(z)(x^4+6x^2y^2+5y^4) - \frac{1}{16}C_3^{[2]}(z)(3x^4+6x^2y^2-5y^4) \\ +C_5(z)(5x^4-30x^2y^2+5y^4) + O(x,y)^5. \end{aligned} \tag{3.19}$$

We have similar expressions for the other components of $\mathbf{B}$.

We have seen that the on-axis gradients specify the field completely, and are obtained using only information about the field on the elliptic cylindrical boundary.

Maxwell's equations are satisfied by construction. It remains to demonstrate convergence of the represented sums (3.13,3.14,3.15) and to establish reasonable cutoffs for numerical computation.

3.2 Numerical Implementation

The previous method has been implemented in the code MaryLie [4] as a Fortran 90 user-defined routine. The routine accepts as input magnetic field data provided on a three-dimensional grid with uniformly spaced mesh points of the form $(x_0 + jh_x, y_0 + kh_y, z_0 + lhz)$ for integers j, k, and l. The mesh spacing along each direction h_x, h_y, and h_z is set internally. The data may be provided in tabular form with columns (z, x, y, B_z, B_x, B_y) as provided by the Vector Fields software OPERA-3d. The input parameters (U, f) define the boundary geometry. Required in addition are parameters specifying the cutoff for the Fourier transform and the number of sampled values in v used for computation of the angular Mathieu coefficients. The routine produces as output, as desired, either the on-axis gradients $C_n^{[m]}(z)$ or the coefficients of the vector potential series $\mathbf{A}(x, y, z)$. These coefficients may then be used in the MaryLie routine GENMAP to compute maps.

The routine has several features designed to minimize sources of error. The fit for each transverse component B_α, with $\alpha = x, y$, of the field data from the initial mesh onto the surface of the elliptical cylinder is obtained using interpolation by polynomial (cubic) splines. The values B_α are then computed at uniformly-spaced values of v and z over the surface of the elliptical cylinder. The use of interpolating

splines ensures that the error due to fitting onto the surface is controlled and may be estimated if necessary. In addition, the approximation of mesh data by splines provides preliminary smoothing of the angular dependence of the data, improving convergence of the Fourier-type series (D.10).

Use of (3.8,3.9) requires a Fourier transform of the field values $B_u(U, v, z)$ in the variable z for each value of the azimuthal coordinate v. The use of such a large number of Fourier transforms can be quite slow, providing a bottleneck for computation time. For this reason, we developed a *fast* Filon-spline algorithm, a generalization of the fast Fourier transform, for producing improved Fourier transforms of discrete data. The use of such an algorithm is described in detail in Appendix C.

Extensive computation with Mathieu functions is made difficult by the fact that these are highly transcendental functions of both the variable v and the parameter q [21]. For example, there does not exist a known expression for the nth coefficient of the Taylor series of ce_n or se_n in the variable q. In addition, suppose we express the functions ce_n and se_n as Fourier series in the variable v of the form

$$ce_n(v, q) = \sum_{m=0}^{\infty} A_m^{(n)}(q) \cos(mv), \tag{3.20}$$

$$se_n(v, q) = \sum_{m=0}^{\infty} B_m^{(n)}(q) \sin(mv). \tag{3.21}$$

Then the functions $A_m^{(n)}$ and $B_m^{(n)}$ themselves are transcendental functions of the variable q.

As a result, we found difficulty with several standard algorithms for computing Mathieu functions (especially for extreme values of the parameter q)–many of which are numerically unstable. Mathematica deals poorly with the regime $q < 0$, as can

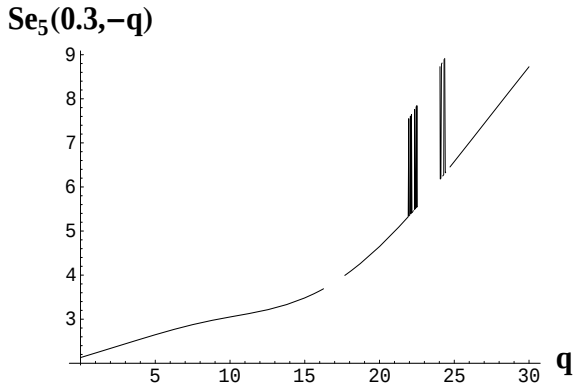

Figure 3.3: Output of Mathematica for the function $Se_5(u,q) = -ise_5(iu,q)$ for $u = 0.3$ and $-30 < q < 0$, illustrating numerical instability for various values of q. The problem can be avoided to some degree by using known relationships to express $Se_5(u,-q)$ in terms of positive q.

be seen in the Fig. (3.3). Alternative algorithms for computing Mathieu functions represent ce_n and se_n as series of Bessel function products. For example, there exist expressions of the form [32]

$$Se_{2r+1}(u,q) = \frac{se'_{2r+1}(0,q)se_{2r+1}(\pi/2,q)}{\sqrt{q}(B_1^{(2r+1)}(q))^2}\sum_{k=0}^{\infty}(-1)^k B_{2k+1}^{2r+1}(q)[J_k(\sqrt{q}e^{-u})J_{k+1}(\sqrt{q}e^{u}) - J_{k+1}(\sqrt{q}e^{-u})J_k(\sqrt{q}e^{u})] \qquad (3.22)$$

for $r = 0, 1, 2, \ldots$ and $q > 0$. For fixed q, we find that these series converge rapidly. However, for extreme values of q the computation of these series involves ratios of small quantities. The appearance of spurious zero crossings in the denominator $\sqrt{q}(B_1^{2r+1}(q))^2$ can cause numerical results to diverge. Furthermore, Taylor coefficients about $q = 0$ of the quantities involved are difficult to implement for arbitrary r. For these reasons, we use an 11th-order Adams integrator [4] to numerically in-

tegrate the Mathieu equations directly together with the surface integrals (3.8,3.9) for the angular Mathieu coefficients F_m and G_m.

Finally, the sums (3.13,3.14) may be truncated after a number of terms required to achieve convergence within an acceptable tolerance. The convergence of the sums (3.13,3.14) will be discussed in Section 3.4.4.

3.3 Benchmarks of Numerical Accuracy

3.3.1 Monopole-Pair Benchmark

It is required that the surface fitting procedure just described be capable of reproducing high derivatives of fields that are rapidly varying and have nontrivial fringe-field behavior. The case of a field due to a pair of magnetic monopoles was treated in Section 2.3.1. As a comparison with these results, on-axis gradients were computed numerically from surface data using the method described in Section 3.2. Fitting was performed using an elliptical cylinder with semimajor axis of 4.0cm and semiminor axis of 0.8cm, corresponding to the parameters $(U, f) = (0.2027, 3.919)$ cm. The known function $\tilde{B}_u(v, k)$ was evaluated using (2.42) at each value of v required during Adams integration over the angular coordinate. The coefficients $F_n(k_j)$ and $G_n(k_j)$ were then computed for an array of values n and $k_j = -k_{max} + (j-1)\delta k$ for $j = 1, 2, \cdots$. Due to the symmetry of the field, the only nonvanishing coefficients are the $F_n(k_j)$ for n odd. These quantities were used to construct the on-axis gradients from (3.16). A plot of the resulting gradients $C_1(z)$, $C_3(z)$, and $C_5(z)$ is included in Fig. 3.5. We find that the computed on-axis gradients C_1, C_3,

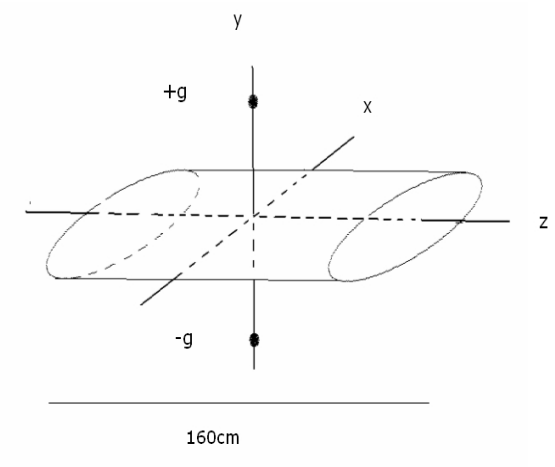

Figure 3.4: Fitting a monopole-pair field using an elliptical cylinder.

and C_5 are accurate to 2.6×10^{-6}.

As an additional test, the computed on-axis gradient functions were used to compute the Taylor coefficients of the magnetic field through $O(x, y)^6$. The field at the transverse location $x = 0.4$ cm, $y = 0.2$ cm was computed for an array of values z_j uniformly spaced in the interval $[-180, 180]$ cm using the series (3.19). The resulting maximum error relative to peak for the vertical field was $\delta B_y / B_{peak} = 4.7 \times 10^{-6}$. The maximum error for the x and z components was 3.8×10^{-4}.

As a demonstration of this algorithm's insensitivity to noise, we added numerical noise to field values for the finite dipole at each grid point used on the boundary of the form $B^{new}_{x,y} = B_{x,y}(1 + \epsilon_i)$. Here each ϵ_i is a uniform random variable in the interval $[-\frac{\Delta}{2}, \frac{\Delta}{2}]$, and the index i specifies the grid point. We discuss the case $\Delta = 0.05$, corresponding to a peak relative error of 5 percent. Using parameters identical to those described in Section 4, we find a peak relative error in $C_1(z)$ of 0.003. Similarly, we find a peak relative error in $C_3(z)$ of 0.025. The resulting error

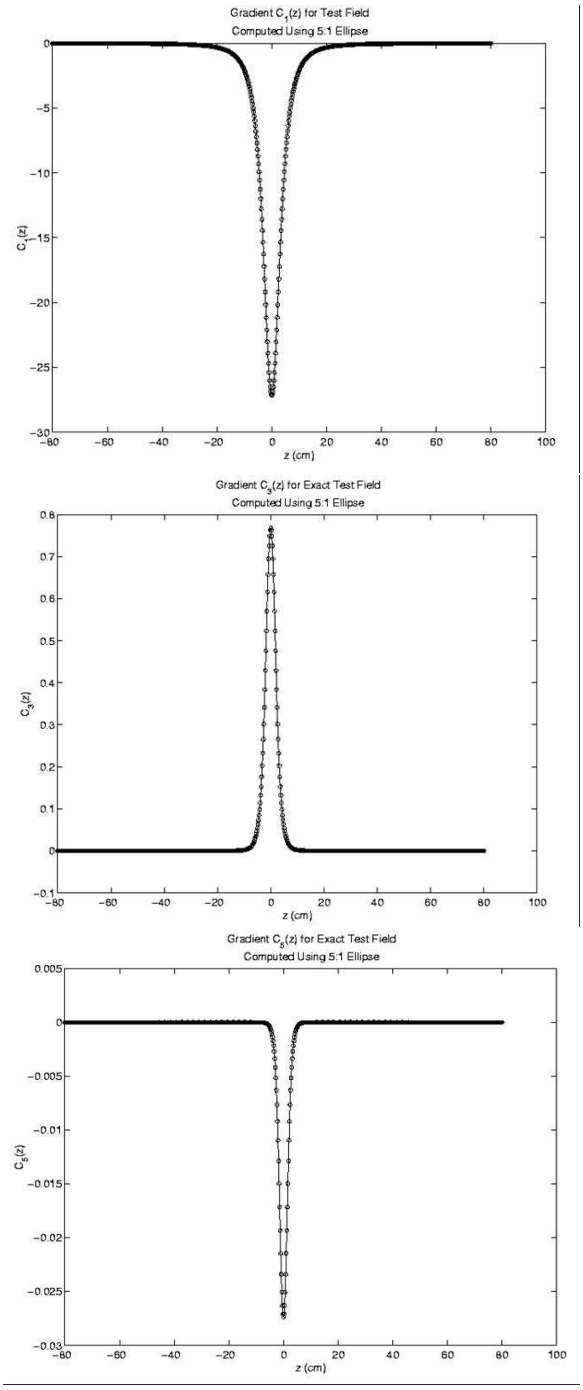

Figure 3.5: On-axis gradients C_1 (upper), C_3 (center) and C_5 (lower) for the monopole-pair test field. Solid lines are the exact values (2.40), dots are values computed from data on the surface of an elliptical cylinder. Fitting was done using an ellipse with semimajor axis 4.0 cm and semiminor axis 0.8 cm.

in each case is of order less than or equal to the error on the boundary. In Section 3.4.2, we show that this result is a consequence of an effective cutoff proved by the integration kernel appearing in the on-axis gradients.

The case of a monopole pair is a very stringent test because of the rapid variation of the monopole pair magnetic field. Its successful passage guarantees, by superposition, that tests comprised of multiple monopole pairs, which might be used to model wigglers, will also be passed successfully.

3.3.2 Application to ILC Wiggler

A less stringent test of the accuracy of this procedure (but also a test of the quality of the magnetic data on the mesh) is that the magnetic field computed from the surface data should reproduce the magnetic field at the interior mesh points. We computed such an interior fit, and the associated transfer map, for the modified CESR-c design of the Cornell wiggler, which has been adopted as the design prototype for use in International Linear Collider studies (see Chapter 6). Cornell provided data obtained from the 3-dimensional finite element modeling code OPERA-3d for the field components B_x, B_y, and B_z on a mesh of spacing $0.4 \times 0.2 \times 0.2$ cm in a volume $10.4 \times 5.2 \times 480$ cm, extending beyond the fringe-field region. The field components are provided to a precision of 0.05G relative to a peak field of 16.7kG. An elliptic cylinder with semimajor axis 4.4 cm and semiminor axis 2.4 cm was placed in the domain of the data, and the field on the elliptic cylinder boundary was constructed using nearest-neighbor interpolation with cubic splines

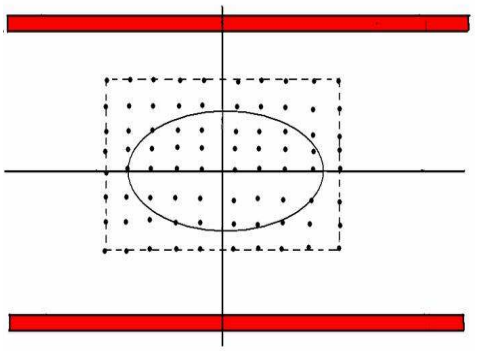

Figure 3.6: Illustration of mesh used for interpolation of field data onto the surface of an elliptical cylinder for the purpose of computing transfer maps.

(Fig. 3.6).

The interior field was computed using the on-axis gradients through terms of degree 6 in x, y over the domain of the original data. This solution for the interior field was then compared to the original data at each grid point. The first figure in Fig. 3.7 provides a fit to the vertical field B_y off-axis at $(x, y) = (0.4, 0.2)$ cm along the length of the wiggler. Plots of the field data (points) are shown versus computed values (solid lines). Note that the fitted field captures the fringe-field behavior. The RMS error obtained was $\delta|\mathbf{B}_{data} - \mathbf{B}_{fit}|/|\mathbf{B}|_{peak} = 3.5 \times 10^{-4}$. The following figure illustrates the horizontal roll-off of the vertical field at $y = 0.1$ cm, $z = 104.2$ cm for $0 \leq x \leq 1$ cm. Note the discrete jumps in the original data, reflecting the number of digits retained in the output of the numerical computation. Despite the small variation of B_y in x, the fit goes through the interior data. Finally, Fig. 3.8 illustrates the fit to the longitudinal field B_z, again at $(x, y) = (0.4, 0.2)$ cm along the wiggler. Note that no information about B_z was used to generate this field, since

only the component of **B** normal to the elliptic cylinder surface is used to generate the interior solution.

The error for B_y on-axis lies in the range 0.1-0.2G along the length of the wiggler, increasing slightly near the end poles. A plot of residuals in the plane $y = 0$ is displayed in Fig. 3.9. Note that the error is within 0.3G over this region of the x-z plane. A second plot includes residuals on a coarser grid given out to $x = 2.5$cm, indicating that error begins to increase suddenly at about $x = 2$cm. This may be due to the finite radius of convergence of the power series for $B_y(x, y, z)$. We intend to show in Section 3.4.2 that the error can be decreased by fitting on an ellipse with larger semimajor axis, or by using data values on a grid with smaller mesh spacing.

The on-axis gradients computed above were then used in MaryLie to integrate, simultaneously, i) equations for the reference trajectory of a 5 GeV positron through the wiggler, ii) equations for the matrix elements of the linear part of the transfer map through the wiggler, and iii) equations for the coefficients of the generating polynomials f_3,...,f_6 appearing in the Lie factorization of the transfer map. Each generator of the symplectic transfer map $\mathcal{M}$ is computed in variables representing deviation from the reference trajectory. The reference trajectory itself is illustrated in Fig. 3.10.

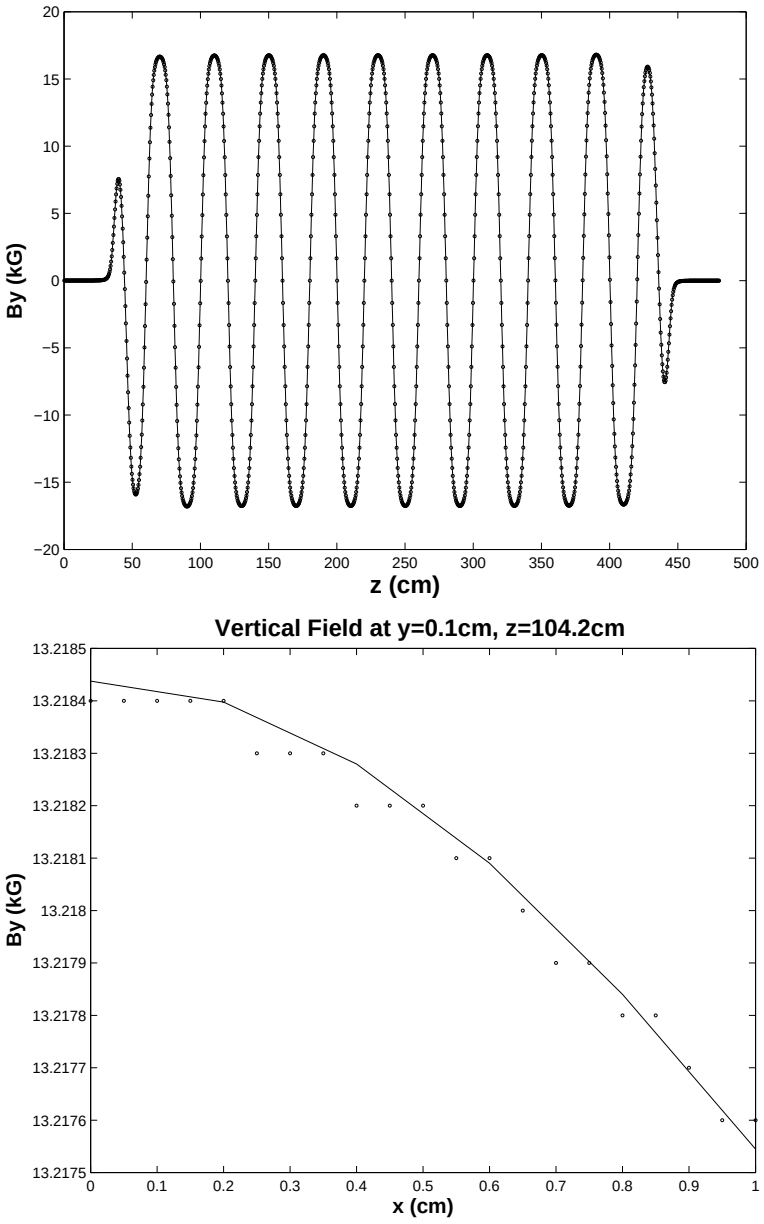

Figure 3.7: Fit obtained to proposed ILC wiggler vertical field using an ellipse with $x_{max} = 4.4$cm, $y_{max} = 2.4$cm. The solid lines are computed from surface data using expressions of the form (3.19); dots are numerical data provided by OPERA-3d.

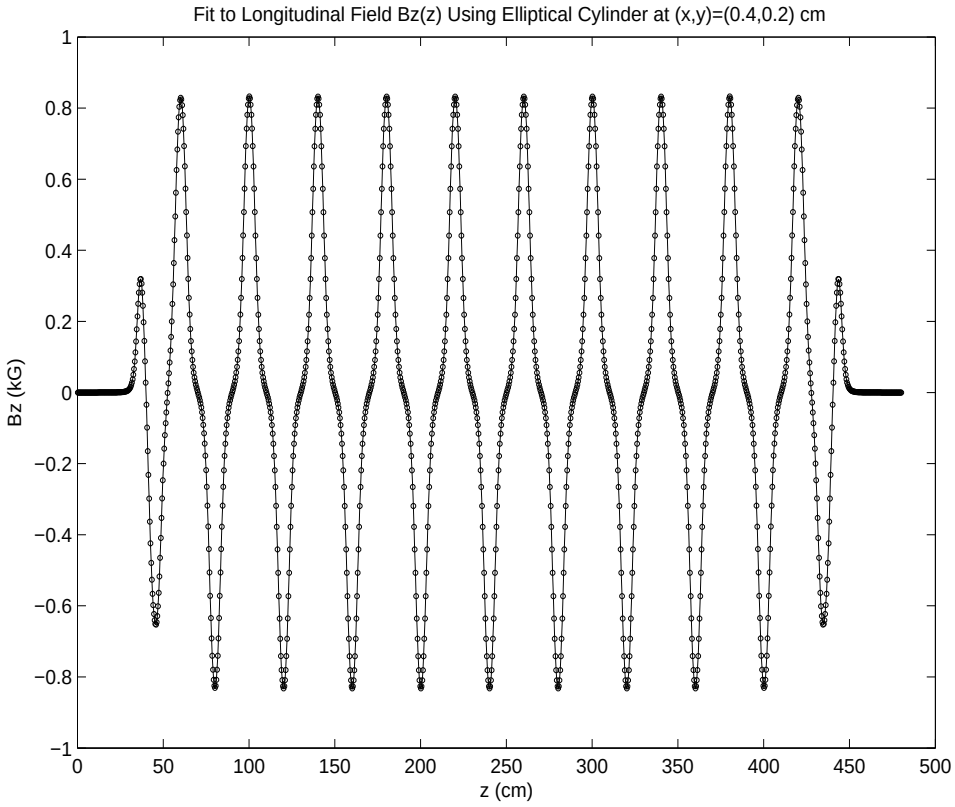

Figure 3.8: Fit obtained to proposed ILC wiggler longitudinal field using an ellipse with $x_{max} = 4.4$cm, $y_{max} = 2.4$cm. The solid lines are computed from surface data using expressions of the form (3.19); dots are numerical data provided by OPERA-3d.

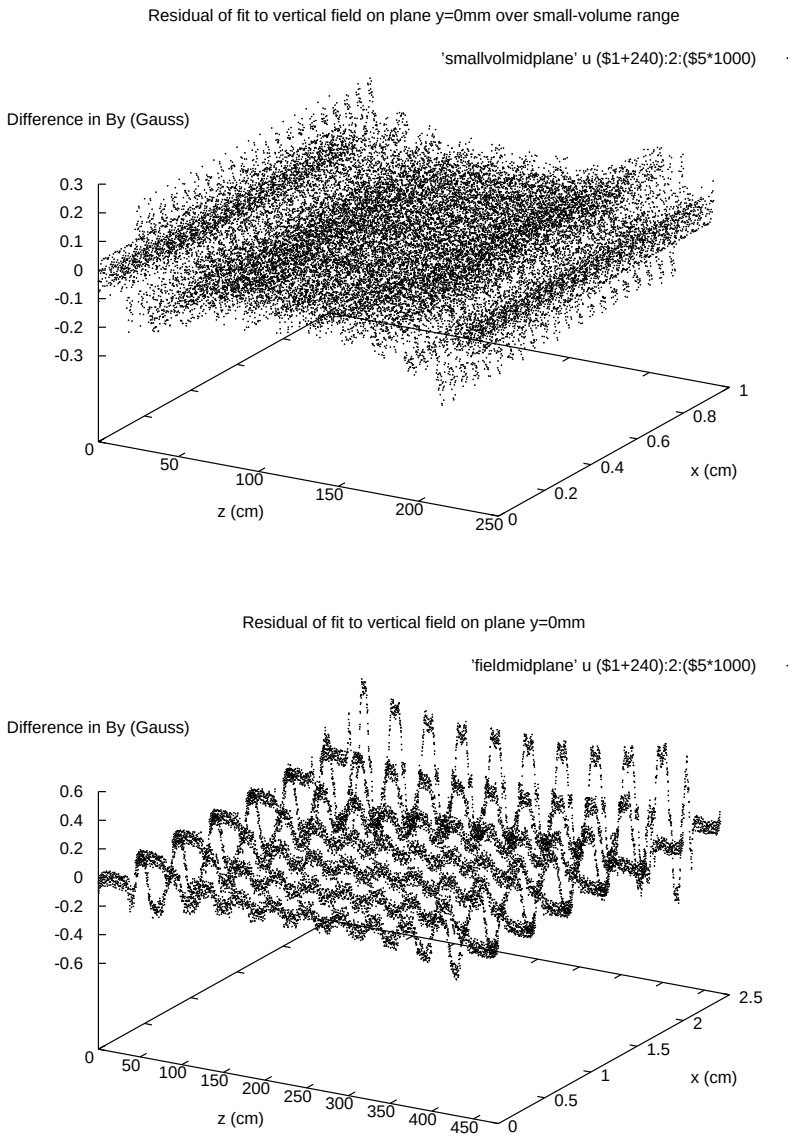

Figure 3.9: Difference (Gauss) between the vertical field B_y of the proposed ILC wiggler and its fitted value across the midplane $y = 0$. Peak field is 16.7 kG. (Upper) Difference over a small-volume range. Fitted values of B_y are compared against numerical field values provided on a mesh with fine transverse spacing. (Lower) Difference over a larger volume range. The same fitted field values are compared against numerical values provided on a mesh with coarser transverse spacing.

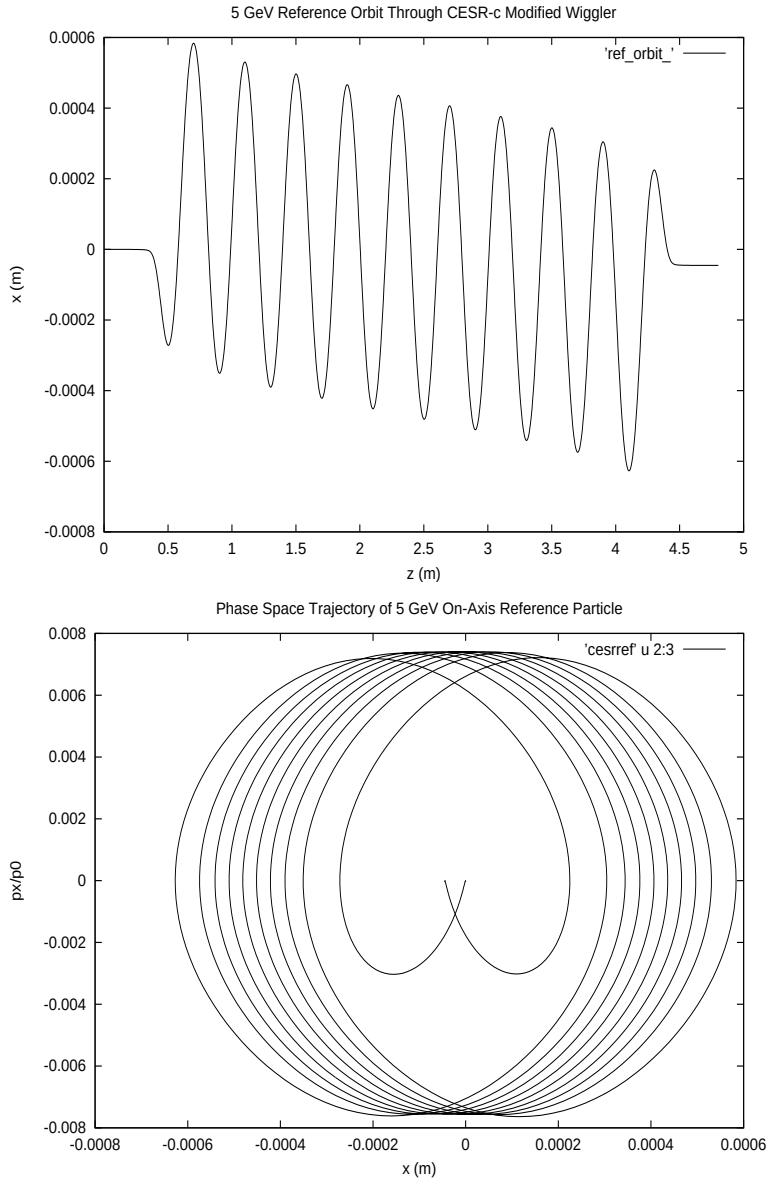

Figure 3.10: Reference trajectory for a 5 GeV positron through the proposed ILC wiggler. (Upper) Coordinate x(m) along the length of the wiggler z(m). (Lower) Trajectory of the reference positron in the phase space defined by coordinates x(m) and p_x/p^0.

3.4 Insensitivity to Numerical Noise

3.4.1 Amplification of On-Axis Noise

When computing symplectic maps we are particularly interested in higher-order derivatives of the field data. One straightforward method of computing these derivatives involves fitting an interpolating function to data near the axis of the magnetic element and approximating derivatives using derivatives of this interpolant. As a comparison with this technique, we examine the effect of noise on derivatives computed from on-axis data for comparison to the effect of noise on derivatives computed from boundary-value data. In particular, we examine the longitudinal derivatives

$$C_1^{[n]}(z) \;=\; \frac{\partial^n}{\partial z^n} B_y(x,y,z)|_{x=0,y=0}. \tag{3.23}$$

On-axis derivatives were computed using the Filon-spline Fourier transform algorithm described in Appendix C. This algorithm computes the exact Fourier transform of a cubic-spline interpolant through the on-axis data, and derivatives may then be computed by

$$C_1^{[n]}(z) = \frac{1}{\sqrt{2\pi}} \int_{-\infty}^{\infty} dk (-ik)^n e^{ikz} \tilde{C}_1(k) \tag{3.24}$$

where

$$\tilde{C}_1(k) = \frac{1}{\sqrt{2\pi}} \int_{-\infty}^{\infty} dz e^{-ikz} C_1(z). \tag{3.25}$$

As the frequency cutoff $k_c \to \infty$ and sampling $\delta k \to 0$, the computed derivatives converge to those computed using a spline interpolant. In this way we illustrate the appearance of high-frequency noise and the effect of the choice of cutoff frequency.

We begin by artificially adding noise to the on-axis values $C_1(z) = B_y(x, y, z)|_{x=0,y=0}$ for the field of the monopole pair described in Section 2.3.1. Differentiation was performed as in (3.24) for $n = 1, ..., 4$ using the noisy values $\hat{C}_1(z_i) = C_1(z_i)(1 + \epsilon_i)$, where each ϵ_i is a uniform random variable taking on values $\epsilon_i \in [-0.1, 0.1]$. In Figure 3.11 we compare derivatives computed from this noisy on-axis data to those produced from noisy data on the elliptic cylindrical boundary. Note that by the third derivative, the computed on-axis derivative no longer resembles its true value. The derivative computed from boundary-value data, however, is accurate to 10^{-2}.

We perform a similar comparison for the ILC wiggler data. Values for the on-axis vertical field are taken along the length of the wiggler at intervals of 0.2cm, and derivatives are computed as above. The power spectra of $D_z^2 B_y(x, y, z)$ and $D_z^4 B_y(x, y, z)$ are illustrated in Fig 3.12. Through the second derivative, spectral weight is effectively confined to the interval $[-3\text{cm}^{-1}, 3\text{cm}^{-1}]$. By the fourth derivative, however, the factor k^n appearing in (3.24) has amplified the high-frequency values of $\tilde{C}_1(k)$, producing a significant spectral weight for $|k| \geq 10cm^{-1}$, well within the Nyquist band $-15.7\text{cm}^{-1} \leq k \leq 15.7\text{cm}^{-1}$. In Fig. 3.13 we illustrate the effect of this noise on the computed derivative by using various cutoffs that are multiples of $kc = \pi\text{cm}^{-1}$, leaving frequency resolution δk unchanged. It is clear that by the third figure, the derivative has become dominated by noise. This illustrates that derivatives can be computed through an optimal choice of cutoff, providing the effects of aliasing are minimized, a process known as smoothing. In general, however, the use of an artificial cutoff is an unsatisfactory solution, contributing to

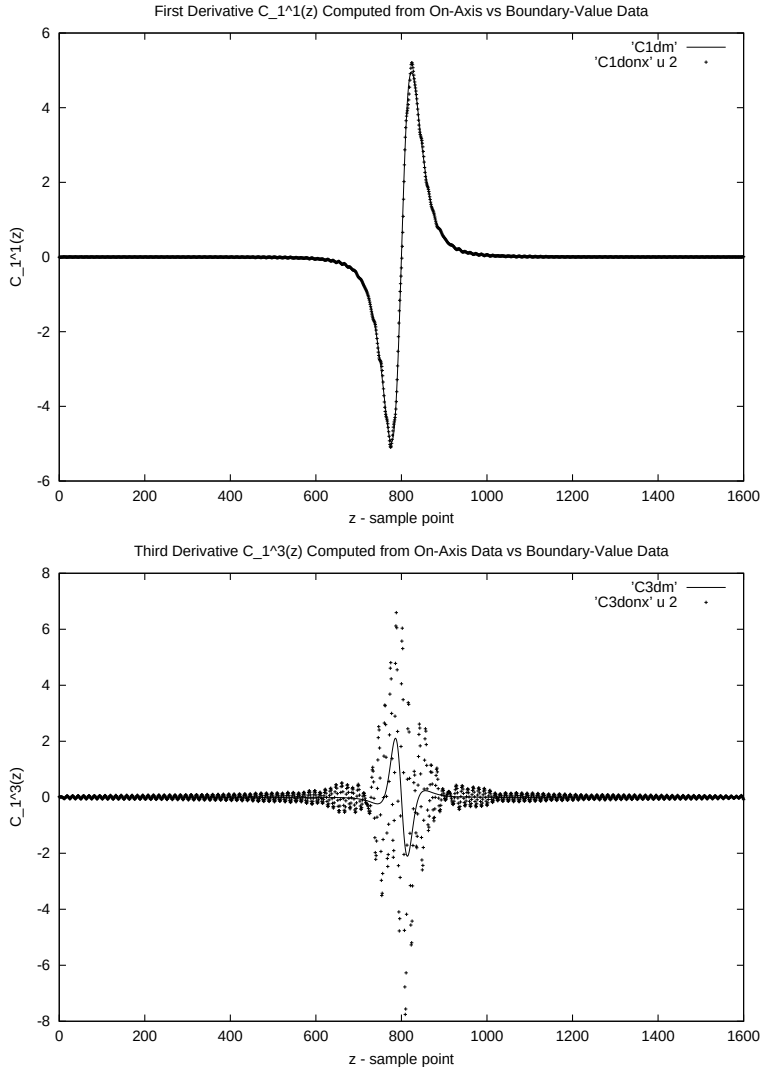

Figure 3.11: Derivatives of the on-axis gradient $C_1(z)$ of the monopole-pair test field of Section 2.3.1. Points represent values computed using (3.24) from on-axis data with random 10% noise added. Solid lines represent values computed from surface data with random 10% noise added. (Upper) The first derivative $C_1^1(z)$. (Lower) The third derivative $C_1^3(z)$.

truncation error

$$||\Delta D_z^4 B_y(x,y,z)||^2 = \int_{|k|\geq kc} |k^4 \tilde{B}_y(x,y,k)|^2 dk, \tag{3.26}$$

as information about high derivatives residing in the tail of the spectrum $\tilde{B}_y$ is lost entirely. We now illustrate a natural smoothing mechanism that avoids this problem.

3.4.2 Study of Smoothing: Circular versus Elliptical Cylinders

In Section 2.4.1 we studied the smoothing properties of the kernels appearing the circular cylinder solution (2.20). In the present section, we investigate similar smoothing behavior in the case of the elliptical cylinder. We first write the on-axis gradients (3.16) as integrals of the angular Mathieu coefficients against a sequence of kernels. For example, for odd r we have:

$$C_{r,s}(z) = \frac{1}{\sqrt{2\pi}} \int_{-\infty}^{\infty} dk e^{ikz} \Lambda_{1,s}^r(k) F_1(k) + \frac{1}{\sqrt{2\pi}} \int_{-\infty}^{\infty} dk e^{ikz} \Lambda_{3,s}^r(k) F_3(k) + \cdots \tag{3.27}$$

where the kernels are given by

$$\Lambda_{n,s}^r(k) = \frac{1}{2^r r!} \frac{k^r g_s^n(k) B_r^n(k)}{Se'(U,k)}. \tag{3.28}$$

A similar expression holds for each $C_{r,c}$, with kernels given by

$$\Lambda_{n,c}^r(k) = \frac{1}{2^r r!} \frac{k^r g_c^n(k) A_r^n(k)}{Ce'(U,k)}. \tag{3.29}$$

The kernels are determined by the parameters (U, f) defining the boundary geometry. Figure 3.14 illustrates the sequence of kernels appearing in the evaluation of $C_{5,s}(z)$ for an elliptic cylinder with $x = 4$ cm, $y = 1$ cm. Note that

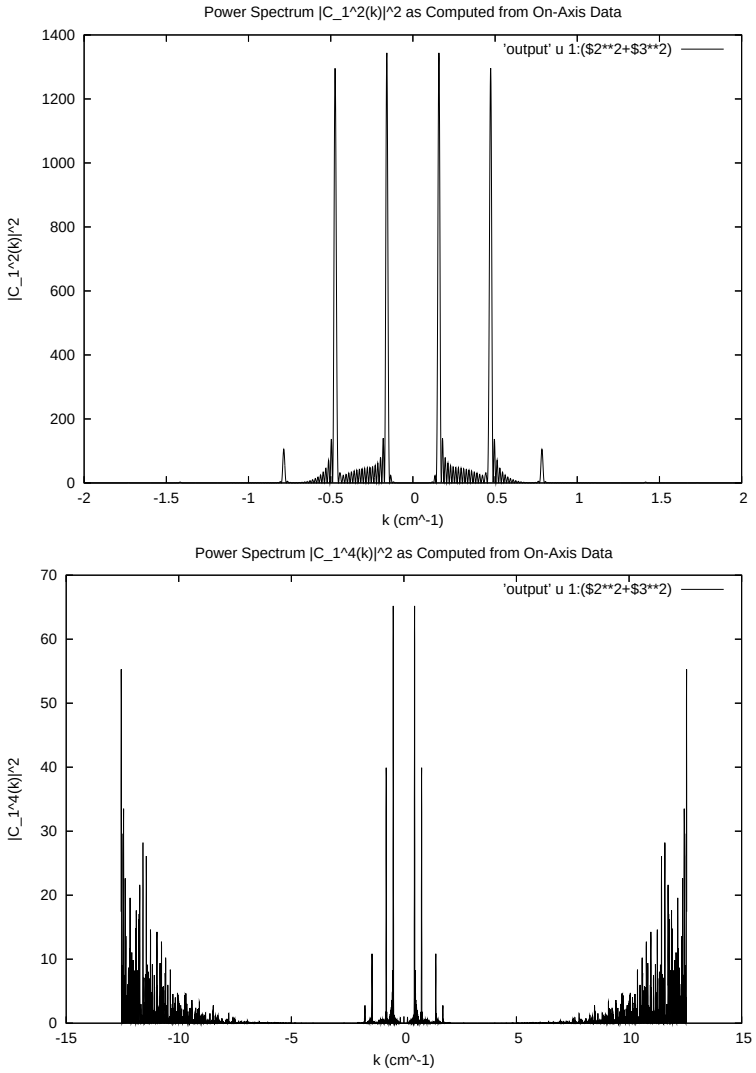

Figure 3.12: Power spectrum for derivatives $\partial^2 B_y/\partial z^2$ (upper) and $\partial^4 B_y/\partial z^4$ (lower) on-axis, as computed from data provided from OPERA-3d for the proposed ILC wiggler.

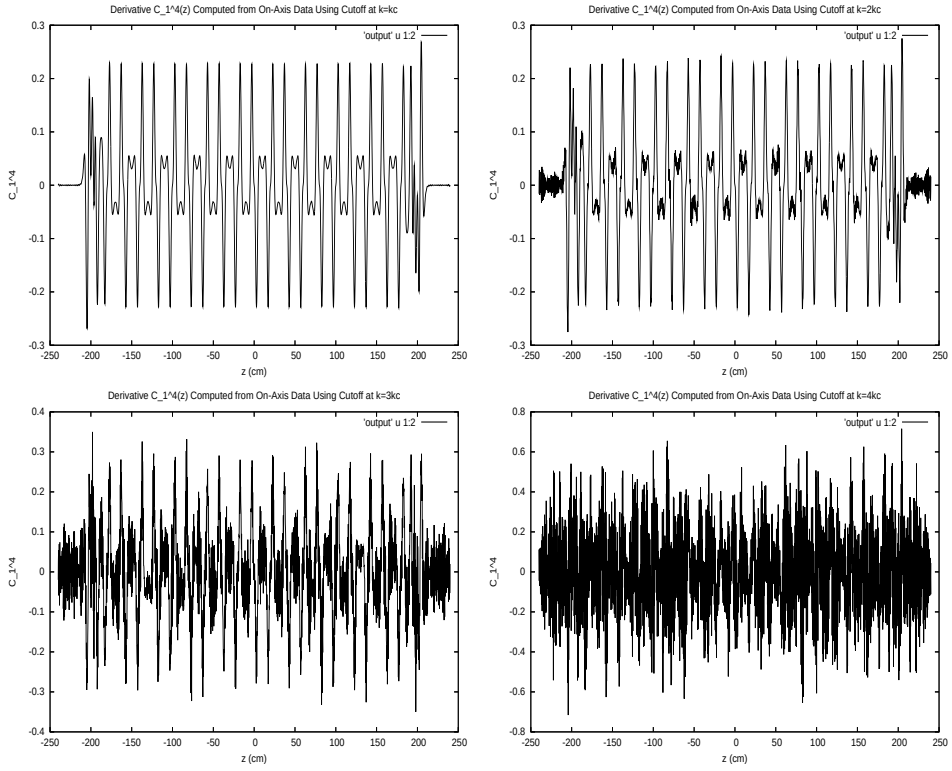

Figure 3.13: Fourth derivative $\partial^4 B_y/\partial z^4$ obtained using (3.24) from on-axis magnetic field data for the proposed ILC wiggler. A sequence of cutoffs $k = \pi\text{cm}^{-1}$, $2\pi\text{cm}^{-1}$, $3\pi\text{cm}^{-1}$, $4\pi\text{cm}^{-1}$ for the Fourier integral illustrates the appearance of high-frequency noise.

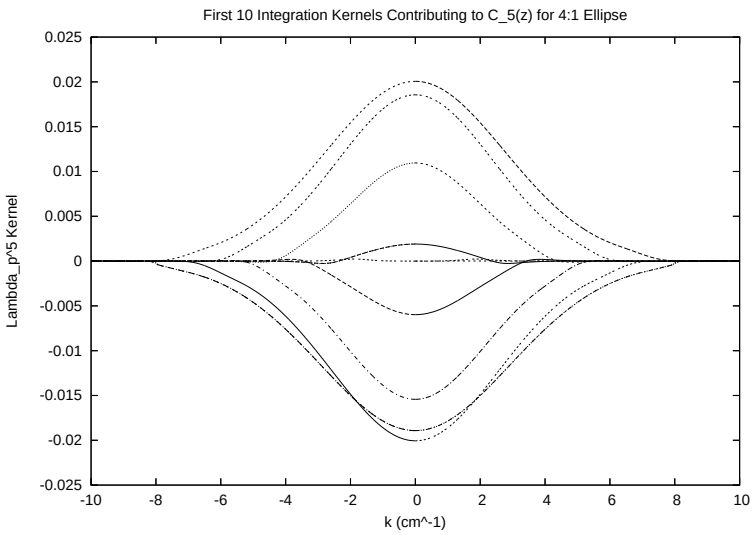

Figure 3.14: First 10 nonvanishing integration kernels contributing to the on-axis gradient $C_{5,s}$ for an elliptical cylinder with $x_{max} = 4$cm, $y_{max} = 1$cm.

$\Lambda^5_{1,s}(k), \Lambda^5_{3,s}(k) \to 0$ as $k \to 0$. The remaining kernels attain their maximum at $k = 0$, and alternate sign with increasing n. Most importantly, each kernel multiplying the surface functions F_m and G_m falls off rapidly with frequency k. Note that the kernels illustrated have been suppressed by one order of magnitude relative to their peak values by $k = 6$ cm^{-1}. The high-frequency behavior of the kernels can be described by the asymptotic representation given in Appendix D.1.2:

$$\Lambda^r_{n,s}(k) \sim \frac{k^r}{2^r r!}\sqrt{\frac{f}{y}} q^{-1/4}\pi^{1/2}\alpha_n^{-1} B^n_r(k) e^{-kx}(1 + O(1/k)), \tag{3.30}$$

where the Fourier coefficient B^n_r falls off as an inverse power of q as described in Appendix D.1.2. Beyond a value $q_c(n)$, the kernel falls off exponentially at a rate that increases with the length x of the semimajor axis of the ellipse.

As illustrated in Section 3.4.1 and Appendix A, the presence of noise in the boundary-value data, varying on the length scale h, introduces spectral weight to

the angular Mathieu coefficients $F_m(k)$ and $G_m(k)$ at high frequencies $k_{Nyq} \sim \pi/h$. As a result of multiplication by the kernels $\Lambda^r_{n,\alpha}$, however, the on-axis gradients $\tilde{C}^{[m]}_{r\alpha}(k)$ have little weight for frequencies beyond 6 cm^{-1}. The kernels $\Lambda^r_{n,\alpha}$ serve as a low-pass filter to minimize the weight that such high frequencies contribute to the interior solution. A reasonable numerical cutoff may now be imposed on the Fourier integral with the knowledge that the spectral weight of the relevant functions is negligible for frequencies beyond 6 cm^{-1} due to the high-frequency suppression illustrated in (3.30). For this reason, the behavior of noise on the boundary has little influence on the interior solution in terms of the $C^{[m]}_{r,\alpha}(z)$, a property we call *smoothing*.

We will see that the amount of smoothing increases with domain size. Note that this insensitivity to noise is improved by choosing the geometry of the boundary such that the kernels approach zero quickly. To study how this smoothing behavior depends on domain geometry, suppose we are interested in fitting within a large aspect-ratio domain. We may fix the semiminor axis y and increase the semimajor axis x, stretching the elliptic cylinder horizontally and enlarging the enclosed cross-sectional area to include the "wings" of the domain. We see that for a fixed semiminor axis y, each weight function falls off more quickly with increasing k as the semimajor axis x is lengthened. In Fig. 3.15 we have illustrated the computation of the gradient $C_{5,s}(z)$ for the ILC wiggler, for three different domains. The first was computed using a small elliptic cylinder $(x_{max}, y_{max}) = (1, 0.6)$ cm. Note that little structure is apparent, and the gradient is quite noisy; in addition, a small cutoff has been imposed, producing some artificial smoothing. The

second figure was obtained by extending the semimajor axis to fill the domain horizontally, with $(x_{max}, y_{max}) = (4.4, 0.6)$ cm. Here clear structure is apparent, with only a small amount of high-frequency noise visible. The third was obtained by extending the semimajor axis to fill the domain permitted by the data, with $(x_{max}, y_{max}) = (4.4, 2.4)$ cm. Note that little change appears between the second and third figures, indicating that increasing the horizontal domain size alone is sufficient in this case to eliminate high-frequency noise. Figure 3.15 illustrates that, even for a small vertical aperture, use of a large aspect-ratio ellipse can dramatically improve accuracy.

3.4.3 Relationship to the Circular Case

We have the following relations between the angular Mathieu coefficients (F_m, G_m) and the upright and skew multipole coefficients (B_m, A_m) for the circular cylinder expansion:

$$k^{r-1}\frac{\tilde{B}_r(R,k)}{I_r'(Rk)} = k^r \sum_{m=0}^{\infty} g_s^m(k) B_r^{(m)}(k) \left[\frac{F_m(U,k)}{Se_m'(U,q)}\right], \tag{3.31}$$

$$k^{r-1}\frac{\tilde{A}_r(R,k)}{I_r'(Rk)} = k^r \sum_{m=0}^{\infty} g_c^m(k) A_r^{(m)}(k) \left[\frac{G_m(U,k)}{Ce_m'(U,q)}\right], \tag{3.32}$$

where

$$B_\rho(\rho = R, \phi, z) = \sum_{m=0}^{\infty} B_m(R,z)\sin(m\phi) + A_m(R,z)\cos(m\phi). \tag{3.33}$$

If we take the limit $U \to \infty$ and $f \to 0$ such that $x_{max} \to fe^U = R$ is finite, the elliptic cylinder (U, f) degenerates into a circular cylinder of radius R. In this limit, $y_{max}/x_{max} = \tanh(U) \to 1$. The sum appearing in (3.31,3.32) is dominated

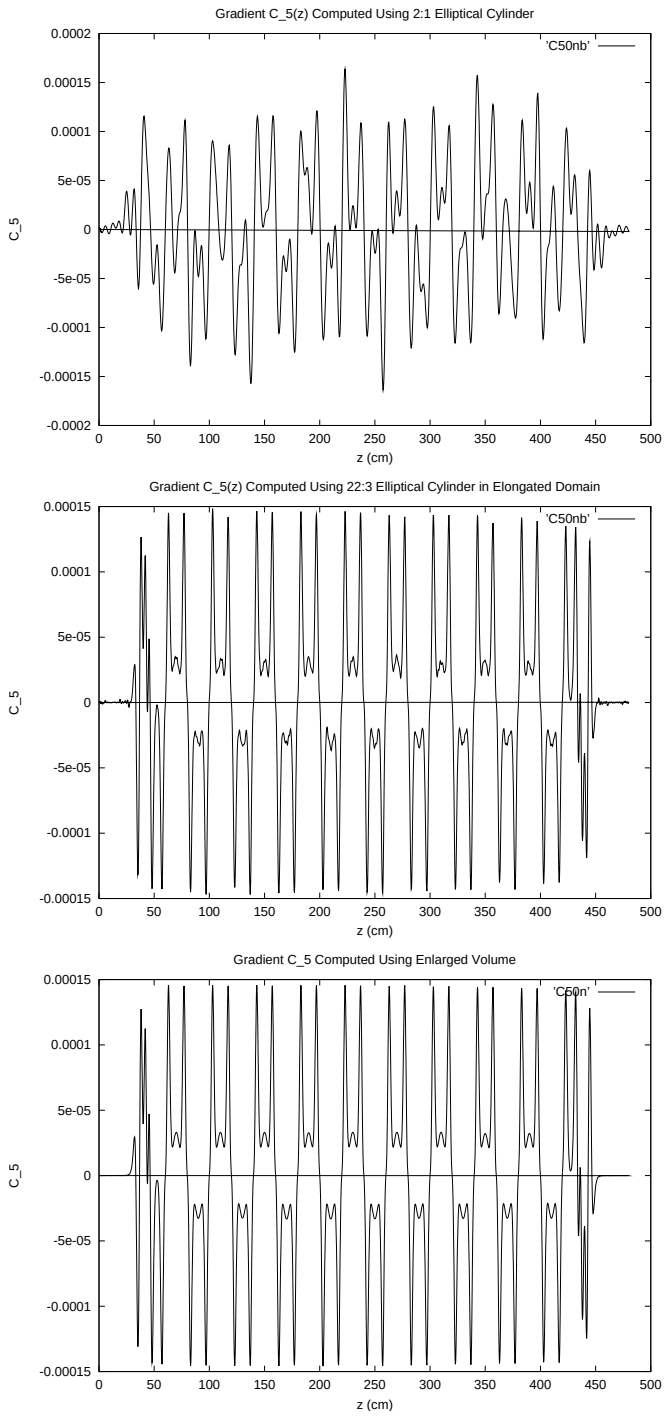

Figure 3.15: Illustration of the effect of domain size on smoothing of numerical errors. (Upper) Gradient $C_{5,s}(z)$ computed using a small elliptical cylinder $(x_{max}, y_{max}) = (1, 0.6)$cm. (Middle) Gradient computed with $(x_{max}, y_{max}) = (4.4, 0.6)$cm. (Lower) Gradient computed with $(x_{max}, y_{max}) = (4.4, 2.4)$cm.

by the term with $m = r$. In particular, the Fourier coefficients become in this limit [20]

$$A_r^{(m)} \to \delta_{r,m}, \tag{3.34}$$

$$B_r^{(m)} \to \delta_{r,m}, \tag{3.35}$$

and the Mathieu functions behave as

$$Ce_n(U,q) \;\to\; g_c^n(k) I_n(kR), \tag{3.36}$$

$$Se_n(U,q) \;\to\; g_s^n(k) I_n(kR), \tag{3.37}$$

$$ce_n(v,q) \;\to\; \cos(n\phi), \tag{3.38}$$

$$se_n(v,q) \;\to\; \sin(v\phi). \tag{3.39}$$

For small eccentricity, we see that the term $r = m$ becomes dominant in (3.31,3.32).

There is one kernel for each gradient in the circular case. The kernels in the circular cylinder case take the form of (2.58):

$$\Lambda_{cir}^m(k) = \frac{1}{2^m m!} \frac{k^{m-1}}{I'_m(kR)}. \tag{3.40}$$

Each kernel is of constant sign, and attains its maximum at $k = 0$ of value $1/(mR^{m-1})$, with the exception of Λ^0, which diverges as $\Lambda^0 \sim 2/(k^2 R)$ near $k \approx 0$. Kernels decrease monotonically as $|k| \to \infty$. Using the asymptotic series for large $\zeta >> 1$ and fixed order m,

$$I'_m(\zeta) \sim \frac{e^\zeta}{\sqrt{2\pi\zeta}} \{1 - \frac{4m^2+3}{8\zeta} + O(\frac{1}{\zeta^2})\}, \tag{3.41}$$

we see that

$$\Lambda_{cir}^n(k) \sim \frac{1}{2^n n!} \sqrt{2\pi R} k^{n-1/2} e^{-kR} (1 + O((kR)^{-1})). \tag{3.42}$$

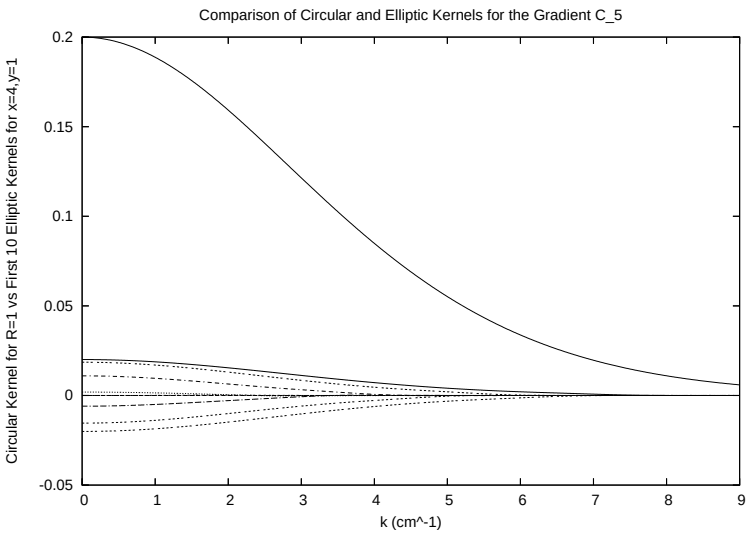

Figure 3.16: The circular kernel Λ^5_{cir} contributing to the on-axis gradient C_5 (upper curve) plotted together with the first 10 elliptical kernels $\Lambda^5_1 \cdots \Lambda^5_{10}$ (lower curve) contributing to C_5.

We compare the effectiveness of this filter with the elliptical case. In Figure 3.16, the circular kernel Λ^5_{cir} contributing to the on-axis gradient $C_{5,s}$ is plotted together with the first 10 elliptical kernels $\Lambda^5_{1,s} \cdots \Lambda^5_{10,s}$ contributing to $C_{5,s}$. The circular kernel is plotted for a cylinder with radius $R = 1$cm. Elliptical kernels are plotted for a cylinder with $y_{max} = 1$cm, $x_{max} = 4$cm. We see that

$$|\Lambda^5_{n,s}(k)| < \Lambda^5_{cir}(k) \tag{3.43}$$

for all $n = 1, \cdots, 10$ and $k \in \mathbb{R}$. Further comparison of the smoothing effect of these kernels can be discussed using the smoothing envelope defined in Section 3.4.4.

3.4.4 Error Estimates

We now wish to establish careful error estimates for the on-axis gradients appearing in (3.16). We estimate the rms error of each function $C_{n,\alpha}^{[m]}(z)$ as follows. Let the fitted normal component of the field on the surface be given by $B_u^{(bv)}$. Defining the surface error $\tilde{E}(v,k) = \sqrt{J(U,v)}\left[\tilde{B}_u^{(bv)}(v,k) - \tilde{B}_u(v,k)\right]$, let $f_n(k) = F_n^{(bv)} - F_n$ and $g_n(k) = G_n^{(bv)} - G_n$ be the resulting errors in the odd and even angular Mathieu coefficients, respectively. We may then write the error on the boundary as

$$\tilde{E}(v,k) = \sum_{n=0}^{\infty}[f_n(k)se_n(v,q) + g_n(k)ce_n(v,q)] \tag{3.44}$$

for each fixed $k \in \mathbb{R}$, where the norm in $L^2[0,2\pi]$ is given by

$$||\tilde{E}||^2(k) = \sum_{n=0}^{\infty}|f_n(k)|^2 + \sum_{n=0}^{\infty}|g_n(k)|^2 < \infty \tag{3.45}$$

for fixed k. We then write the full norm of the error on the boundary for $E \in L^2(\Gamma)$ as

$$||E||_\Gamma^2 = \sum_{n=0}^{\infty}||f_n||_{\mathbb{R}}^2 + \sum_{n=0}^{\infty}||g_n||_{\mathbb{R}}^2 \tag{3.46}$$

where

$$||E||_\Gamma^2 = \int_{-\infty}^{\infty}\int_0^{2\pi}|E(v,z)|^2 dvdz, \tag{3.47}$$

$$||f_n||_{\mathbb{R}}^2 = \int_{-\infty}^{\infty}|f_n(k)|^2 dk. \tag{3.48}$$

Recall that the on-axis gradients may be written in the form

$$\tilde{C}_{n,s}^{[m]}(k) = (ik)^m \sum_{p=0}^{\infty}\Lambda_{\bar{p},s}^n(k)F_{\bar{p}}(k), \tag{3.49}$$

$$\tilde{C}_{n,c}^{[m]}(k) = (ik)^m \sum_{p=0}^{\infty}\Lambda_{\bar{p},c}^n(k)G_{\bar{p}}(k), \tag{3.50}$$

where $\Lambda^n_{p,\alpha}$ are the kernels presented in (3.28,3.29). Here we introduce the index $\bar{p}$ defined by $\bar{p} = 2p$ for n even, and $\bar{p} = 2p+1$ for n odd. The error in a given on-axis gradient is then given by

$$\Delta\tilde{C}^{[m]}_{n,s}(k) = (ik)^m \sum_{p=0}^{\infty} \Lambda^n_{\bar{p},s}(k) f_{\bar{p}}(k), \tag{3.51}$$

$$\Delta\tilde{C}^{[m]}_{n,c}(k) = (ik)^m \sum_{p=0}^{\infty} \Lambda^n_{\bar{p},c}(k) g_{\bar{p}}(k), \tag{3.52}$$

and we wish to estimate

$$||\Delta C^{[m]}_{n,\alpha}||^2 = ||\Delta\tilde{C}^{[m]}_{n,\alpha}||^2 = \int_{-\infty}^{\infty} |\Delta\tilde{C}^{[m]}_{n,\alpha}(k)|^2 dk, \tag{3.53}$$

where the subscript α is taken to denote either of the subscripts s or c. To obtain this estimate requires that we have some knowledge of the behavior of both the error coefficients f_p, g_p and the kernels $\Lambda^n_{p,\alpha}$. A discussion of approximation for the kernels in provided in Appendix D.1.2, to which we refer often. We use these results first to study the convergence of the sums appearing in Eq (3.49-3.52). For a fixed k, note that

$$\lim_{p\to\infty} \left| \frac{\Lambda^n_{p+1,\alpha}(k)}{\Lambda^n_{p,\alpha}(k)} \right| = \lim_{p\to\infty} \left| \frac{\Lambda^n_{p+1,\alpha}(0) + O(q/p)}{\Lambda^n_{p,\alpha}(0) + O(q/p)} \right| = \lim_{p\to\infty} \left| \frac{\Lambda^n_{p+1,\alpha}(0)}{\Lambda^n_{p,\alpha}(0)} \right| = e^{-2U} < 1 \tag{3.54}$$

and the sum $\sum_{n=0}^{\infty} \Lambda^n_{p,\alpha}(k)$ converges absolutely at each k. For p sufficiently large, terms decay exponentially as e^{-2pU} at a rate $2U$, demonstrating that convergence slows slightly with increasing aspect ratio $a.r. = 1/\tanh U$. Furthermore, we claim that convergence is uniform. This result relies on the following.

Conjecture: For $p \geq n$, each kernel $\Lambda^n_{p,s}$, $\Lambda^n_{p,c}$ has a global maximum at $k = 0$.

This has been verified numerically for the cases $n = 1, 3, 5$ with $p = n, n+1, \cdots, 11$. We let $M^n_{p,\alpha}$ denote the value of this maximum for each α, p, n. In this case, $|\Lambda^n_{p,\alpha}(k)| \leq M^n_{p,\alpha}$ with $\sum_{p=0}^{\infty} M^n_{p,\alpha} < \infty$, and convergence of the above sum is uniform by the Weierstrass M-test. In addition, we know that $F_p(k)$, $G_p(k)$, $f_p(k)$, and $g_p(k) \to 0$ as $p \to \infty$, so each of the sums $(3.49 - 3.52)$ converges. A strict upper bound is provided for (3.51-3.52) by the Cauchy inequality according to:

$$|\Delta\tilde{C}^{[m]}_{n,s}(k)|^2 \leq k^{2m} \sum_{p=0}^{\infty} |\Lambda^n_{p,s}(k)|^2 \sum_{p=0}^{\infty} |f_p(k)|^2 \leq k^{2m} ||\tilde{E}||^2(k) \sum_{p=0}^{\infty} |\Lambda^n_{p,s}(k)|^2, \quad (3.55a)$$

$$|\Delta\tilde{C}^{[m]}_{n,c}(k)|^2 \leq k^{2m} \sum_{p=0}^{\infty} |\Lambda^n_{p,c}(k)|^2 \sum_{p=0}^{\infty} |g_p(k)|^2 \leq k^{2m} ||\tilde{E}||^2(k) \sum_{p=0}^{\infty} |\Lambda^n_{p,c}(k)|^2. \quad (3.55b)$$

The sum-square of the kernels appearing on the rhs converges in each case to a continuous function, which we refer to as a *smoothing envelope*. The smoothing envelope for the case $\alpha = s$, $n = 5$ is illustrated in Fig 3.17. The sum of the first 10 square-kernels $|\Lambda^5_{p,s}(k)|^2$ is plotted as an approximation to the true envelope. We have also included an illustration of the corresponding function for the case $\alpha = s$, $n = 5$, $m = 2$. Note that the error function $||\tilde{E}||(k)$, defined in (3.45), is obtained by summing over azimuthal modes in the cross-section of the elliptical cylinder. We see from (3.55) that large-k values of $||\tilde{E}||(k)$ contribute little to the errors $\Delta\tilde{C}^{[m]}_{n,\alpha}$ due to the rapid decay of the corresponding smoothing envelope for large k.

We may now obtain an upper bound on the norm of the error by carrying out the integration in (3.53) as follows. Here we consider only the functions $\Delta C^{[m]}_{n,s}$.

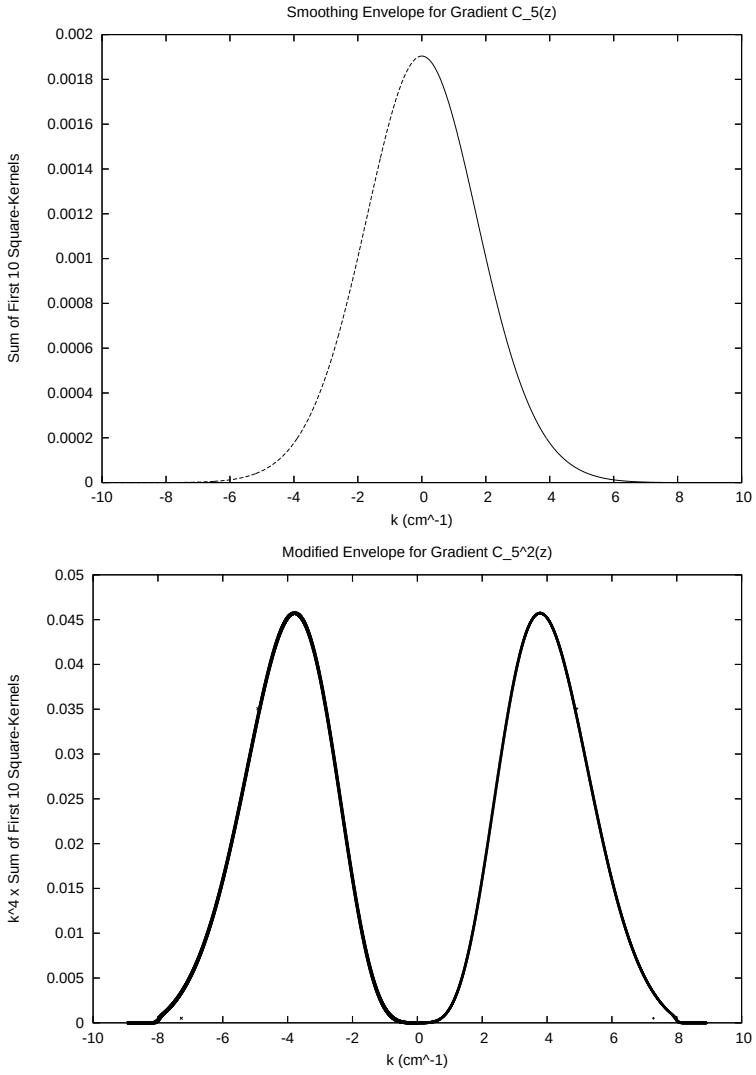

Figure 3.17: (Upper) Smoothing envelope for the gradient $C_5(z)$. (Lower) Corresponding envelope for the gradient $C_5^2(z)$.

Similar results hold for the functions $\Delta C_{n,c}^{[m]}$. We have

$$||\Delta C_{n,s}^{[m]}||^2 = \int_{-\infty}^{\infty} |\Delta \tilde{C}_{n,s}^{[m]}|^2 dk \;\leq\; \max_k \left[k^{2m} \sum_{p=0}^{\infty} |\Lambda_{p,s}^n|^2 \right] \int_{-\infty}^{\infty} ||\tilde{E}||^2(k) dk$$
$$= \;||E||_\Gamma^2 \max_k \left[k^{2m} \sum_{p=0}^{\infty} |\Lambda_{p,s}^n|^2 \right] \tag{3.56}$$

provided the function in brackets can be shown to be bounded. This follows since the sum-square of the kernels is continuous in k, and each kernel goes to zero as $|k| \to \infty$ faster than any power of k. The bound for $C_{5,s}^2$ can be seen in Fig 3.17. The error is strictly less than the given bound by a factor that increases with the rate of decay of the kernels. Note that we may relate (3.56) directly to the error in the values of the field on the surface, which we denote δB_u, by noting that

$$||E||_\Gamma^2 = \int_{-\infty}^{\infty} \int_{-\pi}^{\pi} |\tilde{E}(v,k)|^2 dv dk = \int_{-\infty}^{\infty} \int_{-\pi}^{\pi} |J(U,v) \delta B_u(v,z)|^2 dv dz \leq x_{max}^2 ||\delta B_u||_\Gamma^2, \tag{3.57}$$

where $J(u,v) = f^2(\cosh 2u - \cos 2v)/2$ is the Jacobian of the coordinate transformation from cartesian to elliptic coordinates, which takes its maximum in the variable $v \in [0, 2\pi)$ of value $J = f^2 \cosh(u) = x_{max}^2$.

In practice, we are interested in the rms error of the on-axis gradient functions over a finite length L along the wiggler. If we assume that this length extends into the fringe-field region sufficiently far that

$$\epsilon_1 = ||\Delta C_{n,s}^{[m]}||^2 - \int_{-L/2}^{L/2} |\Delta C_{n,s}^{[m]}|^2 dz = \int_{|z|>L/2} |\Delta C_{n,s}^{[m]}|^2 dz < \epsilon, \tag{3.58}$$

$$\epsilon_2 = ||E||_\Gamma^2 - \int_{-L/2}^{L/2} \int_{-\pi}^{\pi} |E(v,z)|^2 dv dz = \int_{|z|>L/2} \int_{-\pi}^{\pi} |E(v,z)|^2 dz < \epsilon, \tag{3.59}$$

then we may write the rms error as

$$(\Delta C^{[m]}_{n,s})^2_{rms} = \frac{1}{L}\{||C^{[m]}_{n,s}||^2 - \epsilon_1\}, \tag{3.60}$$

$$(E)^2_{rms} = \frac{1}{2\pi L}\{||E||^2_\Gamma - \epsilon_2\}, \tag{3.61}$$

and we may provide the following upper bound:

$$(\Delta C^{[m]}_{n,s})^2_{rms} \leq 2\pi \max_k \left[k^{2m} \sum_{p=0}^{\infty} |\Lambda^n_{p,s}|^2\right] (E)^2_{rms} + \delta \tag{3.62}$$

where $\delta < 2\epsilon/L$ may be made arbitrarily small by considering a sufficient length L along the axis of the wiggler.

In order to obtain a reasonable estimate of this error, we assume that the surface errors are described by the model of noise described in Appendix A. Note that each error coefficient $f_j(k)$ for fixed k is a normal random variable, dependent on the realization of the error over the surface of the elliptic cylinder, with variance given in (A.39). In this case, we may estimate rms error by averaging over an ensemble of surface values as follows. For fixed k,

$$\langle|\Delta\tilde{C}_{n,s}|^2\rangle = \langle|\sum_{p=0}^{\infty} \Lambda^n_{p,s} f_p|^2\rangle = \sum_{i,j=0}^{\infty} \Lambda^n_{i,s}\Lambda^n_{j,s}\langle f_i f_j\rangle = \langle|f_j|^2\rangle \sum_{p=0}^{N} |\Lambda^n_{p,s}|^2 \tag{3.63}$$

where the dependence on k has been suppressed for notational simplicity. Now using the known k dependence of $\langle|f_j(k)|^2\rangle$ we obtain

$$\overline{\langle||\Delta C_{n,s}||^2\rangle} = \overline{\int_{-\infty}^{\infty} \langle|f_j(k)|^2\rangle \sum_{p=0}^{N} |\Lambda^n_{p,s}(k)|^2 dk} = \overline{\langle|f_j(k_p)|^2\rangle} \int_{-\kappa}^{\kappa} \sum_{p=0}^{N} |\Lambda^n_{p,s}|^2 dk \tag{3.64}$$

where the cutoff $k = \kappa$ is placed at the inverse scale of the correlation length of the noise E, which we take to be the longitudinal mesh spacing h such that $\kappa = \pi/h$.

Now we approximate the integral over the smoothing envelope,

$$\int_{-\kappa}^{\kappa}\sum_{p=0}^{N}|\Lambda_{p,s}^{n}|^{2}dk=\sum_{p=0}^{N}\left(\int_{-k_c(p)}^{k_c(p)}|\Lambda_{p,s}^{n}|^{2}dk+\int_{k_c(p)}^{\kappa}|\Lambda_{p,s}^{n}|^{2}dk+\int_{-\kappa}^{-k_c(p)}|\Lambda_{p,s}^{n}|^{2}dk\right), \tag{3.65}$$

where k_c is related to the crossover introduced in Appendix D.1.2 by $q_c = k_c^2 f^2/4$. Note that each of the functions A_r^n, B_r^n, Se', and Ce' appearing in expressions (3.28-3.29) for the kernels $\Lambda_{p,s}^n$, $\Lambda_{p,c}^n$ may be written as a function of the parameter $q = -k^2 f^2/4$, and is therefore an even function of k. Similarly, we see from (D.72) that the products $k^r g_s^n(k)$ and $k^r g_c^n(k)$ are each even in k. Thus, $\Lambda_{p,s}^n$ is an even function of k for all n, p and we have

$$\int_{-\kappa}^{\kappa}\sum_{p=0}^{N}|\Lambda_{p,s}^{n}|^{2}dk=\sum_{p=0}^{N}\int_{-k_c(p)}^{k_c(p)}|\Lambda_{p,s}^{n}|^{2}dk+\sum_{p=0}^{N}2\int_{k_c(p)}^{\kappa}|\Lambda_{p,s}^{n}|^{2}dk. \tag{3.66}$$

In the left-hand term of (3.66) the domain of integration covers the low-q regime. In this region, we use the results of Appendix D.1.2 to make the approximation

$$\begin{aligned}\int_{-k_c(p)}^{k_c(p)}|\Lambda_{p,s}^{n}|^{2}dk &\approx N^{2}\int_{-k_c(p)}^{k_c(p)}(1+\alpha q)^{-2}dk\\ &= N^{2}k_c\left[\frac{1}{1+\alpha q_c}+\frac{1}{\sqrt{\alpha q_c}}\arctan(\sqrt{\alpha q_c})\right].\end{aligned} \tag{3.67}$$

In the right-hand term of (3.66) the domain of integration covers the large-q regime, in which we make the approximation

$$\begin{aligned}\int_{k_c(p)}^{\kappa}|\Lambda_{p,s}^{n}|^{2}dk &\approx \int_{k_c(p)}^{\kappa}\frac{k^{2n}}{2^{2n}(n!)^{2}}\frac{f}{y}q^{-1/2}\pi\alpha_p^{-2}|B_n^p(k)|^{2}e^{-2kx}dk\\ &\le \int_{k_c(p)}^{\kappa}\frac{k^{2n}}{2^{2n}(n!)^{2}}\frac{f}{y}q^{-1/2}\pi\alpha_p^{-2}\left(2\sqrt{\frac{2}{\pi}}q^{-1/4}\right)e^{-2kx}dk\\ &= \frac{\alpha_p^{-2}}{2^{2n-3}(n!)^{2}y}\sqrt{\frac{\pi}{f}}\int_{k_c(p)}^{\kappa}k^{2n-3/2}e^{-2kx}dk.\end{aligned} \tag{3.68}$$

Here we have used the bound given for the Fourier coefficients in (D.70). In this regime we have $k \geq k_c > 2/f$ and

$$\begin{aligned} \int_{k_c(p)}^{\kappa} k^{2n-3/2} e^{-2kx} dk &< \sqrt{\frac{f}{2}} \int_{k_c(p)}^{\infty} k^{2n-1} e^{-2kx} dk \\ &= \sqrt{\frac{f}{2}} \frac{e^{-2xk_c(p)}}{2x} \sum_{j=0}^{m} \frac{m!}{(m-j)!} \frac{k_c^m}{(2xk_c)^j}, \end{aligned} \tag{3.69}$$

where $m = 2n - 1$. Expressions (3.67) and (3.68) may be used to estimate the integral (3.66) after summing over the index p, where we may choose $q_c \sim p^2/2$ as described in Appendix D.1.2.

It remains to relate the error Mathieu coefficients f_j to the statistical error at each mesh point. Assuming the model of white noise described in Appendix A, we have

$$\langle |f_j(k)|^2 \rangle = \frac{L}{\pi^3} (h\delta v) \sigma^2 I \leq \frac{L}{\pi^2} (h\delta v) \sigma^2 x_{max}^2 \tag{3.70}$$

where L is the length of the domain, and h, δv are the longitudinal and azimuthal stepsizes, respectively. Therefore, using (3.64) we find

$$\overline{\langle ||\Delta C_{n,s}||^2 \rangle} \approx \frac{L}{\pi^2} (h\delta v) \sigma^2 x_{max}^2 \int_{-\kappa}^{\kappa} \sum_{p=0}^{N} |\Lambda_{p,s}^n(k)|^2 dk. \tag{3.71}$$

Table 3.1 provides a comparison of the error estimates for the gradient $C_{5,s}$ as computed using an elliptical boundary with $x = 4$ cm, $y = 1$ cm versus an inscribed circular boundary of radius $R = 1$ cm. The upper bound is provided relative to the norm of the error on the surface $||E||_\Gamma^2$, while the average estimate is provided relative to the coefficient $\langle |f_j(k)|^2 \rangle$.

Assume that we have fit field values onto an elliptic cylinder from a rectangular mesh with coordinates uniformly spaced in x and y with spacing $\Delta x = \Delta y$ and

Table 3.1: Error Estimates of $||\Delta C_5||^2$ for the Gradient C_5

Case	Upper Bound	Model Estimate	Scaling of Bound for C_n
Elliptical	0.0028297	0.0164026	$f^{-2n}2^{2n-2}/(n!)^2$
Cylindrical	0.04	0.215348	R^{-2n+2}/n^2

uniformly spaced in z with spacing h, where the values Δx, Δy, and h are identical to those used in Chapter 2. The scale of azimuthal variation δv corresponding to the mesh spacing Δx is then obtained as in Section 2.4.2, with

$$\delta v \approx \frac{\Delta x\sqrt{2}}{x_{max}}. \tag{3.72}$$

We may then define the scaled smoothing envelope

$$g_s(k) = x_{max}\sum_{p=0}^{N}|\Lambda_{p,s}^n(k)|^2 \tag{3.73}$$

so that

$$\langle||\Delta C_{n,s}||^2\rangle = \frac{hL\Delta x\sqrt{2}}{\pi^2}\sigma^2\int_{-\Omega}^{\Omega}g_s(k)dk. \tag{3.74}$$

The factors multiplying the integrand in (3.74) are then identical to those appearing in (2.81), allowing us to compare these expressions directly. The scaled smoothing envelope g_s is illustrated in Fig. 3.18 together with the corresponding quantity for the circular cylinder. It follows from (3.74) that the rms error in the gradient $C_{n,s}(z)$ attained by using the elliptical cylinder is reduced relative to the corresponding value attained using the circular cylinder.

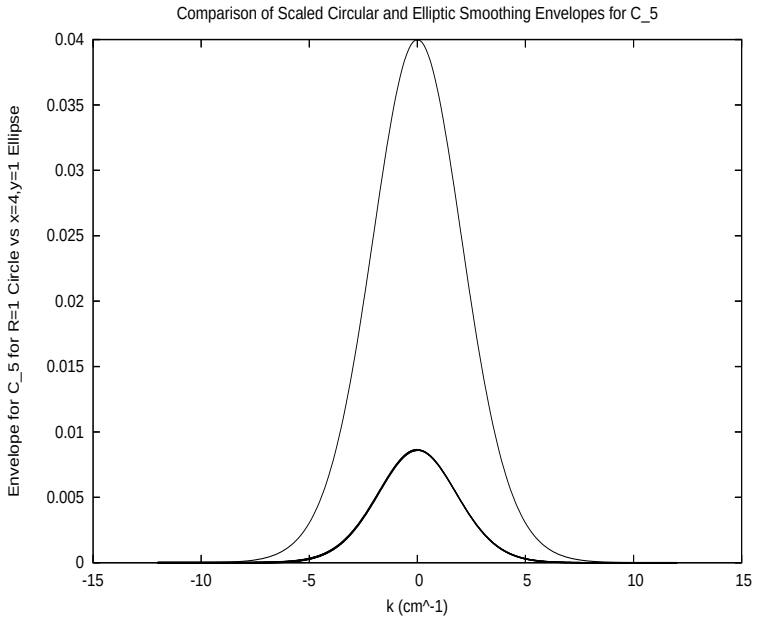

Figure 3.18: Scaled smoothing envelopes for the on-axis gradient $C_5(z)$. (Bold curve) Smoothing envelope appearing in computation from an elliptical cylinder surface with $(x_{max}, y_{max}) = (4, 1)$cm. (Light curve) Smoothing envelope appearing in computation from a circular cylinder surface with $R = 1$. Each envelope has been scaled as in (3.73) to allow direct comparison.

Chapter 4

Use of Rectangular Cylinders

In the present chapter we discuss the use of cylindrical surfaces with rectangular cross section (boxes) for computing transfer maps from numerical field data. This technique may provide an alternative for computing transfer maps for beamline elements with large aspect-ratio apertures.

In this case two new features appear. First, in contrast to Chapters 2-3, the bounding surface can no longer be obtained by holding constant a single coordinate of a smooth curvilinear coordinate system. Instead, the field values B_n on the surface must be fitted to each of the four faces ($x = s$, $x = -s$, $y = d$, $y = -d$) independently. Second, the bounding surface is no longer a smooth, differentiable manifold. This fact has two consequences. First, the outward surface normal is discontinuous at the four corners. Second, for a general field $\mathbf{B}(x, y, z)$, which is an analytic function of the variables (x, y, z), the normal field $\mathbf{n} \cdot \mathbf{B}$ will in general be discontinuous at these corners. We will see that these factors may affect the rate of convergence of the interior solution.

4.1 Analytic Formulation

Consider a rectangular cylinder of half-height d and half-width s, which we define to be the boundary of the domain $\Omega = \{(x, y, z) | -s < x < s, -d < y <$

$d, -\infty < z < \infty\}$, a box of infinite length in z. Provided values for the field $\mathbf{B} = \nabla\psi$ on the surface, we solve the Neumann problem in the interior Ω as follows. After performing a Fourier transform in the variable z, we define the boundary values of the equation $(\nabla_\perp^2 - k^2)\tilde{\psi} = 0$ on each of the four faces $y = d$, $y = -d$, $x = s$, $x = -s$ to be the functions

$$B_y^+(x,k) = \frac{1}{\sqrt{2\pi}} \int_{-\infty}^{\infty} B_y(x,d,z) e^{-ikz} dz, \tag{4.1a}$$

$$B_y^-(x,k) = \frac{1}{\sqrt{2\pi}} \int_{-\infty}^{\infty} B_y(x,-d,z) e^{-ikz} dz, \tag{4.1b}$$

$$B_x^+(y,k) = \frac{1}{\sqrt{2\pi}} \int_{-\infty}^{\infty} B_x(s,y,z) e^{-ikz} dz, \tag{4.1c}$$

$$B_x^-(y,k) = \frac{1}{\sqrt{2\pi}} \int_{-\infty}^{\infty} B_x(-s,y,z) e^{-ikz} dz, \tag{4.1d}$$

for each value of k. We then define the Fourier coefficients of the surface data appearing in (4.1) as

$$\beta_n^T(k) = \frac{1}{s} \int_{-s}^{s} B_y^+(x,k) \cos[(x+s)\lambda_n] dx, \tag{4.2}$$

$$\beta_n^B(k) = -\frac{1}{s} \int_{-s}^{s} B_y^-(x,k) \cos[(x+s)\lambda_n] dx, \tag{4.3}$$

$$\beta_n^R(k) = \frac{1}{d} \int_{-d}^{d} B_x^+(y,k) \cos[(y+d)\tau_n] dy, \tag{4.4}$$

$$\beta_n^L(k) = -\frac{1}{d} \int_{-d}^{d} B_x^-(x,k) \cos[(y+d)\tau_n] dy, \tag{4.5}$$

where

$$\lambda_n = \frac{n\pi}{2s}, \qquad \tau_n = \frac{n\pi}{2d}, \tag{4.6}$$

for $n \neq 0$, together with

$$\beta_0^T(k) = \frac{1}{2s}\int_{-s}^{s} B_y^+(x,k)dx, \tag{4.7}$$

$$\beta_0^B(k) = -\frac{1}{2s}\int_{-s}^{s} B_y^-(x,k)dx, \tag{4.8}$$

$$\beta_0^R(k) = \frac{1}{2d}\int_{-d}^{d} B_x^+(y,k)dy, \tag{4.9}$$

$$\beta_0^L(k) = -\frac{1}{2d}\int_{-d}^{d} B_x^-(x,k)dy. \tag{4.10}$$

Here the superscripts T, B, R, and L denote *top*, *bottom*, *right*, and *left*, respectively. Thus we have the series

$$B_y^+(x,k) = \sum_{n=0}^{\infty} \beta_n^T(k)\cos[(x+s)\lambda_n], \tag{4.11a}$$

$$B_y^-(x,k) = -\sum_{n=0}^{\infty} \beta_n^B(k)\cos[(x+s)\lambda_n], \tag{4.11b}$$

$$B_x^+(x,k) = \sum_{n=0}^{\infty} \beta_n^R(k)\cos[(y+d)\tau_n], \tag{4.11c}$$

$$B_x^-(x,k) = -\sum_{n=0}^{\infty} \beta_n^L(k)\cos[(y+d)\tau_n]. \tag{4.11d}$$

The interior scalar potential ψ may then be written as the sum of four contributions, each determined by the boundary values on a single face. That is, we write

$$\psi(x,y,z) = \psi_T(x,y,z) + \psi_B(x,y,z) + \psi_R(x,y,z) + \psi_L(x,y,z) \tag{4.12}$$

where

$$\tilde{\psi}_T(x,y,k) = \sum_{n=0}^{\infty} \frac{1}{\sqrt{k^2+\lambda_n^2}} \frac{\cosh[(y+d)\sqrt{k^2+\lambda_n^2}}{\sinh[2d\sqrt{k^2+\lambda_n^2}]} \beta_n^T(k)\cos[(x+s)\lambda_n], \tag{4.13}$$

$$\tilde{\psi}_B(x,y,k) = \sum_{n=0}^{\infty} \frac{1}{\sqrt{k^2+\lambda_n^2}} \frac{\cosh[(d-y)\sqrt{k^2+\lambda_n^2}}{\sinh[2d\sqrt{k^2+\lambda_n^2}]} \beta_n^B(k)\cos[(x+s)\lambda_n],$$

$$\tilde{\psi}_R(x,y,k) = \sum_{n=0}^{\infty} \frac{1}{\sqrt{k^2+\tau_n^2}} \frac{\cosh[(x+s)\sqrt{k^2+\tau_n^2}}{\sinh[2s\sqrt{k^2+\tau_n^2}]} \beta_n^R(k)\cos[(y+d)\tau_n],$$

$$\tilde{\psi}_L(x,y,k) = \sum_{n=0}^{\infty} \frac{1}{\sqrt{k^2+\tau_n^2}} \frac{\cosh[(s-x)\sqrt{k^2+\tau_n^2}}{\sinh[2s\sqrt{k^2+\tau_n^2}]} \beta_n^L(k)\cos[(y+d)\tau_n].$$

It can then be shown that this solution satisfies $(\nabla_\perp^2 - k^2)\tilde{\psi} = 0$ subject to the boundary conditions:

$$\left.\frac{\partial\tilde{\psi}}{\partial y}\right|_{y=d} = \left.\frac{\partial\tilde{\psi}_T}{\partial y}\right|_{y=d} = B_y^+(x,z) \tag{4.14}$$

$$\left.\frac{\partial\tilde{\psi}}{\partial y}\right|_{y=-d} = \left.\frac{\partial\tilde{\psi}_B}{\partial y}\right|_{y=-d} = B_y^-(x,z), \tag{4.15}$$

$$\left.\frac{\partial\tilde{\psi}}{\partial x}\right|_{x=s} = \left.\frac{\partial\tilde{\psi}_R}{\partial x}\right|_{x=s} = B_x^+(y,z), \tag{4.16}$$

$$\left.\frac{\partial\tilde{\psi}}{\partial x}\right|_{x=-s} = \left.\frac{\partial\tilde{\psi}_L}{\partial x}\right|_{x=-s} = B_x^-(y,z), \tag{4.17}$$

provided the Fourier series (4.11) converge to the desired values on the surface. Note that the function $\mathbf{B}\cdot\mathbf{n} = B_y$ on the top surface $y = d$ is then determined solely by the normal derivative of the function ψ_T, while the normal derivatives of ψ_B, ψ_R, and ψ_L each vanish at $y = d$. A similar result holds for the other three faces.

4.1.1 Convergence at the Boundary

We now examine the behavior of the series (4.11). First, we note that the set

$$\left\{\frac{1}{\sqrt{2s}}, \frac{1}{\sqrt{s}}\cos[(x+s)\lambda_n] \text{ for } n = 1,2,\cdots\right\} \tag{4.18}$$

forms a complete orthonormal set in $L^2(-s,s)$. (This follows from the completeness of the $\cos(nx)$, $n = 0, 1, \cdots$ on the interval $(0,\pi)$ [67].) The same result holds for the corresponding set of functions of the variable y obtained under $x \to y$, $s \to d$, $\lambda_n \to \tau_n$. It follows that the series (4.11) converge to the functions $B_y^{\pm}$ in $L^2(-s,s)$ and $B_x^{\pm}$ in $L^2(-d,d)$ for each fixed k. That is, these series converge in the mean such that

$$\lim_{N\to\infty} \int_{-s}^{s} |B_y^+(x,k) - \sum_{n=0}^{N} \beta_n^T(k) \cos[(x+s)\lambda_n]|^2 dx = 0, \tag{4.19}$$

etc. However, it is not clear that these series will converge pointwise to the appropriate values.

Indeed, this is not the case for the standard Fourier series of a continuous function f on the interval $(-s,s)$,

$$f(x) = \sum_{n=0}^{\infty} \left(a_n(k) \cos\left[\frac{n\pi x}{s}\right] + b_n(k) \sin\left[\frac{n\pi x}{s}\right] \right). \tag{4.20}$$

The series (4.20) will not converge to f at the endpoints $x = \pm s$ unless $f(s) = f(-s)$. This occurs because the Nth partial sum of (4.20) is a continuous periodic function of period $2s$, while the periodic extension of f, which we denote $\hat{f}$, is discontinuous at the values $x = -s$ and $x = s$. At $x = s$, for example, we have a jump in $\hat{f}$ of value

$$\begin{aligned} a = \lim_{x^+\to s} \hat{f}(x) - \lim_{x^-\to s} \hat{f}(x) &= \lim_{x^+\to s} f(x-2s) - \lim_{x^-\to s} f(x) \\ &= f(-s) - f(s). \end{aligned} \tag{4.21}$$

As a result of the Gibbs phenomenon [90], the Nth partial sum of (4.20), which we denote $S_N f$, possesses large oscillations near this discontinuity. Consider

the case $a > 0$. Near the discontinuity at $x = s$, the adjacent local maxima have amplitudes given by

$$\lim_{N\to\infty} S_N f(s - \frac{s}{N}) = f(s) - a\Delta, \tag{4.22}$$
$$\lim_{N\to\infty} S_N f(s + \frac{s}{N}) = f(s) + a\Delta,$$

and the series at the value $x = s$ converges to the number

$$\lim_{N\to\infty} S_N f(s) = \frac{f(s) + f(-s)}{2}. \tag{4.23}$$

Here

$$\Delta = \frac{G}{\pi} - \frac{1}{2} = 0.08948987\ldots \tag{4.24}$$

and the value

$$G = \int_0^\pi \frac{\sin(t)}{t} dt \tag{4.25}$$

is known as the Wilbraham-Gibbs constant. The overshoot of 9% appearing in (4.22) persists in the first peak of oscillation as $N \to \infty$. Similar behavior occurs at the left endpoint $x = -s$. As a result of this ringing behavior near the endpoints, the series (4.20) do not converge uniformly. Because the limiting function $\hat{f}$ is discontinuous, we have slowly decaying Fourier coefficients which behave asymptotically as [94]

$$|a_n| \sim \frac{1}{n}, \qquad |b_n| \sim \frac{1}{n}. \tag{4.26}$$

We now compare the behavior of the series (4.11). Note that for each basis function $g_n = \cos[(x + s)\lambda_n]$, we have $g_n(x + 2sj) = (-1)^{nj} g_n(x)$ for integer j. If we write a given series of (4.11) in the form

$$f(x) = \sum_{n=0}^{\infty} a_n g_n(x), \tag{4.27}$$

for x in $(-s, s)$, the series therefore converges to a function h satisfying

$$h(x)|_{(-s,s)} = f(x) = \sum_{n=0}^{\infty} a_n g_n(x), \tag{4.28}$$

$$h(x + 2sj) = \sum_{n=0}^{\infty} (-1)^{nj} a_n g_n(x), \tag{4.29}$$

defined on all of $\mathbb{R}$. We define

$$h_E(x) = \sum_{n=0}^{\infty} a_{2n} g_{2n}(x), \qquad h_O(x) = \sum_{n=0}^{\infty} a_{2n+1} g_{2n+1}(x), \tag{4.30}$$

so $h(x) = h_E(x) + h_O(x)$ and $h(x + 2s) = h_E(x) - h_O(x)$ for x in $(-s, s)$. It follows that, for $0 < \delta < s$,

$$h(s - \delta) = h_E(s - \delta) + h_O(s - \delta), \quad \text{and} \tag{4.31}$$

$$h(s + \delta) = h(-(s - \delta) + 2s) = h_E(-(s - \delta)) - h_O(-(s - \delta)) \tag{4.32}$$

$$= h_E(s - \delta) + h_O(s - \delta). \tag{4.33}$$

Therefore,

$$\lim_{\delta \to 0} h(s - \delta) = \lim_{\delta \to 0} h(s + \delta) = h_E(s) + h_O(s) = h(s), \tag{4.34}$$

and h is continuous at $x = s$. A similar result applies at $x = -s$. It follows that the series (4.11) converge pointwise to the desired boundary values. (However, the series of derivatives will *not* in general converge pointwise.) Because the limiting function h is continuous, the coefficients therefore [94] behave asymptotically as

$$|\beta_n^T(k)| \sim \frac{1}{n^2}. \tag{4.35}$$

In particular, there exists a constant C such that

$$|\beta_n^T(k)| \leq \frac{C}{n^2} \tag{4.36}$$

for all n. Since [23]

$$\sum_{n=1}^{\infty} \frac{C}{n^2} = \frac{C\pi^2}{6} \tag{4.37}$$

converges, the sum (4.27) converges uniformly by the Weierstrass M-test. As a result, the sums appearing in (4.13) converge uniformly on $\bar{\Omega}$, up to and including the boundary. However, convergence on the boundary is in general no faster than $1/n^2$.

Note that in Chapters 2-3, uniform convergence of the series on the boundary is guaranteed provided only that the boundary values themselves are continuous, and issues such as those above do not arise. Indeed, for the case that boundary values are analytic, the coefficients must decay faster than any power of $1/n$ (see Appendix C). When the boundary values are known exactly, it follows that the sums appearing in Chapters 2-3 will converge more rapidly, and require fewer terms to obtain accurate interior values, than those described here. The rate of convergence at the boundary for the fit to the monopole-pair field of Section 2.3.1, illustrated by the decay of the Fourier-type coefficients on the surface, is demonstrated in Fig. 4.1 for each of the geometries considered in Fig. 4.7. Note that even after 20 terms, coefficients at the top face of the rectangular cylinder are still on the order of 10^{-3}.

4.1.2 Analyticity/Singularity at Corners

We ask whether the convergence behavior at the boundary can be improved. In particular, consider the ideal case of smooth boundary-values. Suppose that the

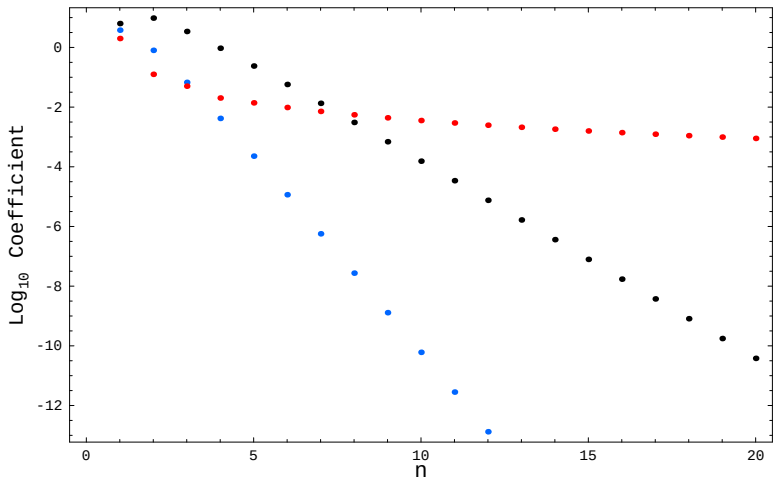

Figure 4.1: Log (base 10) of the magnitude of the Fourier-type coefficients for the monopole-pair field on the boundary surfaces of Chapters 2-4, evaluated for $k = 1$ cm^{-1}. (Blue) Values $B_n(k)$ for the circular cylinder. (Black) Values $F_n(k)$ for the elliptical cylinder. (Red) Values $\beta_n^T(k)$ for the rectangular cylinder.

boundary values $\mathbf{n} \cdot \mathbf{B}^{(bv)}$, as interpolated onto the surface $\partial\Omega$, define a function that can be obtained as the restriction of a function $\mathbf{B}^{(fit)}$ to $\partial\Omega$, where $\mathbf{B}^{(fit)}$ is analytic in x, y, and z. For the case of an analytic boundary $\partial\Omega$, the solution is guaranteed to be analytic on $\bar{\Omega}$. (See Appendix H.3.2.) However, this is not the case for a domain with a corner or edge. In general, one or more of the derivatives may diverge at the corner, and the estimates of Appendix H.3.2 may fail.

Consider, for example, the Neumann problem in a rectangle $(0, \alpha) \times (0, \beta)$ for $\alpha, \beta > 0$ with a corner at $x = y = 0$. To investigate the behavior near a corner, we use local polar coordinates (r, ϕ) such that $x = r\cos\phi$, $y = r\sin\phi$, and r denotes the distance from the corner at the origin. In particular, consider the function

$$u(r, \phi) = \frac{r^4(\ln r \cos 4\phi - \phi \sin 4\phi)}{2\pi} \tag{4.38}$$

in the wedge $\{(r,\phi)|r > 0, 0 < \phi < \pi/2\}$. Note that (4.38) is a solution to the Neumann problem

$$\nabla^2 u = 0, \tag{4.39}$$

$$\left.\frac{\partial u}{\partial n}\right|_{\phi=0} = 0, \qquad \left.\frac{\partial u}{\partial n}\right|_{\phi=\pi/2} = -y^3, \tag{4.40}$$

where the boundary values (4.40) can be obtained as the normal component of the analytic vector field $\mathbf{B}^{(fit)} = y^3\mathbf{e}_x$ on the boundary of the wedge. In rectangular coordinates, u becomes

$$u(x,y) = \frac{1}{4\pi}\{8(-x^3y + xy^3)\arctan^{-1}(y/x) + (x^4 - 6x^2y^2 + y^4)\ln(x^2+y^2)\}, \tag{4.41}$$

which fails to be analytic in the variables x, y at the point $x = y = 0$. In particular, note that the fourth derivatives of ψ behave as

$$\frac{\partial^4 u}{\partial x^4} = \frac{25 + 6\ln(x^2+y^2)}{\pi}, \tag{4.42}$$

$$\frac{\partial^4 u}{\partial y^4} = \frac{25 + 6\ln(x^2+y^2)}{\pi}, \tag{4.43}$$

$$\frac{\partial^4 u}{\partial^2 x \partial^2 y} = -\frac{25 + 6\ln(x^2+y^2)}{\pi}, \tag{4.44}$$

$$\ldots \text{ etc.} \tag{4.45}$$

which diverge as $\ln r$ as $r \to 0$. More generally, solutions for smooth boundary-value data in the rectangle behave near the corners as

$$u(r,\phi) \sim Cr^4(\ln r \cos 4\phi - \phi \sin 4\phi) + w(r,\phi), \tag{4.46}$$

where the harmonic function w is analytic at the corner $r = 0$. Here the functions C and w are determined by the boundary conditions on the surface of the rectangle. The singular behavior of the solution at $r = 0$ is therefore characterized by the divergence of the fourth derivatives. We refer the interested reader to [34], [35], [36].

4.1.3 Determination of Generalized Gradients

We now turn to the problem of computing a representation for ψ and the corresponding vector potential $\mathbf{A}$ in power series about the axis of the rectangular cylinder. We note that the summands in the solution (4.13) may be rewritten using expressions of the form

$$\frac{\cosh[(y+d)\sqrt{k^2+\lambda_n^2}]\cos[(x+s)\lambda_n]}{\sinh[2d\sqrt{k^2+\lambda_n^2}]} = \tag{4.47}$$
$$(-1)^{\lfloor n/2\rfloor}\left\{\begin{array}{l} \pm\dfrac{Re\left\{\begin{matrix}\cos\\ \sin\end{matrix}\right\}[x\lambda_n+iy\sqrt{k^2+\lambda_n^2}]}{2\sinh[d\sqrt{k^2+\lambda_n^2}]}+\dfrac{Im\left\{\begin{matrix}\sin\\ \cos\end{matrix}\right\}[x\lambda_n+iy\sqrt{k^2+\lambda_n^2}]}{2\cosh[d\sqrt{k^2+\lambda_n^2}]} \end{array}\right\},$$

$$\frac{\cosh[(d-y)\sqrt{k^2+\lambda_n^2}]\cos[(x+s)\lambda_n]}{\sinh[2d\sqrt{k^2+\lambda_n^2}]} = \tag{4.48}$$
$$(-1)^{\lfloor n/2\rfloor}\left\{\begin{array}{l} \pm\dfrac{Re\left\{\begin{matrix}\cos\\ \sin\end{matrix}\right\}[x\lambda_n+iy\sqrt{k^2+\lambda_n^2}]}{2\sinh[d\sqrt{k^2+\lambda_n^2}]}-\dfrac{Im\left\{\begin{matrix}\sin\\ \cos\end{matrix}\right\}[x\lambda_n+iy\sqrt{k^2+\lambda_n^2}]}{2\cosh[d\sqrt{k^2+\lambda_n^2}]} \end{array}\right\},$$

together with the corresponding expressions obtained under $x \to y$, $d \to s$, $\lambda_n \to \tau_n$. Here the upper values apply when n is even, while the lower values apply when n is odd. We have introduced the notation $\lfloor x \rfloor$ for the *floor* of the real number x. (The expression $\lfloor n/2 \rfloor$ thus denotes the integer part of $n/2$.) We can therefore use Taylor series for cos and sin of the form

$$\cos[x\lambda_n+iy\sqrt{k^2+\lambda_n^2}] = \sum_{j=0}^{\infty}\frac{(-1)^j}{(2j)!}(x\lambda_n+iy\sqrt{k^2+\lambda_n^2})^{2j} \tag{4.49}$$

to obtain homogeneous polynomial series in the variables x and y. In particular,

$$\frac{\cosh[(y+d)\sqrt{k^2+\lambda_n^2}]\cos[(x+s)\lambda_n]}{\sinh[2d\sqrt{k^2+\lambda_n^2}]} = (-1)^{\lfloor n/2\rfloor}\sum_{j=0}^{\infty}F_j^n(k)(x\lambda_n+iy\sqrt{k^2+\lambda_n^2})^j$$

where

$$F_j^n(k) = \begin{cases} \frac{(-1)^{\lfloor j/2 \rfloor}}{2j! \sinh[d\sqrt{k^2+\lambda_n^2}]} & \text{even } n, \text{ even } j \\ \frac{-i(-1)^{\lfloor j/2 \rfloor}}{2j! \cosh[d\sqrt{k^2+\lambda_n^2}]} & \text{even } n, \text{ odd } j \\ \frac{-(-1)^{\lfloor j/2 \rfloor}}{2j! \sinh[d\sqrt{k^2+\lambda_n^2}]} & \text{odd } n, \text{ odd } j. \end{cases} \tag{4.50}$$

The resulting series may then be used in (4.13) after summing over n to compute the Taylor coefficients of $\tilde{\psi}$ in the variables x and y.

It remains to compute the Taylor coefficients $a_l^w(z)$ of the interior vector potential $\mathbf{A}$. We will compute these coefficients in the gauge $xA_y - yA_x = 0$, corresponding to the gauge $A_\phi = 0$ used in Chapters 2-3. The on-axis gradients may be determined by constructing series in the variable ρ from (4.49) in the form (2.9,2.19) and comparing term-by-term at each degree. Throughout this discussion, we let $f_n(k) = \sqrt{k^2 + \lambda_n^2}$. Note that in cylindrical coordinates we may write

$$\exp[i(x\lambda_n + iyf_n)] = \exp[\rho(i\lambda_n \cos\phi - f_n \sin\phi)] = \sum_{j=0}^{\infty} \frac{\rho^j}{j!}(i\lambda_n \cos\phi - f_n \sin\phi)^j \tag{4.51}$$

and the angular factor appearing in each term may be written as a Fourier series in ϕ as

$$(i\lambda_n \cos\phi - f_n \sin\phi)^j = \left[\frac{i}{2}(s_+ e^{i\phi} + s_- e^{-i\phi})\right]^j = \left(\frac{i}{2}\right)^j \sum_{k=0}^{j} \binom{j}{k} s_+^k s_-^{j-k} e^{i(2k-j)\phi} \tag{4.52}$$

where we have defined $s_+ = \lambda_n + f_n$ and $s_- = \lambda_n - f_n$. Therefore,

$$\exp[i(x\lambda_n + iyf_n)] = \sum_{j=0}^{\infty} \sum_{k=0}^{j} \left(\frac{i}{2}\right)^j \frac{1}{k!(j-k)!} s_+^k s_-^{j-k} \rho^j \exp[i(2k-j)\phi]. \tag{4.53}$$

Noting than any absolutely convergent sum of the above form can be reordered using

$$\sum_{j=0}^{\infty} \sum_{k=0}^{j} a_{jk} = \sum_{l=0}^{\infty} \sum_{m=0}^{\infty} a_{l+m,m}, \tag{4.54}$$

we obtain a double-infinite series of the form

$$\exp[i(x\lambda_n + iyf_n)] = \sum_{l=0}^{\infty}\sum_{m=0}^{\infty}\left(\frac{i}{2}\right)^{l+m}\frac{1}{m!l!}s_+^m s_-^l \rho^{l+m} e^{i(m-l)\phi}. \tag{4.55}$$

Similarly, the series for $\exp[-i(x\lambda_n + iyf_n)]$ can be obtained from (4.55) by taking $\rho \to -\rho$, introducing a factor of $(-1)^{l+m}$. Let

$$\theta_{lm} = \begin{cases} 0 & \text{if } l+m \text{ is even,} \\ \\ 1 & \text{if } l+m \text{ is odd.} \end{cases} \tag{4.56}$$

We therefore have

$$\cos[x\lambda_n + iyf_n] = \sum_{l=0}^{\infty}\sum_{m=0}^{\infty}\left(\frac{i}{2}\right)^{l+m}\frac{1}{m!l!}s_+ s_- \rho^{l+m} e^{i(m-l)\phi}(1-\theta_{lm}), \tag{4.57}$$

$$\sin[x\lambda_n + iyf_n] = \sum_{l=0}^{\infty}\sum_{m=0}^{\infty}\left(\frac{i}{2}\right)^{l+m}\frac{1}{m!l!}s_+ s_- \rho^{l+m} e^{i(m-l)\phi}\theta_{lm}, \tag{4.58}$$

where $s_+ = \lambda_n + \sqrt{k^2+\lambda_n^2}$ and $s_- = \lambda_n - \sqrt{k^2+\lambda_n^2}$. The same argument gives also

$$\cos[y\tau_n + ixg_n] = \sum_{l=0}^{\infty}\sum_{m=0}^{\infty}\left(\frac{1}{2}\right)^{l+m}\frac{(-1)^l}{m!l!}q_-^m q_+^l \rho^{l+m} e^{i(m-l)\phi}(1-\theta_{lm}), \tag{4.59}$$

$$\sin[x\lambda_n + iyf_n] = \frac{1}{i}\sum_{l=0}^{\infty}\sum_{m=0}^{\infty}\left(\frac{1}{2}\right)^{l+m}\frac{(-1)^l}{m!l!}q_-^m q_+^l \rho^{l+m} e^{i(m-l)\phi}\theta_{lm}, \tag{4.60}$$

where $q_+ = \tau_n + \sqrt{k^2+\tau_n^2}$ and $q_- = \tau_n - \sqrt{k^2+\tau_n^2}$.

We may use these expressions to construct series for the solutions $\tilde{\psi}_T$, $\tilde{\psi}_B$, $\tilde{\psi}_R$, and $\tilde{\psi}_L$. Define

$$\delta_{lm}^n = \begin{cases} \theta_{lm} & \text{if } n \text{ is even} \\ \\ 1-\theta_{lm} & \text{if } n \text{ is odd} \end{cases} \tag{4.61}$$

Then we have, for example,

$$\tilde{\psi}_T(\rho,\phi,k) = \sum_{n=0}^{\infty} \frac{(-1)^{\lfloor n/2 \rfloor}}{f_n} \beta_n^T(k) \sum_{l,m=0}^{\infty} \frac{(-1)^{\lfloor (l+m)/2 \rfloor}}{2^{l+m}} \frac{\rho^{l+m}}{m!l!} s_+^m s_-^l \\ \times \left(\frac{(\delta_{lm}^n - 1)^n \cos[(m-l)\phi]}{2\sinh[df_n]} + \frac{\delta_{lm}^n \sin[(m-l)\phi]}{2\cosh[df_n]} \right). \tag{4.62}$$

The on-axis gradients are determined by those terms of (4.62) for which the power of ρ is equal to the order of the multipole. In the cylinder expansion (2.9,2.19), these are the terms with $l = 0$, namely terms of the form

$$\rho^m [C_{m,s}(z) \sin m\phi + C_{m,c}(z) \cos m\phi] \text{ for } m = 0, 1, \cdots. \tag{4.63}$$

Noting that the terms of degree r of this type in (4.62) are those with $(l,m) = (r,0)$ and $(l,m) = (0,r)$, we obtain explicit expressions for the on-axis gradient functions $C_{r,c}^T$, $C_{r,s}^T$ contributing to $\tilde{\psi}_T$. A similar procedure may be used to determine on-axis gradients for each of the functions $\tilde{\psi}^B$, $\tilde{\psi}^R$, and $\tilde{\psi}^L$.

The on-axis gradients may then be written as the sum of four contributions:

$$C_{r,\alpha}(z) = C_{r,\alpha}^T(z) + C_{r,\alpha}^B(z) + C_{r,\alpha}^R(z) + C_{r,\alpha}^L(z) \tag{4.64}$$

for $\alpha = c, s$. We have, contributing from the top face for $r \neq 0$,

$$\tilde{C}_{r,c}^T(k) = \frac{(-1)^{\lfloor r/2 \rfloor}}{2^r r!} \sum_{n=0}^{\infty} \frac{s_+^r + s_-^r}{\sqrt{k^2+\lambda_n^2}} (-1)^{\lfloor n/2 \rfloor} \frac{(\delta_{0q}^n - 1)^n}{2\sinh(d\sqrt{k^2+\lambda_n^2})} \beta_n^T(k), \tag{4.65}$$

$$\tilde{C}_{r,s}^T(k) = \frac{(-1)^{\lfloor r/2 \rfloor}}{2^r r!} \sum_{n=0}^{\infty} \frac{s_+^r - s_-^r}{\sqrt{k^2+\lambda_n^2}} (-1)^{\lfloor n/2 \rfloor} \frac{\delta_{0q}^n}{2\cosh(d\sqrt{k^2+\lambda_n^2})} \beta_n^T(k), \tag{4.66}$$

and

$$\tilde{C}_{0,c}^T(k) = \sum_{n \text{ even}} \frac{(-1)^{n/2}}{\sqrt{k^2+\lambda_n^2}} \frac{\beta_n^T(k)}{2\sinh(d\sqrt{k^2+\lambda_n^2})}, \qquad \tilde{C}_{0,s}^T(k) = 0. \tag{4.67}$$

Similarly, contributing from the bottom face:

$$\tilde{C}^B_{r,c}(k) = \frac{(-1)^{\lfloor r/2 \rfloor}}{2^r r!} \sum_{n=0}^{\infty} \frac{s_+^r + s_-^r}{\sqrt{k^2+\lambda_n^2}} (-1)^{\lfloor n/2 \rfloor} \frac{(\delta^n_{0q}-1)^n}{2\sinh(d\sqrt{k^2+\lambda_n^2})} \beta_n^B(k), \quad (4.68)$$

$$\tilde{C}^B_{r,s}(k) = -\frac{(-1)^{\lfloor r/2 \rfloor}}{2^r r!} \sum_{n=0}^{\infty} \frac{s_+^r - s_-^r}{\sqrt{k^2+\lambda_n^2}} (-1)^{\lfloor n/2 \rfloor} \frac{\delta^n_{0q}}{2\cosh(d\sqrt{k^2+\lambda_n^2})} \beta_n^B(k), \quad (4.69)$$

and

$$\tilde{C}^B_{0,c}(k) = \sum_{n \text{ even}} \frac{(-1)^{n/2}}{\sqrt{k^2+\lambda_n^2}} \frac{\beta_n^B(k)}{2\sinh(d\sqrt{k^2+\lambda_n^2})}, \qquad \tilde{C}^T_{0,s}(k) = 0. \quad (4.70)$$

Contributing from the right face:

$$\tilde{C}^R_{r,c}(k) = \frac{1}{2^r r!} \sum_{n\text{even}}^{\infty} \frac{q_-^r + (-1)^r q_+^r}{\sqrt{k^2+\tau_n^2}} (-1)^{\lfloor n/2 \rfloor} \left(\frac{1-\theta_{0q}}{2\sinh(s\sqrt{k^2+\tau_n^2})} - \frac{\theta_{0q}}{2\cosh(s\sqrt{k^2+\tau_n^2})} \right) \beta_n^R(k), \quad (4.71)$$

$$\tilde{C}^R_{r,s}(k) = \frac{1}{2^r r!} \sum_{n\text{odd}}^{\infty} \frac{q_-^r - (-1)^r q_+^r}{\sqrt{k^2+\tau_n^2}} (-1)^{\lfloor n/2 \rfloor} \left(\frac{-\theta_{0q}}{2\sinh(s\sqrt{k^2+\tau_n^2})} + \frac{1-\theta_{0q}}{2\cosh(s\sqrt{k^2+\tau_n^2})} \right) \beta_n^R(k), \quad (4.72)$$

and

$$\tilde{C}^R_{0,c}(k) = \sum_{n \text{ even}}^{\infty} \frac{(-1)^{n/2}}{\sqrt{k^2+\tau_n^2}} \frac{\beta_n^R(k)}{2\sinh(s\sqrt{k^2+\tau_n^2})}, \qquad \tilde{C}^R_{0,s}(k) = 0. \quad (4.73)$$

Contributing from the left face:

$$\tilde{C}^L_{r,c}(k) = \frac{1}{2^r r!} \sum_{n\text{even}}^{\infty} \frac{q_-^r + (-1)^r q_+^r}{\sqrt{k^2+\tau_n^2}} (-1)^{\lfloor n/2 \rfloor} \left(\frac{1-\theta_{0q}}{2\sinh(s\sqrt{k^2+\tau_n^2})} + \frac{\theta_{0q}}{2\cosh(s\sqrt{k^2+\tau_n^2})} \right) \beta_n^L(k), \quad (4.74)$$

$$\tilde{C}^L_{r,s}(k) = \frac{1}{2^r r!} \sum_{n\text{odd}}^{\infty} \frac{q_-^r - (-1)^r q_+^r}{\sqrt{k^2+\tau_n^2}} (-1)^{\lfloor n/2 \rfloor} \left(\frac{-\theta_{0q}}{2\sinh(s\sqrt{k^2+\tau_n^2})} - \frac{1-\theta_{0q}}{2\cosh(s\sqrt{k^2+\tau_n^2})} \right) \beta_n^L(k), \quad (4.75)$$

and

$$\tilde{C}^L_{0,c}(k) = \sum_{n \text{ even}}^{\infty} \frac{(-1)^{n/2}}{\sqrt{k^2+\tau_n^2}} \frac{\beta^L_n(k)}{2\sinh(s\sqrt{k^2+\tau_n^2})}, \qquad \tilde{C}^R_{0,s}(k) = 0. \tag{4.76}$$

These on-axis gradient functions determine the Taylor coefficients $a^w_l(z)$ of the vector potential from (2.24), just as in Chapters 2-3, which may then be used to compute transfer maps.

4.2 Numerical Implementation

The routine just described has been implemented as a Mathematica notebook, and is given in Appendix I.

4.3 Benchmarks of Numerical Accuracy

Consider the case of the monopole-pair field treated in Section 2.3.1. We again choose the parameters $a = 4.7008$ cm, $g = 0.3$ Tcm^2 for the location and strength of the monopoles. On-axis gradients of the resulting field were computed numerically from surface data using a rectangular cylinder with a half-height of 1 cm and a half-width of 4 cm. The field values $B_x(x,y,z)$ and $B_y(x,y,z)$ are known analytically from (2.27). After taking a Fourier transform in the variable z of the resulting fields, the field values $\tilde{B}_x(y,k)$ and $\tilde{B}_y(x,k)$ of (2.42) were integrated over the faces of the rectangular cylinder for an array of values $k_j = -k_{max} + j\delta k$, $j = 1, \ldots, N$, producing the four sets of coefficients $\beta^T_n(k_j)$, $\beta^B_n(k_j)$, $\beta^R_n(k_j)$, $\beta^L_n(k_j)$. These are stored as two-dimensional arrays in the variables n and j. The interior solution $\tilde{\psi}$ of (4.13) was computed as a function of the variables x, y for each of

the k_j. In this way, we check the convergence of the solution at the boundary and determine the number of Fourier modes required to obtain a desire tolerance. An illustration is given in Fig. 4.2 for the value $k = 2$ cm^{-1}. We then compute the on-axis gradient functions $C^T_{n,s}$, $C^B_{n,s}$, $C^R_{n,s}$, $C^L_{n,s}$ using (4.64-4.76). As a result, we may reconstruct the potential components $\tilde{\psi}^T$, $\tilde{\psi}^B$, $\tilde{\psi}^R$, $\tilde{\psi}^L$ from their corresponding on-axis gradients. These potentials may be checked against the solution (4.13) to verify that the on-axis gradient expressions have been correctly implemented. We then compute the functions $C^{[m]}_{n,s}(z)$ for the cases $(n,m) = (1,0)$, $(n,m) = (3,0)$, $n = (5,0)$, and $(n,m) = (1,4)$. The resulting errors are illustrated in Fig. 4.3. Errors are comparable to those obtained using the circular and elliptical cylinders.

4.4 Insensitivity to Numerical Noise

4.4.1 Theory of Smoothing

The theory of smoothing for the rectangular cylinder parallels that described for the elliptical cylinder in Section 3.4.2. The on-axis gradients may be written in the form

$$C^X_{r,s}(z) = \frac{1}{\sqrt{2\pi}} \int_{-\infty}^{\infty} dk e^{ikz} \sum_{n=0}^{\infty} \Lambda^{r,X}_{n,s}(k) \beta^X_n(k), \tag{4.77}$$

$$C^X_{r,c}(z) = \frac{1}{\sqrt{2\pi}} \int_{-\infty}^{\infty} dk e^{ikz} \sum_{n=0}^{\infty} \Lambda^{r,X}_{n,c}(k) \beta^X_n(k), \tag{4.78}$$

where $X = T, B, R$, or L. In particular, the kernels contributing to $C^T_{r,s}$ are

$$\Lambda^{r,T}_{n,s}(k) = \frac{(-1)^{\lfloor r/2 \rfloor}(-1)^{\lfloor n/2 \rfloor}}{2^r r!} \frac{s^r_+ - s^r_-}{\sqrt{k^2+\lambda^2_n}} \frac{1}{2\cosh(d\sqrt{k^2+\lambda^2_n})}. \tag{4.79}$$

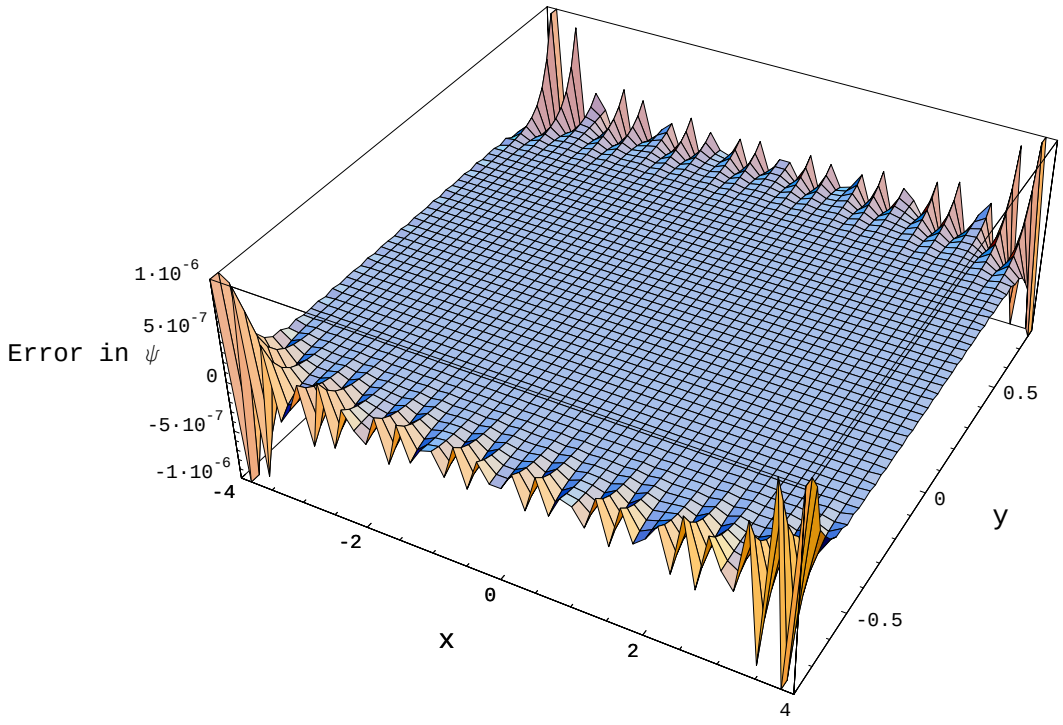

Figure 4.2: Error in the approximate solution $\tilde{\psi}(x, y, k)$ for $k = 2$ cm^{-1} obtained by fitting the monopole-pair field to a rectangular cylinder.

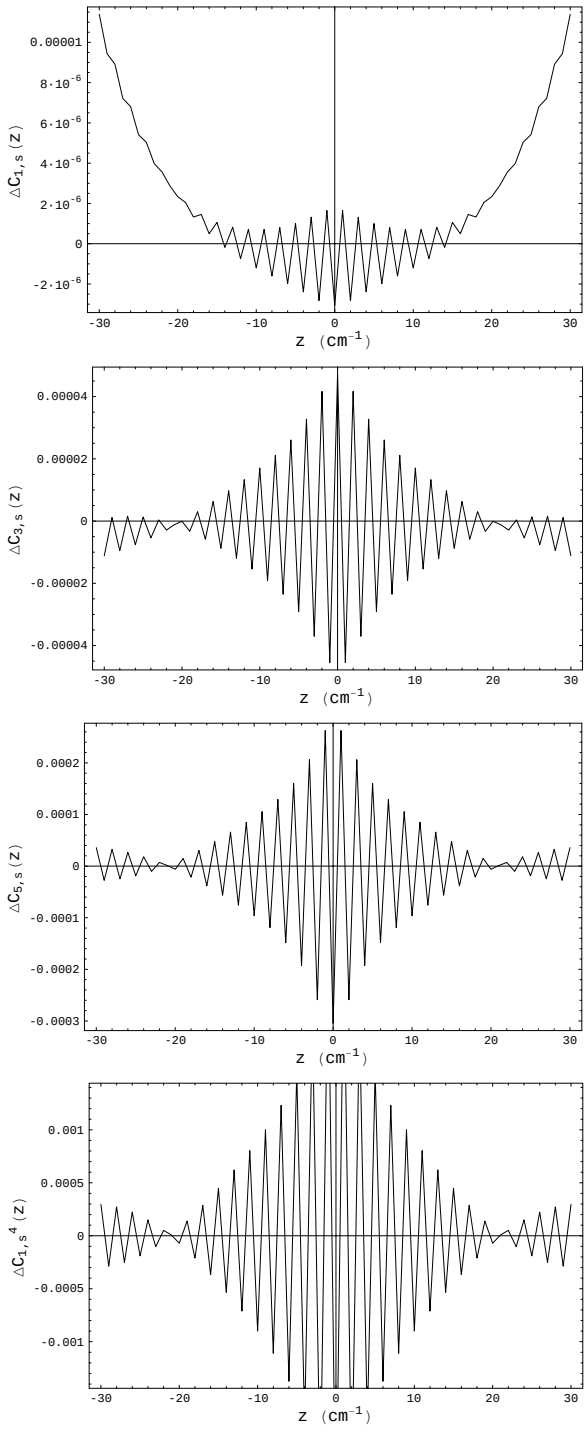

Figure 4.3: Error in the computed on-axis gradient functions $C_{1,s}$, $C_{3,s}$, $C_{5,s}$, and $C_{1,s}^{[4]}$, measured relative to peak values.

Recall that $s_+ = \lambda_n + \sqrt{k^2 + \lambda_n^2}$, $s_- = \lambda_n - \sqrt{k^2 + \lambda_n^2}$ depend on both n and k. Each kernel is determined by the parameters (s, d) defining the dimensions of the boundary box.

In Fig. 4.4 we illustrate the sequence of kernels contributing to $C^T_{5,s}(z)$ for a rectangular cylinder with $s = 4$ and $d = 1$. (Compare Fig. 3.14.) For fixed n, when k becomes large enough that $k >> \lambda_n$, we have for odd r the asymptotic behavior

$$\Lambda^T_{n,r}(k) \sim \frac{(-1)^{\lfloor r/2 \rfloor}(-1)^{\lfloor n/2 \rfloor}}{2^r r!} 2|k|^{r-1} \exp(-d|k|) \left(1 + O\left(\frac{\lambda_n}{k}\right)\right). \tag{4.80}$$

Similarly, the kernels from the right and left faces behave as

$$\Lambda^R_{n,r}(k) \sim \frac{(-1)^{\lfloor r/2 \rfloor}(-1)^{\lfloor n/2 \rfloor}}{2^r r!} 2|k|^{r-1} \exp(-s|k|) \left(1 + O\left(\frac{\tau_n}{k}\right)\right). \tag{4.81}$$

The lower plots in Fig. 4.4 illustrate the log of the magnitude of the kernels. In this figure, the asymptotic behavior of the kernels is clearly visible for large $|k|$. We note that the rate of decay of the kernels, determined by the slope of the curves in Fig. 4.4, is independent of n for sufficiently large values of k.

As we might expect, the high-frequency values of the kernels are exponentially suppressed by a factor which depends on the domain size. In particular, note that the kernels multiplying those Fourier coefficients β^T_n describing surface values on the top face decay more rapidly as the height of the box increases. In general, the smoothing of high-order modes on a given face occurs at a rate which increases with the distance of that particular face from the axis of the rectangular cylinder.

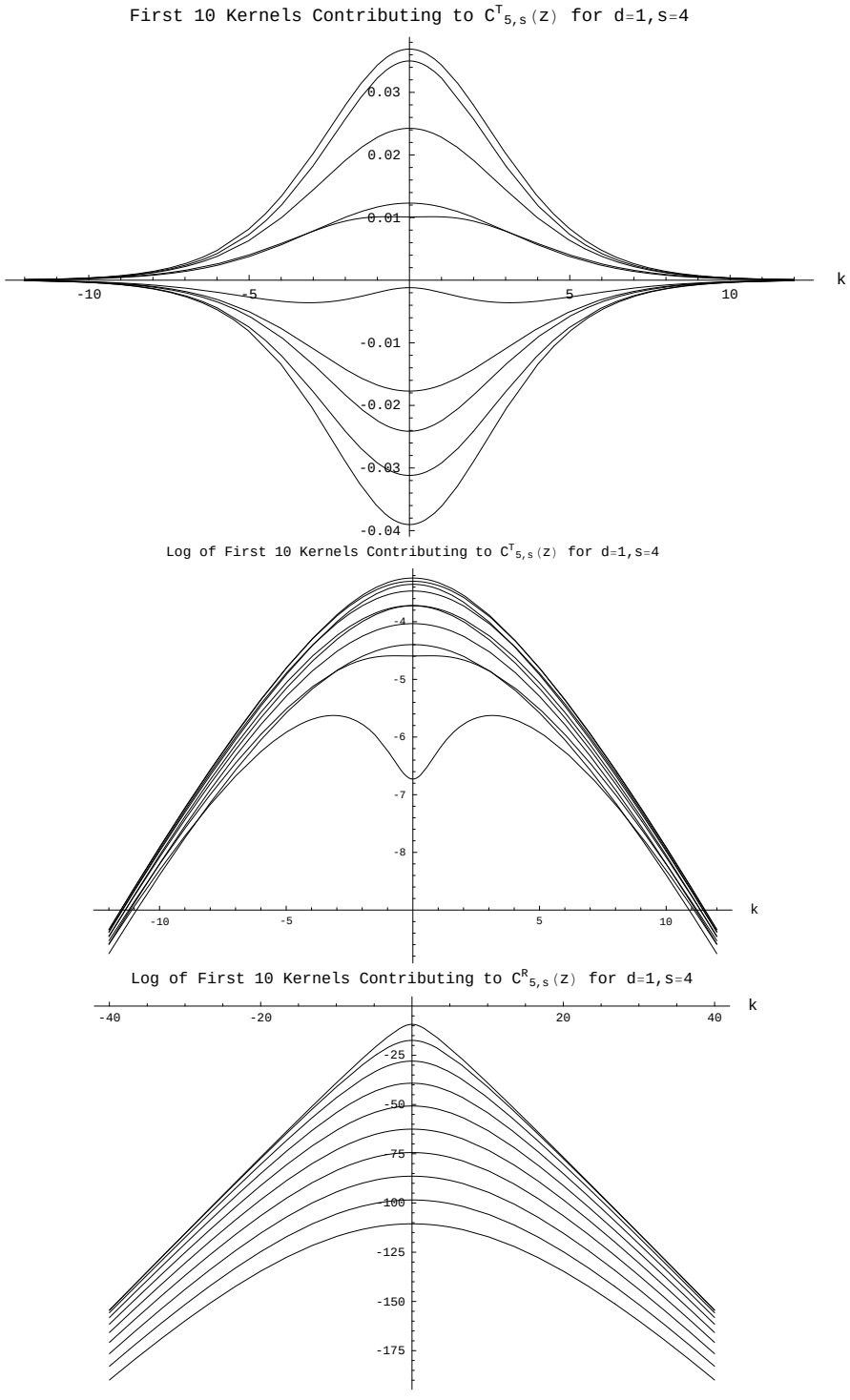

Figure 4.4: Integration kernels contributing the the gradient $C_{5,s}$. (Upper) First 10 kernels $\Lambda_{p,s}^{5,T}$ contributing to $C_{5,s}^T$ for a rectangular cylinder with $d = 1$, $s = 4$. (Lower plots) Log of the magnitude of the first 10 kernels contributing to $C_{5,s}^T$ and $C_{5,s}^R$.

4.4.2 Error Estimates

We wish to obtain estimates for the error of each computed on-axis gradient function $C_{n,\alpha}^{[m]}$ similar to those appearing in Chapters 2-3. Given $B_n^{(bv)}$, the normal component of the interpolated field values on the surface, we have the surface errors on the four faces

$$E^T(x,z) = B_n^{(bv)}\big|_{y=d}(x,z) - B_y(x,d,z), \tag{4.82}$$

$$E^B(x,z) = B_n^{(bv)}\big|_{y=-d}(x,z) - B_y(x,-d,z), \tag{4.83}$$

$$E^R(y,z) = B_n^{(bv)}\big|_{x=s}(y,z) - B_x(s,y,z), \tag{4.84}$$

$$E^L(y,z) = B_n^{(bv)}\big|_{x=-s}(y,z) - B_x(-s,y,z). \tag{4.85}$$

After a Fourier transform in the variable z, the error on a given face may then be written

$$E^{T,B}(x,k) = \sum_{n=0}^{\infty} \alpha_n^{T,B}(k)\cos[(x+s)\lambda_n], \tag{4.86}$$

$$E^{R,L}(y,k) = \sum_{n=0}^{\infty} \alpha_n^{R,L}(k)\cos[(y+d)\tau_n], \tag{4.87}$$

with norms in $L^2([-s,s]\times\mathbb{R})$ and $L^2([-d,d]\times\mathbb{R})$ given by

$$||E^{T,B}||^2 = \sum_{n=0}^{\infty} ||\alpha_n^{T,B}||^2, \qquad ||E^{R,L}||^2 = \sum_{n=0}^{\infty} ||\alpha_n^{R,L}||^2, \tag{4.88}$$

respectively. Here, for example,

$$||E^{T,B}||^2 = \int_{-\infty}^{\infty}\int_{-s}^{s} |E^{T,B}(x,z)|^2 dxdz, \tag{4.89}$$

$$||E^{R,L}||^2 = \int_{-\infty}^{\infty}\int_{-d}^{d} |E^{R,L}(y,z)|^2 dydz, \tag{4.90}$$

and

$$||\alpha_n^X||^2 = \int_{-\infty}^{\infty} |\alpha_n^X(k)|^2 dk \tag{4.91}$$

for $X = T, B, R,$ or L. The corresponding norm of the error over the full surface then satisfies

$$||E||^2 = ||E^T||^2 + ||E^B||^2 + ||E^R||^2 + ||E^L||^2. \tag{4.92}$$

In the discussion that follows, we consider only the error due to field values on the right face. The errors from the other three faces may be obtained similarly and combined using expressions similar to (4.92).

The error in the on-axis gradients $C_{n,\alpha}^R$ is given in terms of the Fourier coefficients of the error on the right face α_n^R by

$$\Delta\tilde{C}_{n,s}^{R[m]}(k) = (ik)^m \sum_{p=0}^{\infty} \Lambda_{p,s}^{n,R}(k)\alpha_p^R(k), \tag{4.93}$$

$$\Delta\tilde{C}_{n,c}^{R[m]}(k) = (ik)^m \sum_{p=0}^{\infty} \Lambda_{p,c}^{n,R}(k)\alpha_p^R(k). \tag{4.94}$$

As shown in Chapter 3, we have as a result that

$$\begin{aligned} ||\Delta C_{n,s}^{R[m]}||^2 = \int_{-\infty}^{\infty} |\Delta\tilde{C}_{n,s}^{R[m]}|^2 dk &\leq \max_k \left[k^{2m} \sum_{p=0}^{\infty} |\Lambda_{p,s}^{n,R}|^2 \right] \int_{-\infty}^{\infty} ||\tilde{E}^R||^2(k) dk \\ &= ||E^R||_\Gamma^2 \max_k \left[k^{2m} \sum_{p=0}^{\infty} |\Lambda_{p,s}^{n,R}|^2 \right], \end{aligned} \tag{4.95}$$

where the sum in brackets converges to a continuous *smoothing envelope* for the right face. In Fig. 4.5 we illustrate the smoothing envelope for both the top and right faces. Note that the envelopes for top-bottom and left-right surfaces are identical.

Using the model of noise as in previous chapters, we estimate the average error

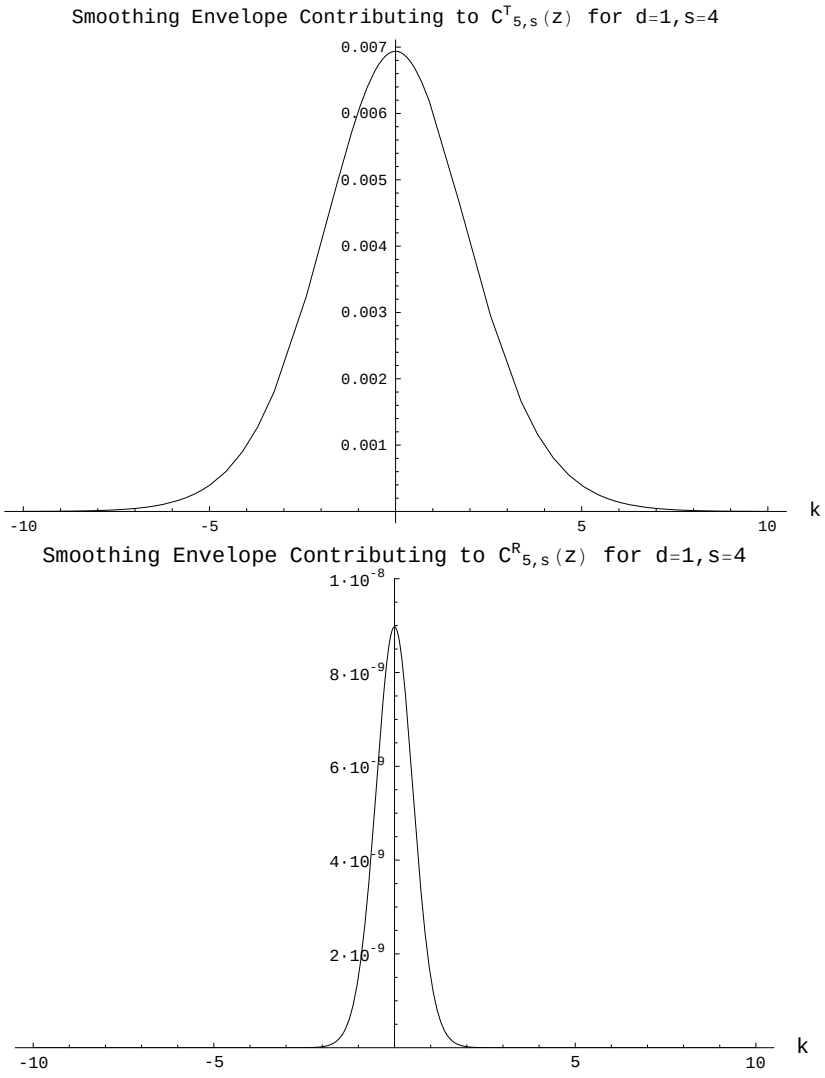

Figure 4.5: Illustration of the smoothing envelopes for the gradient C_5 obtained using a rectangular cylinder with $d = 1$ and $s = 4$. (Upper) Smoothing envelope for the on-axis gradient $C^T_{5,s}$ contributing from the top face. (Lower) Smoothing envelope for the on-axis gradient $C^R_{5,s}$ contributing from the right face.

as

$$\overline{\langle||\Delta C^R_{n,s}||^2\rangle} = \overline{\int_{-\infty}^{\infty} \langle|\alpha^R_j(k)|^2\rangle \sum_{p=0}^{N} |\Lambda^{n,R}_{p,s}(k)|^2 dk} = \overline{\langle|\alpha^R_j(k_p)|^2\rangle} \int_{-\kappa}^{\kappa} \sum_{p=0}^{N} |\Lambda^{n,R}_{p,s}|^2 dk. \tag{4.96}$$

Assuming the model of white noise described in Appendix A, we have

$$\langle|\alpha^T_j(k)|^2\rangle = \frac{L}{\pi d}(h\delta y)\sigma^2 \tag{4.97}$$

where L is the length of the domain, and h, δy are the longitudinal and vertical stepsizes, respectively. Therefore, using (4.96) we find

$$\overline{\langle||\Delta C^R_{n,s}||^2\rangle} = \sigma^2 \left(\frac{Lh}{\pi}\right) \frac{\delta y}{d} \int_{-\kappa}^{\kappa} \sum_{p=0}^{N} |\Lambda^{n,R}_{p,s}|^2 dk. \tag{4.98}$$

Assuming that the errors on each face are independent of one another, we have

$$\overline{\langle||\Delta C_{n,s}||^2\rangle} = \overline{\langle||\Delta C^T_{n,s}||^2\rangle} + \overline{\langle||\Delta C^B_{n,s}||^2\rangle} + \overline{\langle||\Delta C^R_{n,s}||^2\rangle} + \overline{\langle||\Delta C^L_{n,s}||^2\rangle}. \tag{4.99}$$

We have therefore characterized the error in the on-axis gradient functions as the sum of four terms, each of which is determined (and bounded) by the error on a single face of the rectangular cylinder.

We may now investigate the effect of increasing each dimension of the domain independently. Consider increasing the half-width s of the domain for fixed d. In Fig. 4.6 we have illustrated the smoothing envelope appearing in (4.95) for fixed half-height $d = 1$, as the half-width s is increased. Note that the peak values decrease by several orders of magnitude as s increases from 1 to 4. In addition, the spread of the envelopes decreases, becoming more sharply peaked as the right surface moves away from the axis. As a result, the bounds (4.95,4.98) become tighter as s

increases. In addition, the high-frequency Fourier components of the error on the right surface are more rapidly suppressed for large s.

As a final result, we compare the effect of smoothing that is obtained by using a rectangular cylinder surface with those obtained using the circular and elliptical cylinder surfaces (see Fig. 4.7). Assume that we have fit field values onto a rectangular cylinder from a mesh with coordinates uniformly spaced in x and y with spacing $\Delta x = \Delta y$ and uniformly spaced in z with spacing h, where the values Δx, Δy, and h are identical to those used in Chapters 2-3. We may then define the scaled smoothing envelope

$$g_s(k) = \frac{\pi}{s\sqrt{2}} \sum_{p=0}^{N} |\Lambda_{p,s}^{n,T}|^2 + \frac{\pi}{s\sqrt{2}} \sum_{p=0}^{N} |\Lambda_{p,s}^{n,B}|^2 + \frac{\pi}{d\sqrt{2}} \sum_{p=0}^{N} |\Lambda_{p,s}^{n,R}|^2 + \frac{\pi}{d\sqrt{2}} \sum_{p=0}^{N} |\Lambda_{p,s}^{n,L}|^2, \tag{4.100}$$

so that

$$\langle ||\Delta C_{n,s}||^2 \rangle = \frac{hL\Delta x\sqrt{2}}{\pi^2} \sigma^2 \int_{-\kappa}^{\kappa} g_s(k) dk. \tag{4.101}$$

The factor multiplying the integrand in (4.101) is then identical to that appearing in (2.81, 3.74). The scaled smoothing envelope g_s is illustrated in Fig. 4.8 together with the corresponding quantity for the circular and elliptical cylinders. We see that the scaled smoothing envelope for the rectangular cylinder differs only slightly from the corresponding envelope for the inscribed elliptical cylinder of Fig. 4.7. In particular, the peak at $k = 0$ is slightly reduced in the rectangular cylinder case. However, the slow convergence at the boundary requires that a larger number of terms must be retained in (4.64-4.76) to achieve similar accuracy for the gradients $C_n^{[m]}(z)$.

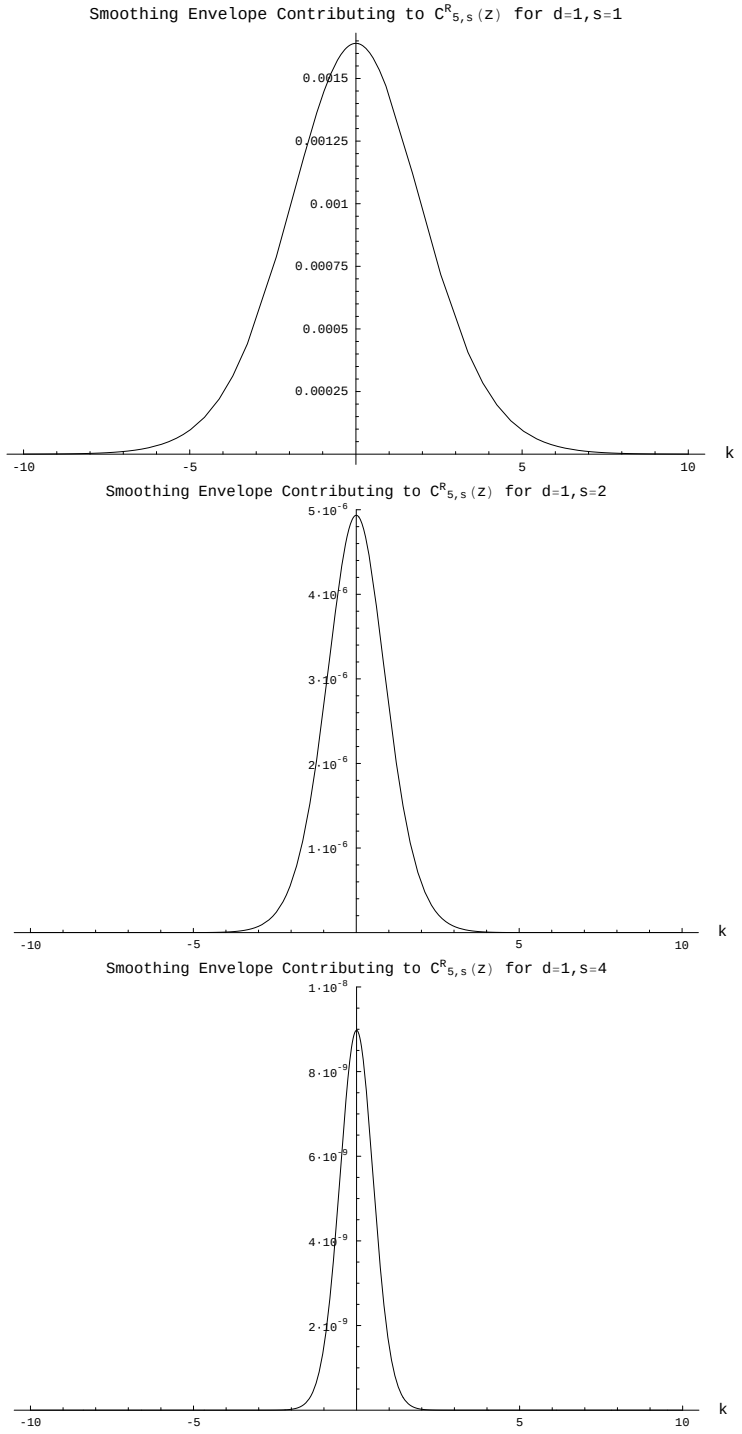

Figure 4.6: Illustration of the smoothing effect of increasing the half-width s of the domain used for surface fitting. Plotted are the smoothing envelopes for the gradient $C^R_{5,s}$ for a rectangular cylinder with $d = 1$ and $s = 1$ (upper), $s = 2$ (middle), $s = 4$ (lower).

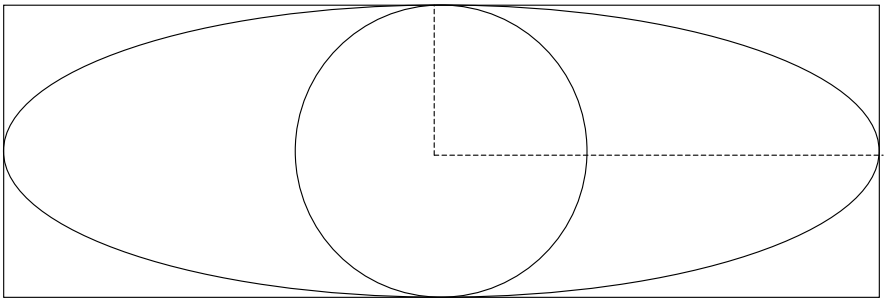

Figure 4.7: Illustration of the circumscribed domains used in computing the smoothing envelopes in Fig. 4.8. The vertical dotted line has length $d =$ cm, while the horizontal dotted line has length $s = 4$ cm.

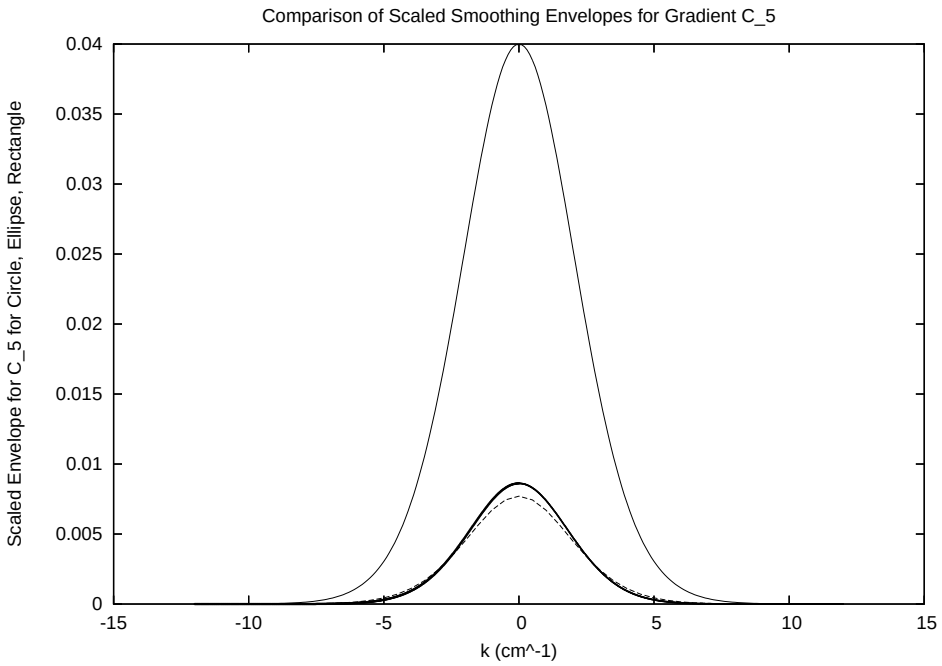

Figure 4.8: Illustration of scaled smoothing envelopes for the domains illustrated in Fig. 4.7. Each envelope is scaled as described in the text, assuming a mesh of fixed spacing in x. (Light curve) Envelope for the circular cylinder. (Bold curve) Envelope for the elliptical cylinder. (Dashed curve) Envelope for the rectangular cylinder.

Chapter 5

Use of General Surfaces

5.1 Comments on Geometry and Separation of Variables

In Chapters 1-4, we have studied techniques for computing charged-particle transfer maps through straight-axis magnetic elements, using field values on a boundary surface surrounding the reference trajectory and enclosing no magnetic sources. In each case, we have used a standard separation of variables technique to represent the Green's function for the surface as a series of orthogonal eigenfunctions of the Laplace operator. While the techniques have been developed for cylinders of various cross-section, this method may be developed for any surface that can be described by holding constant one of the coordinates of a system in which the Laplace equation is separable. It has been known since Bôcher [73],[74] that only 11 such coordinate systems exist: *Cartesian, cylindrical, elliptic cylindrical, parabolic cylindrical, spherical, prolate spheroidal, oblate spheroidal, parabolic, paraboloidal, ellipsoidal,* and *conical*. Recent work [75] has shown that the classification of such coordinate systems follows from the properties of the conformal symmetry group of the Laplace equation. A discussion of these symmetries and their corresponding coordinate systems is presented in Appendix F.

In many cases, we are interested in magnetic elements with significant sagitta, such as dipoles with large bending angles. In these cases, it is not possible in general

to surround the reference trajectory with a cylindrical surface that lies interior to all iron or other magnetic sources (Fig. 5.1). For this reason, we must generalize to more complicated domains for which Laplace's equation is no longer separable. While the previous method of expansion in sets of orthogonal functions cannot be used, we will describe a boundary-element method that employs *all three* components of the field on the surface. In this case we may obtain simple, geometry-independent kernels for computing the interior vector potential and its derivatives. The method makes use of the Helmholtz theorem, together with an application of the Dirac monopole potential, to represent the field in terms of effective single-layer and double-layer source distributions on the surface [19],[42]. The properties of analyticity and insensitivity to noise common to the previous methods will be retained. In particular, the resulting field will be curl and divergence-free and analytic, even in the presence of imperfect surface data and no matter how poorly the surface integrals are evaluated. As before, we may bound the error in the interior field and its derivatives.

5.2 General Domains in $\mathbb{R}^3$

Magnetic elements may have faces with quite complex geometry (Fig. 5.2). In the present chapter, we wish to keep our discussion of general domains as broad as possible. Throughout, we will confine ourselves to a class of domains known as *regular regions* [92], which is general enough to include most cases of interest, but restrictive enough to exclude those cases where standard results may not be applied.

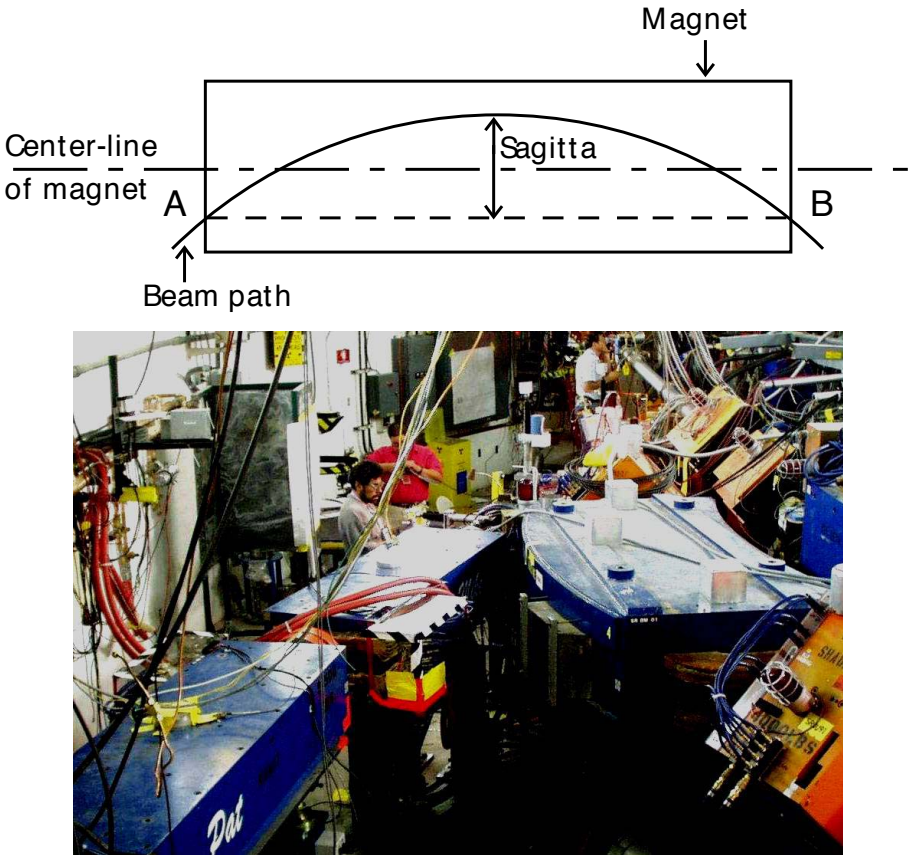

Figure 5.1: (Upper) Illustration of dipole sagitta. (Lower) Connection of the ring injection kicker to the Proton Storage Ring (PSR) at the Los Alamos LANSCE facility. The dipole appearing on the right, which is part of the ring, has a bending angle of 36 degrees, a path length of 2.54948 m, and a sagitta of 23.83 cm.

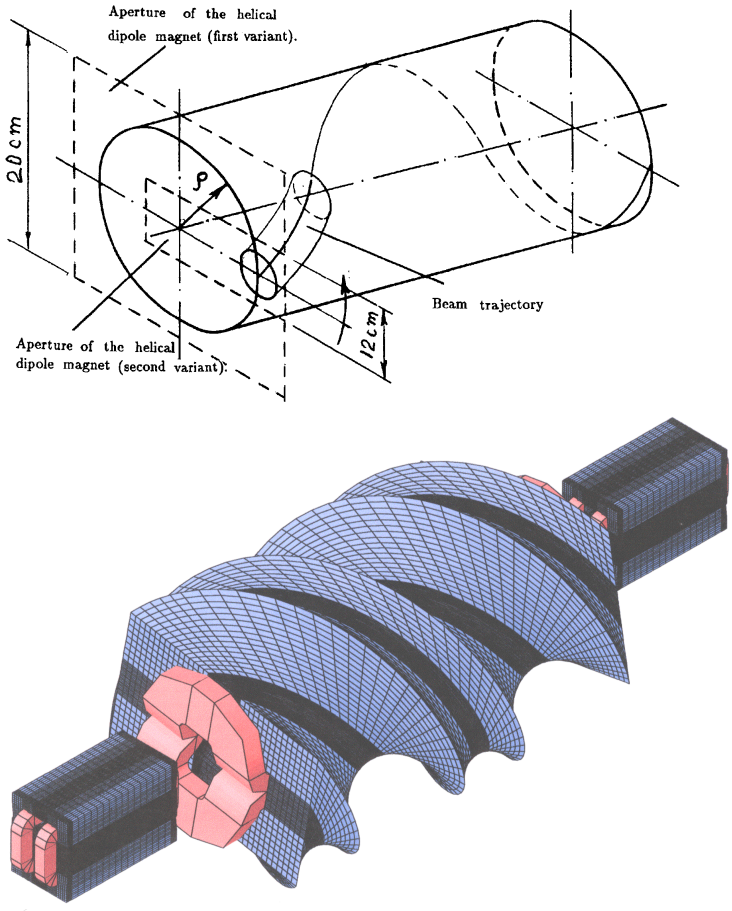

Figure 5.2: (Upper) Proposed helical dipole design [39]. (Lower) Design of the "Warm Snake" helical dipole appearing in the Alternating Gradient Synchrotron (AGS) at Brookhaven National Laboratory [40].

A regular region $\Omega \subset \mathbb{R}^3$ is a bounded open set whose boundary $\Gamma = \partial\Omega$ consists of a finite number of closed, piecewise smooth surfaces. By a piecewise smooth surface, we mean that Γ may be broken into a finite number of surface elements $\Gamma = \bigcup_{j=1}^{n} S_k$ as follows [69]. To each surface element S_k there corresponds a bounded open set D_k in the plane, whose boundary is a single piecewise smooth curve. Each surface element S_k may be represented in $\mathbb{R}^3$ by the parametrization

$$x_1 = \gamma_1(u, v), \qquad x_2 = \gamma_2(u, v), \qquad x_3 = \gamma_3(u, v), \tag{5.1}$$

for all points (u, v) contained in $\bar{D}_k = D_k \cup \partial D_k$. The mapping $\gamma : \bar{D}_k \to S_k$ is a one-to-one C^1 transformation from the plane region $\bar{D}_k$ to the surface element. That is, γ is continuous and has continuous first derivatives on $\bar{D}_k$, and

$$\frac{\partial \mathbf{x}}{\partial u} \times \frac{\partial \mathbf{x}}{\partial v} \neq 0 \tag{5.2}$$

at all points in $\bar{D}_k$. Thus, the inverse of γ exists and is also C^1.

A closed, piecewise smooth surface is the union of a finite number of such smooth surface elements satisfying the following conditions [69]:

i) No two S_i have common interior points.

ii) The intersection of the boundaries of two surface elements $\partial S_i \cap \partial S_j$, $i \neq j$, is either empty, or a single point, or a piecewise smooth arc.

iii) The boundaries of any three distinct elements have at most one point in common.

iv) Any two points of Γ can be joined by a path in Γ.

v) Every point p on the boundary of a surface element S_i lies also on the boundary of at least one other surface element S_j, such that $p \in \partial S_i \cup \partial S_j$ for some $j \neq i$.

The surface Γ is therefore a 2-dimensional manifold consisting of surface elements patched together in a sufficiently regular way. We require, in addition, that Γ satisfies a *cone condition* at each point on the boundary where two or more surface elements meet. A point p on the boundary Γ is said to satisfy an interior cone condition if there exists a right circular cone (a cone whose base is circular and whose vertex lies above the center of its base) with vertex at p, of finite height, that lies entirely within $\overline{\Omega}$ [94]. Similarly, p satisfies an exterior cone condition if there exists a right circular cone with vertex at p, of finite height, that lies entirely within $\mathbb{R}^3 \setminus \Omega$. We require that p satisfies both conditions simultaneously. In this way, we exclude domains with infinitely sharp corners or cusps, such as the Lebesgue spine. (The boundary-value problem may have no unique solution on these domains. See [94] Vol. 2, pp. 303-306 and [95].) The class of regular domains includes, for example: the finite circular cylinder, the volume bounded by two concentric spheres, the torus, the box, or any polyhedron.

5.3 Analytic Formulation

In Chapters 1-5, we solved for the magnetic scalar potential ψ as an intermediate quantity, and the required power series for the vector potential $\mathbf{A}$ was obtained from the power series for ψ using (2.21). In this Chapter, we work directly with the magnetic vector potential and its multiple derivatives. Indeed, for general domains there may exist curl-free fields that cannot be represented globally as the gradient of a scalar potential [46], [47].

5.3.1 Helmholtz Decomposition Theorem

Our result makes use of the Helmholtz decomposition theorem for vector fields [41], which we state as follows. Suppose Ω is an open, bounded domain with a piecewise smooth boundary, in the sense defined in Section 5.2 above. Suppose $\mathbf{F}$ is a vector field which is continuous on $\overline{\Omega} = \Omega \cup \partial\Omega$ and has continuous first derivatives in Ω. Then there are functions Φ and $\mathbf{A}$, also with continuous first derivatives on Ω, such that for $\mathbf{r} \in \Omega$,

$$\mathbf{F} = \nabla \times \mathbf{A} + \nabla\Phi \tag{5.3}$$

and

$$\nabla \cdot \mathbf{A} = 0. \tag{5.4}$$

Thus, $\mathbf{F}$ may be represented as the sum of a *solenoidal* (divergence-free) part and an *irrotational* (curl-free) part. One explicit representation for $\mathbf{A}$ and Φ with $\mathbf{r} \in \Omega$ is given by:

$$\mathbf{A}(\mathbf{r}) = -\frac{1}{4\pi}\int_{\partial\Omega} \frac{\mathbf{n}(\mathbf{r}') \times \mathbf{F}(\mathbf{r}')}{|\mathbf{r}-\mathbf{r}'|} dS' + \frac{1}{4\pi}\int_{\Omega} \frac{\nabla' \times \mathbf{F}(\mathbf{r}')}{|\mathbf{r}-\mathbf{r}'|} dV', \tag{5.5}$$

$$\Phi(\mathbf{r}) = -\frac{1}{4\pi}\int_{\partial\Omega} \frac{\mathbf{n}(\mathbf{r}') \cdot \mathbf{F}(\mathbf{r}')}{|\mathbf{r}-\mathbf{r}'|} dS' - \frac{1}{4\pi}\int_{\Omega} \frac{\nabla' \cdot \mathbf{F}(\mathbf{r}')}{|\mathbf{r}-\mathbf{r}'|} dV'. \tag{5.6}$$

Here ∇' denotes partial differentiation with respect to the components of $\mathbf{r}'$, and $\mathbf{n}(\mathbf{r}')$ denotes the outward normal to the boundary $\partial\Omega$ at the point $\mathbf{r}'$. We will refer to (5.3), (5.5-5.6) together as the Helmholtz theorem.

Proof

We will use the vector identity

$$\nabla^2\mathbf{u} = \nabla(\nabla \cdot \mathbf{u}) - \nabla \times (\nabla \times \mathbf{u}), \tag{5.7}$$

which holds for all $\mathbf{u}$ in $\vec{C}^2(\Omega) = \{\mathbf{f}|$ each of f_x, f_y, f_z is in $C^2(\Omega)\}$. A solution of the vector Poisson equation $\nabla^2\mathbf{u} = \mathbf{F}$ in Ω is given by

$$\mathbf{u}(\mathbf{r}) = -\frac{1}{4\pi}\int_\Omega \frac{\mathbf{F}(\mathbf{r}')}{|\mathbf{r}-\mathbf{r}'|}dV'. \tag{5.8}$$

The integral exists for each $\mathbf{r}$ and $\mathbf{u}$ is $\vec{C}^2(\Omega)$.

We see from (5.7) that a choice of

$$\Phi(\mathbf{r}) = \nabla\cdot\mathbf{u}(\mathbf{r}) \qquad \text{and} \tag{5.9}$$

$$\mathbf{A}(\mathbf{r}) = -\nabla\times\mathbf{u}(\mathbf{r}) \tag{5.10}$$

will satisfy $\mathbf{F} = \nabla\Phi + \nabla\times\mathbf{A}$ as required by (5.3). It remains to evaluate the divergence and curl of $\mathbf{u}$. Note that

$$\nabla\cdot\mathbf{u} = -\frac{1}{4\pi}\int_\Omega \mathbf{F}(\mathbf{r}')\cdot\nabla\left(\frac{1}{|\mathbf{r}-\mathbf{r}'|}\right)dV' = \frac{1}{4\pi}\int_\Omega \mathbf{F}(\mathbf{r}')\cdot\nabla'\left(\frac{1}{|\mathbf{r}-\mathbf{r}'|}\right), \tag{5.11}$$

and

$$\begin{aligned}-\nabla\times\mathbf{u}(\mathbf{r}) =& \frac{1}{4\pi}\int_\Omega \nabla\frac{1}{|\mathbf{r}-\mathbf{r}'|}\times\mathbf{F}(\mathbf{r}')dV' \\ =& -\frac{1}{4\pi}\int_\Omega \nabla'\frac{1}{|\mathbf{r}-\mathbf{r}'|}\times\mathbf{F}(\mathbf{r}')dV',\end{aligned} \tag{5.12}$$

where ∇ denotes partial differentiation with respect to the components of $\mathbf{r}$. We use the identities

$$\nabla'\cdot\left(\frac{\mathbf{F}(\mathbf{r}')}{|\mathbf{r}-\mathbf{r}'|}\right) = \frac{\nabla'\cdot\mathbf{F}(\mathbf{r}')}{|\mathbf{r}-\mathbf{r}'|} + \nabla'\left(\frac{1}{|\mathbf{r}-\mathbf{r}'|}\right)\cdot\mathbf{F}(\mathbf{r}'), \tag{5.13}$$

$$\nabla'\times\left(\frac{\mathbf{F}(\mathbf{r}')}{|\mathbf{r}-\mathbf{r}'|}\right) = \frac{\nabla'\times\mathbf{F}(\mathbf{r}')}{|\mathbf{r}-\mathbf{r}'|} + \nabla'\left(\frac{1}{|\mathbf{r}-\mathbf{r}'|}\right)\times\mathbf{F}(\mathbf{r}') \tag{5.14}$$

to express these integrals in the form

$$\nabla\cdot\mathbf{u} = \frac{1}{4\pi}\int_\Omega \nabla'\cdot\left(\frac{\mathbf{F}(\mathbf{r}')}{|\mathbf{r}-\mathbf{r}'|}\right)dV' - \frac{1}{4\pi}\int_\Omega \frac{\nabla'\cdot\mathbf{F}(\mathbf{r}')}{|\mathbf{r}-\mathbf{r}'|}dV', \tag{5.15}$$

$$-\nabla \times \mathbf{u} = -\frac{1}{4\pi}\int_\Omega \nabla' \times \left(\frac{\mathbf{F}(\mathbf{r}')}{|\mathbf{r}-\mathbf{r}'|}\right) dV' + \frac{1}{4\pi}\int_\Omega \frac{\nabla' \times \mathbf{F}(\mathbf{r}')}{|\mathbf{r}-\mathbf{r}'|} dV'. \quad (5.16)$$

The first terms of (5.15), (5.16) may be rewritten as surface integrals using the divergence theorem as follows. The first term appearing in (5.15) is straightforward:

$$\int_\Omega \nabla' \cdot \left(\frac{\mathbf{F}(\mathbf{r}')}{|\mathbf{r}-\mathbf{r}'|}\right) dV' = \int_{\partial\Omega} \frac{\mathbf{n}(\mathbf{r}') \cdot \mathbf{F}(\mathbf{r}')}{|\mathbf{r}-\mathbf{r}'|} dS'. \quad (5.17)$$

We now demonstrate the identity

$$\int_\Omega \nabla' \times \left(\frac{\mathbf{F}(\mathbf{r}')}{|\mathbf{r}-\mathbf{r}'|}\right) dV' = -\int_{\partial\Omega} \frac{\mathbf{n}(\mathbf{r}') \times \mathbf{F}(\mathbf{r}')}{|\mathbf{r}-\mathbf{r}'|} dS'. \quad (5.18)$$

Let $\mathbf{e}_1, \mathbf{e}_2, \mathbf{e}_3$ be the unit vectors forming an orthonormal basis for $\mathbb{R}^3$. The component of the integrand along $\mathbf{e}_k$ is given by the identity $\nabla \cdot (\mathbf{A} \times \mathbf{B}) = \mathbf{B} \cdot (\nabla \times \mathbf{A}) - \mathbf{A} \cdot (\nabla \times \mathbf{B})$ as:

$$\mathbf{e}_k \cdot \left(\nabla' \times \frac{\mathbf{F}(\mathbf{r}')}{|\mathbf{r}-\mathbf{r}'|}\right) = \nabla' \cdot \left(\frac{\mathbf{F}(\mathbf{r}')}{|\mathbf{r}-\mathbf{r}'|} \times \mathbf{e}_k\right). \quad (5.19)$$

Hence we have that

$$\begin{aligned} \mathbf{e}_k \cdot \int_\Omega \left(\nabla' \times \frac{\mathbf{F}(\mathbf{r}')}{|\mathbf{r}-\mathbf{r}'|}\right) dV' &= \int_\Omega \nabla' \cdot \left(\frac{\mathbf{F}(\mathbf{r}')}{|\mathbf{r}-\mathbf{r}'|} \times \mathbf{e}_k\right) dV' \\ &= \int_{\partial\Omega} \left(\frac{\mathbf{F}(\mathbf{r}')}{|\mathbf{r}-\mathbf{r}'|} \times \mathbf{e}_k\right) \cdot \mathbf{n}(\mathbf{r}') dS' \\ &= \mathbf{e}_k \cdot \int_{\partial\Omega} \frac{\mathbf{n}(\mathbf{r}') \times \mathbf{F}(\mathbf{r}')}{|\mathbf{r}-\mathbf{r}'|} dS'. \end{aligned} \quad (5.20)$$

On the last line we used $(\mathbf{A} \times \mathbf{B}) \cdot \mathbf{C} = \mathbf{B} \cdot (\mathbf{C} \times \mathbf{A})$. The result (5.18) therefore follows. Using (5.17,5.18) in (5.42,5.16) we obtain the desired expressions:

$$\mathbf{A}(\mathbf{r}) = -\frac{1}{4\pi}\int_{\partial\Omega} \frac{\mathbf{n}(\mathbf{r}') \times \mathbf{F}(\mathbf{r}')}{|\mathbf{r}-\mathbf{r}'|} dS' + \frac{1}{4\pi}\int_\Omega \frac{\nabla' \times \mathbf{F}(\mathbf{r}')}{|\mathbf{r}-\mathbf{r}'|} dV', \quad (5.21)$$

$$\Phi(\mathbf{r}) = -\frac{1}{4\pi}\int_{\partial\Omega} \frac{\mathbf{n}(\mathbf{r}') \cdot \mathbf{F}(\mathbf{r}')}{|\mathbf{r}-\mathbf{r}'|} dS' - \frac{1}{4\pi}\int_\Omega \frac{\nabla' \cdot \mathbf{F}(\mathbf{r}')}{|\mathbf{r}-\mathbf{r}'|} dV. \quad (5.22)$$

We make the following remarks:

Remark 1 / The set of smooth vector fields $\mathbf{F}$ on Ω forms a linear space, which we denote as $V(\Omega)$. Let $\mathrm{Im(curl)} = \{\mathbf{F}|\mathbf{F} = \nabla \times \mathbf{A}, \mathbf{A} \in \vec{C}^1(\Omega)\}$ be the subspace of fields that lie in the image of the curl operator. Similarly, we let $\mathrm{Im(grad)} = \{\mathbf{F}|\mathbf{F} = \nabla\Phi, \Phi \in C^1(\Omega)\}$ be the subspace of fields that lie in the image of the gradient operator. We have stated that the space of smooth vector fields may be written as the sum $V(\Omega) = \mathrm{Im(curl)} + \mathrm{Im(grad)}$. This decomposition is in general *not unique*, as the spaces Im(curl) and Im(grad) are not linearly independent. In the case $\Omega = \mathbb{R}^3$, Ω becomes unbounded and the decomposition of (5.3) becomes unique, provided $\mathbf{F}$ and its first derivatives tend to zero sufficiently rapidly at infinity. If we assume that $|\mathbf{F}| = O(1/r^2)$ and $\nabla \cdot \mathbf{F}, |\nabla \times \mathbf{F}| = O(1/r^3)$ as $r \to \infty$, it can be shown that the curl-free (irrotational) and divergence-free (solenoidal) components of $\mathbf{F}$ are orthogonal with respect to the inner product

$$\langle \mathbf{F}, \mathbf{G} \rangle = \int_\Omega \mathbf{F} \cdot \mathbf{G} d^3\mathbf{r}. \tag{5.23}$$

In this case $V = \mathrm{Im(grad)} \oplus \mathrm{Im(curl)}$, and the surface integrals in (5.21,5.22) vanish due to the behavior at infinity. This is the classical statement of the theorem.

Remark 2 / The Helmholtz theorem in this form is a special case of a more general and powerful result known as the Hodge decomposition theorem. This theorem states that a general vector field in $\Omega \subseteq \mathbb{R}^3$ is the sum of as many as *five* orthogonal classes of vector functions. In its general form, the Hodge decomposition applies to spaces of differential forms on domains of any dimension; furthermore, this decomposition is related to the topology of the domain. The Hodge decomposition

has been applied extensively to numerical studies of fluid flow via the Navier-Stokes equations. A readable introduction to this topic can be found in [46], [47]. For a full statement of the theorem in its general form, we refer the reader to [45].

Remark 3 / For the subspace Im(grad) of vector fields which can be written as gradients, the result (5.3), (5.21-5.22) is equivalent to Green's representation theorem of Chapter 1. We refer the reader to Appendix H.4 for details.

5.3.2 Representation in Terms of Surface Data

In the case of interest, we take $\mathbf{F} = \mathbf{B}$ to be a static magnetic field in the source-free region Ω. We know that $\nabla \cdot \mathbf{B} = 0$ always, and also $\nabla \times \mathbf{B} = 0$ by the assumption that Ω is source-free. Then $\mathbf{A}$ and Φ are given by surface integrals alone, and (5.3) through (5.22) take the form:

$$\mathbf{B} = \nabla \times \mathbf{A}^t + \nabla \Phi^n, \tag{5.24}$$

$$\mathbf{A}^t(\mathbf{r}) = -\frac{1}{4\pi} \int_{\partial\Omega} \frac{\mathbf{n}(\mathbf{r}') \times \mathbf{B}(\mathbf{r}')}{|\mathbf{r} - \mathbf{r}'|} dS', \tag{5.25}$$

$$\Phi^n(\mathbf{r}) = \frac{1}{4\pi} \int_{\partial\Omega} \frac{\mathbf{n}(\mathbf{r}') \cdot \mathbf{B}(\mathbf{r}')}{|\mathbf{r} - \mathbf{r}'|} dS'. \tag{5.26}$$

Note that $\mathbf{A}^t$ depends only on the tangential components of $\mathbf{B}$ on the surface, while Φ^n depends only on the normal component of $\mathbf{B}$ on the surface. We have successfully represented interior fields in terms of field data on the surface. Furthermore, (5.25,5.26) may be differentiated under the integral to determine interior derivatives of the field. A field solver using the integral kernels (5.25,5.26) has been implemented by Manikonda and Bertz [43],[44] in the code COSY-Infinity.

For our purposes, however, several problems remain. To employ canonical equations of motion from the Hamiltonian H (1.8), we require that the interior field $\mathbf{B}$ be represented entirely in terms of a vector potential $\mathbf{A}$, such that $\mathbf{B} = \nabla \times \mathbf{A}$ alone (Section 1.2). At present in (5.24), both a vector-valued and scalar-valued potential are required. This raises the question: Can the extra term $\nabla \Phi^n$ be written also as the curl of some vector potential $\mathbf{A}^n$, such that $\nabla \Phi^n(\mathbf{r}) = \nabla \times \mathbf{A}^n(\mathbf{r})$?

In addition, we see that the solution (5.25,5.26) is *overdetermined*. It is known that the specification of *either* the surface normal component or the surface tangential components (equivalently, the scalar potential) is sufficient to determine the interior field uniquely. If we provide numerical data (with errors) for all three components of the field on the boundary, there is in general no interior solution with $\nabla \cdot \mathbf{B} = 0$ and $\nabla \times \mathbf{B} = 0$ which takes on those boundary values. For this reason, we expect that (5.25,5.26) will reproduce the interior field only if additional constraints are imposed on the surface data.

Finally, it can be shown that due to the presence of errors in the surface data or imperfect numerical evaluation of the surface integral (5.25) we can in general have $\nabla \times (\nabla \times \mathbf{A}^t) \neq 0$, introducing fictitious sources into the domain of interest. We expect significant errors to appear in the interior fields computed from (5.25,5.26) in the neighborhood of these fictitious sources. The following two sections describe these difficulties and how they may be overcome.

5.3.2.1 Kernel for the Normal Component of $\mathbf{B}$

We begin by considering (5.26). By construction, $\nabla^2\Phi^n = 0$. Under very general assumptions about the topology of the domain, the vanishing of the divergence $\nabla \cdot (\nabla\Phi) = 0$ implies that the gradient $\nabla\Phi^n$ is in the space of fields $\mathrm{Im(grad)} \cap \mathrm{Im(curl)}$. (We assume that the domain contains no "cavities." That is, the boundary $\partial\Omega$ is connected.) In particular, there exists a vector potential $\mathbf{A}^n$ such that $\nabla \times \mathbf{A}^n = \nabla\Phi^n$. We construct such a vector potential using a distribution of Dirac monopoles.

The Dirac monopole is discussed in some detail in Appendix G. In the present section, we work in the gauge defined in Section G.2.1. Consider a Dirac monopole with its source at the point $\mathbf{r}'$. The Dirac string, which we denote $\mathcal{D}$, is taken to be a straight line that extends from the point $\mathbf{r}'$ to infinity in the direction of $\mathbf{m}$ ([19]). That is, $\mathcal{D} = \{\mathbf{r} \in \mathbb{R}^3 | \mathbf{r} = \mathbf{r}' + t\mathbf{m} : 0 \leq t < \infty\}$. The vector potential at the point $\mathbf{r}$ of a Dirac monopole of charge $g = 1$ at a location $\mathbf{r}' \in \mathbb{R}^3$ is given in this gauge by (G.59) as

$$\mathbf{G}^n(\mathbf{r}; \mathbf{r}', \mathbf{m}) = \frac{\mathbf{m} \times (\mathbf{r} - \mathbf{r}')}{4\pi|\mathbf{r} - \mathbf{r}'|(|\mathbf{r} - \mathbf{r}'| - \mathbf{m} \cdot (\mathbf{r} - \mathbf{r}'))}. \tag{5.27}$$

As a function of its first argument $\mathbf{r}$, $\mathbf{G}^n$ is analytic on $\mathbb{R}^3 \setminus \mathcal{D}$, away from the Dirac string. The magnetic field of the Dirac monopole is given in turn by

$$\mathbf{F}_m(\mathbf{r}) = \nabla \times \mathbf{G}^n(\mathbf{r}; \mathbf{r}', \mathbf{m}) = -\frac{1}{4\pi}\nabla\left(\frac{1}{|\mathbf{r} - \mathbf{r}'|}\right) \tag{5.28}$$

for all $\mathbf{r} \notin \mathcal{D}$, as demonstrated in Appendix G. We note that a change in $\mathbf{m}$ is equivalent to the change of gauge given in (G.3.1), leaving $\mathbf{F}_m$ unchanged. The Dirac string forms a ray of singular points whose direction we may change at will,

without affecting the field elsewhere.

It follows from (5.28) that $\nabla \times (\nabla \times \mathbf{G}^n) = -\frac{1}{4\pi} \nabla \times \nabla \left(\frac{1}{|\mathbf{r}-\mathbf{r}'|} \right) = 0$ for all $\mathbf{r} \notin \mathcal{D}$. In addition, it is shown in Section (G.1) that any such monopole vector potential $\mathbf{G}^n$ satisfies the Coulomb gauge condition $\nabla \cdot \mathbf{G}^n = 0$ for all $\mathbf{r} \notin \mathcal{D}$. These properties motivate us to define the vector field $\mathbf{A}^n$ by the surface integral:

$$\mathbf{A}^n(\mathbf{r}) = \int_{\partial\Omega} [\mathbf{n}(\mathbf{r}') \cdot \mathbf{B}(\mathbf{r}')] \mathbf{G}^n(\mathbf{r}; \mathbf{r}', \mathbf{m}(\mathbf{r}')) dS', \tag{5.29}$$

using (5.27) as the kernel. We allow the string direction $\mathbf{m}(\mathbf{r}')$ to vary from point to point $\mathbf{r}' \in \partial\Omega$ on the surface. We refer to a function $\mathbf{m} : \partial\Omega \to S^2$ as an *orientation* for the strings, provided the surface may be partitioned into surface elements such that $\mathbf{m}$ is continuous on the interior of each surface element.

Suppose we choose an orientation for the strings such that *at no point on the surface does the corresponding string intersect the volume of interest* Ω. Then all strings lie outside Ω, and the property (5.28) guarantees that:

$$\begin{aligned} \nabla \times \mathbf{A}^n &= \int_{\partial\Omega} [\mathbf{n}(\mathbf{r}') \cdot \mathbf{B}(\mathbf{r}')] \nabla \times \mathbf{G}^n(\mathbf{r}; \mathbf{r}', \mathbf{m}(\mathbf{r}')) dS' \\ &= -\frac{1}{4\pi} \int_{\partial\Omega} [\mathbf{n}(\mathbf{r}') \cdot \mathbf{B}(\mathbf{r}')] \nabla \left(\frac{1}{|\mathbf{r}-\mathbf{r}'|} \right) dS' = -\nabla \Phi^n. \end{aligned} \tag{5.30}$$

Furthermore, since the divergence of the kernel with respect to $\mathbf{r}$ vanishes, the divergence of the integrand is zero for each $\mathbf{r}'$. Hence, the divergence of the integral itself must vanish, and $\nabla \cdot \mathbf{A}^n = 0$ in Ω. Thus, it follows from the properties of $\mathbf{G}^n$ that:

i) $\mathbf{A}^n$ is real-analytic in Ω.

ii) $\nabla \times (\nabla \times \mathbf{A}^n) = 0$ in Ω.

iii) $\nabla \cdot \mathbf{A}^n = 0$ in Ω.

Furthermore, in accord with i), the expression (5.29) may be differentiated with respect to the components of $\mathbf{r}$ by differentiating the kernel $\mathbf{G}^n$ under the integrand, provided $\mathbf{r} \in \Omega$. These properties hold independently of the factor $\mathbf{n}(\mathbf{r}') \cdot \mathbf{B}(\mathbf{r}')$ in (5.29) and no matter how badly the integral is evaluated numerically. The expression (5.29) describes a distribution of magnetic charge with surface density $(\mathbf{B} \cdot \mathbf{n})$. We therefore refer to $\mathbf{A}^n$ as the *single-layer* potential associated with the surface values $\mathbf{B} \cdot \mathbf{n}$ [94].

5.3.2.2 Kernel for the Tangential Component of $\mathbf{B}$

We now consider (5.25). We have seen that the term $\mathbf{A}^n$ given by expression (5.29) will produce a field that is everywhere curl and divergence-free, independently of the surface values. However, this is not the case for the term $\mathbf{A}^t$. We illustrate this as follows. Note that the integrand of (5.25) satisfies the Laplace equation

$$\nabla^2 \left(\frac{\mathbf{n}(\mathbf{r}') \times \mathbf{B}(\mathbf{r}')}{|\mathbf{r} - \mathbf{r}'|} \right) = 0 \tag{5.31}$$

for any vector $\mathbf{n}(\mathbf{r}') \times \mathbf{B}(\mathbf{r}')$, provided $\mathbf{r} \in \Omega$ and $\mathbf{r}' \in \partial\Omega$, where derivatives are taken with respect to the coordinate $\mathbf{r}$. It follows from (5.25) that

$$\nabla^2 \mathbf{A}^t = 0 \tag{5.32}$$

for all $\mathbf{r} \in \Omega$. Using the usual vector identities we have, everywhere in Ω,

$$\nabla \times (\nabla \times \mathbf{A}^t) = -\nabla^2 \mathbf{A}^t + \nabla(\nabla \cdot \mathbf{A}^t) = \nabla(\nabla \cdot \mathbf{A}^t). \tag{5.33}$$

If the function $\mathbf{n} \times \mathbf{B}$ and its integral are evaluated exactly on the surface, it can be shown that $\mathbf{A}^t$ satisfies the Coulomb condition $\nabla \cdot \mathbf{A}^t = 0$, and therefore by the above result $\nabla \times (\nabla \times \mathbf{A}^t) = 0$. However, this is not true in general. We show, in fact, that

$$\nabla \cdot \mathbf{A}^t = \frac{1}{4\pi} \int_{\partial\Omega} \frac{\mathbf{n} \cdot (\nabla' \times \mathbf{B})}{|\mathbf{r} - \mathbf{r}'|} dS', \tag{5.34}$$

provided the first derivatives of $\mathbf{B}$ exist on the surface.

Proof

Taking the divergence of the integrand in (5.25) we have

$$\begin{aligned} \nabla \cdot \left(\frac{\mathbf{n} \times \mathbf{B}}{|\mathbf{r} - \mathbf{r}'|} \right) &= \nabla \left(\frac{1}{|\mathbf{r} - \mathbf{r}'|} \right) \cdot (\mathbf{n} \times \mathbf{B}) = -\mathbf{n} \cdot \left[\nabla \left(\frac{1}{|\mathbf{r} - \mathbf{r}'|} \right) \times \mathbf{B} \right] \\ &= \mathbf{n} \cdot \left[\nabla' \left(\frac{1}{|\mathbf{r} - \mathbf{r}'|} \right) \times \mathbf{B} \right]. \end{aligned} \tag{5.35}$$

Furthermore, we apply the identity

$$\nabla' \times (\mathbf{B}\mathcal{E}) = \mathcal{E}(\nabla' \times \mathbf{B}) + (\nabla' \mathcal{E} \times \mathbf{B}), \tag{5.36}$$

which applies for any differentiable scalar function $\mathcal{E}$. Letting

$$\mathcal{E}(\mathbf{r}') = \frac{1}{|\mathbf{r} - \mathbf{r}'|}, \tag{5.37}$$

we find that

$$\begin{aligned} \int_{\partial\Omega} \mathbf{n} \cdot \left[\nabla' \times \left(\frac{\mathbf{B}}{|\mathbf{r} - \mathbf{r}'|} \right) \right] dS' &= \int_{\partial\Omega} \frac{\mathbf{n} \cdot (\nabla' \times \mathbf{B})}{|\mathbf{r} - \mathbf{r}'|} dS' \\ &+ \int_{\partial\Omega} \mathbf{n} \cdot \left[\nabla' \left(\frac{1}{|\mathbf{r} - \mathbf{r}'|} \right) \times \mathbf{B} \right] dS'. \end{aligned} \tag{5.38}$$

The surface integral of a curl over a closed surface must vanish by Stokes' theorem, and therefore the above sum must vanish. Thus, combining the above results,

$$\nabla \cdot \mathbf{A} = -\frac{1}{4\pi} \int_{\partial\Omega} \mathbf{n} \cdot \left[\nabla' \left(\frac{1}{|\mathbf{r} - \mathbf{r}'|} \right) \times \mathbf{B} \right] dS' = \frac{1}{4\pi} \int_{\partial\Omega} \frac{\mathbf{n} \cdot (\nabla' \times \mathbf{B})}{|\mathbf{r} - \mathbf{r}'|} dS', \tag{5.39}$$

as desired. Furthermore, suppose that $\nabla \times \mathbf{B} = 0$ up to and including the boundary. Then we have that $\nabla \cdot \mathbf{A}^t = 0$ by (5.39) and, by (5.33), $\nabla \times (\nabla \times \mathbf{A}^t) = 0$ as expected. □

The vanishing of (5.34) imposes a constraint relating the tangential derivatives of $\mathbf{B}$ on the surface. Values obtained by the interpolation of numerical data onto the surface cannot be expected to satisfy this constraint. Indeed, derivatives of the surface data may fail to exist. Consider the following example. Suppose our domain is the cube $\Omega = \{(x, y, z) : -1 < x < 1, -1 < y < 1, -1 < z < 1\}$. We add a small numerical error of the form $\mathbf{B}_E = B\hat{\mathbf{z}}$ on the top ($y = 1$) surface of the cube, where B is constant. We will see that this error introduces fictitious source currents in the domain Ω. On the top surface of the cube we have the factor

$$\mathbf{n}(\mathbf{r}') \times \mathbf{B}(\mathbf{r}') = B\hat{\mathbf{x}}. \tag{5.40}$$

The vector potential $\mathbf{A}_E^t$ obtained from (5.25) is then given by

$$\mathbf{A}_E^t(\mathbf{r}) = \int_{-1}^{1}\int_{-1}^{1} \frac{B\hat{\mathbf{x}}}{\sqrt{(z'-z)^2 + (x'-x)^2 + (1-y)^2}} dz'dx' \tag{5.41}$$

and its divergence is given by

$$\begin{aligned}
\nabla \cdot \mathbf{A}_E^t(\mathbf{r}) &= -B\int_{-1}^{1}\int_{-1}^{1} \frac{x - x'}{[(z'-z)^2 + (x'-x)^2 + (1-y)^2]^{3/2}} dz'dx' \\
&= B\left[-\operatorname{arctanh}\left(\frac{1-z}{d_{11}}\right) + \operatorname{arctanh}\left(\frac{1-z}{d_{1-1}}\right)\right. \\
&\qquad \left. - \operatorname{arctanh}\left(\frac{1+z}{d_{-11}}\right) + \operatorname{arctanh}\left(\frac{1+z}{d_{-1-1}}\right)\right],
\end{aligned} \tag{5.42}$$

where the four functions $d_{jk} = \sqrt{(j-z)^2 + (k-x)^2 + (1-y)^2}$ denote distances from each of the four corners of the top face of the cube. The interior field computed

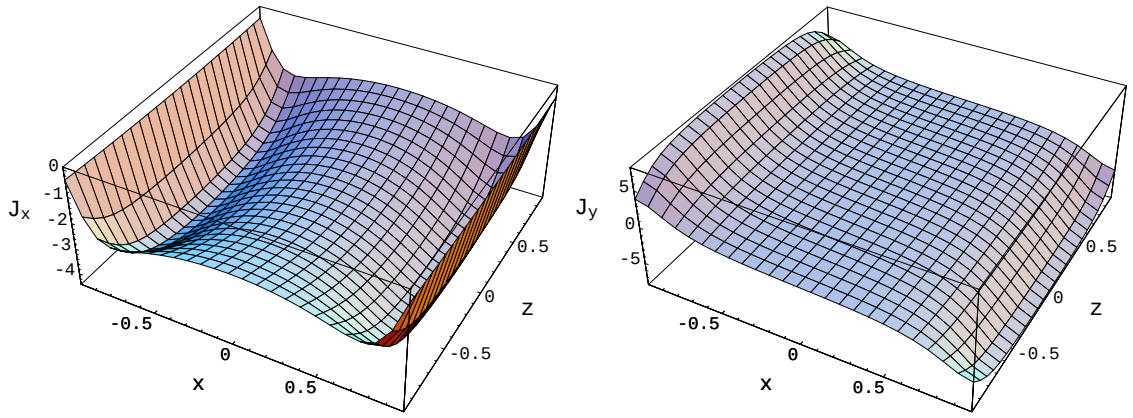

Figure 5.3: Components J_x and J_y of fictitious current corresponding to the field error $\mathbf{B}_E$, evaluated in the plane $y = 0.75$. Provided in units of B.

from (5.25) therefore has nonvanishing curl within Ω, corresponding to the fictitious current density $\mathbf{J} = \nabla \times (\nabla \times \mathbf{A}^t) = \nabla(\nabla \cdot \mathbf{A}^t) \neq 0$ as follows:

$$
\begin{aligned}
J_z &= \frac{\partial}{\partial z}(\nabla \cdot \mathbf{A}_E^t) = B\left(\frac{1}{d_{11}} - \frac{1}{d_{-11}} - \frac{1}{d_{1-1}} + \frac{1}{d_{-1-1}}\right), \\
J_x &= B\left(-\frac{(z-1)(x-1)}{[(x-1)^2+(y-1)^2]d_{11}} + \frac{(z+1)(x-1)}{[(x-1)^2+(y-1)^2]d_{-11}}\right. \\
&\qquad \left. + \frac{(z-1)(x+1)}{[(x+1)^2+(y-1)^2]d_{1-1}} - \frac{(z+1)(x+1)}{[(x+1)^2+(y-1)^2]d_{-1-1}}\right), \\
J_y &= B\left(\frac{(1-y)(-1+z)}{[(x-1)^2+(y-1)^2]d_{11}} + \frac{(1-y)(-1-z)}{[(x-1)^2+(y-1)^2]d_{-11}}\right. \\
&\qquad \left. + \frac{(1-y)(1-z)}{[(x+1)^2+(y-1)^2]d_{-11}} + \frac{(1-y)(1+z)}{[(x+1)^2+(y-1)^2]d_{-1-1}}\right).
\end{aligned}
$$

In Fig. 5.3 we have provided an illustration of the components J_x and J_y of the current density $\mathbf{J}$ in the plane $y = 0.75$.

The source of this problem is that the surface values $\mathbf{B}_E$ cannot be obtained as the restriction of a smooth, curl-free field to the boundary $\partial\Omega$. If this were the

case, all line integrals of the surface data of the form

$$\oint \mathbf{B}_E \cdot d\mathbf{r}, \tag{5.43}$$

when taken over a closed path lying in the surface of the box, should vanish. This is certainly not the case for our example. Consider the path beginning at the point $(x, y, z) = (0, 1, -1)$ on the top face of the cube, traveling in the plane $x = 0$ along a square obtained by first increasing z to $(0, 1, 1)$, then moving to $(0, -1, 1)$, then to $(0, -1, -1)$, then back to the original point. We have

$$\oint \mathbf{B} \cdot d\mathbf{r} = \int_{-1}^{1} B dz = 2B \neq 0. \tag{5.44}$$

This problem may be avoided by use of a scalar potential. We assume that $\mathbf{B} = \nabla\psi$ for some $\psi \in C^2(\Omega)$, and suppose we have available the values $\psi \mid_{\partial\Omega}$ as surface data. Note that the specification of ψ locally on the surface is equivalent to the specification of the tangential components of $\mathbf{B}$, provided $\nabla \times \mathbf{B} = 0$. We now exploit identity (H.74) appearing in Appendix H.4. There we demonstrated a corollary of Stokes' theorem (H.72) which states that for any bounded, closed piecewise smooth surface $\partial\Omega$, and any $\phi \in C^1(\Omega)$,

$$\int_{\partial\Omega} (\nabla\phi \times \mathbf{n}) dS = 0. \tag{5.45}$$

Setting $\phi(\mathbf{r}') = \psi(\mathbf{r}')/|\mathbf{r} - \mathbf{r}'|$ we obtain the identity (H.72):

$$\int_{\Gamma} \frac{\mathbf{n}(\mathbf{r}') \times \nabla'\psi(\mathbf{r}')}{|\mathbf{r} - \mathbf{r}'|} dS' = -\int_{\Gamma} \psi(\mathbf{r}')\mathbf{n}(\mathbf{r}') \times \nabla' \left(\frac{1}{|\mathbf{r} - \mathbf{r}'|} \right) dS'. \tag{5.46}$$

This allows us to express the integral for $\mathbf{A}^t$ in the form

$$\mathbf{A}^t(\mathbf{r}) = \int_{\Gamma} \psi(\mathbf{r}')\mathbf{G}^t(\mathbf{r}; \mathbf{r}', \mathbf{n}(\mathbf{r}'))dS' \tag{5.47}$$

where $\mathbf{G}^t$ is given by

$$\mathbf{G}^t(\mathbf{r};\mathbf{r}',\mathbf{n}(\mathbf{r}')) = \frac{1}{4\pi}\mathbf{n}(\mathbf{r}') \times \nabla' \left(\frac{1}{|\mathbf{r}-\mathbf{r}'|}\right) = \frac{\mathbf{n}(\mathbf{r}') \times (\mathbf{r}-\mathbf{r}')}{4\pi|\mathbf{r}-\mathbf{r}'|^3}. \tag{5.48}$$

We note that $\mathbf{G}^t(\mathbf{r};\mathbf{r}',\mathbf{n}(\mathbf{r}'))$ is the value at $\mathbf{r}$ of the vector potential for a dipole located at $\mathbf{r}'$ of magnetic moment $\mathbf{n}$ (G.23). As a result, we know that $\nabla \cdot \mathbf{G}^t = 0$ and $\nabla \times (\nabla \times \mathbf{G}^t) = 0$ for $\mathbf{r} \neq \mathbf{r}'$, where derivatives are taken with respect to the coordinate $\mathbf{r}$. This may be seen by noting that

$$\nabla \cdot \mathbf{G}^t(\mathbf{r};\mathbf{r}',\mathbf{n}) = \frac{1}{4\pi}\nabla \cdot \left(\mathbf{n} \times \nabla' \left(\frac{1}{|\mathbf{r}-\mathbf{r}'|}\right)\right) = -\frac{\mathbf{n}}{4\pi} \cdot \left(\nabla \times \nabla' \left(\frac{1}{|\mathbf{r}-\mathbf{r}'|}\right)\right) = 0 \tag{5.49}$$

and

$$\nabla \times (\nabla \times \mathbf{G}^t) = \nabla \times \mathbf{F}_d = -\nabla \times \nabla \Phi_d = 0 \tag{5.50}$$

where Φ_d is the scalar potential of an electric dipole (G.8) with $\mathbf{p}_d = \mathbf{n}$. As a consequence, $\nabla^2 \mathbf{G}^t = 0$ for $\mathbf{r} \neq \mathbf{r}'$ and we see immediately that each component of $\mathbf{G}^t$ is real-analytic in Ω. It follows from the properties of $\mathbf{G}^t$ that:

i) $\mathbf{A}^t$ is real-analytic in Ω.

ii) $\nabla \times (\nabla \times \mathbf{A}^t) = 0$ in Ω.

iii) $\nabla \cdot \mathbf{A}^t = 0$ in Ω.

Furthermore, in accord with i), the expression (5.47) may be differentiated with respect to the components of $\mathbf{r}$ by differentiating the kernel $\mathbf{G}^t$ in the integrand, provided $\mathbf{r} \in \Omega$. These properties hold independently of the factor $\psi(\mathbf{r}')$ in (5.47) and no matter how badly the integral is evaluated numerically.

Note that the desired scalar potential ψ on the surface is often available from finite-element modeling codes, in addition to the usual magnetic field $\mathbf{B}$. In case

such information is unavailable, the scalar potential may be obtained from those components of $\mathbf{B}$ that lie tangent to the surface of the domain, through line integrals of the form

$$\psi(\mathbf{r}_b) - \psi(\mathbf{r}_a) = \int_a^b \mathbf{B} \cdot d\mathbf{r}. \tag{5.51}$$

Here the integral is taken along a path lying in the surface $\partial\Omega$, with endpoints $\mathbf{r}_a$ and $\mathbf{r}_b$. Interesting complications arise in the case when the domain Ω is not simply-connected [46]. In this case (eg., a torus), there exist fields which cannot be written in the form $\mathbf{B} = \nabla\psi$ over the whole surface (eg., the field due to a current-carrying wire running through the hole of the torus). In this case, any such scalar potential ψ must possess a jump discontinuity, or "cut," along some curve lying in the surface, where $\nabla\psi$ is not defined. The general validity of (5.47) in such cases is currently under investigation. For the purposes of this Dissertation, we will assume that no net current flows through "holes" in such a domain, and therefore (5.47) is valid. A general treatment of domains with such nontrivial topologies introduces subtleties worth exploring in future work. We refer the reader to [46], [47].

The expression (5.47) describes a distribution of dipoles with surface density ψ. We therefore refer to $\mathbf{A}^t$ as the *double-layer* potential associated with the surface values $\psi(\mathbf{r}')$ [94].

Summary. Our final result may be stated as follows. Given $\mathbf{B}$ on the boundary $\Gamma = \partial\Omega$, we may write $\mathbf{B}$ in the interior Ω as the curl of a vector potential

$\mathbf{B} = \nabla \times \mathbf{A}$, where $\mathbf{A} = \mathbf{A}^n + \mathbf{A}^t$. Here

$$\mathbf{A}^n = \int_\Gamma [\mathbf{n}(\mathbf{r}') \cdot \mathbf{B}(\mathbf{r}')] \mathbf{G}^n(\mathbf{r}; \mathbf{r}', \mathbf{m}(\mathbf{r}')) dS', \tag{5.52a}$$

$$\mathbf{A}^t = \int_\Gamma \psi(\mathbf{r}') \mathbf{G}^t(\mathbf{r}; \mathbf{r}', \mathbf{n}(\mathbf{r}')) dS', \tag{5.52b}$$

where

$$\mathbf{G}^n(\mathbf{r}; \mathbf{r}', \mathbf{m}(\mathbf{r}')) = \frac{\mathbf{m} \times (\mathbf{r} - \mathbf{r}')}{4\pi |\mathbf{r} - \mathbf{r}'| (|\mathbf{r} - \mathbf{r}'| - \mathbf{m} \cdot (\mathbf{r} - \mathbf{r}'))}, \tag{5.53a}$$

$$\mathbf{G}^t(\mathbf{r}; \mathbf{r}', \mathbf{n}(\mathbf{r}')) = \frac{\mathbf{n}(\mathbf{r}') \times (\mathbf{r} - \mathbf{r}')}{4\pi |\mathbf{r} - \mathbf{r}'|^3}. \tag{5.53b}$$

Furthermore, the total vector potential $\mathbf{A}$ shares properties (i-iii) of $\mathbf{A}^n$ and $\mathbf{A}^t$ as described previously. As a consequence, we will have $\nabla \cdot \mathbf{B} = 0$ and $\nabla \times \mathbf{B} = 0$ for any functions $\mathbf{n} \cdot \mathbf{B} \mid_\Gamma$ and $\psi \mid_\Gamma$ on the surface Γ.

5.3.3 Computing Transfer Maps from $\mathbf{A}$

We have shown that the kernels (5.53) are real-analytic. We now wish to compute the required power-series representation for $\mathbf{A}$ using (5.52). Consider a point $\mathbf{r}_d$ in the interior Ω of the volume of interest, lying along the design orbit for the beam. We let $\delta\mathbf{r} = (\delta x)\hat{\mathbf{x}} + (\delta y)\hat{\mathbf{y}} + (\delta z)\hat{\mathbf{z}}$ denote displacement relative to $\mathbf{r}_d$. For each point $\mathbf{r}'$ on the surface, there is a neighborhood of $\mathbf{r}_d$ in which the kernels are represented by the (absolutely convergent) multivariable power series

$$\mathbf{G}^n(\mathbf{r}_d + \delta\mathbf{r}; \mathbf{r}', \mathbf{m}) = \sum_{\alpha=0}^{\infty} \mathbf{G}^n_\alpha(\mathbf{r}_d; \mathbf{r}', \mathbf{m}) P_\alpha(\delta x, \delta y, \delta z), \tag{5.54a}$$

$$\mathbf{G}^t(\mathbf{r}_d + \delta\mathbf{r}; \mathbf{r}', \mathbf{n}) = \sum_{\alpha=0}^{\infty} \mathbf{G}^t_\alpha(\mathbf{r}_d; \mathbf{r}', \mathbf{n}) P_\alpha(\delta x, \delta y, \delta z), \tag{5.54b}$$

where each P_α is a monomial in the deviation variables $\delta x, \delta y$, and δz. Because the sums (5.54) are absolutely convergent, we may re-order the terms of the sum as

desired. In particular, we may group the terms in (5.54) by degree such that, for each component $w = x, y, z$ we have the unique homogeneous polynomial series

$$G_w^n(\mathbf{r}_d + \delta\mathbf{r}; \mathbf{r}', \mathbf{m}) = \sum_{j=0}^{\infty} G_{j,w}^n(\mathbf{r}_d; \mathbf{r}', \mathbf{m}, \delta x, \delta y, \delta z), \tag{5.55a}$$

$$G_w^t(\mathbf{r}_d + \delta\mathbf{r}; \mathbf{r}', \mathbf{n}) = \sum_{j=0}^{\infty} G_{j,w}^t(\mathbf{r}_d; \mathbf{r}', \mathbf{n}, \delta x, \delta y, \delta z), \tag{5.55b}$$

where $G_{j,w}^n$ and $G_{j,w}^t$ are the homogeneous polynomials of degree j obtained by summing all terms in (5.54) of degree j.

We may then write the vector potential at a point $\mathbf{r} = \mathbf{r}_d + \delta\mathbf{r}$ in Ω by integrating (5.54) term-by-term as

$$\mathbf{A}(\mathbf{r}) = \mathbf{A}^n(\mathbf{r}) + \mathbf{A}^t(\mathbf{r}) \tag{5.56}$$

with

$$\mathbf{A}^n(\mathbf{r}) = \sum_{\alpha=0}^{\infty} P_\alpha(\delta x, \delta y, \delta z) \int_\Gamma [\mathbf{n}(\mathbf{r}') \cdot \mathbf{B}(\mathbf{r}')] \mathbf{G}_\alpha^n(\mathbf{r}_d; \mathbf{r}', \mathbf{m}) dS', \tag{5.57a}$$

$$\mathbf{A}^t(\mathbf{r}) = \sum_{\alpha=0}^{\infty} P_\alpha(\delta x, \delta y, \delta z) \int_\Gamma \psi(\mathbf{r}') \mathbf{G}_\alpha^t(\mathbf{r}_d; \mathbf{r}', \mathbf{n}) dS'. \tag{5.57b}$$

It follows that, given the coefficients $\mathbf{G}_\alpha^n(\mathbf{r}_d; \mathbf{r}', \mathbf{m})$, $\mathbf{G}_\alpha^t(\mathbf{r}_d; \mathbf{r}', \mathbf{n})$ we may compute Taylor coefficients of the vector potential through any order by computing the surface integrals above. This expansion may be performed about any interior point $\mathbf{r}_d \in \Omega$. Since each component of the kernels $\mathbf{G}^n$ and $\mathbf{G}^t$ is harmonic in the variable $\mathbf{r}$ inside Ω, it follows that the polynomials $G_{j,w}^n$, $G_{j,w}^t$ in the series (5.55) are themselves harmonic for all $(\delta x, \delta y, \delta z)$. In addition, the series are guaranteed to converge everywhere within the largest ball about $\mathbf{r}_d$ in which $\mathbf{G}^n$ and $\mathbf{G}^t$ are harmonic, respectively (see Appendix H). The domain of convergence is therefore set

by the presence of magnetic sources at $\mathbf{r}'$ and along the Dirac string $\mathcal{D}$. Similarly, the series (5.57) are guaranteed to converge within a ball of radius r_{min} about $\mathbf{r}_d$, where r_{min} is the distance of closest approach to the surface $\partial\Omega$.

Suppose now that we wish to compute the transfer map relative to a reference trajectory $\mathbf{r}_d(t)$ contained in Ω. We choose to work in a Cartesian coordinate system that is fixed relative to the magnetic element and independent of the reference trajectory. Recall that we use the longitudinal coordinate z, measuring the distance travelled along the magnetic element, as the independent variable. This is possible provided $dz/dt > 0$ at every point on the trajectory, in which case we write $\mathbf{r}_d = \mathbf{r}_d(z)$. We then require a power series in the transverse deviation variables δx and δy, which may be obtained from (5.57) by setting $\delta z = 0$. Expanding each component $A_w,\ w = x, y, z$ of the vector potential in the deviation variables as in (1.29) we have, through degree N,

$$A_w(\delta x, \delta y, \delta z) = \sum_{l=1}^{L} a_l^w(z) P_l(2; \delta x, \delta y). \tag{5.58}$$

Here, the upper limit L denotes the number of linearly independent monomials $P_l(2; \delta x, \delta y)$ in the two variables δx and δy through degree N, as in (1.29). The desired Taylor coefficients are then given from (5.57) as

$$\boxed{a_l^w(z) = \int_\Gamma [\mathbf{n}(\mathbf{r}') \cdot \mathbf{B}(\mathbf{r}')] G_l^{n,w}(\mathbf{r}_d; \mathbf{r}', \mathbf{m}) dS' + \int_\Gamma \psi(\mathbf{r}') G_l^{t,w}(\mathbf{r}_d; \mathbf{r}', \mathbf{n}) dS'} \tag{5.59}$$

for $l = 1, 2, \ldots L$. Computation therefore requires that we have available the Taylor coefficients $G_l^{n,w}$ and $G_l^{t,w}$ of the kernels $\mathbf{G}^n$ and $\mathbf{G}^t$ in the variable $\mathbf{r}$, as functions of z. These are obtained numerically, as discussed in the following section.

5.4 Numerical Implementation

This technique has been implemented in a Fortran 90 module to be used with the code MaryLie to compute transfer maps. The routine accepts as input numerical data of the form (B_z, B_x, B_y, ψ) at a series of mesh points located on a regular grid with a uniform spacing in each direction. The surface must be represented parametrically in a fixed rectangular coordinate system that is chosen such that $dz/dt > 0$ along the design orbit through the magnetic element. In addition, the surface must enclose the design trajectory and exclude all iron and other magnetic sources. Given tabulated mesh data, the routine will produce as output the following quantities:

1. The vector potential $\mathbf{A}$ at any interior point $\mathbf{r}_d$ in the domain.

2. Taylor coefficients a_l^w of the vector potential about the point $\mathbf{r}_d$ through degree N.

3. The interior magnetic field $\mathbf{B}$ at the point $\mathbf{r}_d$.

4. Taylor coefficients of the components B_x, B_y, B_z about the point $\mathbf{r}_d$ through degree $N-1$.

5. The quantities $\nabla \cdot \mathbf{A}$ and $\nabla \times \mathbf{A}$ in the form of Taylor coefficients about $\mathbf{r}_d$ through degree $N-1$.

6. The quantities $\nabla \cdot \mathbf{B}$ and $\nabla \times \mathbf{B}$ in the form of Taylor coefficients about $\mathbf{r}_d$ through degree $N-2$.

Transfer maps are then computed from the values of the Taylor coefficients $a_l^w(z)$ along the design orbit $\mathbf{r}_d(z)$. Computation of the quantities 3-6 serves to provide a series of benchmarks of numerical accuracy, as discussed in Section 5.5. The degree N is set internally through the use of numerical power-series algebra routines to be described in the following discussion. In addition, the gauge in which the vector potential is evaluated is set by specifying the function $\mathbf{m}(\mathbf{r}')$.

The surface integrals (5.59) contributing to each coefficient $a_l^w(z)$ at a fixed $\mathbf{r}_d(z)$ along the design orbit are computed from the numerical values of each integrand over the surface $\partial\Omega$ using high-order cubature formulas. The surface is first partitioned into a mesh of small, non-overlapping coordinate patches. Within each patch, the integrals take the form in local coordinates of integrals over a simple domain in $\mathbb{R}^2$. These integrals are then approximated using values of the integrand at several points within the domain. We use integration routines from the Fortran 90 library STROUD, each of which implements a two-dimensional cubature formula from the collection of Arthur Stroud (described in [50]).

As in the routines described in Chapters 2-4, the field values B_x, B_y, and B_z are interpolated onto the bounding surface using polynomial splines. In addition, the value of the scalar potential ψ (which is also available numerically as the output of 3-d field solvers) is interpolated onto the bounding surface using an interpolation of the same order. In contrast to the previous routines, the B-spline coefficients are stored internally. These stored coefficients are then used to reconstruct the field and potential values as needed during the surface integration at only those points required by the Stroud cubature formulas.

The Taylor coefficients $G_l^{n,w}(\mathbf{r}_d;\mathbf{r}',\mathbf{m})$ and $G_l^{t,w}(\mathbf{r}_d;\mathbf{r}',\mathbf{n})$ of the kernels about the design point $\mathbf{r}_d$ must be computed numerically for each $\mathbf{r}'$ on the surface. A collection of efficient truncated power series algebra (TPSA) routines, implemented in MaryLie, is used together with recursion relationships to produce these coefficients on-the-fly as needed by the surface integration routine.

5.5 Benchmarks of Numerical Accuracy

5.5.1 Monopole-Pair Benchmark

The routine described above has been benchmarked using the monopole-pair test field described in Section 2.3. We produced a table of values of the form (B_z, B_x, B_y, ψ) for this field on a uniform mesh with a spacing of 0.2 cm in each direction, covering a large rectangular domain that does not contain the monopole source points. Within this region, we tested the techniques of this chapter by fitting the field using each of domains illustrated in Fig. 5.4. Interpolation was used to compute each of the values B_w and ψ on the boundary surfaces as needed. For each domain illustrated, we tested our Fortran 90 routine by computing the following quantities. First, the Taylor coefficients $a_l^w(\mathbf{r}_d)$ of the vector potential were computed about a single point $\mathbf{r}_d$ in the interior Ω. Because these coefficients were not known exactly for the choice of gauge determined by $\mathbf{m}(\mathbf{r}')$, we verified the accuracy of the a_l^w using a number of other quantities.

The routine was used to produce the Taylor coefficients of the function $\nabla \cdot \mathbf{A}$ about $\mathbf{r}_d$ directly from the a_l^w. We verified that $\nabla \cdot \mathbf{A} = 0$ to machine precision.

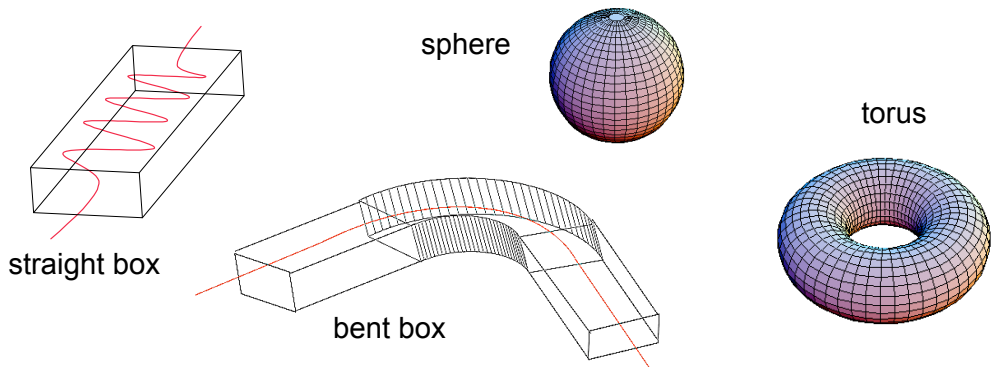

Figure 5.4: Domains used for benchmarking the computation of the Taylor coefficients a_l^w from boundary-value data on general surfaces.

That is, each coefficient c_l of $\nabla \cdot \mathbf{A}$ through the desired order satisfies $|c_l| \sim 10^{-16}$. Next, we computed the Taylor coefficients of each field component $B_w = (\nabla \times \mathbf{A})_w$ about $\mathbf{r}_d$ through the desired order from the a_l^w. These values were compared against the known Taylor coefficients of the field obtained using (2.27). In each case, we found that the absolute error in the desired Taylor coefficients was comparable and of order 10^{-6}. Finally, the routine then used these values to compute the Taylor coefficients of the functions $\nabla \cdot \mathbf{B}$ and $(\nabla \times \mathbf{B})_w$ through the appropriate order. We found that each Taylor coefficient vanished to within machine precision through the appropriate order. In this way, we verify that the field $\mathbf{B}$ computed from the a_l^w satisfies Maxwell's equations at the point $\mathbf{r}_d$. This procedure was repeated for several interior points $\mathbf{r}_d$ throughout each domain, yielding similar results for each point tested.

While the values $\mathbf{B}$ and ψ are known exactly on the boundary of a given

domain, error appears in the surface values due to interpolation from the original mesh onto the boundary. We found for the spherical domain that our choice of parameters produced an error of 10^{-4} in the surface values. Given this error on the surface, the interior coefficients at each point $\mathbf{r}_d$ considered were accurate to 10^{-6}, suggesting the presence of numerical smoothing.

5.5.2 Application to ILC Wiggler

As a second test of our routine, we obtained from Cornell tabulated numerical field data describing the interior of the proposed ILC wiggler magnet. Each of the values (B_z, B_x, B_y, ψ) was fitted from a rectangular mesh onto the surface of a bent box with small bending angle. Using only the interpolated values of these quantities on the surface of the box, we computed the Taylor coefficients a_l^w of the vector potential and the corresponding field $\mathbf{B}$ at several interior points $\mathbf{r}_d$. In order to benchmark these values, we considered the points $\mathbf{r}_d$ in the interior of the bent box that lie on the original mesh. At these points, we computed the field values B_x, B_y and B_z and compared these with the original finite-element data. A comparison for several points is shown in Table 5.1. The peak field is 17 kG, yielding a largest error/peak of 10^{-4}.

Table 5.1: Error in the Reconstruction of ILC Wiggler Field from Surface Data

Difference (G)	$(0.4, 0.2, 31.2)$ cm	$(2, 2, 1)$ cm	$(0, 1.4, 31.2)$ cm
B_x	0.0417	0.187	0.230
B_y	0.299	2.527	0.054
B_z	0.161	0.626	0.916

5.6 Insensitivity to Numerical Noise

5.6.1 Error Estimates

We have seen that the use of (5.52) produces a smooth field that is curl- and divergence-free. We now ask, how close is this reconstructed field to the true field $\mathbf{B}$? Given the error in the values of $\mathbf{B}$ on the surface, we wish to bound the error in the computed field and its partial derivatives. Error in the computed interior field may appear from three sources:

1) Error in the surface values themselves, arising from errors in the original data and its interpolation onto the boundary surface.

2) Error in numerical evaluation of the surface integrals.

3) Error resulting from truncation of the polynomial series.

We focus first on 1). Let $\mathbf{B}^{(bv)}(\mathbf{r}')$ and $\psi^{(bv)}(\mathbf{r}')$ denote the value of the field and scalar potential as interpolated onto the boundary surface at the point $\mathbf{r}'$. We then let ϵ^n and ϵ^t describe errors in these interpolated surface values, such that

$$\epsilon^n(\mathbf{r}') = \mathbf{n}(\mathbf{r}') \cdot [\mathbf{B}^{(bv)}(\mathbf{r}') - \mathbf{B}(\mathbf{r}')], \tag{5.60}$$

$$\epsilon^t(\mathbf{r}') = \psi^{(bv)}(\mathbf{r}') - \psi(\mathbf{r}'), \tag{5.61}$$

at each point $\mathbf{r}'$ on the surface. For a given gauge (determined by the string orientation $\mathbf{m}$), the error $\delta\mathbf{A}$ in the resulting interior vector potential is given from (5.59) by

$$\delta\mathbf{A} = \delta\mathbf{A}^n + \delta\mathbf{A}^t \tag{5.62}$$

where

$$\delta\mathbf{A}^n(\mathbf{r}) = \int_\Gamma \epsilon^n(\mathbf{r}')\mathbf{G}^n(\mathbf{r};\mathbf{r}',\mathbf{m}(\mathbf{r}'))dS', \tag{5.63}$$

$$\delta\mathbf{A}^t(\mathbf{r}) = \int_\Gamma \epsilon^t(\mathbf{r}')\mathbf{G}^t(\mathbf{r};\mathbf{r}',\mathbf{n}(\mathbf{r}'))dS'. \tag{5.64}$$

By construction, we work in a gauge with $\nabla\cdot\mathbf{A}=0$, and $\nabla\times\nabla\times\mathbf{A}=0$. It follows that $\nabla^2\mathbf{A}=0$. Therefore, each component of $\delta\mathbf{A}$ is a harmonic function on Ω and takes its maximum on the boundary $\partial\Omega$. Furthermore, the error in the Taylor coefficient $a_l^w(z)$ is given from (5.59) by

$$\delta a_l^w(z) = \int_\Gamma \epsilon^n(\mathbf{r}')G_l^{n,w}(\mathbf{r}_d;\mathbf{r}',\mathbf{m})dS' + \int_\Gamma \epsilon^t(\mathbf{r}')G_l^{t,w}(\mathbf{r}_d;\mathbf{r}',\mathbf{n})dS'. \tag{5.65}$$

We may now place an upper bound on this error as follows. Using the Schwarz inequality, we find for each component $w=x,y$, and z and for every $\mathbf{r}\in\Omega$ that

$$|\delta A_w^n(\mathbf{r})| = \left|\int_\Gamma \epsilon^n(\mathbf{r}')G_w^n(\mathbf{r};\mathbf{r}',\mathbf{m}(\mathbf{r}'))dS'\right| \le ||\epsilon_n||\cdot||G_w^n(\mathbf{r};\cdots)||, \tag{5.66}$$

$$|\delta A_w^t(\mathbf{r})| = \left|\int_\Gamma \epsilon^t(\mathbf{r}')G_w^t(\mathbf{r};\mathbf{r}',\mathbf{n}(\mathbf{r}'))dS'\right| \le ||\epsilon_t||\cdot||G_w^t(\mathbf{r};\cdots)||, \tag{5.67}$$

where we denote

$$||\epsilon_n|| = \left[\int_\Gamma |\epsilon^n(\mathbf{r}')|^2 dS'\right]^{1/2}, \tag{5.68}$$

$$||G_w^n(\mathbf{r};\cdots)|| = \left[\int_\Gamma |G_w^n(\mathbf{r};\mathbf{r}',\mathbf{m}(\mathbf{r}'))|^2 dS'\right]^{1/2}, \tag{5.69}$$

provided these integrals exist. Therefore, the error in each component of $\mathbf{A}$ obeys the inequality

$$|\delta A_w| \le |\delta A_w^n| + |\delta A_w^t| \le ||\epsilon_n||\cdot||G_w^n(\mathbf{r};\cdots)|| + ||\epsilon_t||\cdot||G_w^t(\mathbf{r};\cdots)||. \tag{5.70}$$

Note that this bound varies from point to point within the domain Ω through its dependence on the variable $\mathbf{r}$. The bound also depends on the choice of boundary

geometry and gauge through the functions G_w^n and G_w^t. The bounding functions $||G_w^n(\mathbf{r};\cdots)||$ and $||G_w^t(\mathbf{r};\cdots)||$ for the choice of a spherical boundary are illustrated in Fig 5.5. These are evaluated in the gauge defined by setting the orientation of the Dirac strings according to $\mathbf{m}(\mathbf{r}') = \mathbf{r}'/|\mathbf{r}'|$. Note that absolute errors are suppressed relative to their surface values by 6-7 orders of magnitude at the center of the sphere.

By an identical argument, it follows from (5.65) that each Taylor coefficient a_l^w obeys the inequality

$$|\delta a_l^w| \leq ||\epsilon^n|| \cdot ||G_l^{n,w}(\mathbf{r}_d;\cdots)|| + ||\epsilon^t|| \cdot ||G_l^{t,w}(\mathbf{r}_d;\cdots)|| \tag{5.71}$$

for $l = 1, 2, \ldots L$, where L is determined by the desired degree N. Assuming that the surface errors ϵ^n and ϵ^t take the form of independent random variables ϵ_{jk}^n, ϵ_{jk}^t at each mesh point (see Appendix A), we estimate the error δa_l^w as follows. Let

$$\sigma_n^2 = \langle|\epsilon_{jk}^n|^2\rangle, \qquad \sigma_t^2 = \langle|\epsilon_{jk}^t|^2\rangle \tag{5.72}$$

denote the variance of errors on the surface. We estimate the surface integrals appearing in (5.65) as Riemann sums. Averaging over errors on the surface, we find that

$$\langle|\delta a_l^w|^2\rangle \approx \sigma_n^2 \sum_{j,k} |G_l^{n,w}(\mathbf{r}_d;\mathbf{r'}_{jk},\mathbf{n})|^2\Delta^2 + \sigma_t^2 \sum_{j,k} |G_l^{t,w}(\mathbf{r}_d;\mathbf{r'}_{jk},\mathbf{n})|^2\Delta^2, \tag{5.73}$$

where $\Delta \sim h^2$ is the area of each element of the surface mesh. We then have the estimate

$$\mathrm{rms}(\delta a_l^w) = \Delta^{1/2}\sqrt{\sigma_n^2||G_l^{n,w}(\mathbf{r}_d;\cdots)||^2 + \sigma_t^2||G_l^{t,w}(\mathbf{r}_d;\cdots)||^2} \tag{5.74}$$

where $||G_l^{n,w}(\mathbf{r}_d;\cdots)||$ and $||G_l^{t,w}(\mathbf{r}_d;\cdots)||$ are the bounding functions appearing in (5.71).

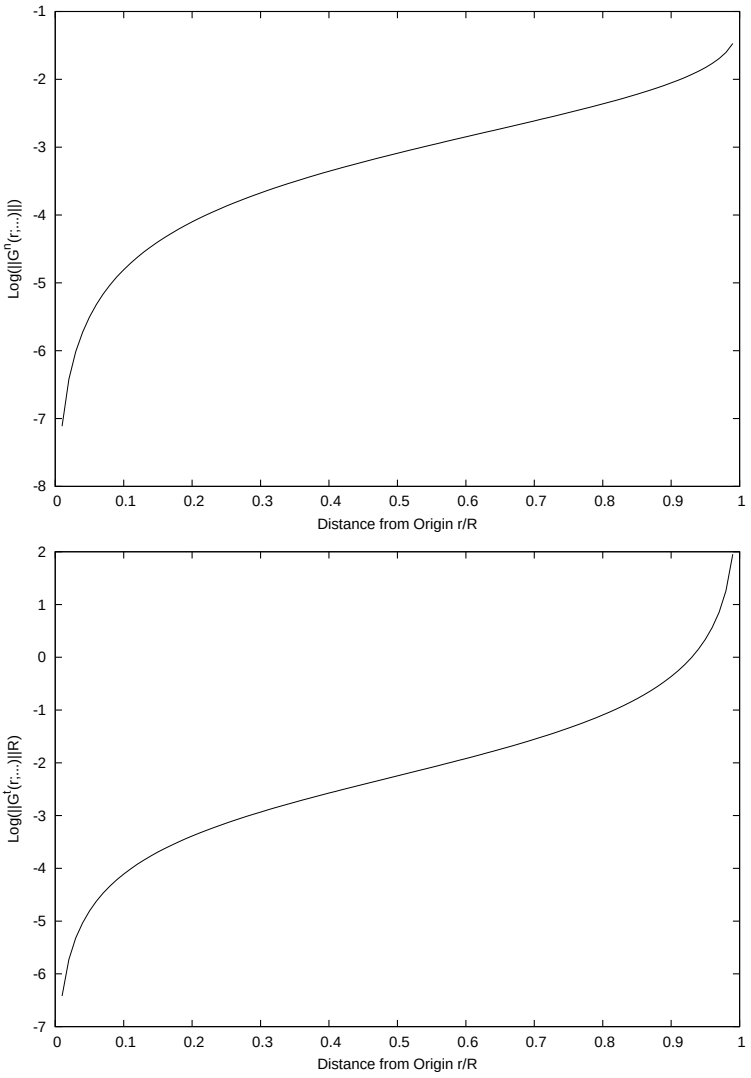

Figure 5.5: Log (to the base 10) plot of the error bounds appearing in (5.70) obtained when fitting onto a sphere of radius R. (Upper) Log of the dimensionless quantity $||G_w^n(\mathbf{r};\cdots)||$ versus distance from the center of the sphere in units of R. (Lower) Log of the dimensionless quantity $||G_w^n(\mathbf{r};\cdots)||R$ versus distance from the center of the sphere in units of R. The two cases $w = x$ and $w = y$ are identical due to symmetry.

5.6.2 Theory of Smoothing

In previous chapters, we saw that high-frequency Fourier modes in the function B_n on the surface contribute little to the on-axis gradient functions $C_{n,s}^{[m]}$, $C_{n,c}^{[m]}$, which determine the Taylor coefficients $a_l^w(z)$ appearing in the transfer map equations. The bounds given in the previous section do not clearly indicate whether a similar smoothing phenomenon occurs using the techniques described in this chapter. In this section, we show that this is indeed the case, and we outline a theory of smoothing for general-geometry domains.

Begin by recalling the result [24]

$$\frac{1}{|\mathbf{r}-\mathbf{r}'|} = \sum_{n=0}^{\infty} \sum_{m=-n}^{n} \frac{4\pi}{2n+1} \frac{r^n}{r'^{n+1}} Y_n^{m*}(\theta,\phi) Y_n^m(\theta',\phi'), \tag{5.75}$$

valid for $r < r'$, where we have expressed $\mathbf{r}$ and $\mathbf{r}'$ in spherical coordinates (r,θ,ϕ). The Y_n^m are the spherical harmonics given by

$$Y_n^m(\theta,\phi) = \sqrt{\frac{2n+1}{4\pi}\frac{(n-m)!}{(n+m)!}} P_n^m(\cos\theta) e^{im\phi} \tag{5.76}$$

in terms of the associated Legendre functions P_n^m. The set of Y_n^m is therefore normalized such that

$$\int_0^{\pi} \int_{-\pi}^{\pi} Y_n^{m*}(\theta,\phi) Y_{n'}^{m'}(\theta,\phi) \sin\theta d\theta d\phi = \delta_{n,n'}\delta_{m,m'}. \tag{5.77}$$

We wish to make use of expressions similar to (5.75) for the kernels $\mathbf{G}^t(\mathbf{r};\mathbf{r}',\mathbf{n})$ and $\mathbf{G}^n(\mathbf{r};\mathbf{r}',\mathbf{m})$. These will be constructed indirectly as follows. Consider a single component $G_w^t(\mathbf{r};\mathbf{r}',\mathbf{n})$ of the kernel (5.48), where $w = x, y,$ or z. Recall that $G_w^t(\mathbf{r};\mathbf{r}',\mathbf{n})$ is real-analytic at all points in space except at $\mathbf{r} = \mathbf{r}'$. Let $R = |\mathbf{r}'| - \delta$

denote a distance lying just within r', where the constant $\delta > 0$ may be arbitrarily small. We surround the origin by a sphere S^2 of radius R. The restriction of G_w^t to S^2

$$g(\theta, \phi) = G_w^t(\mathbf{r}; \mathbf{r}', \mathbf{m})|_{\mathbf{r}=(R,\theta,\phi)} \tag{5.78}$$

is then a real-analytic function on the sphere, which we may write as the uniformly convergent series

$$g(\theta, \phi) = \sum_{n=0}^{\infty} \sum_{m=-n}^{n} a_{nm} Y_n^m(\theta, \phi), \tag{5.79}$$

in terms of the usual coordinates on the sphere. The coefficients are given by

$$a_{nm} = \int_{-\pi}^{\pi} \int_{0}^{\pi} g(\theta, \phi) Y_n^{m*}(\theta, \phi) \sin\theta d\theta d\phi. \tag{5.80}$$

It follows that the coefficients a_{mn} obey the bound

$$|a_{mn}| \leq M \tag{5.81}$$

for all m and n, where

$$M = \left(\int_{-\pi}^{\pi} \int_{0}^{\pi} |g(\theta, \phi)|^2 \sin\theta d\theta d\phi \right)^{1/2} < \infty. \tag{5.82}$$

Note that these coefficients in general depend on $\mathbf{r}'$ and the surface normal $\mathbf{n}$, as does the bound M. In addition, the coefficients a_{mn} oscillate as the coordinate $\mathbf{r}'$ moves over the surface, as anticipated in (5.75). Additional bounds on the coefficients of the series (5.79) are discussed in [48],[49].

We know that G_w^t is harmonic in the ball enclosed by the sphere S^2. The unique solution of the Dirichlet problem which takes on the surface values (5.79) is given by

$$G_w^t(\mathbf{r}; \mathbf{r}', \mathbf{n}) = \sum_{n=0}^{\infty} \sum_{m=-n}^{n} a_{nm}(\mathbf{r}', \mathbf{n}) \left(\frac{r}{R} \right)^n Y_n^m(\theta, \phi). \tag{5.83}$$

Now given the error ϵ^t on the surface as defined in (5.61), the interior error for the vector potential becomes

$$\begin{aligned}\delta A_w^t(\mathbf{r}) &= \int_{\partial\Omega} \epsilon^t(\mathbf{r}') G_w^t(\mathbf{r};\mathbf{r}',\mathbf{n}) dS' \\ &= \sum_{n=-\infty}^{\infty} \sum_{m=-n}^{n} r^n Y_n^m(\theta,\phi) \int_{\partial\Omega} \epsilon^t(\mathbf{r}') \frac{a_{nm}(\mathbf{r}',\mathbf{n})}{R^n} dS'. \end{aligned} \tag{5.84}$$

We expect the integrand to become highly oscillatory for large values of the indices m, n. Let r_{min} denote the distance of closest approach between the surface and the origin

$$r_{min} = \inf\{r' : \mathbf{r}' \in \partial\Omega\}, \tag{5.85}$$

and let

$$M_{max} = \sup\{M(\mathbf{r}') : \mathbf{r}' \in \partial\Omega\}. \tag{5.86}$$

Therefore $R = r' - \delta \geq r_{min} - \delta$ at all points on the surface $\partial\Omega$. In this case, the integral appearing in (5.84) is bounded by

$$\begin{aligned}\int_{\partial\Omega} \epsilon^t(\mathbf{r}') \frac{a_{nm}(\mathbf{r}',\mathbf{n})}{R^n} dS' &\leq \frac{1}{(r_{min}-\delta)^n} \int_{\partial\Omega} |\epsilon^t(\mathbf{r}') a_{nm}(\mathbf{r}',\mathbf{n})| dS' \\ &\leq \frac{1}{(r_{min}-\delta)^n} \int_{\partial\Omega} |\epsilon^t(\mathbf{r}') M(\mathbf{r}',\mathbf{n})| dS' \\ &\leq \frac{M_{max}}{(r_{min}-\delta)^n} \int_{\partial\Omega} |\epsilon^t(\mathbf{r}')| dS'. \end{aligned} \tag{5.87}$$

As this holds for all $0 < \delta < r_{min}$, no matter how small, we may take the limit $\delta \to 0$ of both sides in the above inequality. Then we have from (5.84) that δA_w^t may be represented for $r < r_{min}$ as the series

$$\delta A_w^t(\mathbf{r}) = \sum_{n=0}^{\infty} \sum_{m=-n}^{n} b_{mn} \left(\frac{r}{r_{min}}\right)^n Y_n^m(\theta,\phi) \tag{5.88}$$

where

$$|b_{mn}| \leq M_{max} \int_{\partial\Omega} |\epsilon^t(\mathbf{r}')| dS'. \tag{5.89}$$

Suppose we surround the origin with a small sphere of radius $r < r_{min}$. On this sphere, the error in the vector potential takes the form

$$\delta A_w^t(\mathbf{r})|_{\mathbf{r}=(R,\theta,\phi)} = \sum_{n=0}^{\infty} \sum_{m=-n}^{n} c_{mn} Y_n^m(\theta, \phi) \tag{5.90}$$

where

$$c_{mn} = b_{mn} \left(\frac{r}{r_{min}} \right)^n. \tag{5.91}$$

At a given distance r, we find that the coefficients c_{mn} are guaranteed to decay with n at least as fast as

$$e^{-n\lambda}, \tag{5.92}$$

where the rate of decay

$$\lambda = \log \left(\frac{r_{min}}{r} \right) \tag{5.93}$$

is determined by the distance to the surface r_{min}. As a result, the contribution of high-order harmonics to the error near the origin (5.90) is exponentially suppressed. This occurs despite the high-frequency variations of the error ϵ^t on the surface $\partial\Omega$.

An identical argument may be used to discuss the smoothing of errors in δA_w^n due to the kernel $G_w^n(\mathbf{r}; \mathbf{r}', \mathbf{m})$. In this case, the factor M_{max} appearing in (5.89) will differ. Behavior of the error δA_w near a point $\mathbf{r}_d$ other than the origin may be obtained in the same manner. In this case, we surround the point $\mathbf{r}_d$ (rather than the origin) by a sphere of radius R where the sphere lies just inside the nearest singularity, such that $R = |\mathbf{r}' - \mathbf{r}_d| - \delta$. The series (5.83) is then a series in the

variable $r = |\mathbf{r} - \mathbf{r}_d|$ denoting distance from $\mathbf{r}_d$, and successive results follow as before.

As a numerical example of the smoothing just described, we have illustrated the suppression of high-frequency errors in Fig 5.6. In this illustration, we suppose that the domain of interest is a cube with side of length 1. A single Fourier mode of the form

$$\epsilon^n(\mathbf{r}') = \sin(3\pi x')\sin(2\pi y'), \qquad \epsilon^t(\mathbf{r}') = \sin(3\pi x')\sin(2\pi y') \tag{5.94}$$

is added to the surface values $\mathbf{n} \cdot \mathbf{B}$ and ψ in the top plane $z = 1$. We illustrate the resulting errors δA_x and δA_y in the planes $z = 1/2$ and $z = 0$. Note that the amplitude of errors at $z = 0$ is a factor of 10 smaller than the corresponding errors at $z = 1/2$, a suppression of $10^{-4} - 10^{-3}$ relative to their surface values. Furthermore, only the lowest frequency Fourier modes contribute significantly to the error in the midplane $z = 0$.

5.6.2.1 Supplementary Result

Note that each function $Q_n^m(x, y, z) = r^n Y_n^m(\theta, \phi)$ appearing in (5.88) becomes in Cartesian coordinates a homogeneous polynomial of degree n in the variables x,

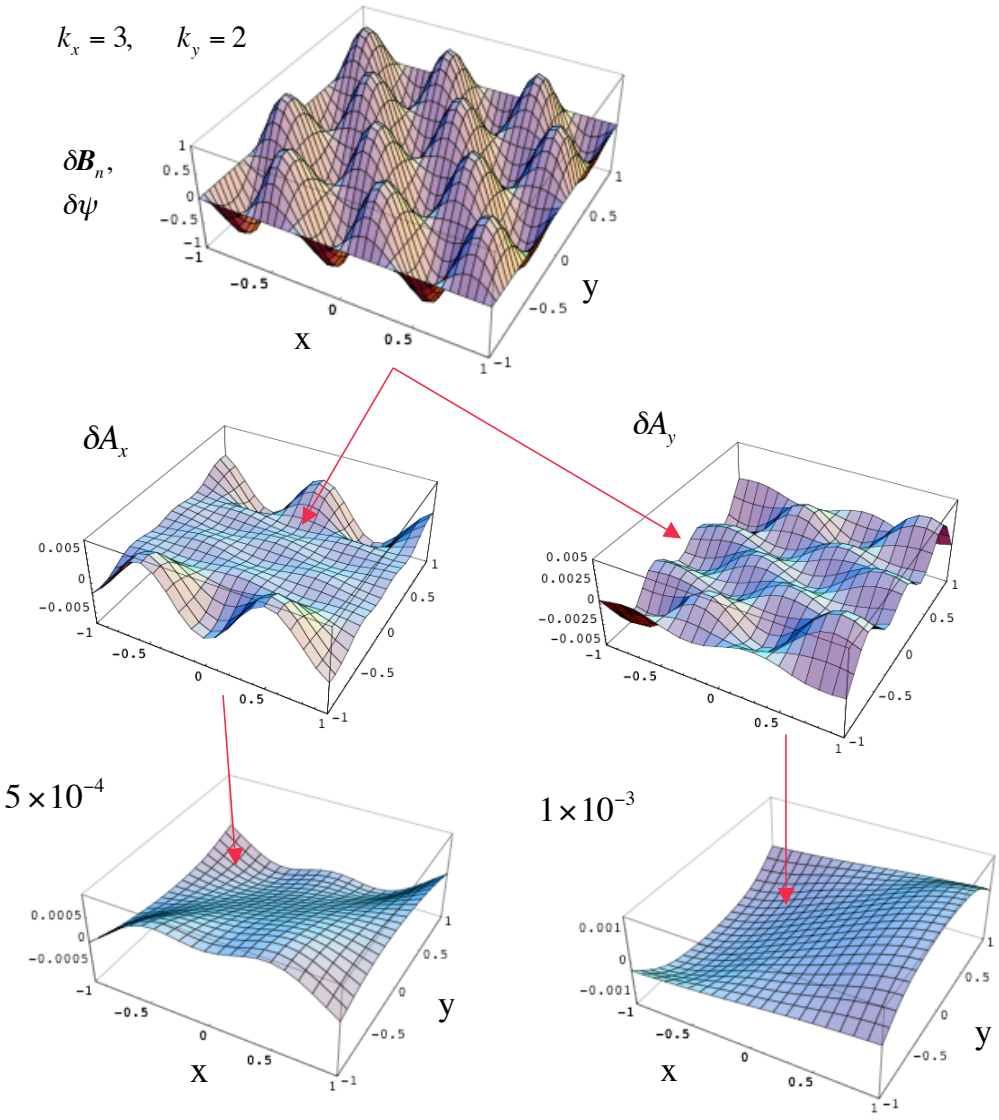

Figure 5.6: An illustration of numerical smoothing for the case of a cube with side of length 1. (Top) A single mode with unit amplitude is added to the surface values $\mathbf{B}_n$, ψ on the top face of the cube. (Middle) Resulting error in the two transverse components of the vector potential in the plane $z = 1/2$. (Bottom) Resulting error in the two transverse components of the vector potential in the plane $z = 0$.

y, and z [93]. For example

$$Q_1^1 = \sqrt{\frac{3}{8\pi}}(x+iy), \tag{5.95}$$

$$Q_1^{-1} = \sqrt{\frac{3}{8\pi}}(x-iy), \tag{5.96}$$

$$Q_2^2 = \sqrt{\frac{5}{96\pi}}3(x+iy)^2, \tag{5.97}$$

$$Q_2^1 = \sqrt{\frac{5}{24\pi}}3z(x+iy), \tag{5.98}$$

and so on. Furthermore, these polynomials $Q_n(x,y,z)$ satisfy $\nabla^2 Q_n(x,y,z) = 0$ everywhere. As a result, we find that in (5.88) we have obtained the unique series for δA_w in homogeneous polynomials about the origin. The result (5.89) then provides a tighter bound for the error in a given Taylor coefficient a_l^w in the variables x, y, and z. For all coefficients a_l^w of degree n, we see that

$$|\delta a_l^w| \leq \frac{M_{max}^t}{r_{min}^n}\int_{\partial\Omega}|\epsilon^t(\mathbf{r}')|dS' + \frac{M_{max}^n}{r_{min}^n}\int_{\partial\Omega}|\epsilon^n(\mathbf{r}')|dS', \tag{5.99}$$

where we have used the superscripts t and n to distinguish the bounds due to the kernels G_w^t and G_w^n, respectively.

Chapter 6

Application to Damping Rings

6.1 Overview of the ILC

In August 2005, a large gathering of accelerator and particle physicists from the Americas, Asia, and Europe met in Snowmass, Colorado for the second Workshop on the International Linear Collider (ILC), accepted by the International Committee for Future Accelerators as *the next major project in high-energy physics.* The Workshop saw the formation of the Global Design Effort (GDE), an international organizing committee whose goal was to unite those institutes around the world involved in linear collider R&D to produce a global design for the International Linear Collider. The proposed International Linear Collider (ILC) is a 200-500 GeV center-of-mass linear electron-positron collider, 30 km in length, with a planned future upgrade to 1 TeV. The machine is to be driven by superconducting radio-frequency (rf) accelerating cavities patterned after those designed by the TESLA Technology Collaboration, which grew out of the DESY facility in Hamburg, Germany. Construction is optimistically projected to begin around 2015, depending on international agreement and on the availability of funding. A site has not yet been chosen. The three primary sample sites for the machine currently being considered are:

- Northern Illinois, near Fermi National Accelerator Laboratory in the USA,

- One of several possible candidate sites in Japan,
- European site located at CERN near Geneva, Switzerland.

The total estimated cost of the machine is 6.65 billion US dollars, of which 4.87 billion is expected to be shared among partner nations. This cost includes construction of the machine, final engineering designs, and construction of all conventional facilities. It does not include manpower, R & D, prototype tests, or the cost of the experimental detectors. A separate estimate can be found for labor. (See [62].)

6.1.1 The Case for the International Linear Collider

The ILC is designed to serve as a precision probe of new Terascale physics, in conjunction with its partner the Large Hadron Collider (LHC). The Large Hadron Collider is a 14 TeV circular proton-proton collider under construction at CERN. The Large Hadron Collider is set to circulate its first beams in early 2008, and is expected to obtain its first glimpse of Terascale physics by late 2008 or early 2009. While the LHC will be the first to investigate this new energy regime, the ILC is required for mapping the regime with precision detail. In particular the ILC will allow a detailed study of the Higgs, provide a window into precision top-quark physics, and explore supersymmetry and other physics beyond the standard model.

All Standard Model predictions for the mass of the Higgs boson(s) lie within the energy range of the ILC. While the LHC is expected to produce the Higgs, the ILC will be capable of measuring its properties in detail. In the proton-proton collisions of the LHC, the reaction energy cannot be controlled; the composite nature of

the proton implies that the polarization and momentum exchange of quarks involved in the collision are unknown. In addition, any Higgs interactions measured at the LHC will have large backgrounds due to the huge number of strong quark-gluon and gluon-gluon scattering events. In the electron-positron collisions of the ILC, however, the collision energy of the beams is fully converted to create new states ($E_{react} = 2E_b$), and both the reaction energy and polarization are controlled. Given the ability to scan between 200-500 GeV with a precision of 0.1%, the ILC will measure the energy dependence of the Higgs production cross section, verifying the mass as well as the spin and other quantum numbers of the Higgs. In addition, the ILC will produce signals with sufficiently small background to measure the coupling strength of the Higgs with other particles of the Standard Model.

One of the first tasks of the ILC is to investigate precision top-quark physics [65]. The energy of the ILC will be sufficient to produce a large number of $t\bar{t}$ pairs at about $2m_t \approx 350$ GeV center-of-mass energy. Because of its large mass, the top quark behaves nearly as a free particle, allowing precision tests of perturbative QCD in the asymptotic regime where strong coupling is small. The ILC will make precision measurements of the top quark mass, its width, and the strong coupling constant α_s together with other electroweak parameters. These parameters can be used to constrain the Standard Model or select between different extensions.

In addition, the ILC will investigate the properties of any physics beyond the Standard Model observed at the LHC. Higgs and top quark measurements will probe for the presence of extra dimensions. Any new dark matter candidates will be investigated. The ILC will also search for and investigate the properties of massive

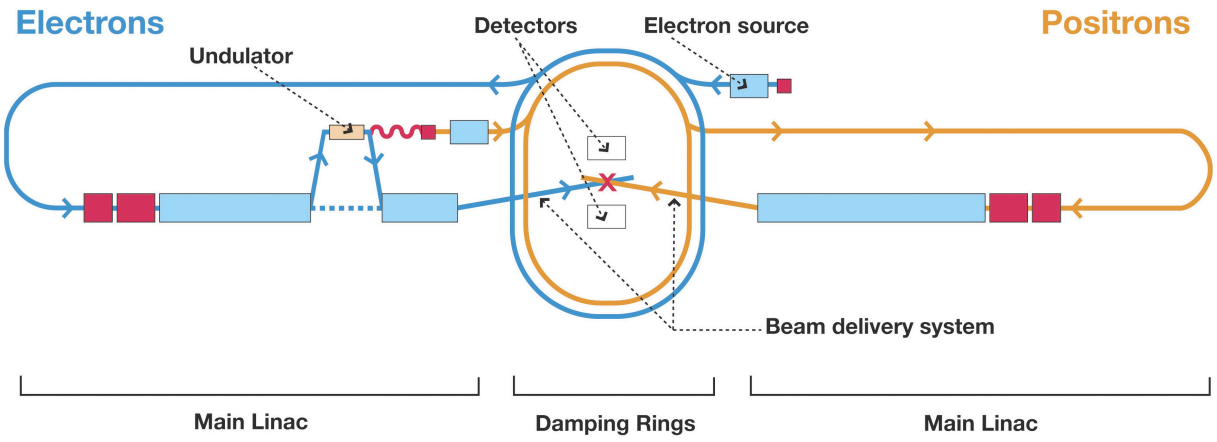

Figure 6.1: Schematic layout of the proposed International Linear Collider. Taken from [62].

supersymmetric particles, which together with previous measurements may select between different models of supersymmetry.

6.1.2 Layout and Baseline Configuration

A schematic of the proposed International Linear Collider is provided in Fig. 6.1. A summary of the primary components of the machine is provided below. We follow the beam from upstream (near the sources) to downstream (near the interaction point). The layout presented here draws from the current draft version of the GDE Reference Design Report, released 8 February 2007 [62].

- **Electron source** - Electrons are produced by photoelectric emission. A titanium-sapphire laser illuminates a GaAs photocathode in a DC gun to eject 2 ns pulses of polarized electrons. The electrons are extracted by a DC field

into a buncher, which produces short 10ps bunches of $2x10^{10}$ electrons/bunch. These polarized electron bunches are directed into a 250-meter long linear accelerator that accelerates the particles to 5 GeV for injection into the electron damping ring.

- **Positron source** - Positrons are produced by polarized γ-ray induced pair-creation. The electron beam is diverted from the main linac at 150 GeV and sent through a 150 m helical undulator magnet before being returned to the main linac. The high-energy (10 MeV) photons produced by synchrotron radiation in the undulator hit a titanium alloy target, producing a (polarized) positron beam via photoproduction. The positrons are captured in bunches of $2x10^{10}$ positrons/bunch. A booster linac accelerates the bunched positrons to 5 GeV for injection into the positron damping ring.

- **Damping ring for electrons** - The Damping Rings are responsible for conditioning those bunches received from the source into tight, cleanly separated bunches of uniform energy required for the downstream systems. Electron bunches are injected into a 6.7 km damping ring at 5 GeV, where they are stored for 10,000 turns. The particles pass repeatedly through 200 m of wiggler magnets, emitting synchrotron radiation. Through radiation damping and longitudinal reacceleration the emittance of the particles is reduced, producing the small, uniform, and stable bunches necessary for acceleration in the main linac.

- **Damping ring for positrons** - Positron bunches are injected into a separate 6.7 km damping ring. The two rings are housed in the same tunnel, surrounding the interaction region.

- **Ring to main linac** (RTML) - The RTML transports the electron and positron beams from their respective Damping Rings to the entrance of the Main Linac. During this process the beam is collimated and rotated in longitudinal phase space, using a bunch compressor that reduces the bunch length from several (6) millimeters to a few hundred (300) microns as required at the interaction point. Also, the energy is increased from 5 GeV to 15 GeV.

- **Main linac** - Two 12-km linear accelerators (linacs) accelerate the electron and positron bunches from 15 GeV to 250 GeV using approximately 16,000 superconducting rf cavities. These 9-cell niobium rf cavities operate at a frequency of 1.3 GHz with a gradient of 31.5 MV/m. A parallel tunnel, adjacent to each linac provides space for support facilities (eg, cryogenics and klystrons).

- **Beam delivery system** - To obtain high luminosity, the beam size at the interaction point must be very small. The luminosity is given by

$$L = \frac{f_{rep} n_b N^2}{4\pi\sigma_x\sigma_y}. \tag{6.1}$$

Here f_{rep} is the repetition rate, n_b is the number of bunches per train, and N is the number of particles per bunch. The required nominal size of each 300 μm bunch is $\sigma_y = 5.7$ nm vertical, $\sigma_x = 640$ nm horizontal. The Beam Delivery System is responsible for focusing the electron and positron beams to the sizes

required at the interaction point (final focus), bringing them to collision, and transporting the remaining beams to the main beam dumps. There is a single collision point with a 14 mrad crossing angle, where bunches collide with a center-of-mass energy of up to 500 GeV. Two detectors are present in the interaction region to collect the new high-energy particles produced during collision.

Table 6.1: Basic ILC Design Parameters

Center-of-mass energy range	GeV	200-500
Peak luminosity	$cm^{-2}s^{-1}$	2x 10^{34}
Beam current	mA	9.0
Pulse rate	Hz	5.0
Pulse length (beam)	ms	1
Number of bunches per pulse	–	1000-5400
Charge per bunch	nC	1.6-3.2
Accelerating gradient	MV/m	31.5
RF pulse length	ms	1.6
Beam power (per beam)	MW	10.8
Typical beam size at IP	nm	640x5.7
Total AC power consumption	MW	230

Table 6.2: Nominal Beam Parameters

Bunch population	10^{10}	2
Number of bunches	–	2670
Linac bunch interval	ns	369
RMS bunch length	μm	300
Normalized horizontal emittance at IP	mm·mrad	10
Normalized vertical emittance at IP	mm·mrad	0.04
Horizontal beta function at IP	mm	20
Vertical beta function at IP	mm	0.4
RMS horizontal beam size at IP	nm	640
RMS vertical beam size at IP	nm	5.7
Vertical disruption parameter	–	19.4
RMS beamstrahlung energy loss	%	2.4

6.2 ILC Damping Ring Design

Electrons/positrons in a bunch enter the appropriate damping ring from the source with a large spread of energy and momenta. They undergo large-amplitude betatron (transverse) and synchrotron (longitudinal) oscillations about the design orbit. The damping rings are responsible for conditioning these bunches into tight, cleanly separated bunches of uniform energy and momentum required for the main linac. The damping rings must perform several functions:

- Accept e^- and e^+ beams with large transverse and longitudinal emittances of 0.01 m·rad and damp to the low emittances (horizontal 8 μm·rad, vertical 20 nm·rad) required for luminosity production, within the 200 ms between machine pulses.

- Inject and extract individual bunches to/from the ring without affecting the emittance or stability of the remaining bunches stored in the ring.

- Maintain beam polarization and a sufficiently large acceptance over nearly 9000 turns.

The properties of the damping rings are set primarily by the requirements of the main linac. The TESLA rf technology is capable of providing 1 ms accelerating pulses of 1.3 GHz, spaced 0.2 s apart. As a result, the damping rings must provide fully damped, 1 ms bunch trains for the main linac. An entire bunch train of $N_b = 2670$ bunches is injected completely into the damping ring. This 1 ms train of 300 km in length must be compressed into the 6.7 km ring for storage. This is

accomplished by filling the damping ring over several ($n = 44$) turns. Every 370 ns a kicker injects a new bunch into an available rf bucket in the ring, which must be done without disturbing its neighbors. The entire bunch train is then stored for 0.2 s (the time between machine pulses), while its emittance is reduced by radiation damping. The train is then extracted as it was injected, by removing every nth bunch, forming a bunch train for the main linac. The damping mechanism is discussed briefly in the following section. A useful overview of the design issues involved can be found in [61].

6.2.1 Radiation damping

The statistics of the beam are often characterized by a sigma matrix $\mathbf{\Sigma}$. For each coordinate $x_i = x, y, z$, we have

$$\mathbf{\Sigma}_i = \begin{bmatrix} \langle x_i^2 \rangle & \langle x_i x_i' \rangle \\ \langle x_i' x_i \rangle & \langle x_i'^2 \rangle \end{bmatrix} = \epsilon_i \begin{bmatrix} \beta_i & -\alpha_i \\ -\alpha_i & \gamma_i \end{bmatrix}. \tag{6.2}$$

The emittance $\epsilon_i = (\det \mathbf{\Sigma}_i)^{1/2}$ characterizes the phase space area occupied by the beam. Here the Twiss parameters α, β, and γ describe the geometry of the phase-space distribution. The normalized emittance $\epsilon_{N,i} = \gamma\beta\epsilon_i$ is an adiabatic invariant.

The power radiated by a charged particle of energy E in a homogeneous magnetic field $\mathbf{B}$ is (see [57])

$$P_\gamma = \frac{e^2 c^3}{2\pi\beta^2} C_\gamma E^2 B^2 = \frac{c C_\gamma}{2\pi} \frac{E^4}{\rho^2} \tag{6.3}$$

where, for e^- and e^+,

$$C_\gamma = \frac{4\pi}{3} \frac{r_c}{(mc^2)^3} = 8.8460 \times 10^{-5} \mathrm{m/GeV}^3 \tag{6.4}$$

and the radius of curvature ρ is given by

$$\frac{1}{\rho} = \frac{ecB}{\beta E} = 0.2998 \frac{B[\mathrm{T}]}{\beta E[\mathrm{GeV}]}. \tag{6.5}$$

Synchrotron radiation is emitted within a narrow cone of angle $\theta = 1/\gamma$ relative to the momentum of the charged particle, producing a recoil opposite the direction of motion. Through the emission of synchrotron radiation in the wigglers, betatron and synchrotron oscillation amplitudes are damped. The damping of synchrotron oscillations occurs due to the energy dependence of (6.3). High-energy particles have a higher rate of energy loss, tending to reduce the spread of beam energy. As a result, the longitudinal emittance and amplitude of synchrotron oscillations are damped. The damping of betatron oscillations occurs due to the direction of emission recoil. Both the transverse and longitudinal momentum are reduced during a single emission, but the energy is restored along the longitudinal direction by the electric fields in the damping ring rf cavities. As a result, the transverse momentum is damped and the divergence of the particle trajectory changes by

$$\Delta y' = -y' \frac{\delta E}{E_0} \tag{6.6}$$

reducing deviations from the design orbit.

The effects of synchrotron emission on the beam are governed by the radiation

integrals [57]

$$\mathcal{I}_2[\mathrm{m}^{-1}] = \oint \rho^{-2} ds, \tag{6.7}$$

$$\mathcal{I}_3[\mathrm{m}^{-2}] = \oint |\rho^{-3}| ds, \tag{6.8}$$

$$\mathcal{I}_4[\mathrm{m}^{-1}] = \oint \rho^{-1}(2k + \rho^{-2}) ds, \tag{6.9}$$

$$\mathcal{I}_5[\mathrm{m}^{-1}] = \oint |\rho^{-3}| H(s) ds, \tag{6.10}$$

$$\tag{6.11}$$

where

$$k = \frac{1}{B\rho}\frac{\partial B_y}{\partial x} \tag{6.12}$$

and $H = \gamma\eta^2 + 2\alpha\eta\eta' + \beta\eta'^2$ for a horizontal dispersion η. The integrals are taken along one full orbit around the ring. In terms of these integrals, the energy loss per turn due to synchrotron radiation may be expressed as

$$U = \frac{C_\gamma}{2\pi} E^4 \mathcal{I}_2. \tag{6.13}$$

The effect of radiation damping competes with quantum excitation to drive the beam toward an equilibrium emittance. The emittances in the ring behave with time as

$$\epsilon_{N,i}(t) = \epsilon_{N,i}(0) e^{-2t/\tau_u} + \epsilon_{N,i}(\infty)(1 - e^{-2t/\tau_u}) \tag{6.14}$$

where $\epsilon_{N,i}(0)$ is the injected (initial) emittance and $\epsilon_{N,i}(\infty)$ is the equilibrium emittance. The damping time τ_u therefore characterizes the time that would be required for a particle to radiate all its energy in the absence of accelerating rf cavities. To damp from 0.01 μm·rad to 20 nm·rad, we therefore need to store the beam for ~ 7

damping times. Given a set storage time of 200 ms in the ILC, the damping time needs to be < 30 ms. This sets the properties of the damping rings.

The damping time is given explicitly by

$$\tau_u = \frac{C}{C_\alpha E^3 \mathcal{I}_2 J_u} \tag{6.15}$$

with $C_\alpha = 2113.1\text{m}^2/\text{GeV}^3/\text{s}$, where the damping partition numbers are

$$J_x = 1 - \frac{\mathcal{I}_4}{\mathcal{I}_2} \qquad J_y = 1 - \frac{\mathcal{I}_4}{\mathcal{I}_2} \qquad J_s = 2 + \frac{\mathcal{I}_4}{\mathcal{I}_2} \qquad . \tag{6.16}$$

The horizontal equilibrium emittance is given by

$$\epsilon_u = C_q \frac{\gamma^2}{J_u} \frac{\mathcal{I}_5^0 + \mathcal{I}_5^w}{\mathcal{I}_2^0 + \mathcal{I}_2^w}, \tag{6.17}$$

where the superscripts 0 and w denote that integrals are taken over dipoles and wigglers, respectively.

6.2.2 Layout and parameters

We give an overview of the main features of the ILC damping rings. A schematic of the most recent proposed lattice design is provided in Figs. 6.2 and 6.3. The primary components of each damping ring are as follows. Detailed information can be found in [63].

- **Injection and extraction kickers** - The kickers provide a brief bending field to inject/extract a bunch within a 3 ns bunch spacing, without disturbing nearby bunches.

- **RF cavities** - Accelerating cavities which replenish energy lost to synchrotron radiation, to maintain a stable 5 GeV beam.

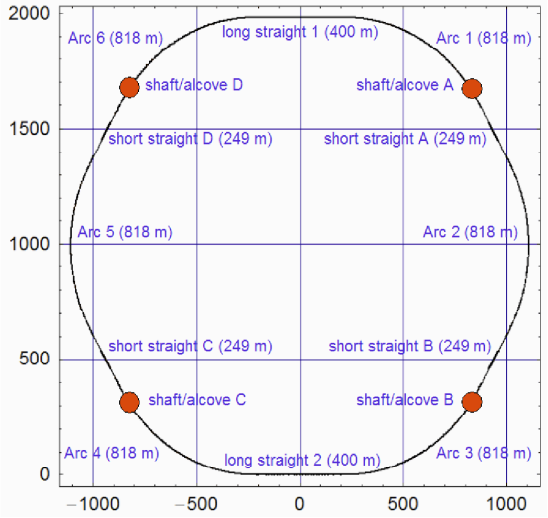

Figure 6.2: Footprint of the OCS6 lattice, the current layout of the Damping Rings for the International Linear Collider [63].

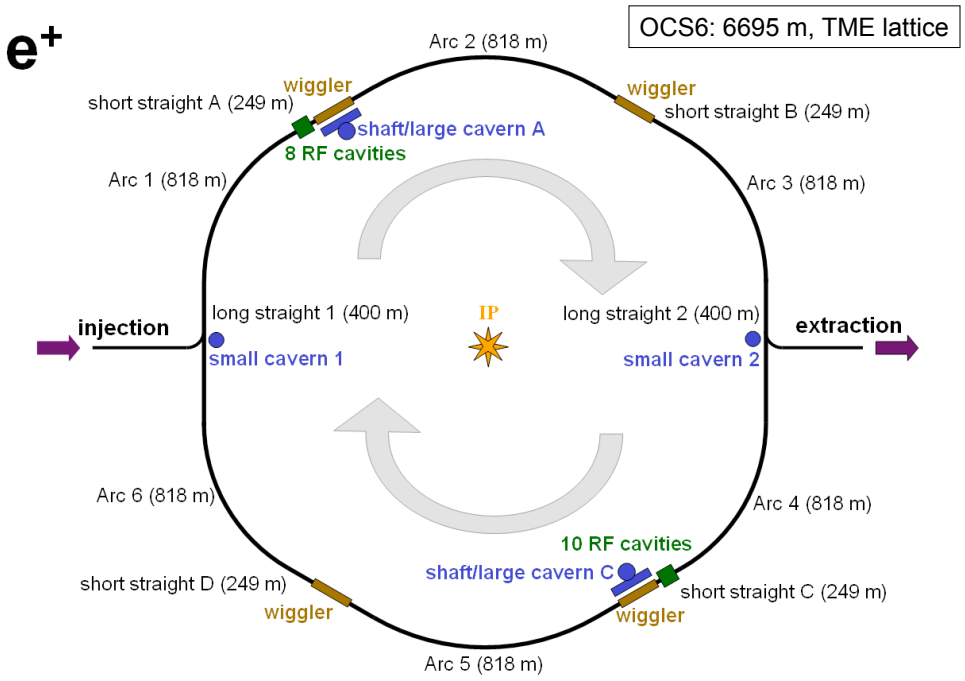

Figure 6.3: Layout of the OCS6 lattice, the current layout of the Damping Rings for the International Linear Collider. Graphic compliments of Andy Wolski.

- **Wiggler magnets** - Magnets with a strongly alternating vertical field, which provide the bulk of radiation damping in the ring.

- **Arc cells** - The primary sequences of multipole magnets responsible for focusing the beam and correcting beam optics aberrations. The style of arc cell influences the natural emittance. The TME (theoretical minimum emittance) arc cell design contains a single bend, separating several quadrupole magnets such that the cell's dispersion and beta functions reach a minimum in the center of the bend (Fig. 6.4).

The layout of Fig. 6.2 is divided into four short and two long straight sections. The short sections contain the wigglers and rf cavities, while the long sections are used for injection and extraction. A table of parameters for the current design of the ring is provided in Table 6.3.

6.3 Dynamic Aperture

The damping rings pose a number of challenges for the ILC. Previous experience at SLAC has shown that damping rings can create nonlinear instabilities whose effects are amplified in the main linac, disrupting the beam and leading to large reductions in luminosity. (See, for example, [60]). In addition, a number of single-particle and collective effects can lead stored particles in the damping rings to be lost against the vacuum chamber. The *dynamic aperture* can be defined as the maximum initial amplitude a particle can have before becoming dynamically unstable and being lost against the vacuum chamber due to single-particle dynam-

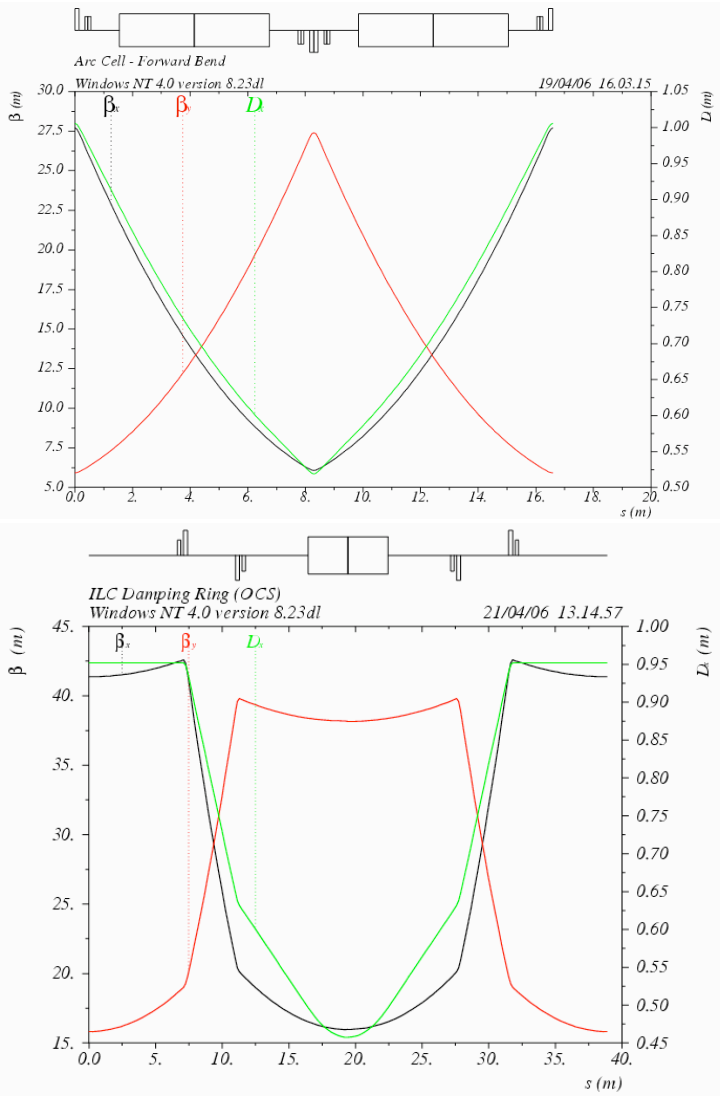

Figure 6.4: Schematic of arc cell types and corresponding lattice functions. (Upper) Standard FODO lattice. (Lower) Theoretical minimum emittance (TME) lattice.

Table 6.3: Basic ILC Damping Ring Parameters

Circumference	m	6695.057
Energy	GeV	5.0
Harmonic number	–	14516
Arc cell type	–	TME
Horizontal tune	–	52.397
Vertical tune	–	49.305
Natural chromaticity (x,y)	–	-63,-62
Momentum compaction	10^{-4}	4.20
Energy loss/turn	MeV	8.69
Transverse damping time	ms	25.7
Longitudinal damping time	ms	12.9
Natural emittance	nm	0.515
Norm. natural emittance	μm	5.04
RF voltage	MV	48.1
RF frequency	MHz	650
Synchrotron tune	–	0.0958
Synchronous phase	deg	169
RF acceptance	%	2.7
Natural bunch length	mm	6.00
Natural energy spread	10^{-3}	1.28
Average current	mA	402
Mean horizontal beta function	m	13.1
Mean vertical beta function	m	12.5
Radiation integral I_1	m	2.8116
Radiation integral I_2	m^{-1}	0.9872
Radiation integral I_3	m^{-2}	0.08876
Radiation integral I_4	10^{-4} m^{-1}	1.8888
Radiation integral I_5	10^{-5} m^{-1}	1.3870

ics effects [56]. The rate at which particles are lost determines the beam lifetime, which in turn affects the integrated luminosity delivered by the collider. Hence, the determination and optimization of dynamic aperture becomes an important part of damping ring design.

6.3.1 Single-particle dynamics

The dynamic aperture is related to the full 6-dimensional nonlinear motion of the particles. In the linear Hamiltonian approximation, each particle is confined in phase space to execute oscillations on a 3-dimensional torus. As an integrable system, the motion is characterized by the existence of action-angle variables $(\mathbf{I}, \theta)$, such that the Hamiltonian $H(\mathbf{I})$ depends on the three action variables I_j alone. Hamilton's equations of motion then become

$$\dot{I}_j = 0, \qquad \dot{\theta}_j = \frac{\partial H(I)}{\partial I_i} = \omega_j(\mathbf{I}), \tag{6.18}$$

where the frequencies $\omega(\mathbf{I})$ are time-independent. In these coordinates, the motion is confined to a torus which is the product of three circles of radii I_1, I_2, and I_3, and the particle executes quasiperiodic motion with a fixed frequency vector $\omega(\mathbf{I})$. We assume the system is nondegenerate, that is

$$\det\left(\frac{\partial \omega}{\partial \mathbf{I}}\right) = \det\left(\frac{\partial^2 H}{\partial I^2}\right) \neq 0. \tag{6.19}$$

The set of action variables $\{I_j\}$ or frequencies $\{\omega_j\}$ each forms a set of integrals of the motion, determined by the initial conditions of the particle and characterizing the corresponding torus. The angles θ_j then express the phase of the transverse betatron and longitudinal synchrotron oscillations, while oscillation amplitudes are determined by the invariant action $\mathbf{I}$.

The presence of nonlinearities due to kinematic effects, high-order multipoles, and fringe fields introduces nonlinear terms into the Hamiltonian. In the presence of such a (nonintegrable) perturbation, the motion on tori and their corresponding

constants of the motion may in general be destroyed [59]. However, the KAM theorem states that for a sufficiently small perturbation, many of these invariant tori survive. These surviving deformed tori are parametrized over a Cantor set Ω_γ of frequency vectors ω, satisfying

$$|\mathbf{k} \cdot \omega| > \frac{\gamma}{|\mathbf{k}|^m} \tag{6.20}$$

for all integer triplets $\mathbf{k} = (k_x, k_y, k_z)$, where $\gamma > 0$ is a measure of the size of the perturbation. On the set of tori corresponding to the frequencies Ω_γ, the system still possesses integrable dynamics. In the gaps of the Cantor set, however, chaotic behavior can occur. A region of the phase space where (6.20) is violated for some $\mathbf{k}$ is characterized by destroyed tori, which are replaced by a nested sequence of resonance islands within a "resonance zone" surrounding the region of the original unperturbed torus. These resonance zones together form a connected network (the Arnold web) that is dense in the available phase space, whose measure approaches zero as $\gamma \to 0$.

In the context of the damping rings, a resonance of order $\sum_\alpha |n_\alpha|$ occurs where a rational relationship exists between beam tunes of the form

$$n_x \nu_x + n_y \nu_y + n_z \nu_z = l \tag{6.21}$$

where n_α, l are integers. Here $\nu_i = \omega_i/(2\pi)$. Particles approaching a low-order resonance can be quickly excited to large amplitudes. A process of chaotic diffusion occurs along these resonances, as the tunes of a particle are no longer fixed but shift throughout the Arnold web. During this chaotic motion the corresponding oscillation amplitudes of the particle increase, quickly leading to particle losses.

6.3.2 Estimating dynamic aperture

The boundary in phase space between stable and unstable motion, as determined by the dynamic aperture, is in general quite complex and presently cannot be computed explicitly. However, the dynamic aperture can be estimated by tracking augmented by frequency map analysis techniques.

Frequency map analysis (FMA) is a technique for visualizing the global dynamics of a Hamiltonian system by computing rates of tune diffusion over a grid of initial conditions $(I_1^0, I_2^0, \theta_1^0, \theta_2^0)$. The appearance of high-diffusion zones in tune space then indicates the presence of resonances that should be avoided. See [64].

Three kinds of tracking are typically used in dynamic aperture studies:

- Matrix-kick method - Element-by-element tracking is performed using the linear (matrix) approximation of various beamline elements, with the addition of multipole kicks to approximate nonlinear effects.

- Symplectic integrators - These techniques numerically integrate the particle trajectory using split-operator algorithms that preserve the symplectic structure of the equations of motion. The matrix-kick method described above is a low-order symplectic integrator.

- Symplectic one-turn maps - A high-order but truncated one-turn map is obtained from the full Hamiltonian. A symplectic approximation to this map is then applied repeatedly to obtain turn by turn behavior.

Finally, the full map must include synchrotron damping, a non-Hamiltonian

process. The map will then take the form

$$\mathcal{M} = \mathcal{M}_{ns}\mathcal{M}_{symp}, \quad \text{where} \tag{6.22}$$

$$\mathcal{M}_{ns} = \exp(\mathcal{G}_2)\exp(\mathcal{G}_3)\exp(\mathcal{G}_4)\cdots \tag{6.23}$$

is a general map "near" the identity, written as a product of exponentials of non-Hamiltonian vector fields $\mathcal{G}_k$ [4], and $\mathcal{M}_{symp}$ is a symplectic map of the usual form (1.21). Dynamic aperture is often computed using only $\mathcal{M}_{symp}$, under the reasonable expectation that the damping provided by $\mathcal{M}_{ns}$ may increase, but never decrease, the dynamic aperture.

6.4 Computation of Transfer Maps

We have seen that, in general, surface methods provide a reliable and numerically robust method to extract transfer maps from numerical field data, and that use of such techniques has several advantages. These techniques construct a representation of the interior field using functions with known completeness properties; these functions form a complete orthonormal set on the solution space. As a least-squares representation of the solution, the resulting solution has known, and optimal, convergence properties. In addition, the resulting polynomial series in x, y may be truncated after terms of a given degree N, with the knowledge that Maxwell's equations are exactly satisfied through order N. Due to the fortunate properties of harmonic functions, the error is globally controlled by its values on the bounding surface. Finally, the smoothing property of the inverse Laplacian operator ensures that computed derivatives are relatively insensitive to errors in the surface

data. We have seen in Chapter 3 that this insensitivity to errors may be greatly improved in domains of small vertical aperture by fitting on the surface of an elliptical cylinder. Such methods provide a promising approach to modeling dynamics in the ILC damping rings and to the general problem of computing realistic transfer maps for real magnets with complicated fringe and high-order multipole error fields.

Past ILC damping ring design studies, including dynamic aperture studies, have employed idealized or approximate models of beamline elements. We intend to use the methods of this thesis to compute realistic transfer maps for all beamline elements, and wigglers in particular, of the proposed ILC damping rings. We may then use these maps to evaluate the performance of various proposed damping ring designs.

Appendix A

Amplification of Noise

The primary goal of this Dissertation is to replace the use of high-order derivative operators in computing transfer maps with bounded integral operators that exploit the structure of Maxwell's equations. In Chapters 2-4, the kernel of this integral operator is the Green's function (and its known derivatives) for Poisson's equation in the domain of interest. However, the Green's function is strongly geometry-dependent, and its series representation may be explicitly constructed for a limited number of geometries. Consequently, in Chapter 5 a geometry-independent kernel is constructed. To motivate these efforts, we first discuss the pitfalls of numerical differentiation and how it leads to the amplification of noise present in the original data.

A.1 Pitfalls of Numerical Differentiation

Let L be a linear transformation from a normed linear space X into a normed linear space Y. Then L is a *bounded* linear transformation [67],[68] if there exists some constant $C > 0$ such that

$$||Lf|| \leq C||f|| \tag{A.1}$$

for all functions $f \in X$. A linear transformation is bounded if and only if it is continuous with respect to the norms on X and Y. Clearly boundedness is compu-

tationally desirable, since it ensures the output Lf is stable with respect to small changes in the input data f.

To see that differentiation is unbounded, consider the sequence of functions $f_n(x) = \sin(nx)$ in the space $C^1[-\pi, \pi]$ using the maximum norm, so that $||f_n|| = \max_{x\in[-\pi,\pi]} |f_n(x)| = 1$. Then under the derivative operator $D : C^1[-\pi, \pi] \to C[-\pi, \pi]$ we have

$$||Df_n|| = \max_{s\in[-\pi,\pi]} n\cos(nx) = n = n||f_n||. \tag{A.2}$$

We see that $||Df_n||$ may be made arbitrarily large by choosing n sufficiently large, and thus D is unbounded. The same result holds if we use the L^2 norm, $||f_n||^2 = \int_{-\pi}^{\pi} |f(x)|^2 dx$, and in fact if we use any of the L^p norms. It is clear from this example that high frequency changes in the data f will lead to large changes in the output Df, with each frequency component amplified by a factor that increases with frequency. The relationship between derivatives and high-frequency behavior will be discussed further in Section A.2.

It follows that differentiation is discontinuous when considered as a linear operator; that is, small changes in the input function can lead to dramatic changes in the output. Consider, as a second example, the function $g(x) = g_0(x) + \epsilon \sin[(x^2 + \epsilon^2)^{-1}]$, where $g_0(x) = \cos(x)$. We imagine that g_0 is a signal to be approximated, while the second term represents additive noise (Fig. A.1). For all $\epsilon \in \mathbb{R}$, g is continuously differentiable on $[-\pi, \pi]$, and therefore $g \in C^1[-\pi, \pi]$. Clearly g can be made arbitrarily close to $\cos(x)$ by choosing ϵ sufficiently small. In fact,

$$||g - g_0|| = \max_{x\in[-\pi,\pi]} \left| \epsilon \sin\left[\frac{1}{x^2 + \epsilon^2}\right] \right| = |\epsilon|. \tag{A.3}$$

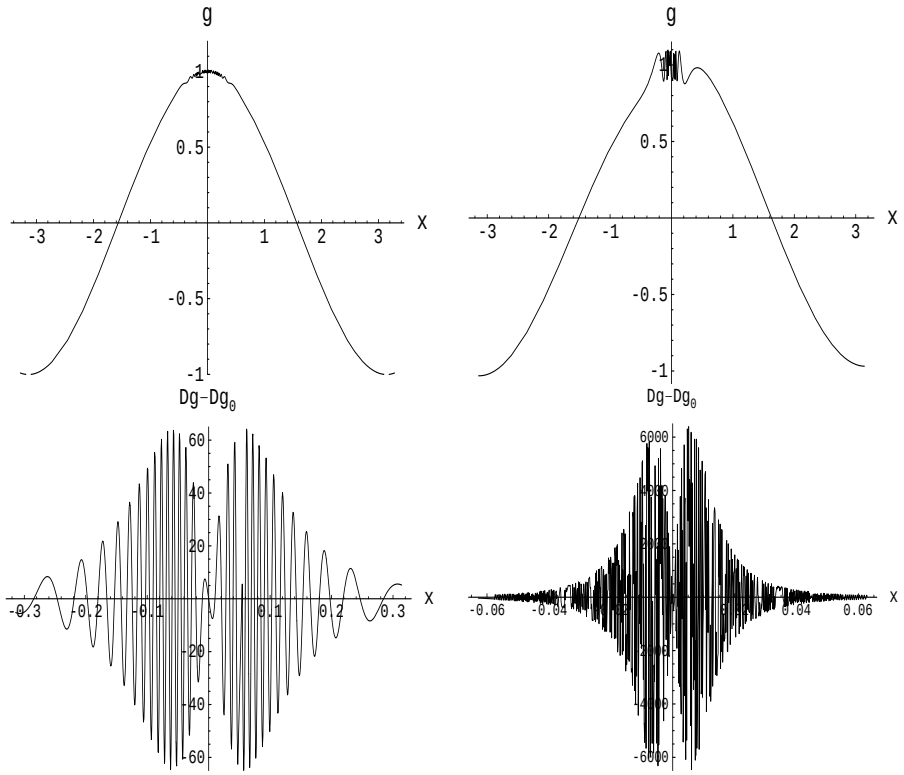

Figure A.1: (Upper) The function g illustrated for the values $\epsilon = -0.01$ and $\epsilon = +0.1$. (Lower) The derivative illustrated for the values $\epsilon = 0.1$ and $\epsilon = 0.01$.

The same cannot be said of the derivatives, however, since for all $\epsilon \neq 0$,

$$||Dg - Dg_0|| = \max_{x \in [\pi, \pi]} \left| \frac{2x\epsilon}{(x^2 + \epsilon^2)^2} \cos\left[\frac{1}{x^2 + \epsilon^2}\right] \right| = \frac{3\sqrt{3}}{8\epsilon^2}. \tag{A.4}$$

In addition, for $\epsilon = 0$, $||Dg - Dg_0|| = 0$. The discontinuity at $\epsilon = 0$ is severe, and the error in the derivative is unbounded as $\epsilon \to 0$. (See Fig. A.2.)

Suppose now that we wish to approximate the Taylor coefficients of the magnetic field about some point in the interior Ω of a magnetic element, using measured or numerical magnetic field data on a discrete mesh of points. Computation of these derivatives requires that we work with an approximation to D in some finite-dimensional subspace of the set of continuously differentiable functions on Ω. We

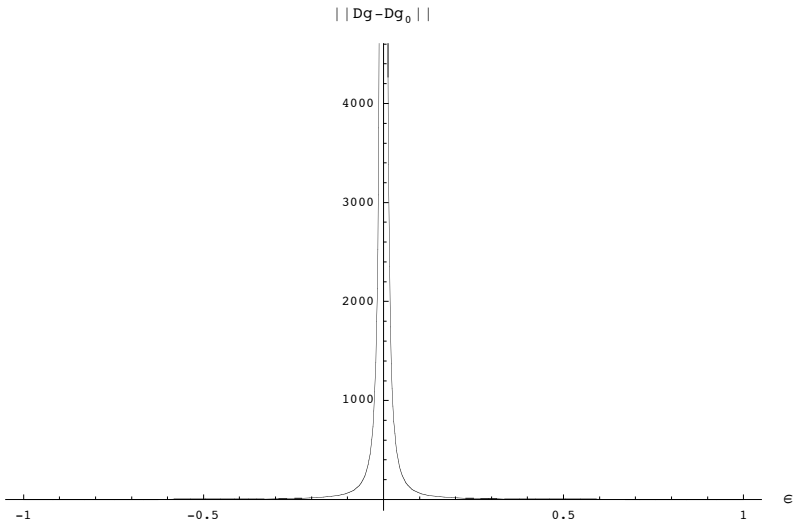

Figure A.2: Illustration of the discontinuity in the derivative operator D at $\epsilon = 0$ as it acts on functions of the form g, given by (A.4) .

may choose, for example, the space of polynomials, splines, or trigonometric polynomials through some degree N [70]. In practice, this reflects the fact that we have information about the function only up to variations on the scale of the mesh spacing h, corresponding to a frequency $\sim \frac{\pi}{h}$. Despite this fact, the unbounded nature of D is reflected in the amplification of noise that appears at this scale.

To illustrate the amplification of noise, consider applying one-dimensional finite differences to some function $f : [a, b] \to \mathbb{R}$ using a uniform mesh with spacing h. In the subinterval $[x_i - h, x_i + h]$, we let $f_{-1} = f(x_i - h)$, $f_0 = f(x_i)$, and $f_1 = f(x_i + h)$. If we suppose the values of f are known exactly at these mesh

points, then three-point formulas for the derivative are given by [10]:

$$f'_{-1} = \frac{1}{2h}(-3f_{-1} + 4f_0 - f_1) + \frac{h^2}{3}f'''(\zeta), \tag{A.5}$$

$$f'_0 = \frac{1}{2h}(-f_{-1} + f_1) - \frac{h^2}{6}f'''(\zeta), \tag{A.6}$$

$$f'_1 = \frac{1}{2h}(f_{-1} - 4f_0 + 3f_1) + \frac{h^2}{3}f'''(\zeta), \tag{A.7}$$

where ζ takes on some value in $[x_i - h, x_i + h]$. The rightmost terms then characterize the error due to truncating the interpolating polynomial after terms of degree 2. We denote this local truncation error as T_i. We now consider the effect of noise on the central point formula (A.6). Suppose that at each point we have measured or computed values $\hat{f}_k = f_k + \Delta_k$, where Δ_k is an unknown error. We suppose that each Δ_k is the value of a random variable allowed to take on values in $\mathbb{R}$ such the point $(\Delta_{-1}, \Delta_0, \Delta_1)$ is described by a joint probability density on $\mathbb{R}^3$. The central point formula (A.6) then gives the computed derivative

$$\hat{f}'_0 = \frac{1}{2h}(-\hat{f}_{-1} + \hat{f}_1) - \frac{h^2}{6}f'''(\zeta) = f'_0 - \frac{h^2}{6}f'''(\zeta) + \frac{1}{2h}(-\Delta_{-1} + \Delta_1). \tag{A.8}$$

We therefore write the total error in the computed derivative at x_i as $E_i = \hat{f}'_0 - f'_0 = T_i + R_i$, where $R_i = \frac{1}{2h}(-\Delta_{-1} + \Delta_1)$ is the error due to noise. We now assume that the errors have zero mean and nonzero deviation σ, such that

$$<\Delta_k> = 0, \tag{A.9}$$

$$<\Delta_k^2> = \sigma^2, \tag{A.10}$$

independently of k. It follows that, at each x_i,

$$<R_i> = 0, \tag{A.11}$$

$$<R_i^2> = \frac{1}{2h^2}\sigma^2 - \frac{1}{2h^2}<\Delta_1\Delta_{-1}>, \tag{A.12}$$

where the correlation must satisfy the inequality $0 \leq <\Delta_1 \Delta_{-1}> \leq \sigma^2$. If the errors at adjacent mesh points are taken to be uncorrelated, then the rms value σ_R of the error due to noise is simply

$$\sigma_R = \frac{1}{\sqrt{2}h}\sigma = \kappa\sigma, \tag{A.13}$$

where for small stepsize, $\kappa > 1$ is a factor describing the amplification of noise. We now estimate the global error on the entire interval $[a, b]$. We denote the average over the values of a function f at N mesh points as $\bar{f}$. We are interested in

$$\overline{<E_i^2>} = \overline{<(T_i + R_i)^2>} = \overline{T_i^2} + <R_i^2> \tag{A.14}$$

where the mean-squared truncation error can be approximated for small stepsize as

$$\overline{T_i^2} = \frac{1}{N}\sum_{k=0}^{N} |f'''(\zeta_k)|^2 \rightarrow \frac{1}{b-a}\int_a^b |f'''(\zeta)|^2 d\zeta = \frac{1}{L}||f'''||^2. \tag{A.15}$$

Thus we may write the rms error as

$$E_{rms}^2 = \frac{h^4}{36}\frac{1}{L}||f'''||^2 + \frac{1}{2h^2}\sigma^2. \tag{A.16}$$

The error cannot be made arbitrarily close to zero for any stepsize. It is clear that for small h, it is dominated by the amplification of noise. This phenomenon is not limited to the simple three-point formula. For the central five-point formula [10]

$$f_0' = \frac{1}{12}(f_{-2} - 8f_{-1} + 8f_1 - f_2) + \frac{h^4}{30}f^v(\zeta), \tag{A.17}$$

we have a similar result with the larger amplification factor

$$\kappa = \sqrt{\frac{65}{72}}\frac{1}{h}. \tag{A.18}$$

Indeed, the degree of amplification increases with the order of derivative desired. At a given order of derivative, the signal-to-noise ratio of the computed values falls below a reasonable threshold, and information about all higher derivatives is lost.

A.2 Models of Noise

In general we may have measured or numerical field data on a discrete mesh of points distributed throughout the interior volume of a magnetic element. Either process, of measurement or numerical computation, will introduce errors at each point, whose statistical properties we now consider. In both cases we can model the error as a *stochastic process*, where each realization is a function that assigns to every mesh point the difference $(\Delta B_x, \Delta B_y, \Delta B_z)$ between the data and the true field values at that point [66]. We assume for the time being that errors in the three components of the field are independent, in which case we let $\epsilon_i = \Delta B_\alpha(\mathbf{x_i})$ for a given component of the field with $\alpha = x, y, z$. The errors ϵ_i may be treated as follows.

Suppose the mesh points are indexed by $j = 1, 2, 3, \ldots, N$. At each point $\mathbf{x}_j$, we let ϵ_j be a random variable defined on the probability space (Ω, Pr). We refer to $\mathbf{w} = (\epsilon_1, \epsilon_2, ..., \epsilon_N)$ as a random vector. The error process is then characterized by the joint probability density $P : \mathbb{R}^N \to \mathbb{R}$, where

$$Pr[\mathbf{w} \in \Omega] = \int_\Omega P(\mathbf{w}) d^3\mathbf{w} \tag{A.19}$$

gives the probability that a given realization of the random vector $\mathbf{w}$ lies within the region $\Omega \subseteq \mathbb{R}^N$. Given a sufficiently large ensemble of possible measurement outcomes, the probability density P then completely characterizes the statistics of the errors at the mesh points and their various correlations. Choosing a model for the error then amounts to specifying the expected properties of P based on the source of those errors, which is in general a difficult task.

It is useful to make several simplifying assumptions. Throughout, we will model the error process as white noise. That is, we make the following assumptions for all i and j:

$$< \epsilon_i > = 0, \tag{A.20a}$$

$$< \epsilon_i \epsilon_j > = \sigma^2 \delta_{ij}, \tag{A.20b}$$

where σ is independent of the indices i and j. When necessary, we will make the stronger assumption that the errors are independent and identically distributed– that is, that the probability density may be written $P(\mathbf{w}) = \prod_{i=1}^{N} p(\epsilon_i)$, where p is the probability density describing each random variable ϵ_i taken alone.

In the case when the values ϵ_j arise from random measurement errors, it is typical to assume that each ϵ_j is normally distributed with a mean near zero, satisfying (A.20). In the case when the values ϵ_j arise from numerical errors, the assumptions of (A.20) are also reasonable under a broad set of circumstances. In particular, consider the error due numerical roundoff of the field values to n decimal places [10]. The random variables ϵ_j are each independently described by the uniform probability density

$$p(\epsilon_i) = \begin{cases} \frac{1}{2|\epsilon|_{max}} & \text{when } |\epsilon| < |\epsilon|_{max} = 5 \times 10^{-n-1} \\ 0 & \text{otherwise} \end{cases}, \tag{A.21}$$

resulting in $\epsilon_{rms} = 0.2887 \times 10^{-n}$.

In the study of smoothing of Chapters 2-4, we will be especially interested in the behavior of the Fourier coefficients (on bounded intervals) and Fourier transforms (on unbounded intervals) of noisy functions satisfying such a model. It is important

to note that any numerical Fourier transform algorithm must make assumptions about the behavior of a given realization of the error $\epsilon(\mathbf{x})$ between the mesh points $\mathbf{x}_i$ (see Appendix C). However, we will see that such assumptions have little effect on the low-frequency behavior of the spectrum. As a simplest case, we consider the one-dimensional discrete-time Fourier transform (DTFT) of the errors $\{\epsilon_i\}$ along the direction $\hat{\mathbf{z}}$ over the length $-L \leq z \leq L$ for some fixed x_n, y_n. Letting $f_j = \epsilon(x_n, y_n, z_j)$ with $z_j = jh$ we have

$$\mathcal{F}[f] \approx \frac{h}{\sqrt{2\pi}} \sum_{j=-p}^{p} f_j e^{ijkh} = \sqrt{\frac{h}{2\pi}} \{Z_R(k) + iZ_I(k)\} \tag{A.22}$$

where we denote the real and imaginary parts as Z_R and Z_I, respectively. For each value of k, $Z_R(k)$ and $Z_I(k)$ are random variables whose outcome depends on the values $\{f_j\}$. If we make the assumptions of (A.20), then it is possible to show that the central limit theorem applies for sufficiently small h, and therefore Z_R and Z_I are approximated by normal distributions. We define the random variables

$$g_j^R = \sqrt{h} f_j \cos(jkh), \qquad g_j^I = \sqrt{h} f_j \sin(jkh), \tag{A.23}$$

so that we may write

$$Z_R(k) = \sum_{j=-p}^{p} g_j^R, \qquad Z_I(k) = \sum_{j=-p}^{p} g_j^I. \tag{A.24}$$

It can be shown that each sequence of variables g_j^R and g_j^I satisfies the Lyapunov condition [72], and therefore their sums converge to limiting normal distributions as

$p \to \infty$ with mean and variance given by

$$\langle Z_R \rangle = \sum_{j=-p}^{p} \langle g_j^R \rangle = 0, \tag{A.25}$$

$$\langle Z_I \rangle = \sum_{j=-p}^{p} \langle g_j^I \rangle = 0, \tag{A.26}$$

and

$$\langle Z_R^2 \rangle = \sum_{j=-p}^{p} \langle |g_j^R|^2 \rangle = \sum_{j=-p}^{p} h \langle f_j^2 \rangle \cos^2(jkh), \tag{A.27}$$

$$\langle Z_I^2 \rangle = \sum_{j=-p}^{p} \langle |g_j^R|^2 \rangle = \sum_{j=-p}^{p} h \langle f_j^2 \rangle \sin^2(jkh). \tag{A.28}$$

In the limit $h \to 0$, $p \to \infty$ such that $hp = L$ is constant, we have

$$\langle Z_R^2 \rangle \to \sigma^2 \int_{-L}^{L} \cos^2(kz) dz = \sigma^2 \left[L + \frac{\sin(2Lk)}{2k} \right], \tag{A.29}$$

$$\langle Z_I^2 \rangle \to \sigma^2 \int_{-L}^{L} \sin^2(kz) dz = \sigma^2 \left[L - \frac{\sin(2Lk)}{2k} \right], \tag{A.30}$$

where we have written $\sigma^2 = \langle |f_j|^2 \rangle$.

Using the fact that Z_R and Z_I are normally distributed, we may compute various moments and correlations of these random variables as follows:

$$\langle Z_R \rangle = \langle Z_I \rangle = 0, \tag{A.31}$$

$$\langle Z_R^2 \rangle = \sigma^2 \left[L + \frac{\sin(2Lk)}{2k} \right], \tag{A.32}$$

$$\langle Z_I^2 \rangle = \sigma^2 \left[L - \frac{\sin(2Lk)}{2k} \right], \tag{A.33}$$

$$\langle Z_R Z_I \rangle = 0, \tag{A.34}$$

$$\langle Z_R^2 Z_I^2 \rangle = \langle Z_R^2 \rangle \langle Z_I^2 \rangle. \tag{A.35}$$

These correlations uniquely determine the behavior of the real and imaginary parts of the Fourier transform. They are directly related to the behavior of the power

spectrum $|\hat{f}(k)|^2$, whose mean and variance for fixed k are given by:

$$\langle \frac{2\pi}{h} |\hat{f}(k)|^2 \rangle = \langle Z_R^2 + Z_I^2 \rangle = 2L\sigma^2, \tag{A.36}$$

$$\langle \left(\frac{2\pi}{h}\right)^2 |\hat{f}(k)|^4 \rangle = \langle (Z_R^2 + Z_I^2)^2 \rangle = \sigma^4 \left[8L^2 + \frac{\sin^2(2Lk)}{k^2} \right]. \tag{A.37}$$

The flat power spectrum (A.36), independent of the frequency k, is the distinguishing characteristic of a white noise process. Note that all moments are determined by the variance σ^2 of the original variables f_j; information about all higher moments of the original noise is lost in this limit.

A numerical illustration of the results presented above is proved in Figs. A.3-A.5. In each of these figures, we have computed the fast Fourier transform (FFT) of a set of 2401 values $f_j = f(z_j)$, where the $z_j = -1+jh$, $j = 1, \ldots, 2401$ are uniformly spaced throughout the interval $[-1, 1]$. Each f_j is the value of a uniform random variable on $[0, 1]$, taken such that f_j, f_k are independent for $j \neq k$. The resulting values of the variables $Z_R(k)$ and $Z_I(k)$ are then computed at the frequencies k_j, $j = 1, \ldots 2401$ in the Nyquist band $[-\pi/h, \pi/h]$. This process is repeated for an ensemble of 1000 independent realizations of the random vector $\{f_1, f_2, \cdots, f_{2401}\}$, and the desired moments of the random variables $Z_R(k)$ and $Z_I(k)$ are computed by averaging over this ensemble. We note that here $L = 1$ and $\sigma^2 = 1/3$.

For comparison, we have included the analogous results obtained when the Fourier integral on $[-1, 1]$ is computed using the Filon-spline Fourier transform algorithm of Appendix C. Note that the results are similar to the previous cases over most of the Nyquist band, except that the values fall off according to a power-law $1/|k|^p$ very near the ends of the interval.

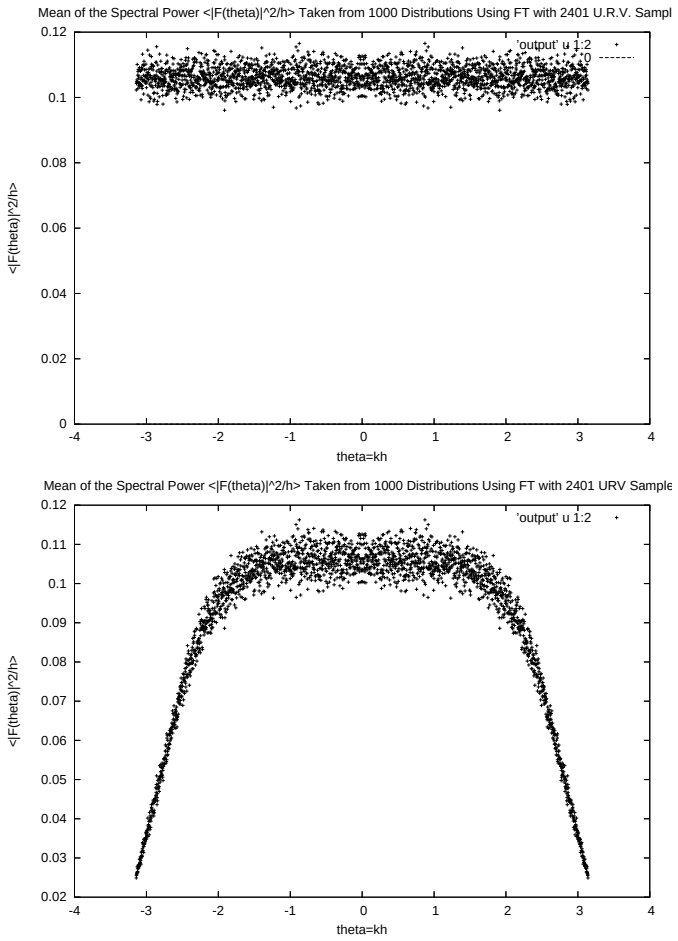

Figure A.3: (Upper) The mean spectral power $\langle \frac{1}{h} |\hat{f}(k)|^2 \rangle$ of a uniform white random vector computed using the discrete Fourier transform, plotted versus the parameter $\theta = kh$. (Lower) The same mean spectral power computed using a Filon-spline Fourier transform.

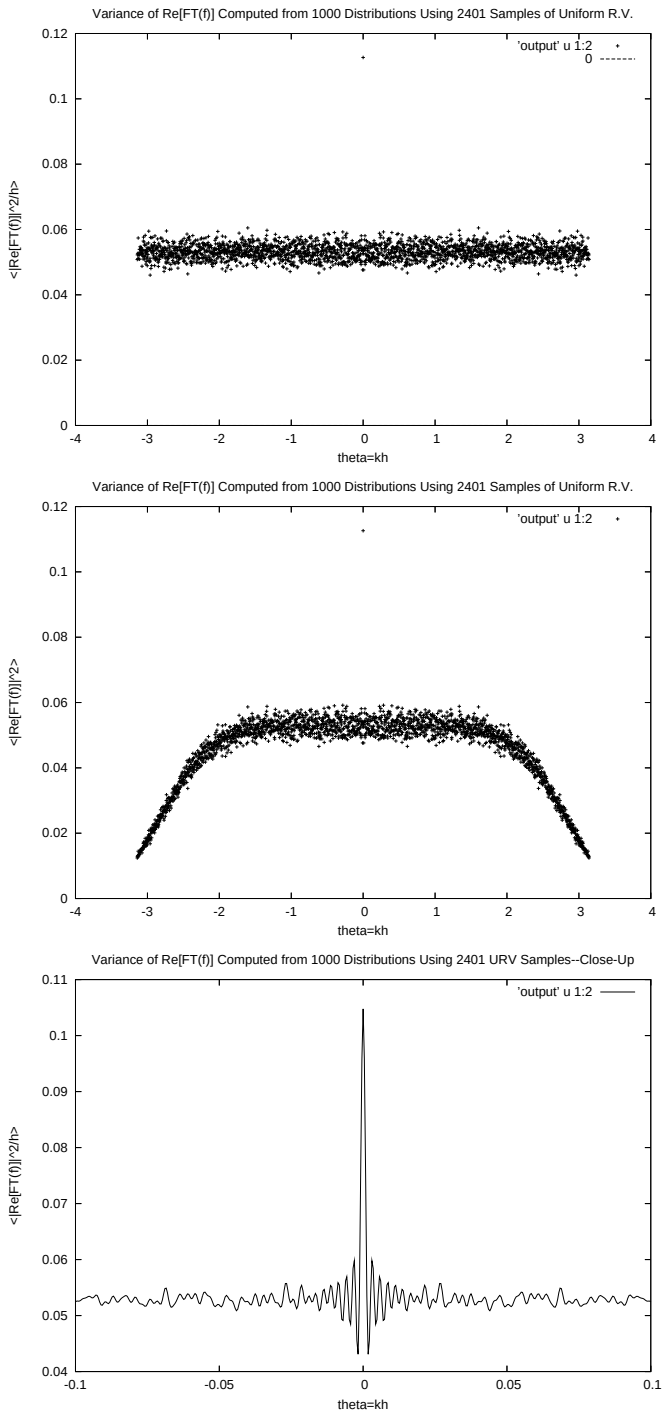

Figure A.4: (Upper) The variance of the Fourier cosine integral, $\langle |Re(\hat{f}(k))|^2 \rangle$, computed using the DTFT, plotted versus $\theta = kh$. (Center) The same variance computed using a Filon-spline Fourier transform. (Lower) Close-up of the behavior near $\theta = 0$ using a finer mesh in θ.

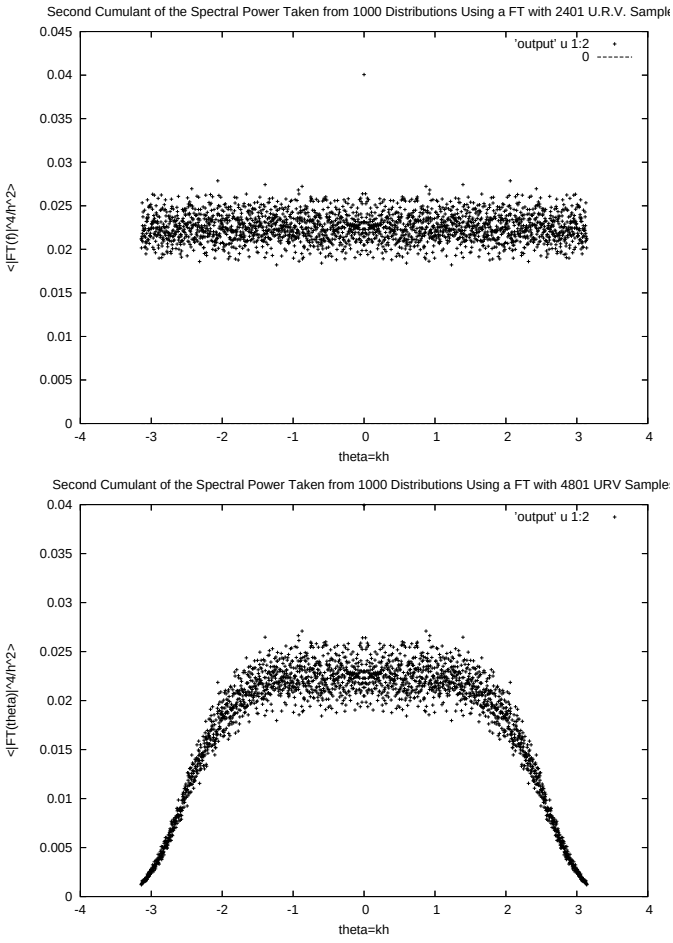

Figure A.5: (Upper) The second cumulant of the power spectrum of a uniform white random vector, $\langle \frac{1}{h} |\hat{f}(k)|^4| \rangle$, computed using the discrete Fourier transform. (Lower) The same quantity, computed using a Filon-spline Fourier transform.

In the previous section, we discussed how repeated numerical differentiation leads to the amplification of noise present in the original data. The amplification of noise becomes clear when we consider the Fourier transform of the derivative of the noisy values f_j. Note that the Fourier transform of the derivative (when it exists) is given by

$$\mathcal{F}\left[\frac{d^n f}{dx^n}\right] = (ik)^n \mathcal{F}[f]. \tag{A.38}$$

Using this result, we may estimate the behavior of the spectrum of various derivatives of f by multiplying the results above by the appropriate values of k. In Fig. A.6 we illustrate the mean spectral power $\langle k^2 |\hat{f}(k)|^2/h\rangle$ of the first derivative of f obtained using (A.38). As in the previous figures, values are provided over the full Nyquist band. We see immediately that differentiation of order p serves to amplify the high-frequency values of the spectral power by the factor k^{2p}.

As a final result, we use the model described in this Appendix to illustrate the effect of random noise on the Fourier coefficients of functions which are defined on the surfaces of a circular cylinder, an elliptic cylinder, and rectangular cylinder. Definitions of the appropriate coefficients involved are provided in the corresponding Sections 2.4.2, 3.4.4, and 4.4.2. We have that

$$\langle |a_n(k)|^2\rangle = \langle |b_n(k)|^2\rangle = \frac{hL(\delta\phi)}{\pi^2}\sigma^2 \quad \text{for a circular cylinder,} \tag{A.39a}$$

$$\langle |f_n(k)|^2\rangle = \frac{hL(\delta v)}{\pi^3}\sigma^2 I_s \quad \text{and}$$

$$\langle |g_n(k)|^2\rangle = \frac{hL(\delta v)}{\pi^3}\sigma^2 I_c \quad \text{for an elliptic cylinder,} \tag{A.39b}$$

$$\langle |\beta_n^{T,B}(k)|^2\rangle = \frac{hL}{\pi}\frac{\Delta x}{s}\sigma^2 \quad \text{and}$$

$$\langle |\beta_n^{R,L}(k)|^2\rangle = \frac{hL}{\pi}\frac{\Delta x}{d}\sigma^2 \quad \text{for a rectangular cylinder.} \tag{A.39c}$$

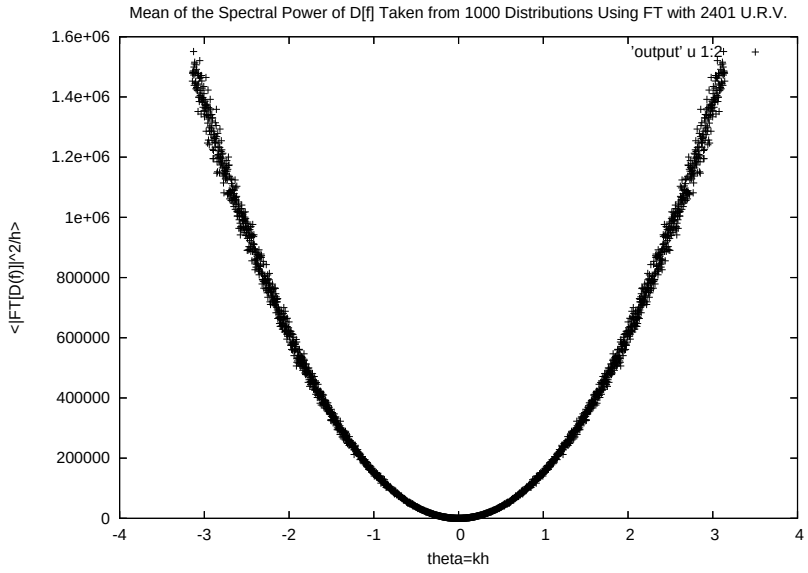

Figure A.6: Mean spectral power of the derivative of a uniform white random vector computed using (A.38) from the discrete Fourier transform. Note that the stepsize $h = 8.3 \times 10^{-4}$, so the Nyquist frequency $k_{Nyq} = 3770$ corresponding to $\theta = kh = \pi$ is very large.

Here

$$I_s = \int_{-\pi}^{\pi} J(U,v) se_n^2(v,q) dv \leq x_{max}^2 \pi, \tag{A.40}$$

$$I_c = \int_{-\pi}^{\pi} J(U,v) ce_n^2(v,q) dv \leq x_{max}^2 \pi, \tag{A.41}$$

J is the Jacobian of the coordinate transformation from elliptic to cylindrical coordinates (see Chapter 3), and σ^2 is the variance of the error in a given field value at each mesh point. The results (A.39) may be obtained in the same manner as those for the discrete-time Fourier transform already considered. We note that errors appearing in Fourier coefficients computed from interpolated surface data will satisfy (A.39) approximately out to a high-order mode n_{max} and k_{max}, beyond which the coefficients decay as $1/n^p$ (for fixed k) and $1/k^q$ (for fixed p) for some integers p, q.

Appendix B

Smooth Cubic Spline Interpolation

B.1 Spline Spaces

We now give a brief overview of general splines and their properties. Suppose that we are interested in approximating a function f on an interval $[a, b]$ by a piecewise polynomial ϕ. The use of splines allows one to enforce the continuity of some number of derivatives.

Definition 1. *[84] Given a knot sequence* $\mathbf{t} = \{t_i\}$ *with* $a = t_0 < ... < t_{m+1} = b$*, we define the spline space of order n by* $S_{\mathbf{t},n} = \{f \in C^{n-2}[a, b] : f|_{[t_i,t_{i+1}]} \in \pi_{n-1}, i = 0, ..., m\}$.

Here π_q denotes the space of polynomials of degree q. We see that each spline is a piecewise polynomial of degree $n - 1$, with joins occurring at the m internal knot locations $\{t_j : j = 1, ..., m\}$. We suppose here that no knots are repeated, $t_i \neq t_j$, $i \neq j$. In this case, $S_{\mathbf{t},n}$ is a linear space of dimension $\dim S_{\mathbf{t},n} = m + n$. We are particularly interested in the case when the knots are equidistant, $t_j = a + hj$, occurring at locations corresponding the sampled values of f.

Given a spline space $S_{\mathbf{t},n}$, we may also construct the space $\hat{S}_{\mathbf{t},n} = \{\mathcal{F}[\phi] : \phi \in S_{\mathbf{t},n}\}$, which is its image under the Fourier transform. The linear transformation $\mathcal{F} : S_{\mathbf{t},n} \to \hat{S}_{\mathbf{t},n}$ is onto and therefore provides an isomorphism between $S_{\mathbf{t},n}$ and $\hat{S}_{\mathbf{t},n}$. Properties of this space will be explored in the following section.

B.1.1 B-Spline Basis

We consider first a useful basis for the above spline space. Consider the normalized *B-splines* of order n [83],[84] given by

$$B_{\mathbf{t},n,j} = (t_{j+n} - t_j)[t_j, ..., t_{j+n}](t - x)_+^{n-1}, \tag{B.1}$$

where $x_+^{n-1} = (\max\{0, x\})^{n-1}$ and $[t_j, t_{j+1}, ..., t_{j+n}]f$ denotes the n-th divided difference for the function f in the points $\{t_i\}_{i=j}^{j+n}$.

It can be shown that the set $\mathcal{B} = \{B_{\mathbf{t},n,-n+1}(x), ..., B_{\mathbf{t},n,m}(x)\}$ forms a basis for the space $S_{\mathbf{t},n}$ of polynomial splines of degree $n-1$. The B-splines have a number of interesting properties [84]:

1. $\operatorname{supp} B_{\mathbf{t},n,i} = [t_i, t_{i+n}]$,
2. $B_{\mathbf{t},n,i} > 0$ for $x \in [t_i, t_{i+n}]$,
3. $\sum_{i=-\infty}^{\infty} B_{\mathbf{t},n,i}(x) = 1$ for all x,
4. $\int_{-\infty}^{\infty} B_{\mathbf{t},n,i}(x)dx = (t_{i+n} - t_i)/n$.

Of primary interest is the fact that the B-splines have minimal support. That is, if $s \in S_{\mathbf{t},n}$ and $\operatorname{supp} s \subset \operatorname{supp} B_{\mathbf{t},n,i}$, then $s = 0$. In the special case of equidistant knots $\{t_i\}$, all B-splines of a fixed order are related by translation and we have

$$B_{\mathbf{t},n,j}(t) = B_{\mathbf{t},n}(t - t_j) \text{ where} \tag{B.2}$$

$$B_{\mathbf{t},n}(t) = (t_n - t_0)\sum_{i=0}^{n} \omega_{i,n}(t - t_i)_+^{n-1} \text{ and} \tag{B.3}$$

$$\omega_{i,n} = \prod_{j=0, j\neq i}^{n} \frac{1}{t_j - t_i}. \tag{B.4}$$

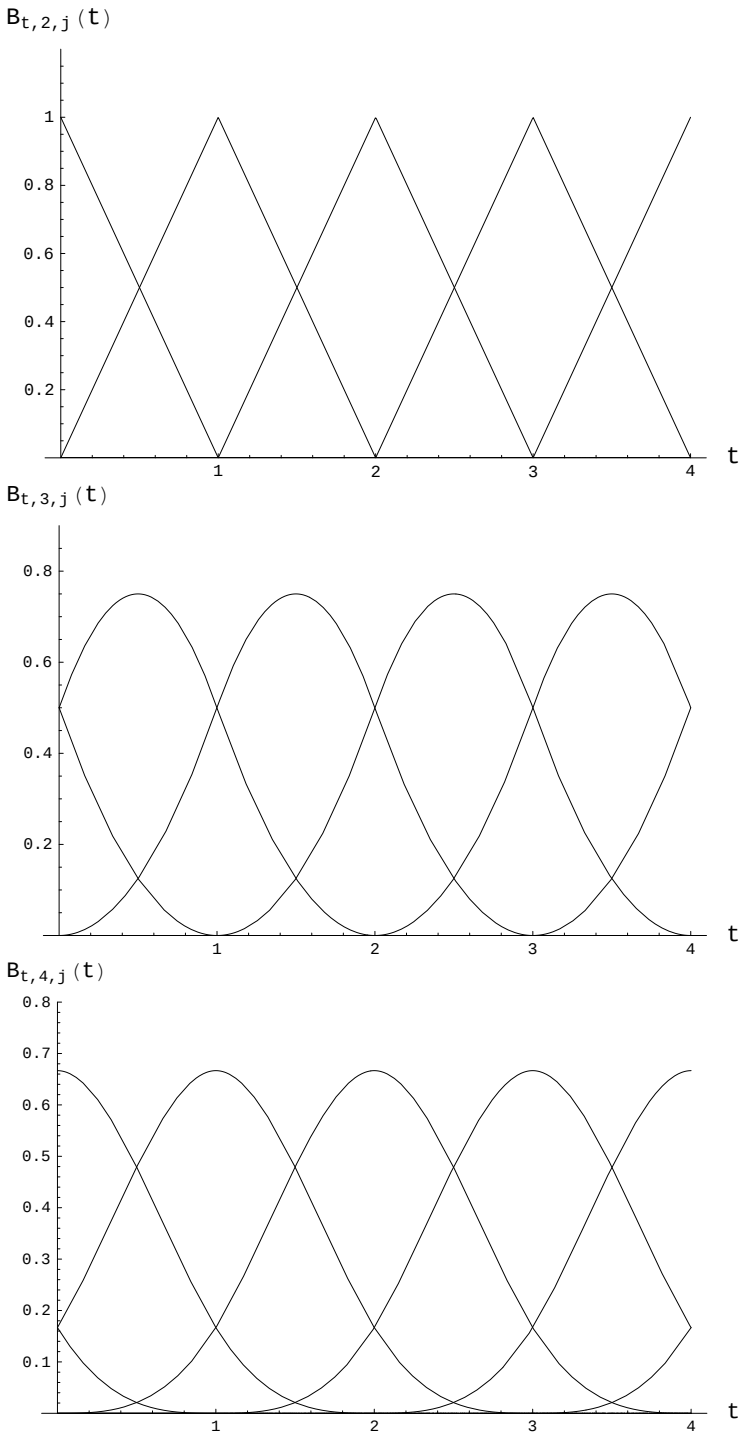

Figure B.1: Illustration of the B-splines $B_{\mathbf{t},n,j}$ of (B.1) which form a basis for the space of splines $S_{\mathbf{t},n}$ with knots at $t = 0, 1, 2, 3, 4$. (Upper) Linear B-splines with $n = 2$. (Middle) Quadratic B-splines with $n = 3$. (Lower) Cubic B-splines with $n = 4$.

In Fig. B.1 we have illustrated linear ($n = 2$), quadratic ($n = 3$), and cubic ($n = 4$) B-splines on the interval $[0, 4]$. In each case, these splines form a basis for $n + 3$ dimensional space $S_{\mathbf{t},n}$ of all polynomial splines with joins at $t_j = t_0 + hj$ for $j = 1, \ldots, 4$, with $t_0 = 0$, $h = 1$. It follows that any spline ϕ has a unique representation

$$\phi(x) = \sum_{j=-n+1}^{m} c_j B_{\mathbf{t},n,j}(x). \tag{B.5}$$

We now investigate the image Fourier space $\hat{S}_{\mathbf{t},n}$. Note that [86]

$$\int_{-\infty}^{\infty} B_{\mathbf{t},n,0}(x) e^{ikx} dx = \frac{n!}{(ik)^n} \sum_{j=0}^{n} e^{it_j k} / \bar{\omega}_n'(t_j) \text{ where} \tag{B.6}$$

$$\bar{\omega}_n(t) = \prod_{i=0}^{n} (t - t_i). \tag{B.7}$$

In the case of equidistant knots this becomes simply

$$\int_{-\infty}^{\infty} B_{\mathbf{t},n,j}(x) e^{ikx} dx = e^{ikt_j} \left(\frac{e^{ihk} - 1}{ihk} \right)^n. \tag{B.8}$$

We therefore have a basis for the space $\hat{S}_{\mathbf{t},n}$, and we note that successive basis spectra differ only by a phase e^{ikh}. In particular, the Fourier transform of $\phi \in S_{\mathbf{t},n}$ represented by the coefficients c_j is given by

$$\mathcal{F}[\phi](k) = \left(\frac{e^{ihk} - 1}{ihk} \right)^n \frac{1}{\sqrt{2\pi}} \sum_{j=-n+1}^{m} c_j e^{ikt_j}. \tag{B.9}$$

Note that the approximation $\phi \in S_{\mathbf{t},n}$ is of class $C^{n-2}(\mathbb{R})$, extends outside the interval $[a, b]$, and has support on the interval $[a - h(n-1), b + h(n-1)]$. As a consequence, the spectrum falls off as $1/k^n$. We discuss later the effect of truncating the Fourier integral over the interval $[a, b]$.

B.1.2 Global Basis

While the above basis has many elegant properties, in practice we are interested in computing the spectrum directly from the sampled values $\{f_i\}$ rather than the B-spline coefficients $\{c_i\}$. We construct a basis that illustrates clearly the relative weight of each sampled value.

Suppose we wish to select a unique spline from the space $S_{\mathbf{t},n}$ to represent a sampled function f. We may have available the values of f and/or some number of its derivatives at the sampling points. Suppose that these values, which we denote $\mathbf{f} = (f_i, f_i^{(p)})$ are sufficient to determine ϕ uniquely. Since the restriction ϕ_k of ϕ to the subinterval $[t_k, t_{k+1}]$ is a polynomial of degree $n-1$, we may write

$$\phi_k(x) = \sum_{j=0}^{n-1} \alpha_{jk} x^j \tag{B.10}$$

for every $k = 0, 1, ..., m$, where the $\alpha_{jk} \in \mathbb{R}$ are $n(m+1)$ unknowns to be determined. The system to be solved consists of the following $n(m+1)$ equations. We have $m+2$ equations of the form

$$\phi_k(x_k) = \sum_{j=0}^{n-1} \alpha_{jk} x_k^j = f_k, \text{ for } k = 0, ..., m, \tag{B.11}$$

$$\phi_m(x_{m+1}) = \sum_{j=0}^{n-1} \alpha_{jk} x_{m+1}^j = f_{m+1}, \tag{B.12}$$

which require that the spline pass through the sampled values. In addition, we have one set of m equations for each of the $n-1$ degrees of continuity $p = 0, ..., n-2$ at the internal knots,

$$\phi_k^{(p)}(x_k) - \phi_{k-1}^{(p)}(x_k) = \sum_{j=p}^{n-1} (\alpha_{jk} - \alpha_{j,k-1}) \frac{j!}{(j-p)!} x_k^{j-p} = 0, \tag{B.13}$$

where here $k = 1, ..., m$. Finally, we impose $n-2$ conditions on the derivatives of ϕ:

$$\phi^{(p)}(x_k) = \sum_{j=p}^{n-1} \alpha_{jk} \frac{j!}{(j-p)!} x_k^{j-p} = f_k^{(p)} \tag{B.14}$$

for some choice of k and $p < n-2$. It is typical to choose $k = 0, m+1$, such that the conditions (B.14) represent boundary conditions on various derivatives of ϕ. This is then a linear system for the α_{jk}'s, and we see that ϕ is uniquely determined if and only if this system is invertible. In general this can be achieved through the appropriate choice of the final $n-2$ endpoint conditions on the derivative.

It follows that, for each $x \in [a, b]$, the value of $\phi(x)$ is a linear functional, which we denote ϕ_x, of the values $\mathbf{f} = (f_i, f_i^{(p)})$ such that $\phi_x[\mathbf{f}] = \phi(x)$. That is,

$$\phi_x[\alpha \mathbf{f} + \mathbf{g}] = \alpha \phi_x[\mathbf{f}] + \phi_x[\mathbf{g}]. \tag{B.15}$$

Therefore we may write

$$\phi(x) = \phi_x[\mathbf{f}] = \sum_p \alpha_p(x) f_0^{(p)} + \sum_p \beta_p(x) f_{m+1}^{(p)} + \sum_{i=0}^{m+1} \gamma_i(x) f_i, \tag{B.16}$$

where the functions $\{\alpha_p, \beta_p, \gamma_i\}$ form a new basis for the space $S_{\mathbf{t},n}$.

We are interested primarily in the space of cubic splines $S_{\mathbf{t},4}$. To construct the basis functions, we require two endpoint conditions of the form (B.14). For the present work, we will choose the conditions $\phi'(a) = f'(a)$ and $\phi'(b) = f'(b)$. Consider a single interval $[t_{k-1}, t_k]$ and suppose that the endpoint derivatives s'_{k-1}, s'_k are known. The cubic polynomial on $[x_{k-1}, x_k]$ is given by the Hermite interpolation formula [10]

$$\begin{aligned} \phi_{k-1}(x) = {} & s'_{k-1} \frac{(x_k - x)^2 (x - x_{k-1})}{h_k^2} - s'_k \frac{(x - x_{k-1})^2 (x_k - x)}{h_k^2} \\ & + f_{k-1} \frac{(x_k - x)^2 [2(x - x_{k-1}) + h_k]}{h_k^3} + f_k \frac{(x - x_{k-1})^2 [2(x_k - x) + h_k]}{h_k^3} \end{aligned} \tag{B.17}$$

where $h_k = x_k - x_{k-1}$. A similar expression may be written if the derivatives s''_{k-1}, s''_k are known. Imposing the continuity conditions (B.13) gives us the spline equations [10]

$$s'_{k+1} + 4s'_k + s'_{k-1} = \frac{6}{h}\mu\delta f_k, \text{ or equivalently} \tag{B.18}$$

$$s''_{k+1} + 4s''_k + s''_{k+1} = \frac{6}{h^2}\delta^2 f_k, \tag{B.19}$$

where δf_k, $\delta^2 f_k$ are divided differences. Together with the endpoint conditions, this provides a band diagonal system for the derivatives s'_k, sufficient to specify ϕ uniquely. Solving $(B.18)$ for the s'_k and constructing ϕ from (B.17) provides us with the basis functions $\{\alpha, \beta, \gamma_i\}$, such that

$$\phi(x) = \alpha(x)f'_0 + \beta(x)f'_{m+1} + \sum_{i=0}^{m+1} \gamma_i(x) f_i. \tag{B.20}$$

By definition the basis function $\gamma_i(x)$ attains its peak value $\gamma_i(x_i) = 1$ at the sample point x_i, and vanishes for all $x = x_j$, $j \neq i$. The basis function α has derivative $\alpha'(x_0) = 1$ at the left endpoint and passes through zero at every knot. Similarly, β has derivative $\beta'(x_{m+1}) = 1$ at the right endpoint and passes through zero at every knot. Plots of the cubic basis functions for the case $m = 1022$ are provided in Fig. B.2. These were obtained numerically using the routines "spline" and "splint" described in [91]. By setting only the value $f_i = 1$ with $f_j = 0$ for all $j \neq i$ and $f'_0 = f'_{m+1} = 0$, we compute the resulting interpolating spline γ_i. Similarly, we may compute α by setting $f'_0 = 1$ and $f_j = 0$ for all j.

The basis functions α, β, and γ_i illustrate the effect of changing a single sample value on the cubic spline interpolant. Expressions may be determined for the basis

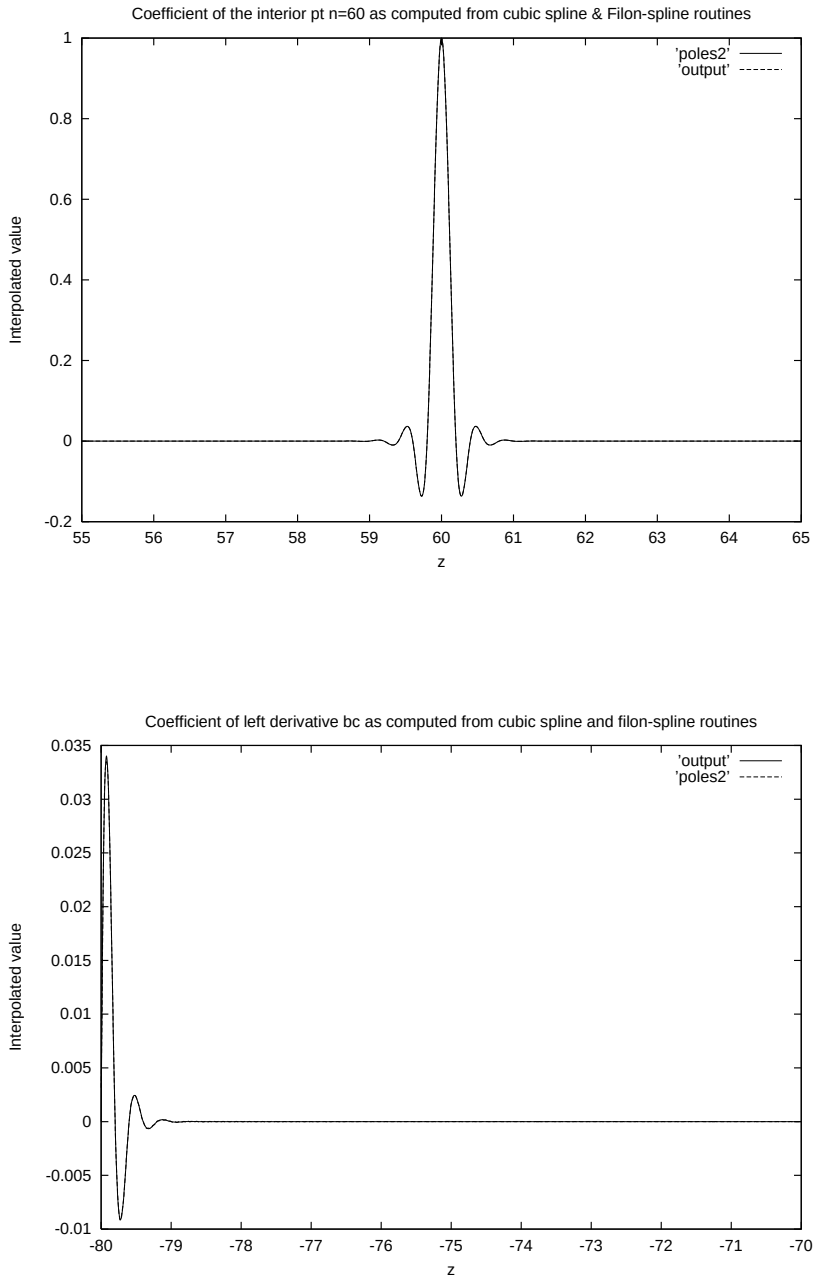

Figure B.2: Illustration of the global spline basis functions α (lower) and γ_i (upper) of (B.20) which lie in the basis for the space of cubic splines $S_{\mathbf{t},4}$ with 1024 knots uniformly distributed on $[-80, 80]$. Here γ_i corresponds to the point $z = 60$.

functions in terms of the stepsize h, the number of sampled values (knots) $m+2$, and the desired interval $[x_{k-1}, x_k]$. Consider the function γ_i. A number of oscillations is required such that the function passes through the value zero at every sample point except at x_i. As we consider intervals farther from the point x_i, we see that these oscillations are damped such that [10]

$$\gamma_i(x) \sim \exp(-|k-i|d), \tag{B.21}$$

where

$$d = \log(2+\sqrt{3}). \tag{B.22}$$

Similar behavior occurs in α and β as we move away from the left and right endpoints, respectively.

The Fourier transform of the spline approximant ϕ is then given by

$$\mathcal{F}[\phi](k) = \hat{\alpha}(k)f'_0 + \hat{\beta}(k)f'_{m+1} + \sum_{i=0}^{m+1} \hat{\gamma}_i(k)f_i, \tag{B.23}$$

where $\hat{\alpha}$, $\hat{\beta}$, and $\hat{\gamma}_i$ are the Fourier transforms of the basis functions above. The function $\hat{\gamma}_i$ is illustrated in Fig. B.3. These functions play a central role in the Filon-spline routine to be discussed in Appendix C.

B.1.3 Change of Basis

To understand the relationship between these bases, consider the conditions (B.11)-(B.14) applied to the B-spline representation of ϕ. By construction, the

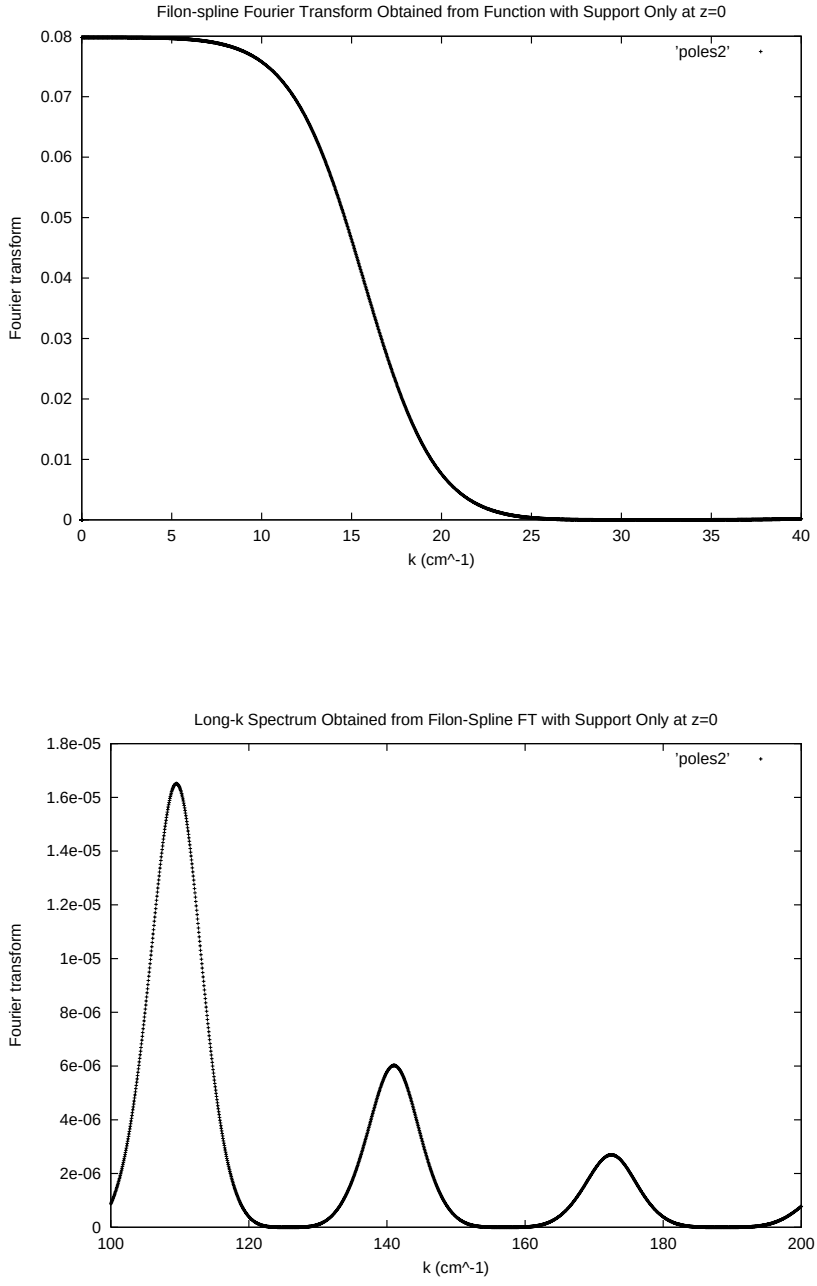

Figure B.3: Fourier transform of the global spline basis function γ_i corresponding to the point $z = 0$. Only the real part is shown here; the imaginary part vanishes. (Upper) Fourier transform over the range $k \in [0, 40]$. (Lower) Large-k tail of the Fourier transform.

continuity conditions are satisfied and we obtain

$$\phi(x_j) = \sum_{i=-n+1}^{m} c_i B_{\mathbf{t},4,i}(x_j) = f_j, \tag{B.24}$$

$$\phi'(x_0) = \sum_{i=-n+1}^{m} c_i B'_{\mathbf{t},4,i}(x_0) = f'_0, \tag{B.25}$$

$$\phi'(x_{m+1}) = \sum_{i=-n+1}^{m} c_i B'_{\mathbf{t},4,i}(x_{m+1}) = f'_{m+1}. \tag{B.26}$$

For simplicity, let B_i denote the B-spline $B_{\mathbf{t},4,i}$. If we order the elements in the global basis as $(\alpha, \gamma_0, ..., \gamma_{m+1}, \beta)$, then the matrix M representing the change of basis $M\mathbf{c} = \mathbf{f}$ is

$$[M]_{ij} = B_i(x_j) \text{ for j=0,...,m+1,} \tag{B.27}$$

$$[M]_{i,-1} = B'_i(x_0), \tag{B.28}$$

$$[M]_{i,m+2} = B'_i(x_{m+1}). \tag{B.29}$$

The fact that the B-splines B_i have support only on $[t_i, t_{i+n}]$ now implies that M is band diagonal. For example,

$$M_i(x_j) = \delta_{j,i+1} M_i(x_{i+1}) + \delta_{j,i+2} M_i(x_{i+2}) + \delta_{j,i+3} M_i(x_{i+3}). \tag{B.30}$$

For cubic splines with uniform sample spacing, M takes the especially simple, sparse form

$$\begin{pmatrix} -c & 0 & c & & & & \\ b & a & b & & & & \\ & b & a & b & & & \\ & & b & a & b & & \\ & & & * & * & * & \\ & & & & b & a & b \\ & & & & -c & 0 & c \end{pmatrix}$$

where $a = M_0(x_2) = 4b$, $b = M_0(x_1) = M_0(x_2)$, and $c = M'_0(x_1) = -M'_0(x_3)$. In particular, it follows that M is invertible. Such inversion is efficient to implement numerically [83].

Appendix C

Fast and Accurate Fourier Transform Algorithms

C.1 Overview of Fourier Transform Algorithms

A large literature exists on algorithms available for the integration of rapidly oscillatory functions. A particularly useful survey can be found in [77]. As introduction, we briefly discuss four classes of Fourier transform algorithms.

Discrete Fourier Transform - Consider a continuous function g on $\mathbb{R}$ whose values g_j are known at a set of sampling points x_j: $g_j = g(x_j)$ for $x_j = jh$, $j \in \mathbb{Z}$. The truncated discrete-time Fourier transform (DTFT) of the values $\{g_j\}$ is given by [90]

$$DTFT\{g_j\}(k) = h \sum_{j=-N}^{N} g_j e^{-ikhj}, \tag{C.1}$$

where we have included the factor h so that

$$DTFT\{g_j\} \to \sqrt{2\pi}\mathcal{F}[g] \tag{C.2}$$

in the limit $h \to 0$ and $N \to \infty$, provided the Fourier integral $\mathcal{F}[g]$ of the function g converges. The DTFT therefore approximates the Fourier transform of g by a Riemann sum. To see the effect of this approximation, we may relate (C.1) to the continuous Fourier transform as follows.

The DTFT differs from the true Fourier transform due to the effects sampling g only at the set of values $x_j = jh$ and truncating the Fourier integral over some finite

interval $[-L, L]$. To examine these effects, define the sampling function (actually a tempered distribution),

$$\Delta(x) = \sum_{j=-\infty}^{\infty} h\delta(x - jh), \tag{C.3}$$

whose Fourier transform exists (in the sense of distributions) and is given by [90]

$$\mathcal{F}[\Delta](k) = \sqrt{2\pi} \sum_{j=-\infty}^{\infty} \delta\left(k - \frac{2\pi j}{h}\right). \tag{C.4}$$

We also consider the window function χ and its Fourier transform, given by the pair

$$\chi(x) = \begin{cases} 1 & \text{if } -L < x < L \\ 0 & \text{otherwise} \end{cases} \leftrightarrow \frac{2L}{\sqrt{2\pi}} \operatorname{sinc}(kL). \tag{C.5}$$

Here we have defined the function sinc as

$$\operatorname{sinc}(x) = \frac{\sin x}{x}. \tag{C.6}$$

Now the effects of sampling and truncation can be understood as resulting from the convolution of the true Fourier transform $\mathcal{F}[g]$ with the Fourier transforms of Δ and χ. To see that this is the case, note that in the time domain

$$\begin{aligned} g(x)\Delta(x)\chi(x) = g(x)\chi(x) \sum_{j=-\infty}^{\infty} h\delta(x - jh) &= \chi(x) \sum_{j=-\infty}^{\infty} g(x_j)h\delta(x - jh) \\ &= h \sum_{j=-N}^{N} g_j\delta(x - jh), \end{aligned} \tag{C.7}$$

where N is the largest integer such that $hN \leq L$. Then we have

$$\begin{aligned} \mathcal{F}[g] \star \mathcal{F}[\Delta] \star \mathcal{F}[\chi] = \mathcal{F}[g\Delta\chi] &= \frac{1}{\sqrt{2\pi}} \int_{-\infty}^{\infty} h \sum_{j=-N}^{N} g_j\delta(x - jh)e^{ikx}dx \\ &= \frac{h}{\sqrt{2\pi}} \sum_{j=-N}^{N} g_j e^{ikx_j} = \frac{1}{\sqrt{2\pi}} DTFT\{g_j\}. \end{aligned} \tag{C.8}$$

Thus, the DTFT approximation generates the exact Fourier transform of the function (C.7), treating the function g as a sequence of delta-function peaks. The effect of convolution with the sampling function (C.4) has been to introduce aliasing of high frequencies; the spectrum becomes periodic with period $2\pi/h$. The effect of convolution with the window function is to introduce spectral spreading and leakage, resulting from the width and side-lobe characteristics of the sinc function (C.5). A primary goal of signal analysis [90] is to minimize these effects by using well-behaved interpolating functions and choosing alternative forms of the window function χ.

Truncated series of orthogonal polynomials - Another approach is to approximate the function g as a truncated series of orthogonal polynomials over the interval of interest, using the sampled values g_j. This leads to a single polynomial of high degree, whose Fourier transform may be computed exactly. The use of Legendre and Chebyshev polynomials is explored in [80],[81]. These techniques have the advantage that the interpolating function is smooth; derivatives exist to all orders. As a result, the aliasing problem is minimized due to the attenuation of high frequencies. However, the derivatives computed using a single polynomial fit are poorly approximated, and the polynomial need not converge to g as the stepsize goes to zero [70].

Integration between zeros - In this technique [77], the zeros of the oscillatory part of the integrand are located, $a \leq x_1 < x_2 < ... < x_p \leq b$ and each subintegral is evaluated by a standard (Gaussian quadrature-type) integration rule. This requires that samples of g be available between zeros of $\sin(kx)$ and $\cos(kx)$, which fails for frequencies near or above the sampling frequency. The number of sampled values

required is often unavailable.

Piecewise approximation by low degree polynomials on the integration interval. - In this technique, the function g is approximated by piecewise polynomials, and the Fourier integral over each subinterval is evaluated exactly. These techniques include Filon's rule [78], the Filon-trapezoidal rule [82], the Filon-spline rule [79], and an extension to higher degree by Marsden and Taylor [82]. We are particularly interested in the case when the interpolating function is a polynomial spline, which allows one to bound the error appearing in some number of derivatives. Information about these derivatives is therefore reflected accurately in the appropriate part of the spectrum, and the first few derivatives may be reconstructed accurately from the computed spectrum. In addition, the effect of aliasing is minimized due to the attenuation of high frequency values of the spectrum.

C.2 Statement of the Problem

Let $g : \mathbb{R} \to \mathbf{C}$ be a function whose values are known at a set of equidistant sampling points $t_j = jh$, $j \in \mathbf{Z}$. If g is provided on a set of sample points that does not include 0, but values are available at some $t_j + a$ with $a \in \mathbb{R}$, we consider instead the function g^a defined by $g^a(t) = g(t-a)$. We write the samples as $\{g_i : i = 1, ..., N\}$ with $g_j = g(t_j)$ for $t_j = jh$, $j \in \mathbf{Z}$. We are in general interested in computing

$$\hat{g}(k) = \mathcal{F}[g](k) = \int_{-\infty}^{\infty} g(t)e^{ikt}dt, \tag{C.9}$$

where we drop the factor $\sqrt{2\pi}$ here for convenience. In particular, we are interested in the finite sine and cosine integrals

$$\int_a^b g(x)\cos(kx)dx \text{ and} \tag{C.10}$$

$$\int_a^b g(x)\sin(kx)dx. \tag{C.11}$$

These are the real and imaginary parts, respectively, of the finite Fourier integral $\mathcal{F}_B[g](k) = \int_a^b g(x)e^{ikx}dx$. Note that the Fourier transform and the finite Fourier integral are related by $\mathcal{F}_B(f) = \mathcal{F}(f\chi_B) = \mathcal{F}(f) * \mathcal{F}(\chi_B)$, where χ_B is the characteristic function of the interval $B = [a, b]$. The results below will apply in the finite case provided that we choose $g_i = 0$ for all i such that t_i lies outside the interval $[a, b]$.

In general, the information provided by the sample values $\{g_i\}$ alone is insufficient to determine the above integrals uniquely. To see how much information is lost by sampling, we construct the set Ω of all possible spectra of g as follows. (We follow a remark of [87].) Given a function $\hat{s} : \mathbb{R} \to \mathbf{C}$ in $L_1(\mathbb{R})$, we define a corresponding "aliased" function $\hat{s}_A$ on the interval $B = [-\frac{\pi}{h}, \frac{\pi}{h}]$ by

$$\hat{s}_A(k) = \sum_{n=-\infty}^{\infty} \hat{s}\left(k + \frac{2\pi}{n}\right)\Bigg|_B, \tag{C.12}$$

where the sum converges to an element in $L_1(B)$. Given two functions $\hat{s}$ and $\hat{q}$ in $L_1(\mathbb{R})$, we say that $\hat{s}$ is equivalent to $\hat{q}$ if and only if $\hat{s}_A(k) = \hat{q}_A(k)$ for all $k \in B$.

Aliasing Theorem 1. *Let $\hat{s}$ be any function in $L_1(\mathbb{R})$ satisfying*

$$g_n = \mathcal{F}^{-1}[\hat{s}](t_n) = \frac{1}{2\pi}\int_{-\infty}^{\infty} e^{ikt_j}\hat{s}(k)dk \tag{C.13}$$

for all n. Let $[\hat{s}]$ be the equivalence class containing $\hat{s}$. Then the set Ω of absolutely integrable spectra whose inverse Fourier transforms attain the values g_n at the sample points t_n is given by $\Omega = [\hat{s}]$.

Lemma 1. *Given any frequency $k \in \mathbb{R}$ we may write*

$$e^{ikt_n} = e^{iknh} = e^{i(k+2\pi m/h)nh} = e^{ik_A t_n} \tag{C.14}$$

for all t_n where $k_A = k + 2\pi m/h$. We may choose the unique value of k_A satisfying $-\frac{\pi}{h} \leq k_A \leq \frac{\pi}{h}$, by an appropriate choice of $m \in \mathbf{Z}$. We refer to k_A as the principal alias of k. Similarly we refer to $k_c = \frac{\pi}{h}$ as the Nyquist frequency, and $B = [-k_c, k_c]$ as the Nyquist band. Thus, for all $k \in \mathbb{R}$ there exists a unique $k_A \in B$.

Proof of Aliasing Theorem. Let $\hat{q} \in [\hat{s}]$. Then we know that $\hat{q}_A(k) = \hat{s}_A(k)$ for all $k \in B$, so that

$$\int_B e^{ikt} \hat{q}_A(k) dk = \int_B e^{ikt} \hat{s}_A(k) dk \tag{C.15}$$

for all t. Now for all t_j,

$$\begin{aligned}
\int_B e^{ikt_j} \hat{q}_A(k) dk &= \sum_{n=-\infty}^{\infty} \int_{-k_c}^{k_c} e^{ik_A t_j} \hat{q}(k + 2\pi n/h) dk \\
&= \sum_{n=-\infty}^{\infty} \int_{-k_c}^{k_c} e^{i(k+2\pi n/h)t_j} \hat{q}(k + 2\pi n/h) dk \\
&= \sum_{n=-\infty}^{\infty} \int_{-k_c}^{k_c} e^{i(k+2nk_c)t_j} \hat{q}(k + 2nk_c) dk \\
&= \sum_{n=-\infty}^{\infty} \int_{-k_c+2nk_c}^{k_c+2nk_c} e^{ikt_j} \hat{q}(k) dk = \int_{-\infty}^{\infty} e^{ikt_j} \hat{q}(k) dk.
\end{aligned} \tag{C.16}$$

An identical argument shows that

$$\int_B e^{ikt_j} \hat{s}_A(k) dk = \int_{-\infty}^{\infty} e^{ikt_j} \hat{s}(k) dk. \tag{C.17}$$

Therefore,

$$\begin{aligned}\mathcal{F}^{-1}[\hat{q}](t_j) &= \frac{1}{2\pi}\int_{-\infty}^{\infty} e^{ikt_j}\hat{q}(k)dk = \frac{1}{2\pi}\int_B e^{ikt_j}\hat{q}_A(k)dk \\ &= \frac{1}{2\pi}\int_B e^{ikt_j}\hat{s}_A(k) = \frac{1}{2\pi}\int_{-\infty}^{\infty} e^{ikt_j}\hat{s}(k)dk = g(t_j), \qquad \text{(C.18)}\end{aligned}$$

so $\hat{q}$ is a possible spectrum of g and $\hat{q} \in \Omega$. Now given $\hat{p} \in \Omega$, we show $\hat{p} \in [\hat{s}]$. Note that

$$g(t_j) = \frac{1}{2\pi}\int_{-\infty}^{\infty} e^{ikt_j}\hat{p}(k)dk = \frac{1}{2\pi}\int_B e^{ikt_j}\hat{p}_A(k)dk \quad \text{and} \qquad \text{(C.19)}$$

$$g(t_j) = \frac{1}{2\pi}\int_{-\infty}^{\infty} e^{ikt_j}\hat{s}(k)dk = \frac{1}{2\pi}\int_B e^{ikt_j}\hat{s}_A(k)dk, \qquad \text{(C.20)}$$

so that

$$\int_B e^{ikt_j}\hat{p}_A(k)dk = \int_B e^{ikt_j}\hat{s}_A(k)dk \qquad \text{(C.21)}$$

for all t_j. It remains to show that $\hat{p}_A(k) = \hat{s}_A(k)$ for all $k \in B$. Define $\theta = kh$ so

$$g(t_n) = \int_{-\pi/h}^{\pi/h} e^{ikt_n}\hat{p}_A(k)dk = \frac{1}{h}\int_{-\pi}^{\pi} e^{i\theta t_n/h}\hat{p}_A(\theta/h)d\theta \quad = \frac{1}{h}\int_{-\pi}^{\pi} e^{in\theta}\hat{p}_A(\theta/h)d\theta. \qquad \text{(C.22)}$$

By construction, the aliased function $\hat{p}_A$ is periodic in k with a period of $2\pi/h$. It follows that $\hat{p}_A(\theta/h)$ is periodic in θ with a period of 2π, and may be written as a Fourier series in θ. From the above result, we see that the values g_n are the corresponding Fourier coefficients, and

$$\hat{p}_A(\theta/h) = h\sum_{n=-\infty}^{\infty} e^{-in\theta}g_n \qquad \text{(C.23)}$$

so that

$$\hat{p}_A(k) = h\sum_{n=-\infty}^{\infty} e^{-ikt_n}g_n, \qquad \text{(C.24)}$$

which is the DTFT of g. Therefore $\hat{p}_A(k) = DTFT\{g_n\}(k)$. Similarly, $\hat{s}_A(k) = DTFT\{g_n\}(k) = \hat{p}_A(k)$ and $\hat{p} \in [\hat{s}]$, as desired. Thus we've shown that $\Omega = [\hat{s}]$, where we may take $\hat{s}$ to be the restriction of the DTFT to the Nyquist band, $\hat{s} = DTFT\{g_n\} \mid_B$. □

Sampling Theorem 1. *Suppose the spectrum of g is bandlimited. That is, suppose that the support of $\hat{g}$ is contained in the Nyquist band B corresponding to the samples $\{g_i : i = 1, ..., n\}$. Then the spectrum of g is uniquely determined by these samples.*

Proof. Let $\hat{q} \in \Omega$ be some potential spectrum of g, and suppose that $\hat{q}$ is bandlimited to B. Then $\hat{q}(k) = 0$ for $k < -k_c$ or $k > k_c$ so

$$\hat{q}(k) = \sum_{-\infty}^{\infty} \hat{q}(k + 2nk_c) = \hat{q}_A(k) = \hat{s}_A(k) = \hat{s}(k) = DTFT\{g_n\} \tag{C.25}$$

for all $k \in B$. Thus $\hat{q} = \hat{s}$ and Ω contains only one bandlimited element. Therefore the spectrum of g is uniquely determined. In addition, g itself is uniquely determined from its samples, and it can be shown that $g(t) = \sum_{-\infty}^{\infty} g(t_n) \operatorname{sinc}(k_c t - n\pi)$. □

Note that the construction of Ω assumes no information about the sampled function g, other than its values at a set of equidistant sampling points. As shown in the introduction, the discrete Fourier transform assumes that g is a distribution consisting of delta-function peaks at the sampled points $\{x_i\}$. In many cases, however, additional information about the function g is available. Our goal is to select from Ω a representative that 1) is consistent with all available information about the function g, and 2) can be implemented in a reasonable algorithm. One piece of information that is commonly available is the continuity class of g. We note that

the continuity class of g is reflected in the asymptotic behavior of its spectrum. In particular, the spectrum of any smooth function $f \in C^\infty$ falls off faster than any power of k.

Theorem 1. *[77] Let $g \in C^n[a,b]$. Then, using integration by parts,*

$$I(s) = \int_a^b e^{isx} g(x)dx = e^{isb} \sum_{k=0}^{n-1} i^{k-1} g^{(k)}(b) s^{-k-1} - e^{isa} \sum_{k=0}^{n-1} i^{k-1} g^{(k)}(a) s^{-k-1}$$
$$+ (-is)^{-n} \int_a^b e^{isx} g^{(n)}(x)dx. \tag{C.26}$$

Corollary 1. *[77] Let $g \in C^n[a,b]$, and suppose that $g^{(k)} \to 0$ as $|x| \to \infty$ for each $k = 0, 1, ..., n-1$. Suppose also that $\int_a^b |g^{(n)}(x)|dx < \infty$. Then*

$$I(s) = \int_{-\infty}^{\infty} e^{isx} g(x)dx = (-is)^{-n} \int_{-\infty}^{\infty} e^{isx} g^{(n)}(x)dx. \tag{C.27}$$

Our objective is to construct a spectrum with tightly bound error for high frequencies that allows accurate extraction of derivatives. The solution is to approximate g by some ϕ with similar smoothness properties, and then take $\mathcal{F}[\phi]$ to approximate $\mathcal{F}[g]$. As a bonus, ensuring differentiability of the interpolant provides preliminary smoothing of noise present in the original sampled data. For this purpose, we consider polynomial splines in $S_{\mathbf{t},n}$ of degree $n-1$. These are discussed in Appendix B. Recall that $\hat{S}_{\mathbf{t},n}$ is the image of $S_{\mathbf{t},n}$ under the Fourier transform. For a given set of samples $\{g_i\}$, the approximate Fourier spectra we consider will then lie in the subspace $\Omega \cap \hat{S}_{\mathbf{t},n}$.

C.3 Properties of the Space of Approximated Spectra

Consider the set Ω of approximated spectra for a set of samples $\{g_i\}$ introduced in Section C.2. We note from the definition that Ω is a linear space if and only if $g_j = 0$ for all j. We are interested in the properties of this set, and in particular the space $\Omega \cap \hat{S}_{\mathbf{t},n}$. We will see that this is a translation of a linear space of dimension $n-2$. We consider here the cubic case $n = 4$.

Note that we may write the spline space as a direct sum $S_{\mathbf{t},n} = S_D \oplus S_I$, where the independent subspaces S_D and S_I are given by $S_D = \text{Span}\{\alpha, \beta\}$ and $S_I = \text{Span}\{\gamma_i\}_{i=0}^{m+1}$. This allows us to separate that part of the space due to the values at the sample points from that part due to the boundary conditions. Note that S_D contains all splines that vanish at the knots, and S_I contains all splines with boundary conditions of vanishing derivative at both ends. Similarly, we may decompose the image space $\hat{S}_{\mathbf{t},n} = \hat{S}_D \oplus \hat{S}_I$, where $\hat{S}_D = \mathcal{F}(S_D)$ and $\hat{S}_I = \mathcal{F}(S_I)$. Then each $\phi \in \hat{S}_{\mathbf{t},n}$ can be written uniquely as $\phi = \phi_I + \phi_D$, where $\phi_I \in \hat{S}_I$ and $\phi_D \in \hat{S}_D$. We show the following.

Theorem 1. *There exists a unique $v \in \hat{S}_I$ such that $\Omega \cap \hat{S}_I = \{v\}$. If $g_j = 0$ for all j, then $v = 0$.*

Proof. We construct the element v. Consider first those splines in S_I. By construction, the set $(\gamma_0, \gamma_1, ...\gamma_{m+1})$ forms an ordered basis for S_I. For a given spline f, the coordinates in this basis are the values $f_i = f(x_i)$. Let β be the unique spline in S_I given by the coordinates $\beta_i = g(x_i)$ defined by the sample values of g for $i = 0, ..., m+1$. Define $v = \mathcal{F}(\beta)$. Then $v \in \Omega$ since $\mathcal{F}^{-1}[v](x_i) = \beta(x_i) = g_i$ for all

i. Also, $v \in \hat{S}_I$ so $v \in \Omega \cap \hat{S}_I$. We now demonstrate uniqueness. Suppose also that $v' \in \Omega \cap \hat{S}_I$. We have $\mathcal{F}^{-1}(v') \in S_I$. Let $\beta' = \mathcal{F}^{-1}(v')$. Then β' has coordinates $\beta'_i = \beta'(x_i)$ for all i. Since $v' \in \Omega$, $g_i = \mathcal{F}^{-1}[v'](x_i) = \beta'(x_i) = \beta'_i$ for all i. Thus, $\beta' = \beta$ and $v' = \mathcal{F}(\beta') = \mathcal{F}(\beta) = v$. In the case that $g_j = 0$ for all j, we see that $\beta = 0$ is the unique spline in S_I with $\beta(x_j) = 0$ for all j, and $v = \mathcal{F}(\beta) = 0$. □

Theorem 1. *Suppose $\alpha \in \hat{S}_{\mathbf{t},n}$ with $\alpha = \alpha_D + \alpha_I$. Then $\alpha \in \Omega$ iff $\alpha_I \in \Omega$.*

Proof. Suppose $\alpha \in \hat{S}_{\mathbf{t},n}$ with $\alpha = \alpha_D + \alpha_I$. We first prove the forward implication. Suppose $\alpha \in \Omega$ and let $\beta = \mathcal{F}^{-1}(\alpha) \in S_{\mathbf{t},n}$. We write $\beta = \beta_I + \beta_D$, where $\beta_I \in S_I$ and $\beta_D \in S_D$. Since $\alpha \in \Omega$, $g_i = \mathcal{F}^{-1}[\alpha](x_i) = \beta(x_i)$ for all i. Since $\beta_D \in S_D$ we have that $\beta_D(x_i) = 0$ for all i. Therefore, $\beta(x_i) = (\beta_I + \beta_D)(x_i) = \beta_I(x_i) + \beta_D(x_i) = \beta_I(x_i) = g_i$ for all i. Thus it follows that $\mathcal{F}(\beta_I) = \alpha_I \in \Omega$. Conversely, suppose that $\alpha_I \in \Omega$. Define $\beta_I = \mathcal{F}^{-1}(\alpha_I)$ and $\beta_D = \mathcal{F}^{-1}(\alpha_D)$. Since $g_i = \mathcal{F}^{-1}[\alpha_I](x_i) = \beta_I(x_i) = \beta_I(x_i) + \beta_D(x_i) = \beta(x_i)$, we have that $\alpha = \mathcal{F}(\beta) \in \Omega$. □

Theorem 1. $\Omega \cap \hat{S}_{\mathbf{t},n} = \hat{S}_D + v = \{\alpha_D + v : \alpha_D \in \hat{S}_D\}$, *where v is the unique element in $\Omega \cap \hat{S}_I$.*

Proof. Let $\alpha \in \Omega \cap \hat{S}_{\mathbf{t},n}$. We write $\alpha = \alpha_I + \alpha_D$ where $\alpha_I \in \hat{S}_I$ and $\alpha_D \in \hat{S_D}$. By the previous result, $\alpha_I \in \Omega$. Therefore $\alpha_I \in \Omega \cap \hat{S}_I$ and it follows that $\alpha_I = v$. Thus, $\alpha \in \hat{S}_D + v$. Conversely, suppose $\alpha \in \hat{S}_D + v$, so $\alpha = \alpha_I + v$ for some $\alpha_I \in \hat{S}_I$. Clearly $\alpha \in \hat{S}_{\mathbf{t},n}$, and it follows from the previous result that $\alpha \in \Omega$. Thus we have shown that $\Omega \cap \hat{S}_{\mathbf{t},n} = \hat{S}_D + v$. □

In the special case that $g_i = 0$ for all i, we have $v = 0$ and $\Omega \cap \hat{S}_{\mathbf{t},n} = \hat{S}_D$, a linear space. We see that in general $\Omega \cap \hat{S}_{\mathbf{t},n} \in \hat{S}_{\mathbf{t},n}/\hat{S}_D$. The equivalence relation

on $\hat{S}_{\mathbf{t},n}$ defined by $\hat{S}_{\mathbf{t},n}/\hat{S}_D$ is exactly that appearing in the Aliasing Theorem, and v is the representative in $\hat{S}_{\mathbf{t},n}/\hat{S}_D$ corresponding to the values $\{g_i\}$.

C.4 Development of Filon-Spline Formulae

We now turn to the explicit formulae used in computing the finite sine and cosine integrals as promised in Section C.2. Beginning with the result of Section C.3.2, we see that this involves computing the finite sine and cosine integrals of the approximating spline basis functions. For comparison, we first present a simpler related result of approximation using piecewise-quadratic interpolation.

C.4.1 Filon's Formula

Filon's formula [78] is obtained by fitting a quadratic to each double interval $[x_{2j-2}, x_{2j}]$, where $j = 0, ..., n$, using the three available sample values at the knots x_{2j-2}, x_{2j-1}, and x_{2j}. The interpolating function is therefore continuous, but no attempt is made to enforce continuity of the derivatives at the points x_{2j}. The interpolating function is therefore not an element of the quadratic spline space $S_{\mathbf{t},3}$. Explicit integration of the finite Fourier transform gives the Filon formulae (see

[22]):

$$\int_a^b g(x)\cos(kx)dx = h[\alpha(\theta)(g_{2n}\sin(kx_{2n}) - g_0\sin(kx_0)) \tag{C.28a}$$

$$+ \beta(\theta)C_{2n} + \gamma(\theta)C_{2n-1}],$$

$$\int_a^b g(x)\sin(kx)dx = h[\alpha(\theta)(g_0\cos(kx_0) - g_{2n}\cos(kx_{2n})) \tag{C.28b}$$

$$+ \beta(\theta)S_{2n} + \gamma(\theta)S_{2n-1}],$$

where we use the notation $\theta = hk$. The first two terms on the right side of (C.28a) and the first two terms on the right side of (C.28b), known as endpoint terms, appear due to the fact that the function is nonvanishing at the endpoints of the integration interval. That is, the choice of a rectangular window for the Fourier transform ensures that the above integrals provide the Fourier transform of a function which is discontinuous at the two endpoints $x_0 = a$ and $x_{2n} = b$. These endpoint contributions therefore fall off as $1/\theta$.

The primary contribution is from the last two terms, consisting of even and odd discrete Fourier transforms given by

$$C_{2n} = \sum_{i=0}^{n} g_{2i}\cos(kx_{2i}) - \frac{1}{2}[g_{2n}\cos(kx_{2n}) + g_0\cos(kx_0)], \tag{C.29a}$$

$$S_{2n} = \sum_{i=0}^{n} g_{2i}\sin(kx_{2i}) - \frac{1}{2}[g_{2n}\sin(kx_{2n}) + g_0\sin(kx_0)], \tag{C.29b}$$

$$C_{2n-1} = \sum_{i=1}^{n} g_{2i-1}\cos(kx_{2i-1}), \tag{C.29c}$$

$$S_{2n-1} = \sum_{i=1}^{n} g_{2i-1}\sin(kx_{2i-1}). \tag{C.29d}$$

Note that each term is multiplied by an attenuation function α, β, or γ, where the

attenuation functions are given by:

$$\alpha(\theta) = \frac{1}{\theta} + \frac{\sin(2\theta)}{2\theta^2} - \frac{2\sin^2(\theta)}{\theta^3}, \tag{C.30a}$$

$$\beta(\theta) = 2\left(\frac{1+\cos^2(\theta)}{\theta^2} - \frac{\sin(2\theta)}{\theta^3}\right), \tag{C.30b}$$

$$\gamma(\theta) = 4\left(\frac{\sin(\theta)}{\theta^3} - \frac{\cos(\theta)}{\theta^2}\right). \tag{C.30c}$$

The function α given above determines the asymptotic behavior of the endpoint terms of (C.28), and therefore falls off as $1/\theta$. However, the attenuation functions β and γ given above ensure that the contributions of the discrete Fourier transforms C_m and S_m in (C.28) are not periodic, but fall off asymptotically as $1/\theta^2$. This is what we would expect due to the continuity of the interpolating function on the interval (a, b). Note the strong contrast with methods which use a Fast Fourier Transform, which produces a spectrum that is periodic in k (and therefore in θ), resulting in the associated aliasing [85].

C.4.2 Filon-spline Formula

To construct the Filon-spline formula, we choose from the space $S_{\mathbf{t},4}$ the unique cubic spline ϕ representing the function g, as given in (B.20), obtained by imposing the boundary conditions $\phi'(a) = g'(a)$ and $\phi'(b) = g'(b)$. The result may be written in terms of the basis functions $\hat{\alpha}$, $\hat{\beta}$, and $\hat{\gamma}$ for $i = 1, \ldots, m$ introduced in Appendix B. To determine explicit integration formulas, the spline difference equation (B.19) must be solved for the second derivative values of ϕ at the knot points x_j for $j = 0, \ldots, N$. In fact, only the values at the two endpoints are required, which we denote

$M_0 = \phi_0''$ and $M_N = \phi_N''$. Explicit evaluation gives (see [79]):

$$\int_a^b g(x)\cos(kx)dx = h\{(\alpha g_N - \beta h^2 M_N)\sin(kb) - (\alpha g_0 - \beta h^2 M_0)\sin(ka) + (\frac{\epsilon}{2}g_N + \delta h g_N')\cos(kb) + (\frac{\epsilon}{2}g_0 - \delta h g_0')\cos(ka) + \epsilon\sum_{i=1}^{N-1} g_i\cos(kx_i)\}, \tag{C.31a}$$

$$\int_a^b g(x)\sin(kx)dx = h\{-(\alpha g_N - \beta h^2 M_N)\cos(kb) + (\alpha g_0 - \beta h^2 M_0)\cos(ka) + (\frac{\epsilon}{2}g_N + \delta h g_N')\sin(kb) + (\frac{\epsilon}{2}g_0 - \delta h g_0')\sin(ka) + \epsilon\sum_{i=1}^{N-1} g_i\sin(kx_i)\}. \tag{C.31b}$$

Define $\kappa = 1 - \frac{2}{3}\sin^2\frac{\theta}{2}$. We have the attenuation functions:

$$\alpha = \frac{1}{\theta} - \frac{4\sin^2\frac{\theta}{2}}{\kappa\theta^4}\sin(\theta), \tag{C.32a}$$

$$\beta = \frac{1}{\theta^3} - \frac{\sin(\theta)}{\kappa(\theta^4)}, \tag{C.32b}$$

$$\delta = \frac{1}{\theta^2} - \frac{4\sin^2\frac{\theta}{2}}{\kappa\theta^4}, \tag{C.32c}$$

$$\epsilon = \frac{16\sin^4\frac{\theta}{2}}{\kappa\theta^4}. \tag{C.32d}$$

Note that the discrete-time Fourier transforms appearing in (C.31) are attenuated by the function ϵ, which decays as $1/\theta^4$ due to the continuity of the first two derivatives of the splines in $S_{\mathbf{t},4}$. We therefore expect greater suppression of aliasing in comparison with the result of Section C.4.1.

C.5 Discussion of Global Error Bounds

The asymptotic behavior of the spectra resulting from the use of the integration formulas (C.28,C.31) may be investigated as follows. As discussed previously,

the endpoint terms (those containing the attenuation factor α) result from discontinuities of the interpolating function at the endpoints, which occur due to truncating the Fourier integral over a finite interval. This idea may be extended also to higher-order derivatives. Let $\Delta s_j^{(d)}$ denote the value of a jump discontinuity in the dth derivative of the interpolating polynomial s at the sampling point x_j. In Filon's formula, for example, such discontinuities appear in the first derivative. The asymptotic behavior of the Filon spectrum may be seen in the expression:

$$\int_a^b s(x)e^{ikx}dx = \frac{i}{k}(s_0e^{ika} - s_ne^{ikb}) - \frac{1}{k^2}\sum_{j=0}^{n/2-1}\Delta s'_{2j}e^{ikx_{2j}} - \frac{i}{k^3}\sum_{j=0}^{n/2-1}\Delta s''_{2j}e^{ik_{2j}}, \quad \text{(C.33)}$$

where s is piecewise quadratic on the double intervals $[x_{2j-2}, x_{2j}]$, $j = 0, 1, \cdots, n/2$. Similarly, the asymptotic behavior of Filon-spline spectrum may be seen in the expression:

$$\begin{aligned}\int_a^b s(x)e^{ikx}dx = \frac{i}{k}(s_0e^{ika} - s_ne^{ikb}) - \frac{1}{k^2}(s'_0e^{ika} - s'_ne^{ikb}) - \frac{i}{k^3}(s''_0e^{ika} - s''_ne^{ikb}) \\ + \frac{1}{k^4}\sum_{j=0}^{n-1}\Delta s'''_j e^{ikx_j}, \end{aligned} \quad \text{(C.34)}$$

where $s \in S_{\mathbf{t},4}$ is a cubic spline. Each of these expressions may be verified using successive integration by parts. As a result of this asymptotic behavior, we expect the error appearing in the Fourier transform of a smooth function computed using (C.28) or (C.31) to decay at a similar rate, allowing us to provide a global bound on the error that is valid for all frequencies k. These bounds may be determined by noting that the error in the resulting spline interpolant on each subinterval $[x_k, x_{k+1}]$ is bounded by [10]:

$$g(x) - s(x) = \frac{h^4}{24}\lambda^2(1-\lambda)^2 g^{(4)}(x_k) + O(h^5), \quad \text{(C.35)}$$

where $\lambda = (x - x_k)/h$ so that $0 \leq \lambda \leq 1$. Using this result on each subinterval allows us to obtain local errors for the Fourier integral, which we sum to obtain a global error bound for the error E in the Filon-spline formula (C.31):

$$\begin{aligned} E(\theta) &= -\frac{h^5}{\theta^2}\left[\frac{i}{\theta^3}(e^{i\theta}-1)+\frac{1}{2\theta^2}(e^{i\theta}+1)+\frac{i}{12\theta}(1-e^{i\theta})\right]\sum_{n=0}^{N-1} g_n^{(4)} e^{ikx_n} + O(h^5) \\ &= -\frac{h^4}{\theta^2}\left[\frac{i}{\theta^3}(e^{i\theta}-1)+\frac{1}{2\theta^2}(e^{i\theta}+1)+\frac{i}{12\theta}(1-e^{i\theta})\right] DTFT\{g_n^{(4)}\} + O(h^5). \end{aligned} \tag{C.36}$$

Note that the error is of order h^4 and decays as $1/\theta^3$, where $\theta = kh$. This occurs due to the behavior of the difference $g-s$ at the endpoints of the integration interval $[a, b]$. Note that, on the open interval (a, b), the function $g - s$ has continuous first and second derivatives, and we would expect the error to decay as $1/\theta^4$. In addition, the spline s is chosen to be that unique interpolating cubic spline satisfying the boundary conditions $s(a) = g(a)$, $s(b) = g(b)$, $s'(a) = g'(a)$, and $s'(b) = g'(b)$ at the endpoints a and b. It follows that the function $g - s$ and its first derivative are also continuous at the endpoints. However, $s''(a) \neq g''(a)$ and $s''(b) \neq g''(b)$ in general, so that the second derivative of $g - s$ is discontinuous at the points a and b. The total error therefore decays as $1/\theta^3$.

C.6 Implementation

The procedure described in the previous section has been implemented in a Fortran-90 routine for extracting high-precision Fourier integrals. The routine requires boundary conditions on the derivatives g'_0 and g'_N, which are used, together with the samples $\{g_j\}$, to solve (B.19) via the Numerical Recipes routine *spline* [91].

The resulting values M_0 and M_N, as described in the previous section, are used in (C.31) to compute the desired Fourier integrals. The discrete-time Fourier transforms appearing in (C.31) are evaluated using a Fast Fourier Transform algorithm, producing the values of the DTFT at a uniformly spaced sequence of frequencies in the Nyquist band $[-\pi/h, \pi/h]$. These results are used, together with the periodicity of the discrete Fourier transform, to compute the desired integrals for frequencies k which lie outside the Nyquist band. Thus, our Filon-spline Fourier transform algorithm has the same intrinsic speed as the discrete Fast Fourier Transform.

The procedure has been benchmarked by computing the Filon-spline integrals of cubic polynomials on various intervals. The known value of these integrals may be compared with those obtained using (C.31), and we find agreement to 10^{-12}, as expected. In addition, the error resulting in the case of quartic and sixth degree polynomials of the form $1 - x^4$ and $1 - x^6$ has been investigated on the interval $[-1, 1]$. The results are shown in Fig. C.1, together with estimated error bounds. The dotted line in each figure of Fig. C.1 is obtained by taking the absolute value of (C.36) with the $O(h^5)$ terms set to zero, which is used together with the inequality

$$|DTFT\{g_n^{(4)}\}| \leq (b-a) \max_k |g_n^{(4)}|, \tag{C.37}$$

to approximately bound the absolute error. Note that here $a = -1$ and $b = 1$. The resulting bound is plotted together with the absolute error in the Fourier cosine integral (C.10) as computed using the Filon-spline algorithm of (C.31). Note the tightening of the bound as $k \to \infty$. For some values of k, the bound is exceeded by terms of $O(h^5)$, as expected.

Finally, we demonstrate in Figs. C.2-C.4 the use of the Filon-spline algorithm in extracting derivatives using the relation

$$\mathcal{F}\left[\frac{\partial^n g}{\partial x^n}\right] = (ik)^n \mathcal{F}[g]. \tag{C.38}$$

Because the first and second derivatives of an interpolating cubic spline converge uniformly to the derivatives of the true function as $h \to 0$ (see [10]), we expect the use of (C.38) to produce corresponding derivatives of high accuracy. Indeed, we see that this occurs through derivatives of third order, where convergence occurs at all points except along the discontinuities at the endpoints (see Fig. C.3). In Fig. C.4, we see that the approximation (C.38) is not valid for derivatives of fourth order. This occurs because the fourth derivatives of the interpolating spline fail to exist at the joins. In particular, the third derivative of the interpolating spline is discontinuous at the sampling points x_i, $i = 1, \ldots, n$. Thus, the fourth derivative, when taken as a distribution, consists of a sequence of delta-function peaks at the points x_i. The approximation of these peaks is apparent in Fig. C.4. As a result, the information about derivatives of g that may be obtained using (C.38) is confined at best to the first three derivatives.

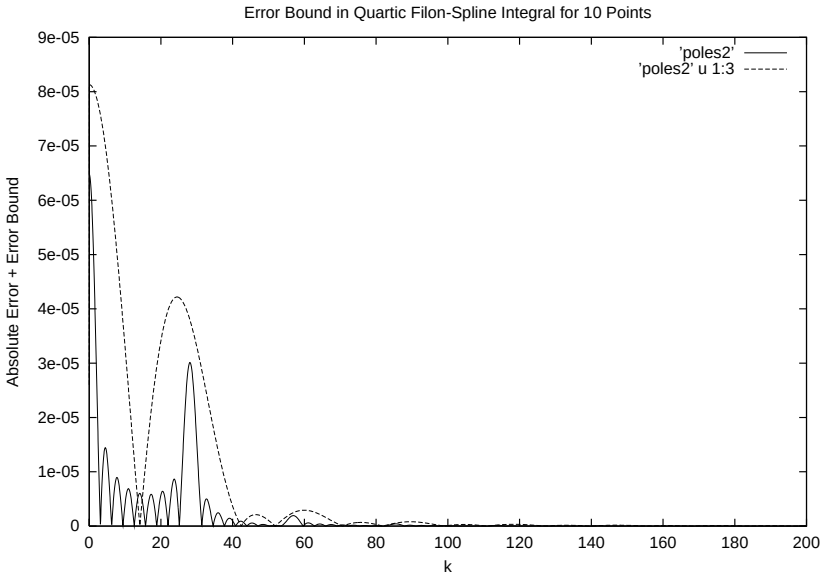

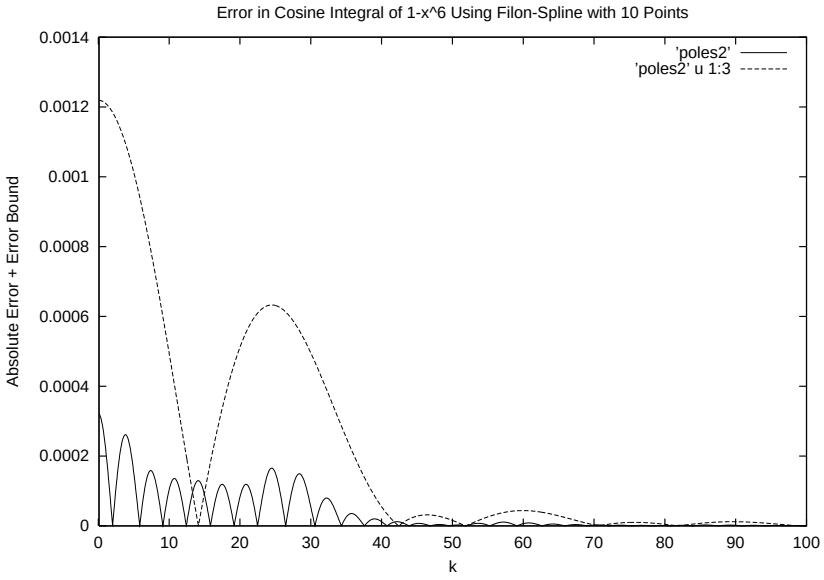

Figure C.1: Error in the Fourier cosine integral of the polynomials $1-x^4$ (upper) and $1-x^6$ (lower) computed using the Filon-spline algorithm. The integral is computed on the interval $[-1,1]$ using 10 uniformly distributed values. Dotted curves represent the error bound (C.36).

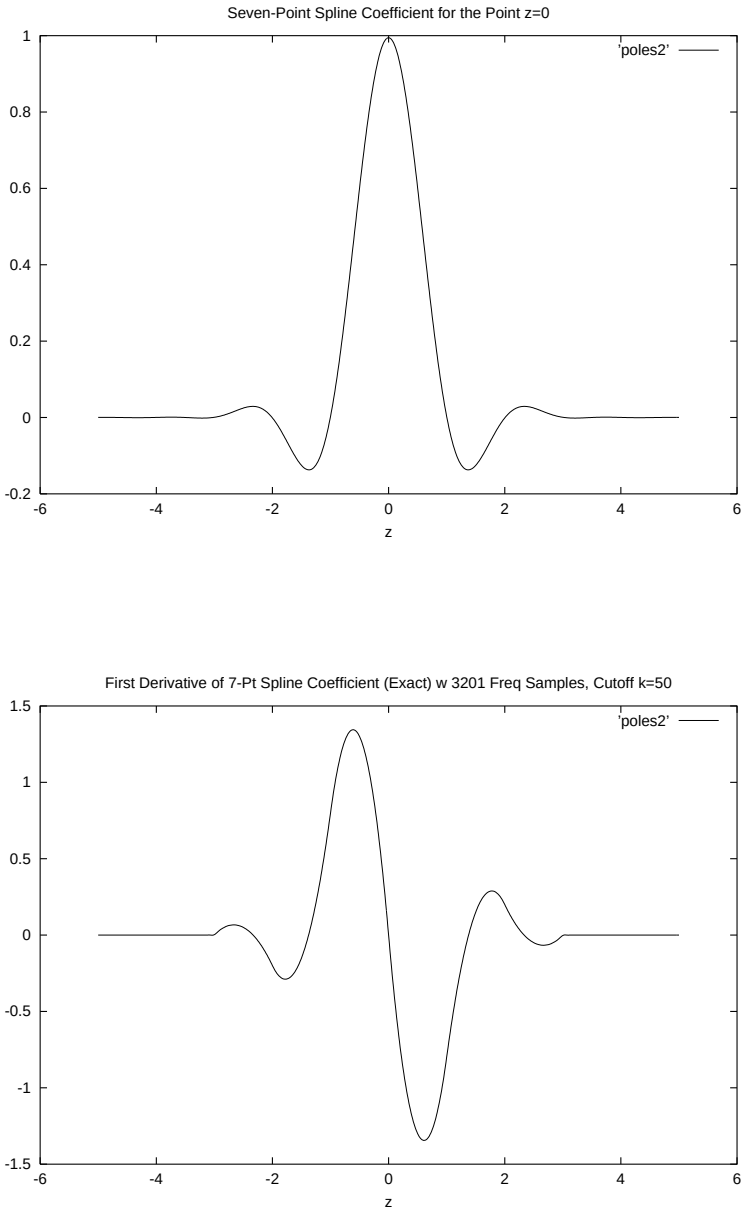

Figure C.2: Derivatives of the global basis function γ_4 of (B.20) as extracted using the Filon-spline algorithm. Here seven sampling points are uniformly distributed in the interval $[-5, 5]$. The function γ_4 takes the value 1 at the point $z = 0$, and vanishes at the other 6 sample points. (Upper) The function γ_4. (Lower) First derivative γ_4'.

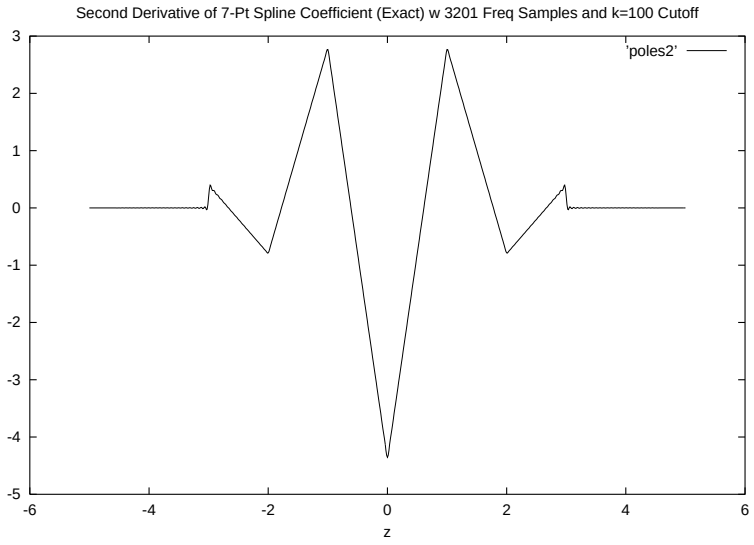

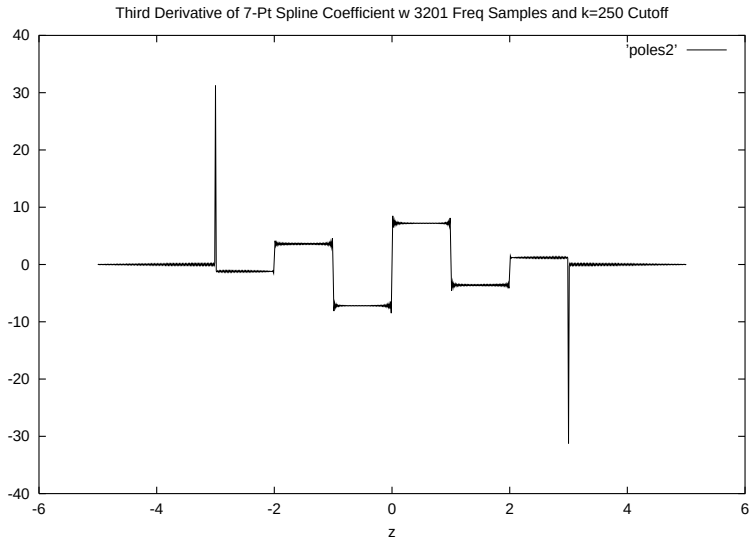

Figure C.3: Derivatives of the global basis function γ_4 as extracted using the Filon-spline algorithm. (Upper) Second deriviative γ_4''. (Lower) Third derivative $\gamma_4^{(3)}$.

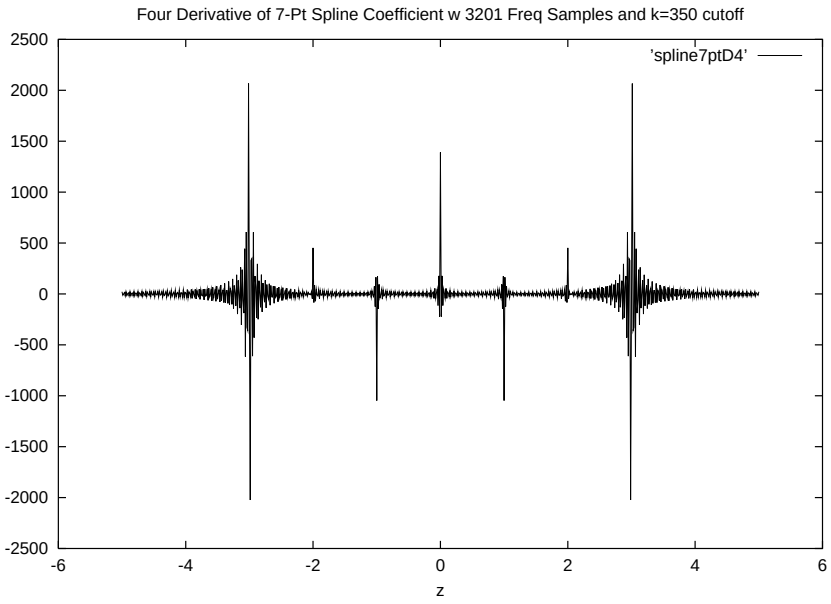

Figure C.4: Derivatives of the global basis function γ_4 as extracted using the Filon-spline algorithm. Illustrated here is the fourth derivative $\gamma_4^{(4)}$.

Appendix D

Mathieu Functions

D.1 Definition and Properties

The separation of variables in the Helmholtz equation $(\nabla^2 - k^2)\Psi = 0$ leads to the following equations in elliptic cylindrical coordinates:

$$\frac{d^2V}{dv^2} + [\lambda - 2q\cos(2v)]V = 0, \tag{D.1}$$

$$\frac{d^2U}{du^2} + [\lambda - 2q\cosh(2u)]U = 0, \tag{D.2}$$

where $q = -\frac{k^2 f^2}{4}$. The first is known as Mathieu's equation, and the the second is the modified Mathieu equation. (See [20],[21],[22].) The theory of Mathieu's equation and its solutions have found increasing application in accelerator physics, where it is a canonical model of parametric resonance [30]. In atomic optics, solutions are wavefunctions for a particle in a sinusoidal potential. For a detailed application to solutions in an optical lattice, see [27].

Note that equation (D.1) is periodic, invariant under $v \to v + n\pi$ for all integer n. It follows from Floquet's theorem that there exist one or more solutions of the form $w_\mu(v, q) = e^{i\mu v}w(v)$, where w is a function of v with period π and the parameter μ, known as the *characteristic exponent*, depends on the parameters q and λ, but not on the independent variable v. A second solution is given by $w_{-\mu}(v, q) = w_\mu(-v)$, with $w_{-\mu}(v) = e^{-i\mu v}w(-v)$. If μ is not an integer, then these two Floquet solutions

are linearly independent and span the space of solutions to (D.1). Of particular interest are the linear combinations

$$ce_\mu(v,q) = \frac{1}{2}\left[w_\mu(v,q) + w_{-\mu}(v,q)\right] \tag{D.3}$$

$$se_\mu(v,q) = \frac{1}{2i}\left[w_\mu(v,q) - w_{-\mu}(v,q)\right]. \tag{D.4}$$

In the case that μ is an integer, it is readily seen that each Floquet solution becomes periodic with period π (for μ even) or 2π (for μ odd). Furthermore, the solutions w_μ and $w_{-\mu}$ become multiples, and we have one of the two cases $ce_\mu(v,q) \to w_\mu(v,q)$, $se_\mu(v,q) \to 0$ or $ce_\mu(v,q) \to 0$, $se_\mu(v,q) \to iw_{-\mu}(v,q)$. For each integer μ and $q \neq 0$, there are two sets of parameters λ_c and λ_s such that the Floquet solution of (D.1) has characteristic exponent μ, corresponding to the solutions (D.3) and (D.4), respectively.

We are interested here in solutions to Mathieu's equation (D.1) periodic in the variable v with period 2π, obtained as $(\lambda, q) \to \mu = n$ for integer n. These are eigenfunctions of the self-adjoint operator

$$M = -\frac{d^2}{dv^2} - 2q\cos(2v) \tag{D.5}$$

which we take to act on the space $H = L^2(-\pi, \pi)$ with the periodic boundary condition $f(-\pi) = f(\pi)$. For each q the operator M has a countably infinite spectrum of eigenvalues λ_n, called *characteristic values*, which we may index by the value of the corresponding characteristic exponent $\mu = ... - 2, -1, 0, 1, 2, ...$ It is useful to write the space H as the orthogonal direct sum $H = H_0^+ \oplus H_1^+ \oplus H_0^- \oplus H_1^-$, where the superscripts $\pm$ indicate the set of functions symmetric and antisymmetric with

respect to $v = 0$, and the subscripts $0, 1$ indicate the set of functions symmetric and antisymmetric with respect to $v = \pi/2$. Then M leaves each subspace invariant, and can be similarly decomposed with the action of M in each subspace being again self-adjoint [29]. We obtain four classes of eigenfunctions, corresponding to the four subspaces

$$H_0^+ \quad : \quad \lambda_0, ce_0, \text{ and } \lambda_{+n}, ce_n, \quad n = 2, 4, 6, ... \tag{D.6}$$

$$H_1^+ \quad : \quad \lambda_{+n}, ce_n, \quad n = 1, 3, 5, ... \tag{D.7}$$

$$H_0^- \quad : \quad \lambda_{-n}, se_n, \quad n = 1, 3, 5, ... \tag{D.8}$$

$$H_1^- \quad : \quad \lambda_{-n}, se_n, \quad n = 2, 4, 6, ... \tag{D.9}$$

Those eigenfunctions in H_0^+ are even in v, symmetric about $v = \pi/2$, and hence have period π. Similarly, those in H_1^+ are even in v, antisymmetric about $v = \pi/2$, and have period 2π, etc. We have associated the characteristic exponent $\mu = n$ with that value of λ corresponding to solutions even in v. Similarly, we associate $\mu = -n$ with the second value of λ, corresponding to solutions odd in v. To conform with standard notation we now write $a_0 = \lambda_0$, $a_n = \lambda_n$ and $b_n = \lambda_{-n}$ for $n = 1, 2, 3, ...$ The Mathieu functions ce_3 and se_3 are illustrated in Fig. D.1 for a range of values of the parameter q.

In accord with our desire for periodicity, we search for solutions to (D.1) of the form [20]

$$ce_m(v, q) = \sum_{n=0}^{\infty} A_n^m(q) \cos nv, \tag{D.10a}$$

$$se_m(v, q) = \sum_{n=0}^{\infty} B_n^m(q) \sin nv. \tag{D.10b}$$

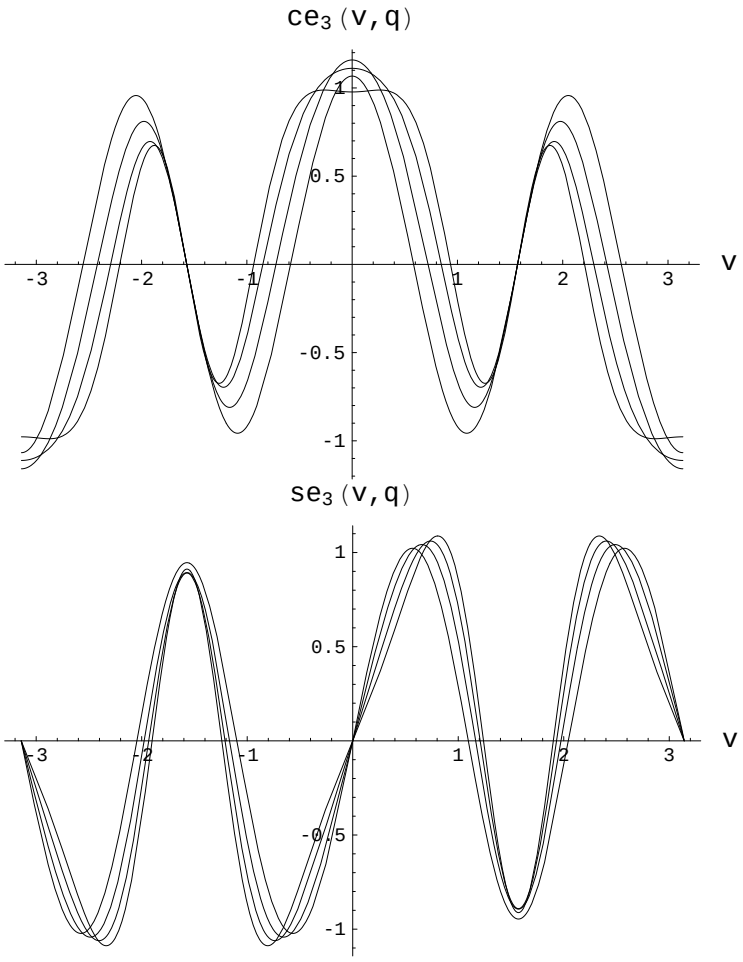

Figure D.1: The Mathieu functions ce_3 (upper) and se_3 (lower) illustrated for $q =$ 1.0, 3.0, 5.0, and 7.0 on the interval $[-\pi, \pi]$

This Ansatz results in four sets of decoupled recursion relations for the Fourier coefficients A_n^m and B_n^m. These expressions take the form (see [20]):

$$\lambda A_0^{2r} - qA_2^{2r} = 0, \tag{D.11a}$$

$$(\lambda - 4)A_2^{2r} - q(2A_0^{2r} + A_4^{2r}) = 0,$$

$$(\lambda - (2k)^2)A_{2k}^{2r} - q(A_{2k-2}^{2r} + A_{2k+2}^{2r}) = 0;$$

$$(\lambda - 1 - q)A_1^{2r+1} - qA_3^{2r+1} = 0, \tag{D.11b}$$

$$(\lambda - (2k+1)^2)A_{2k+1}^{2k+1} - q(A_{2k-1}^{2r+1} + A_{2k+3}^{2r+1}) = 0;$$

$$(\lambda - 1 + q)B_1^{2r+1} - qB_3^{2r+1} = 0, \tag{D.11c}$$

$$(\lambda - (2k+1)^2)B_{2k+1}^{2r+1} - q(B_{2k-1}^{2r+1} + B_{2k+3}^{2r+1}) = 0;$$

$$(\lambda - 4)B_2^{2r+2} - qB_4^{2r+2} = 0, \tag{D.11d}$$

$$(\lambda - (2k+2)^2)B_{2k+2}^{2r+2} - q(B_{2k}^{2r+2} + B_{2k+4}^{2r+2}) = 0.$$

Solutions for the Fourier coefficients A_n^m with $n = 0, 1, 2, \cdots$ exist only for a single characteristic value denoted $\lambda = a_m$, while solutions for the coefficients B_n^m with $n = 0, 1, 2, \cdots$ exist only for the characteristic value $\lambda = b_m$. (Note that a_m and b_m will depend on the parameter q.) Requiring that the recursion relations above be satisfied provides a transcendental equation for the values $\lambda(q) = a_m(q)$ or $\lambda(q) = b_m(q)$. The relations (D.11), together with an appropriate normalization, are sufficient to determine the Fourier coefficients uniquely. Here we choose the normalization such

that

$$\frac{1}{\pi}\int_0^{2\pi} ce_m^2(v,q)dv = \frac{1}{\pi}\int_0^{2\pi} se_m^2(v,q)dv = 1. \tag{D.12}$$

The periodic Mathieu functions are complete on the interval $[-\pi,\pi]$, and each of the four classes is complete in its own subspace H_j^α, $j = 0,1$, $\alpha = \pm$. To investigate this further, suppose we consider the following functions of $v \in [-\pi,\pi]$ for fixed q:

$$f_n^E(v) = \frac{1}{\sqrt{\pi}} ce_n(v,q), \tag{D.13}$$

$$f_n^O(v) = \frac{1}{\sqrt{\pi}} se_n(v,q), \tag{D.14}$$

$$g_n^E(v) = \frac{1}{\sqrt{\pi}} \cos(nv), n \neq 0, \tag{D.15}$$

$$g_n^O(v) = \frac{1}{\sqrt{\pi}} \sin(nv), \tag{D.16}$$

$$g_0^O(v) = \frac{1}{\sqrt{2\pi}}. \tag{D.17}$$

Each of $\{f_j^E, f_k^O\}$ and $\{g_j^E, g_k^O\}$ forms a complete orthonormal set on $L^2[-\pi,\pi]$. We may then write, using the standard inner product,

$$A_0^{(2n)}(q) = \frac{1}{\sqrt{2}}(f_n^E, g_0^E), \tag{D.18}$$

$$A_r^{(n)}(q) = (f_n^E, g_r^E), n \neq 0, \tag{D.19}$$

$$B_r^{(n)}(q) = (f_n^O, g_r^O), \tag{D.20}$$

for all values of the parameter q, together with the completeness identities

$$\sum_{n=0}^{\infty} A_j^{(n)}(q)A_k^{(n)}(q) = \delta_{jk}(1-\frac{1}{2}\delta_{j0}), \tag{D.21}$$

$$\sum_{n=0}^{\infty} B_j^{(n)}(q)B_k^{(n)}(q) = \delta_{jk}, \tag{D.22}$$

$$2A_0^{(j)}A_0^{(k)} + \sum_{r=1}^{\infty} A_r^{(j)}(q)A_r^{(k)}(q) = \delta_{jk}, \tag{D.23}$$

$$\sum_{r=1}^{\infty} B_r^{(j)}(q)B_r^{(k)}(q) = \delta_{jk}. \tag{D.24}$$

These relations are useful for understanding the behavior of the coefficients A_n^m, B_n^m, which appear in the kernels Λ_n^r and in the Mathieu-Bessel relations (Section D.2). As a final remark, we note the following symmetries of solutions under $q \to -q$ (see [20]):

$$a_{2r}(-q) = a_{2r}(q), \tag{D.25}$$

$$a_{2r+1}(-q) = b_{2r+1}(q), \tag{D.26}$$

$$b_{2r}(-q) = a_{2r+1}(q), \tag{D.27}$$

$$b_{2r+2}(-q) = b_{2r+2}(q); \tag{D.28}$$

$$A_{2k}^{2r}(-q) = (-1)^{k+r}A_{2k}^{2r}(q), \tag{D.29}$$

$$A_{2k+1}^{2r+1}(-q) = (-1)^{k+r}B_{2k+1}^{2r+1}(q), \tag{D.30}$$

$$B_{2k+1}^{2r+1}(-q) = (-1)^{k+r}A_{2k+1}^{2r+1}(q), \tag{D.31}$$

$$B_{2k+2}^{2r+2}(-q) = (-1)^{k+r}B_{2k+2}^{2r+2}(q); \tag{D.32}$$

$$ce_{2r}(v,-q) = (-1)^r ce_{2r}(\pi/2-v,q), \tag{D.33}$$

$$ce_{2r+1}(v,-q) = (-1)^r se_{2r+1}(\pi/2-v,q), \tag{D.34}$$

$$se_{2r+1}(v,-q) = (-1)^r ce_{2r+1}(\pi/2-v,q), \tag{D.35}$$

$$se_{2r+2}(v,-q) = (-1)^r se_{2r+2}(\pi/2-v,q). \tag{D.36}$$

D.1.1 General Solutions

The associated solutions of the Modified Mathieu Equation regular at the origin are given by

$$Ce_m(u,q) = ce_m(iu,q) \quad \text{for } \lambda = a_m, \tag{D.37}$$

$$Se_m(u,q) = -ise_m(iu,q) \quad \text{for } \lambda = b_m, \tag{D.38}$$

corresponding to characteristic values $a_m(q)$ and $b_m(q)$, respectively. The general solution to the Helmholtz equation is therefore

$$\tilde{\psi}(u,v,k) = \sum_{m=0}^{\infty} [\alpha(k) Ce_m(u,q) ce_m(v,q) + \beta(k) Se_m(u,q) se_m(v,q)] \tag{D.39}$$

with $q = \frac{-k^2 f^2}{4}$.

In general, we are interested in expressing product solutions of the form $Ce_n(u,q)ce_n(v,q)$ and $Se_n(u,q)se_n(v,q)$ in terms of homogeneous polynomials in the Cartesian coordinates x, y where $q = -\frac{k^2 f^2}{4}$. Inverting coordinates to obtain these solutions as functions of x, y requires a careful choice of branch; we obtain inverse trigonometric functions whose arguments are roots of a quartic equation. In

particular:

$$u = \mathcal{R}e[\text{arccosh}(z)] \tag{D.40}$$
$$= \text{arccosh}\left[\frac{|x|\sqrt{2}}{\sqrt{1+x^2+y^2-\sqrt{4y^2+(-1+x^2+y^2)^2}}}\right],$$

$$v = \mathcal{I}m[\text{arccosh}(z)] \tag{D.41}$$
$$= \pm\text{arccos}\left[\frac{\pm\sqrt{1+x^2+y^2-\sqrt{4y^2+(-1+x^2+y^2)^2}}}{\sqrt{2}}\right].$$

Note from Fig. D.2 that the function $ce_m(v(x,y))$ is not differentiable on the domain $\{(x,y) : y = 0, x \in (-\infty, f)\}$. Similarly, $Ce_m(u(x,y))$ is not differentiable on the domain $\{(x,y) : y = 0, x \in [-f, f]\}$. It is not obvious that a simple representation of the power series for the product $Ce_m(u,q)ce_m(v,q)$ exists, although the function does appear smooth (Fig. D.3). This behavior also occurs for the functions $Se_m(u(x,y))$ and $se_m(v(x,y))$.

This can be compared to the cylinder case, which exhibits the same phenomena. In that case we have

$$\rho = |z| = \sqrt{x^2+y^2}, \tag{D.42}$$
$$\phi = \text{Arg}(z) = \arctan\left(\frac{y}{x}\right),$$

and the functions $I_n(k\rho(x,y))$, $\sin(n\phi(x,y))$, and $\cos(n\phi(x,y))$ fail to be differentiable in the plane with respect to the variables (x,y). Nevertheless, the products $I_n(k\rho)\cos(n\phi)$ and $I_n(k\rho)\sin(n\phi)$ are analytic on all of $\mathbb{R}^2$.

To illustrate the analyticity of the Mathieu function products in the variables corresponding to the Cartesian coordinates x, y, we present the integral representa-

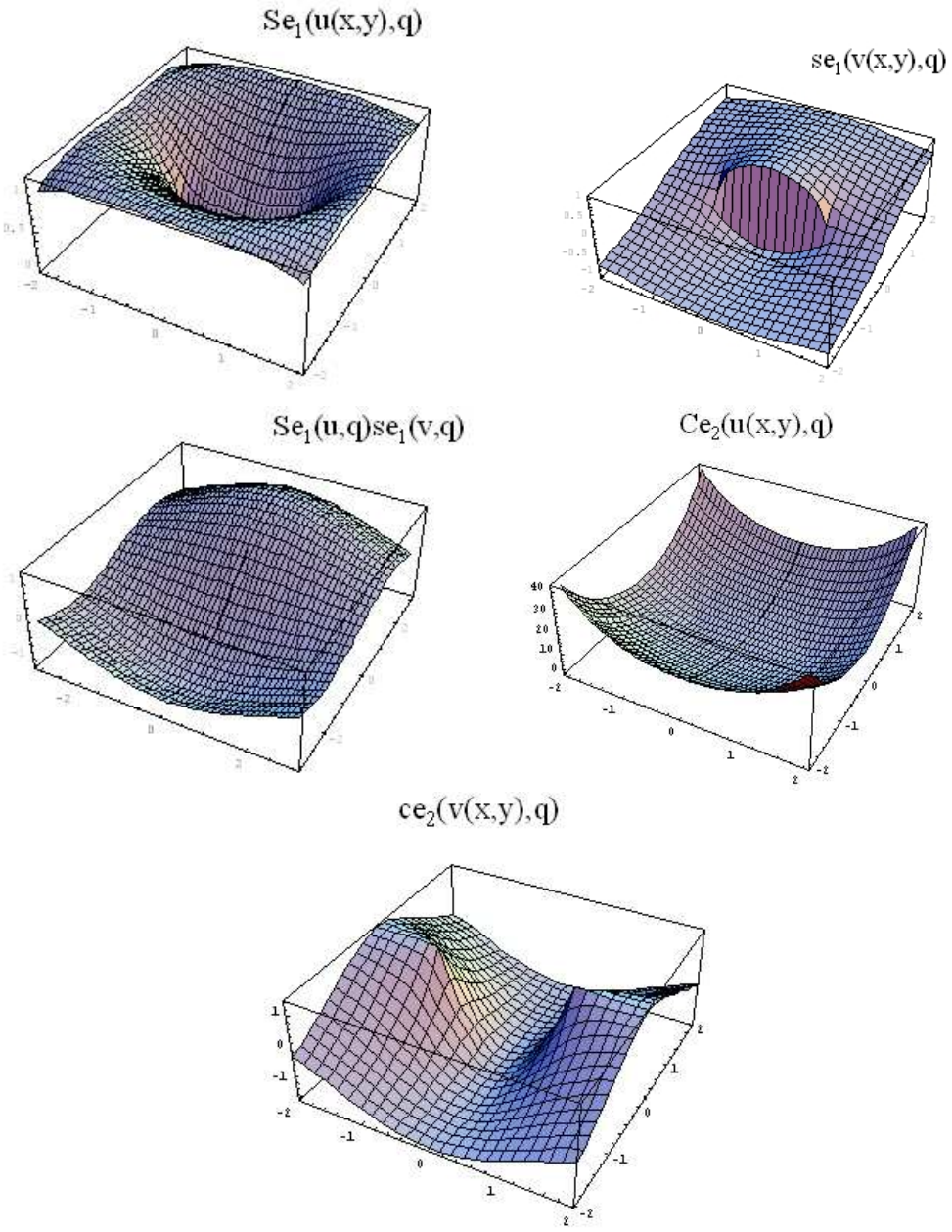

Figure D.2: Various Mathieu functions of the coordinates (u, v) plotted in the x, y plane.

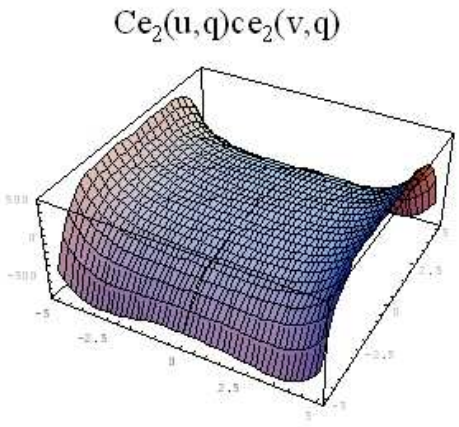

Figure D.3: The product $Ce_2(u,q)ce_2(v,q)$ plotted as a function of cartesian coordinates (x,y) in the plane.

tion given in Bateman et al. [21]:

$$\mathcal{K}(x,y,a) = \exp\left[-k(x\cos a + y\sin a)\right], \tag{D.43a}$$

$$Ce_n(u,q)ce_n(v,q) = \frac{2}{\pi}g_c^n(k)\int_0^{2\pi}\mathcal{K}(x,y,a)ce_n(a,q)da, \tag{D.43b}$$

$$Se_n(u,q)se_n(v,q) = \frac{2}{\pi}g_s^n(k)\int_0^{2\pi}\mathcal{K}(x,y,a)se_n(a,q)da, \tag{D.43c}$$

where g_c^n and g_s^n are given in (D.72). In particular, it follows that such products are analytic with derivatives to all orders given by

$$\frac{\partial^{p+q}}{\partial x^p\partial y^q}Ce_n(u,q)ce_n(v,q) = \frac{2}{\pi}g_c^n(k)(-k)^{p+q}\int_0^{2\pi}\mathcal{K}(x,y,a)\cos^p(a)\sin^q(a)ce_n(a,q)da \tag{D.44}$$

where the integral on the right is guaranteed to converge since

$$|\mathcal{K}(x,y,a)\cos^p(a)\sin^q(a)ce_n(v,q)| \le e^{|k|(|x|+|y|)}|ce_n(a,q)| \tag{D.45}$$

and the Mathieu functions are absolutely integrable on $[0,2\pi]$. A similar expression exists for $Se_n(u,q)se_n(v,q)$ with $ce_n(v,q)\to se_n(v,q)$ in the integrand of (D.44).

D.1.2 Asymptotic Forms

The kernels Λ_n^r introduced in Section 3.4.2 are in general complicated functions of the spatial frequency k. Understanding their behavior therefore requires appropriate approximate representations of the Mathieu functions in various regimes of the parameter $q = -\frac{k^2 f^2}{4}$. We find it sufficient to consider two asymptotic forms for each Mathieu function corresponding to low-frequency and high-frequency behavior. We choose as the crossover point for a given order n the quantity $q_c > 0$, defined as the unique root of $a_n(q) = 2q$. We then refer to the low-frequency regime when $|q| < q_c$, and to the high-frequency regime when $|q| > q_c$.

The significance of the crossover q_c is illustrated in Fig. D.4. Here the characteristic values a_n and b_n are plotted for $n = 0, ..., 20$ and $q > 0$. For fixed q, the values $a_n(q)$ and $b_n(q)$ each increase with n, becoming large and positive for large orders n. For $q \neq 0$, the values a_n and b_n are distinct and do not cross with increasing $|q|$. It is known [20] that near $q = 0$, $a_n \sim b_n$ and for $n \geq 7$,

$$\begin{matrix} a_n \\ b_n \end{matrix} \sim n^2 + \frac{q^2}{2(n^2-1)} + \frac{(5n^2+7)q^4}{32(n^2-1)^3(n^2-4)} + O(q^6/n^{10}). \tag{D.46}$$

Similarly, as $q \to \infty$, $a_n \sim b_{n+1}$ and

$$\begin{matrix} a_n \\ b_{n+1} \end{matrix} \sim -2q + 2mq^{1/2} - (m^2+1)2^{-3} - (m^3+3m)q^{-1/2}2^{-7} + O(m^4/q) \tag{D.47}$$

where $m = 2n+1$. The line $y = 2q$ is included in Fig. D.4 to illustrate the partition of each characteristic value into low-frequency and high-frequency regimes. The value $q = q_c$ appears to be an inflection point $a_n''(q_c) = 0$ for each $n \neq 0$, and neatly divides the asymptotic behaviors described in (D.46,D.47). Plotted in Fig. D.4 is

also a comparison of the true value a_{50} with the approximations (D.46,D.47), where the crossover q_c is illustrated by the intersection with the line $y = 2q$.

We note that the crossover scales as $q_c \propto n^2$. As a result, we expect the form (D.46) to be valid in the limit $q/n^2 \to 0$, except for $n \leq 3$. Similarly, we expect (D.47) to be valid as $n^2/q \to 0$, except in a neighborhood of $q \approx 0$. To quantify this further, define the scaled parameter $\tilde{a}$ in each regime by $\tilde{a} = 2q/a$ for $|q| < q_c$ and $\tilde{a} = (1/2)(a/2q + 1)$ for $|q| > q_c$. It can be shown that $0 \leq \tilde{a} \leq 1$ for all q. In fact, we have that $\tilde{a} \to 0$ as $q/q_c \to 0$, and $\tilde{a} \to 0$ as $q_c/q \to 0$. The parameter $\tilde{a}$ may then be used to characterize the "size" of the perturbation relative to each of the asymptotic forms.

A remarkably accurate estimate of the relative error obtained by taking the first N terms in (D.46) is given by

$$\epsilon_N = \frac{a_n - a_n^{(N)}}{a_n^{(N)}} \approx \left(\frac{q}{\sqrt{2} a_n} \right)^{2N} \tag{D.48}$$

valid over a range of values of q and n.

D.1.2.1 Low-frequency regime $|q| < q_c$

Near $q = 0$, when the perturbation $\tilde{a} = 2q/a_n << 1$, we see that Mathieu's equation is dominated by the term containing the characteristic value, and the equation approaches that of a harmonic oscillator $V'' + \lambda V = 0$ with frequency $\sqrt{\lambda}$. For $q = 0$, the eigenfunctions are given by $\cos(nv)$, $\sin(nv)$, corresponding to the characteristic value $\lambda = n^2$ for integer n. As q increases, the perturbed solutions are

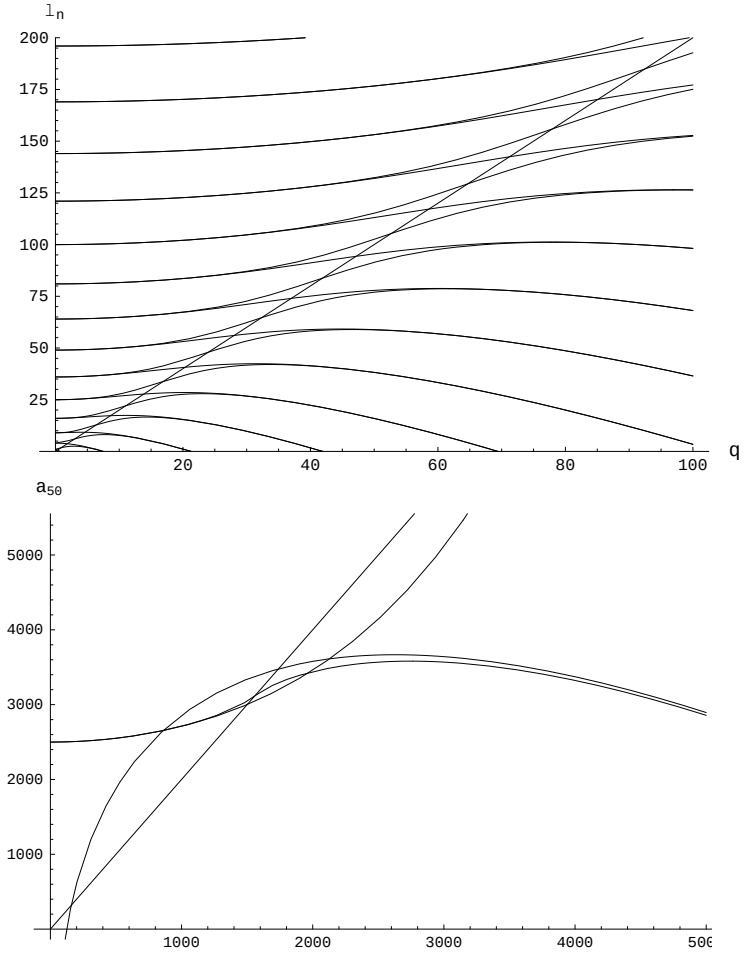

Figure D.4: (Upper) Characteristic values a_n and b_n plotted versus q for $q > 0$, together with the line $y = 2q$. (Lower) Small-q and large-q approximations to $a_{50}(q)$, illustrating the crossover at q_c.

given by [22]

$$ce_n(v,q) = \tag{D.49}$$
$$\cos(nv) - q\left[\frac{\cos(n+2)v}{4(n+1)} - \frac{\cos(n-2)v}{4(n-1)}\right] + q^2\left[\frac{\cos(n+4)v}{32(n+1)(n+2)} + \frac{\cos(n-4)v}{32(n-1)(n-2)}\right]$$
$$- \frac{1}{32}\left(\frac{1}{(n+1)^2} + \frac{1}{(n-1)^2}\right)\cos(nv) + O(q^3/n^3),$$

$$se_n(v,q) = \tag{D.50}$$
$$\sin(nv) - q\left[\frac{\sin(n+2)v}{4(n+1)} - \frac{\sin(n-2)v}{4(n-1)}\right] + q^2\left[\frac{\sin(n+4)v}{32(n+1)(n+2)} + \frac{\sin(n-4)v}{32(n-1)(n-2)}\right]$$
$$- \frac{1}{32}\left(\frac{1}{(n+1)^2} + \frac{1}{(n-1)^2}\right)\sin(nv) + O(q^3/n^3).$$

The resulting series are known to have a finite, nonzero radius of convergence, although a general expression for this radius could not be found in the literature. For $n \geq 3$, a lower bound on this radius of convergence is known [29] to be $r_n \geq n-1$. In general, however, the first few terms of these series provide an accurate approximation for small q, even outside the known radius of convergence, provided the series is truncated at some optimal number of terms N. (In this case the error is of order $O(q^N)$.) In addition, we verify numerically that the *same* series are approximately valid as $n \to \infty$ for fixed q, with error $O(n^{-N})$. We therefore use (D.49,D.50) to approximate the Mathieu functions in the domain $|q| < q_c$. Corresponding series approximations for the modified Mathieu functions are obtained by taking $v \to iu$.

We also require an approximation for the Fourier coefficients $A_r^{(n)}$, $B_r^{(n)}$. Using the recursion relations (D.11) together with the series (D.47,D.46) allows us to obtain

for $n \geq r$ that

$$\frac{B_r^n(-q)}{B_1^n(-q)} = (-1)^{(r-1)/2} 2^{r-1} \frac{(n-L-1)!}{L!} q^{-(r-1)/2} \left(1 - \frac{q}{n^2-1} + O(q^2/n^4)\right), \tag{D.51}$$

where $n = r + 2L$.

We obtain the following rational Padé approximation for the kernels for $n \geq r$:

$$\Lambda_n^r(k) \approx N(1+\alpha q)^{-1} \tag{D.52}$$

where

$$N = f^{-r} 2^{r-1} (-1)^L \frac{(n-L-1)!}{r!L!} \frac{1}{\cosh(nu)}, \tag{D.53}$$

$$\alpha = \frac{(n+2)\cosh[(n+2)u]}{4n(n+1)\cosh(nu)} - \frac{(n-2)\cosh[(n-2)u]}{4n(n-1)\cosh(nu)}. \tag{D.54}$$

A further approximation for small q is then obtained as

$$\Lambda_n^r(k) \sim N(1 - \alpha q + O(q^2/n^2)), \tag{D.55}$$

although we use the more accurate approximation (D.52) throughout. The approximations (D.52,D.55) for the kernel Λ_5^5 are illustrated in Fig. D.5.

D.1.2.2 High-frequency regime $|q| > q_c$

A careful treatment of the uniform asymptotic approximation of Mathieu functions in the regime $|q| > q_c$ is given in Dunster [28], together with error bounds. For large $q < 0$, we determine from McLachlan the asymptotic form of the modified

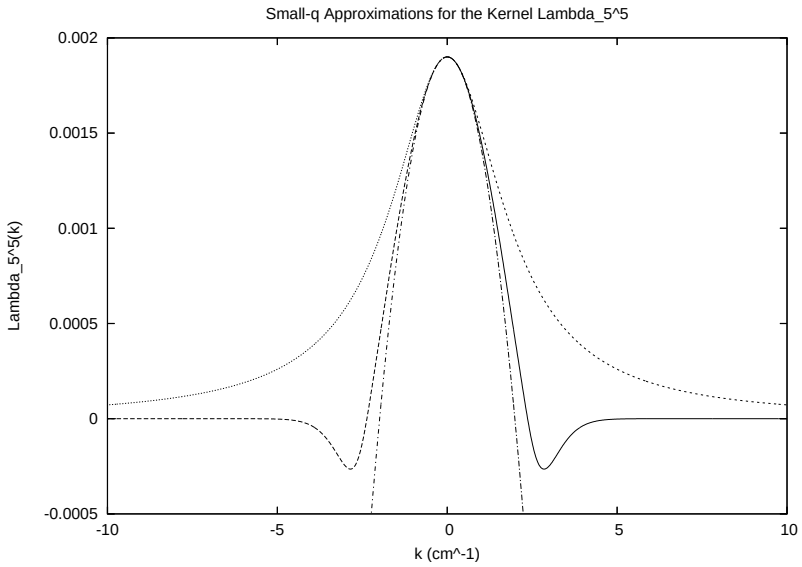

Figure D.5: The kernel $\Lambda_5^5(k)$ is plotted together with the small-q approximations (D.52) and (D.55) for the values u, f used in Section 3.4.1.

Mathieu functions to lowest order:

$$Ce_n(U,q) \sim \frac{1}{2}\sqrt{\frac{f}{y}}q^{-1/4}\pi^{-1/2}g_c^n(q)\alpha_n \exp(kx)\left[1+O\left(\frac{1}{\sqrt{q}}\right)\right], \tag{D.56}$$

$$Se_n(U,q) \sim \frac{1}{2}\sqrt{\frac{f}{y}}q^{-1/4}\pi^{-1/2}g_s^n(q)\alpha_n \exp(kx)\left[1+O\left(\frac{1}{\sqrt{q}}\right)\right], \tag{D.57}$$

where we have used x, y to denote the semiminor and semimajor axes of the corresponding ellipse, $x = x_{max} = f\cosh(U)$ and $y = y_{max} = f\sinh(U)$, and $q = -\frac{k^2 f^2}{4}$. The functions g_c^n and g_s^n are presented in (D.72). Here

$$\alpha_m = \left[\frac{1-\epsilon}{1+\epsilon}\right]^{(2m+1)/4} \tag{D.58}$$

is a geometrical factor where $\epsilon = \cosh(U)^{-1}$ is the eccentricity of the ellipse. Note that $0 < \epsilon < 1$ and $0 < \alpha_m < 1$ for any m. Similarly, we may obtain

$$Ce'_n(U,q) \sim \sqrt{\frac{y}{f}} q^{1/4} \pi^{-1/2} g_c^n(q) \alpha_n \exp(kx) \left[1 + O\left(\frac{1}{\sqrt{q}}\right)\right], \tag{D.59}$$

$$Se'_n(U,q) \sim \sqrt{\frac{y}{f}} q^{1/4} \pi^{-1/2} g_s^n(q) \alpha_n \exp(kx) \left[1 + O\left(\frac{1}{\sqrt{q}}\right)\right]. \tag{D.60}$$

To obtain a rough estimate of error, note that the $O(1/\sqrt{q})$ term in (D.56,D.57) is given by

$$\eta = -\frac{2n+1}{4kf\sinh^2(U)} + \frac{(n^2+n+1)\cosh(U)}{4kf\sinh^2(U)}. \tag{D.61}$$

We also require expressions for the behavior of the Fourier coefficients $B_r^{(n)}$ and $A_r^{(n)}$. The asymptotic behavior of these coefficients has been studied in [26] in terms of generalized Hermite polynomials. Following [27], we define the variable $\zeta = j(4/q)^{1/4}$. The Fourier coefficients are then obtained from the expression

$$f_j^{(n)} = \sqrt{\frac{\sqrt{2}}{2^{n-1} n! (q\pi^2)^{1/4}}} \exp\left(\frac{-\zeta^2}{2}\right) H_n(\zeta) \tag{D.62}$$

where the H_n are the Hermite polynomials. The coefficients behave as

$$A_{2j}^{(2r)}(-q) \sim f_j^{(n=2r)}, \tag{D.63}$$

$$B_{2j}^{(2r)}(-q) \sim f_j^{(n=2r+1)}, \tag{D.64}$$

$$A_{2j+1}^{(2r+1)}(-q) \sim f_{j+\frac{1}{2}}^{(n=2r)}, \tag{D.65}$$

$$B_{2j+1}^{(wr+1)}(-q) \sim f_{j+\frac{1}{2}}^{(n=2r+1)}. \tag{D.66}$$

Expanding (D.62) in ζ and retaining terms through order $O(\zeta^3)$ we have [27]

$$f_j^{(n=2r)} = \frac{(-1)^r n!}{r!} \sqrt{\frac{\sqrt{2}}{2^{n-1} n! \sqrt{\pi}}} q^{-1/8} \left[1 - \frac{(2n+1)j^2}{\sqrt{q}} + O\left(\frac{1}{q}\right)\right], \tag{D.67}$$

$$f_j^{(n=2r+1)} = \frac{2j(-1)^r n!}{r!}\sqrt{\frac{\sqrt{2}}{2^{n-2}n!\sqrt{\pi}}}q^{-3/8}\left[1 - \frac{(2n+1)j^2}{3\sqrt{q}} + O(\frac{1}{q})\right]. \tag{D.68}$$

We note that all coefficients go to zero as $q \to \infty$, although the rate of falloff is quite slow. As a final result, we note that the Hermite polynomials can be bounded for all x by [22]

$$|H_n(x)| < e^{x^2/2}\kappa 2^{n/2}\sqrt{n!} \tag{D.69}$$

where $\kappa \approx 1.086435$ is a constant independent of n. It then follows that

$$|f_j^{(n)}|^2 = \frac{\sqrt{2}}{2^{n-1}n!(q\pi^2)^{1/4}}\exp(-\zeta^2)[H_n(\zeta)]^2 < 2\kappa^2\sqrt{\frac{2}{\pi}}q^{-1/4} \tag{D.70}$$

for $q > q_c$ sufficiently large. We now have a bound for the asymptotic behavior of the Fourier coefficients that is independent of both indices j and r, where we may take $\kappa \approx 1$.

D.2 Mathieu-Bessel Relations

We show that the following relations hold at every point in the plane defined by coordinates (x,y) for $k \neq 0$.

$$Ce_{2m}(u,k)ce_{2m}(v,k) = g_c^{2m}(k)\sum_{r=0}^{\infty} A_{2r}^{2m}(k)I_{2r}(k\rho)\cos(2r\phi), \tag{D.71a}$$

$$Ce_{2m+1}(u,k)ce_{2m+1}(v,k) = g_c^{2m+1}(k)\sum_{r=0}^{\infty} A_{2r+1}^{2m+1}(k)I_{2r+1}(k\rho)\cos[(2r+1)\phi], \tag{D.71b}$$

$$Se_{2m+1}(u,k)se_{2m+1}(v,k) = g_s^{2m+1}(k)\sum_{r=0}^{\infty} B_{2r+1}^{2m+1}(k)I_{2r+1}(k\rho)\sin[(2r+1)\phi], \tag{D.71c}$$

$$Se_{2m}(u,k)se_{2m}(v,k) = g_s^{2m}(k)\sum_{r=0}^{\infty} B_{2r+2}^{2m+2}(k)I_{2r}(k\rho)\sin(2r\phi), \tag{D.71d}$$

where we have

$$g_s^{2m+1}(k) = \frac{2se_{2m+1}(\frac{\pi}{2},k)se'_{2m+1}(0,k)}{kfB_1^{2m+1}(k)}, \tag{D.72a}$$

$$g_c^{2m}(k) = \frac{ce_{2m}(\frac{\pi}{2},k)ce_{2m}(0,k)}{A_0^{2m}(k)}, \tag{D.72b}$$

$$g_s^{2m+2}(k) = \frac{-4se'_{2m+2}(\frac{\pi}{2},k)se'_{2m+2}(0,k)}{k^2f^2B_2^{2m+2}(k)}, \tag{D.72c}$$

$$g_c^{2m+1}(k) = \frac{-2ce'_{2m+1}(\frac{\pi}{2},k)ce_{2m+1}(0,k)}{kfA_1^{2m+1}(k)}. \tag{D.72d}$$

The above series are absolutely and uniformly convergent for $k \neq 0$ in any finite region. At $k = 0$, the general solution to Laplace's equation becomes

$$\tilde{\psi}(u,v,k) = \sum_{m=0}^{\infty} \alpha(k)\cosh(mu)\cos(mv) + \beta(k)\sinh(mu)\sin(mv) \tag{D.73}$$

and the limiting forms of the above relations are

$$\sinh(nu)\sin(nv) = \sum_{m=0}^{[n/2]} b_m^n \left(\frac{\rho}{f}\right)^{n-2m} \sin[(n-2m)\phi], \tag{D.74a}$$

$$\cosh(nu)\cos(nv) = \sum_{m=0}^{[n/2]} b_m^n \left(\frac{\rho}{f}\right)^{n-2m} \cos[(n-2m)\phi], \tag{D.74b}$$

where

$$b_m^n = (-1)^m \frac{n}{m} \binom{n-m-1}{m-1} 2^{n-2m-1}, \tag{D.75}$$

$$b_0^n = 2^{n-1}. \tag{D.76}$$

These may be used to obtain limiting expressions for the on-axis gradients as $k \to 0$:

$$\tilde{C}_{n,s}(0) = f^{-n} 2^{n-1} \left[\frac{F_n}{n\cosh(nU)} + \sum_{L=1}^{\infty} (-1)^L \frac{1}{L} \binom{n+L-1}{L-1} \frac{F_{L+2n}}{\cosh((n+2L)U)} \right], \tag{D.77a}$$

$$\tilde{C}_{n,c}(0) = f^{-n} 2^{n-1} \left[\frac{F_n}{n\sinh(nU)} + \sum_{L=1}^{\infty} (-1)^L \frac{1}{L} \binom{n+L-1}{L-1} \frac{F_{L+2n}}{\sinh((n+2L)U)} \right]. \tag{D.77b}$$

We demonstrate the first Mathieu-Bessel identity (D.71a) above, and the others follow similarly. The demonstration follows a remark of Erdélyi [31]. The general solution of the Helmholtz equation regular at the origin can be written

$$\tilde{\psi}(\rho, \phi, k) = \sum_{-\infty}^{\infty} D_n(k) I_n(k\rho) e^{in\phi}. \tag{D.78}$$

In elliptic coordinates, we have the interior solutions

$$Ce_{2m}(u,k)ce_{2m}(v,k) = \sum_{-\infty}^{\infty} D_n(k) I_n(k\rho) e^{in\phi}. \tag{D.79}$$

To determine the coefficients $D_n(k)$, note that the right hand side of (D.79) can be expressed in elliptic coordinates using

$$\rho = f[cosh(u+iv)cosh(u-iv)]^{1/2}, \tag{D.80}$$

$$e^{in\phi} = \left[\frac{cosh(u)+iv}{cosh(u)-iv}\right]^{n/2}. \tag{D.81}$$

Letting

$$\begin{aligned} F_n(u,v,k) &= I_n(k\rho)e^{in\phi} \qquad (D.82)\\ &= I_n(kf[[cosh(u+iv)cosh(u-iv)]^{1/2}])\left[\frac{cosh(u)+iv}{cosh(u)-iv}\right]^{n/2}, \end{aligned}$$

we have

$$Ce_{2m}(u,k)ce_{2m}(v,k) = \sum_{-\infty}^{\infty} D_n(k)F_n(u,v,k). \tag{D.83}$$

Now define the differential operator

$$\mathcal{L} = \partial_v^2 + \lambda + \frac{k^2f^2}{2}\cos(2v), \tag{D.84}$$

where λ is the characteristic value for ce_{2m} as described in Section D.1. Mathieu's equation (D.1) can then be written

$$\mathcal{L}[ce_{2m}(v,k)] = 0. \tag{D.85}$$

Acting on (D.83) from the left, we have that

$$\sum_{-\infty}^{\infty} D_n^{2m}(k)\mathcal{L}[F_n(u,v,k)] = 0. \tag{D.86}$$

We need to know how the differential operator acts on the function F_n. Use of recursion relations involving the modified Bessel functions allows us to write

$$\mathcal{L}F_n = (\lambda - n^2)F_n + \frac{k^2f^2}{4}[F_{n-2} + F_{n+2}]. \tag{D.87}$$

Using (D.86) we have that

$$\sum_{-\infty}^{\infty}\{D_n^{2m}(k)(\lambda-n^2)+\frac{k^2f^2}{4}[D_{n+2}^{2m}(k)+D_{n-2}^{2m}(k)]\}F_n=0. \tag{D.88}$$

We know that the F_n are orthogonal functions, and therefore the D_n^{2m} must obey recursion relations of the form

$$D_n^{2m}(k)(\lambda-n^2)+\frac{k^2f^2}{4}[D_{n+2}^{2m}(k)+D_{n-2}^{2m}(k)]=0. \tag{D.89}$$

Suppose we write

$$ce_{2m}(v,k)=\sum_{-\infty}^{\infty}E_n^{2m}(k)e^{inv} \tag{D.90}$$

such that the E_n^{2m} are related to coefficients A_n^{2m} by $E_0^{2m}=A_0^{2m}$ and $E_n^{2m}=\frac{1}{2}A_{2n}^{2m}$. Then

$$\sum_{n=-\infty}^{\infty}E_n^{2m}(k)\mathcal{L}e^{inv}=0, \text{ and} \tag{D.91}$$

$$\mathcal{L}e^{inv}=(\lambda-n^2)e^{inv}+\frac{k^2f^2}{4}[e^{iv(n-2)}+e^{iv(n+2)}]. \tag{D.92}$$

It follows that the coefficients E_n^{2m} obey the same recursion relations as the D_n^{2m}. Consequently, for fixed k, the coefficients are multiples,

$$D_n^{2m}(k)=g_c^{2m}(k)E_n^{2m}(k). \tag{D.93}$$

Therefore,

$$\begin{aligned} Ce_{2m}(u,k)ce_{2m}(v,k) &= g_c^{2m}(k)\sum_{n=-\infty}^{\infty}E_n^{2m}(k)I_n(k\rho)e^{in\phi} \\ &= g_c^{2m}(k)\sum_{n=0}^{\infty}A_n^{2m}(k)I_n(k\rho)e^{in\phi}, \end{aligned} \tag{D.94}$$

as desired. The factor g_c^{2m} is obtained by equating the limits $u\to 0$,$v\to\frac{\pi}{2}$ of each side of (D.94). A similar procedure is used to demonstrate the other three relations in (D.71).

These results may also be proven using (D.43) together with integral representations of the Bessel functions.

D.3 Numerical Computation

The methods of Section D.2 were used for making the analytical estimates in Section 3.4. Here we describe the methods used to compute the quantities $a_n(q)$, $b_n(q)$, $ce_m(v,q)$, $se_m(v,q)$, $Ce_m(u,q)$, $Se_m(u,q)$, $A_n^m(q)$, $B_n^m(q)$, $g_c^l(k)$, and $g_s^l(k)$, with high numerical accuracy, as is required for the numerical implementation outlined in Section 3.2.

The characteristic values $a_n(q)$ and $b_n(q)$ were obtained using the routine "CVA2" described in [32], which is numerically stable and produces values that agree well with those produced by Mathematica for a range of n and q. After computing the appropriate characteristic value $\lambda = a_n$ or b_n, the corresponding Mathieu function and its Fourier coefficients were computed by integrating a corresponding system of equations using an 11th order Adams integrator. For example, the Fourier coefficients $B_n^m(q)$ of the Mathieu function $se_m(v,q)$ were computed together with the angular coefficients $F_m(U,k)$ of (3.8) by integrating the system

$$f_1'(t) = f_2(t), \qquad f_2'(t) = -[\lambda - 2q\cos(2t)]f_1(t), \tag{D.95a}$$

$$f_3'(t) = [f_1(t)]^2, \qquad f_4'(t) = f_1(t)\sqrt{J(U,t)}\tilde{B}_u(u=U,t), \tag{D.95b}$$

$$f_5'(t) = f_1(t)\sin(t), \qquad f_6'(t) = f_1(t)\sin(nt), \tag{D.95c}$$

from $t = 0$ to $t = 2\pi$, subject to the initial conditions $f_k(0) = 0$ for $k \neq 2$ and $f_2(0) = 1$. Note that the pair of equations (D.95a) is equivalent to Mathieu's

equation for the function f_1. The appropriate normalization for f_1 is determined by the quantity N, where

$$N^2 = \frac{f_3}{\pi} = \frac{1}{\pi}\int_0^{2\pi} f_1(t)^2 dt. \tag{D.96}$$

Note that $N = 1$ if $f_1(t) = se_m(t, q)$ for all t, q. In this way, we obtain the functions $F_m(U, k) = f_4(2\pi)/(\pi N)$, the Fourier coefficients $B_n^m(q) = f_6(2\pi)/(\pi N)$, and so on. When values of $se_m(v, q)$ are required for $v \neq 2\pi$, a similar integration is performed from $t = 0$ to $t = v$, using the normalization determined above. The values of $ce_m(v, q)$ may be similarly obtained by changing the initial conditions for equations (D.95a) such that $f_1(0) = 1$ and $f_2(0) = 0$. As one benchmark of this technique, we verified that the computed functions $se_m(v, q)$ and $ce_m(v, q)$ satisfy the conditions $se_m(0, q) = se_m(2\pi, q)$ and $ce_m(0, q) = ce_m(2\pi, q)$ to high accuracy for a range of q. This benchmark also validates the accuracy of the CVA2 routine. The functions $Ce_m(u, q)$ and $Se_m(u, q)$ were computed similarly, by integrating the Modified Mathieu equation together with the appropriate initial conditions.

Finally, the functions $g_c^l(k)$ and $g_s^l(k)$ can be computed using expressions (D.72). Note the poor limiting behavior of these expressions as $k \to 0$. However, the quantities $g_c^r(k)$ and $g_s^r(k)$ appear in our expressions for the kernels $\Lambda_{n,\alpha}^r(k)$ of Chapter 3. Limiting arguments can be used to show that these kernels are well-behaved as $k \to 0$. Motivated by this result, we computed products of the form $k^r g_s^n(k) B_r^n(q)$ and $k^r g_c^n(k) A_r^n(q)$ as they appear in (3.28-3.29). It can be shown using (D.11c), for example, that the quantities $k^{r-1} B_r^n(q)/B_1^n(q)$ obey a recursion relationship in the index r, each term of which is well-behaved as $k \to 0$. These were used to determine

numerically the ratios $k^{r-1}B_r^n(q)/B_1^n(q)$ as they appear in the kernels $\Lambda_{n,\alpha}^r(k)$. For example, let

$$R_r = \left(\frac{q}{4}\right)^{(r-1)/2} \frac{B_r^{(n)}(q)}{B_1^{(n)}(q)}, \tag{D.97}$$

$$V_r = \frac{1}{4}(b_n - r^2), \tag{D.98}$$

where $q = -k^2 f^2/4$. Then the quantities R_r and V_r are $O(1)$ as $q \to 0$, and obey the recursion

$$R_1 = 1, \tag{D.99}$$

$$R_3 = V_1 + q/4, \tag{D.100}$$

$$R_{r+2} = V_r R_r - \left(\frac{q}{4}\right)^2 R_{r-2}. \tag{D.101}$$

Similar relationships exist for the other products of this form.

Appendix E

Alternative Wiggler Fitting Techniques

E.1 Idealized wiggler models

An ideal wiggler is a periodic array of alternating dipole magnets whose purpose is to decrease the beam emittance through radiation damping, while minimizing other effects on beam dynamics. In the simplest approximation, we suppose that the magnet is periodic in z and uniform in x. It can be shown that the field is uniquely determined by its values in the x-z plane. In particular, we require that the midplane field be vertical. In the case of a single longitudinal mode, the midplane field is then $B_y(x,z) = B_y \sin(kz+\phi)$, where $k = \frac{2\pi}{\lambda_w}$ and λ_w is the wiggler period. If we consider higher modes in z, then we have

$$B_y(x,y,z) = \sum_{n=1}^{N_z} B_y^{(n)} \cosh[(2n-1)ky] \sin[(2n-1)kz+\phi_n], \tag{E.1a}$$

$$B_z(x,y,z) = \sum_{n=1}^{N_z} B_y^{(n)} \sinh[(2n-1)ky] \cos[(2n-1)kz+\phi_n], \tag{E.1b}$$

$$B_x(x,y,z) = 0. \tag{E.1c}$$

We will see that due to symmetry considerations, only odd modes contribute. Even ideal fields of the form (E.1) generate linear focusing and nonlinear perturbations of the beam dynamics.

We now consider deviations from the ideal wiggler. Any real wiggler has finite width poles, and as a result we have a transverse field roll-off in x. This introduces

a number of new features. In particular, we have that $B_x = 0$ at the poles faces while $B_x \neq 0$ in the interior. Furthermore, the finite length and nonzero fringe fields of the wiggler ensure that longitudinal modes other than those appearing in (E.1) contribute to the total field. As an example of a realistic wiggler field, consider the numerical model of the prototype ILC wiggler described in Chapter 3. We illustrate in Fig. E.1 the first three nonvanishing angular Mathieu coefficients $F_m(k)$ obtained by fitting the field to the surface on an elliptical cylinder as described in Section 3.3.2. The sharp, uniformly spaced peaks are located at odd multiples of the fundamental spatial frequency $k = \frac{2\pi}{\lambda_w}$, as seen in (E.1). However, note the nontrivial behavior of these functions for other spatial frequencies.

E.2 Fourier fitting

Alternative methods of modeling realistic wiggler fields have been developed that do not require a Fourier transform. We discuss a method used by Sagan and others at Cornell [54] that relies on nonlinear optimization. The field is written as

$$\mathbf{B}_{fit} = \sum_{n=1}^{N} \mathbf{B}_n(x, y, z; C_n, k_{xn}, k_{zn}, \phi_{zn}, f_n), \tag{E.2}$$

where each term $\mathbf{B}_n$ is written in one of three forms, indexed by $f_n = 1, 2, 3$. The first form, with $f_n = 1$, is given as:

$$B_x = -C\frac{k_x}{k_y}\sin(k_x x)\sinh(k_y y)\cos(k_z z + \phi_z), \tag{E.3a}$$

$$B_y = C\cos(k_x x)\cosh(k_y y)\cos(k_z z + \phi_z), \tag{E.3b}$$

$$B_z = -C\frac{k_z}{k_y}\cos(k_x x)\sinh(k_y y)\sin(k_z z + \phi_z), \tag{E.3c}$$

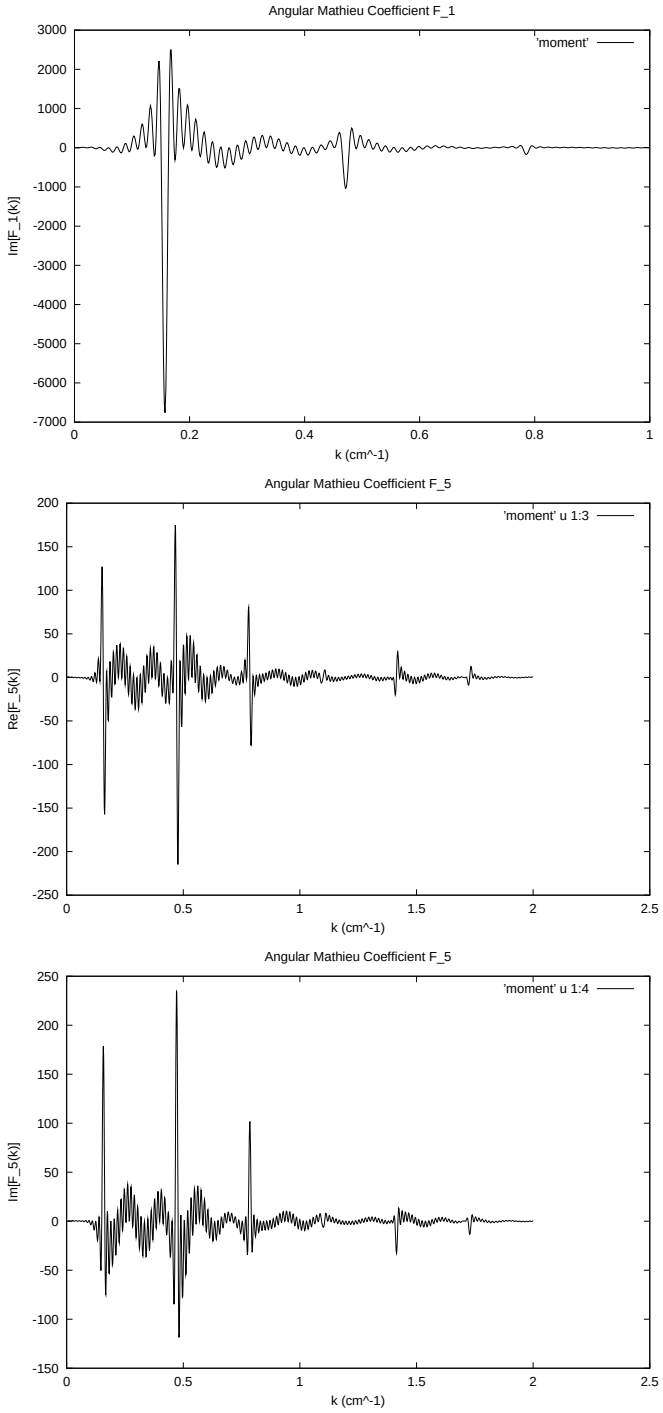

Figure E.1: The first three nonvanishing coefficients $F_1(k)$, $F_3(k)$, and $F_5(k)$ contributing to the field of the prototype ILC wiggler, illustrating the dominant longitudinal modes.

with the constraint $k_y^2 = k_x^2 + k_z^2$, imposed to ensure that $\mathbf{B}$ satisfies $\nabla \times \mathbf{B} = 0$, $\nabla \cdot \mathbf{B} = 0$. The second form $f_n = 2$ is given as

$$B_x = C\frac{k_x}{k_y}\sinh(k_x x)\sinh(k_y y)\cos(k_z z + \phi_z), \tag{E.4a}$$

$$B_y = C\cosh(k_x x)\cosh(k_y y)\cos(k_z z + \phi_z), \tag{E.4b}$$

$$B_z = -C\frac{k_z}{k_y}\cosh(k_x x)\sinh(k_y y)\sin(k_z z + \phi_z), \tag{E.4c}$$

where $k_y^2 = k_z^2 - k_x^2$. The third form $f_n = 3$ is

$$B_x = C\frac{k_x}{k_y}\sinh(k_x x)\sin(k_y y)\cos(k_z z + \phi_z), \tag{E.5a}$$

$$B_y = C\cosh(k_x x)\cos(k_y y)\cos(k_z z + \phi_z), \tag{E.5b}$$

$$B_z = -C\frac{k_z}{k_y}\cosh(k_x x)\sin(k_y y)\sin(k_z z + \phi_z), \tag{E.5c}$$

where $k_y^2 = k_x^2 - k_z^2$. We let $f_n = 1$ if $0 < k_x$, $f_n = 2$ if $-|k_z| \leq k_x \leq 0$, and $f_n = 3$ if $k_x < -|k_z|$.

The set of parameters $\{C_n, k_{xn}, k_{zn}, \phi_{zn} : n = 1, ..., N\}$ is allowed to vary continuously, in such a way as to minimize the merit function:

$$M = \sum_{\text{data pts}} |\mathbf{B}_{fit} - \mathbf{B}_{data}|^2 + w_c \sum_{n=1}^{N} |C_n|, \tag{E.6}$$

where the sum of residuals is taken over all points in the interior of a box lying on a uniform rectangular mesh with uniform spacing in x, y, and z . Note that the parameters k_x, k_y are allowed to take on any value, and are not confined to transverse modes available for specific boundary values. As a result, the expression for $\mathbf{B}$ is a linear combination of solutions to Maxwell's equations, corresponding terms of which are in general not orthogonal. This method has the advantage of avoiding a

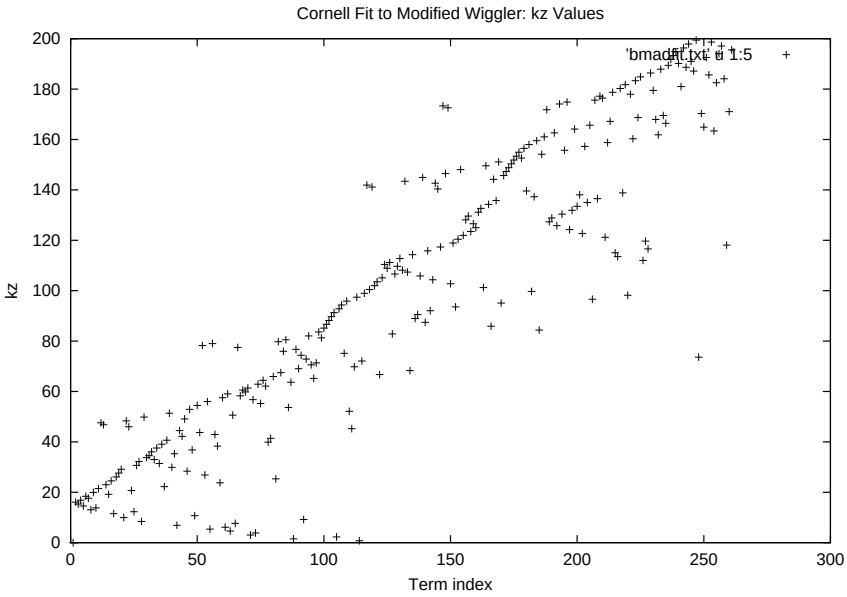

Figure E.2: Set of values k_z selected for use in fitting the field of the Cornell ILC wiggler prototype. These are obtained by minimizing (E.6).

large number of Fourier transforms. However, convergence of $\mathbf{B}_{fit}$ with increasing index N is not guaranteed, and the set of available solutions is not guaranteed to be complete. That is, it is possible that there may be solutions which cannot be approximated arbitrarily closely by this algorithm. Finally, the optimization process required to minimize the merit function M requires extensive computation, typically one day on a fast workstation.

Fig. E.2 illustrates the set of values k_z resulting from the optimization for the Cornell wiggler design. In this case, all k_x values are equal, and the k_z values are uniformly distributed between $[0, 200]$, in no particular order. Here $f_n = 1$ for all n.

This method may also be used to numerically estimate various derivatives of

the true field, by differentiating (E.2). In particular, we may numerically estimate the on-axis gradient functions $C_n^m(z)$ of Chapters 2-4 by using the expression (E.2) for $\mathbf{B}_{fit}$. We wish to compare the on-axis gradient functions obtained in this manner with those obtained using boundary-value data on the surface on an elliptical cylinder, as described in Section 3.3.2. Because $f_n = 1$ for all n, we may use (E.3) to write $\mathbf{B} = \nabla\psi$ where

$$\psi(x, y, z) = \sum_{n=1}^{N} C_n g_n(x, y) \cos(k_{zn} z + \phi_n). \tag{E.7}$$

For terms with $f_n = 1$, we have $g_n(x, y) = \frac{1}{k_{yn}} \cos(k_{xn} x) \sinh(k_{yn} y)$. This is to be compared with the expression

$$\psi(x, y, z) = \sum_{m=0}^{\infty} \sum_{l=0}^{\infty} \kappa_{l,2m+1} (x^2 + y^2)^l C_{2m+1,s}^{[2l]}(z) \mathcal{I}m(x + iy)^{(2m+1)}. \tag{E.8}$$

Comparing the series for (E.7) term by term with that above, we find that the on-axis gradients can be written

$$C_m^{[2l]}(z) = \sum_{n=1}^{N} C_n f_{m,l}(k_{xn}, k_{yn}) \cos(k_{zn} z + \phi_n), \tag{E.9}$$

where the functions $f_{m,l}$ are homogeneous polynomials in the variables k_x and k_y of degree $m + 2l - 1$. The first few are listed below.

$$f_{1,0} = 1, \tag{E.10a}$$

$$f_{1,1} = k_x^2 - k_y^2, \tag{E.10b}$$

$$f_{3,0} = -\frac{1}{8} k_x^2 - \frac{1}{24} k_y^2, \tag{E.10c}$$

$$f_{1,2} = (k_x^2 - k_y^2)^2, \tag{E.10d}$$

$$f_{3,1} = \frac{1}{24}(-3k_x^4 + k_y^4 + 2k_x^2 k_y^2), \tag{E.10e}$$

$$f_{5,0} = \frac{1}{384}(k_x^4 + \frac{1}{5} k_y^4 + 2k_x^2 k_y^2). \tag{E.10f}$$

In Figs. E.3-E.5, these gradients are compared with those obtained from the method described in Section 3.3.2. We find agreement to 4×10^{-5} for the lowest-lying gradient $C_1(z)$, while the difference increases with increasing order. For $C_1^4(z)$ we find a difference (relative to peak) of 0.03, for $C_3(z)$ of 0.01, and for $C_5(z)$ of 0.3, a full 30 percent. We conclude that, while this method provides excellent agreement to the field values $\mathbf{B}_{data}$ themselves, significant errors may appear in the high-order derivatives of the field (as represented by the high-order on-axis gradient functions). Nevertheless, techniques using fields of the form (E.2) might in principle be used in conjunction with boundary-value fitting to improve accuracy in these high-order derivatives.

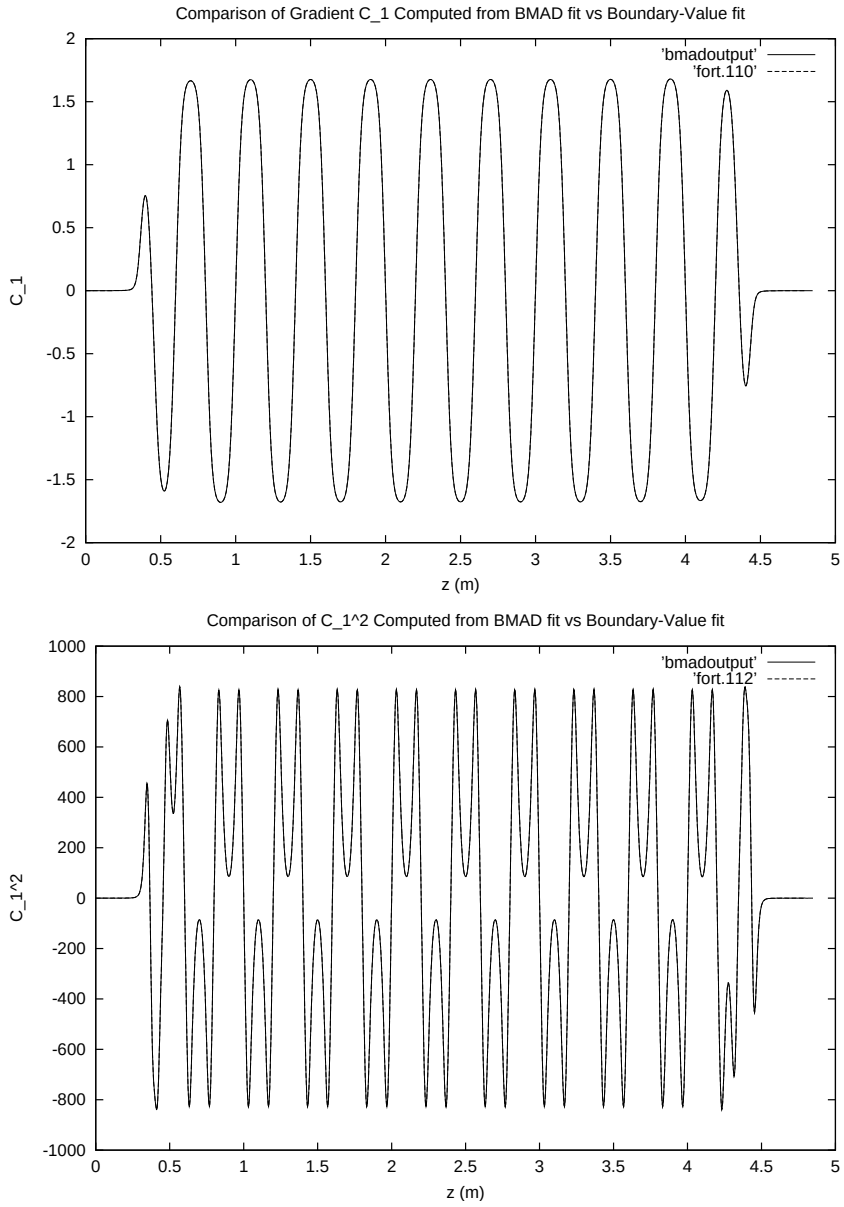

Figure E.3: Comparison of on-axis gradient functions for the field of the prototype ILC wiggler obtained by fitting using (E.9) versus fitting to an elliptical cylinder as in Section 3.3.2. Solid lines denote values obtained using (E.9), while dotted lines denote values computed by fitting to an elliptical cylinder. (Upper) The function $C_{1,s}$. (Lower) The function $C_{1,s}^2$. The two curves in each figure are nearly indistinguishable in this case.

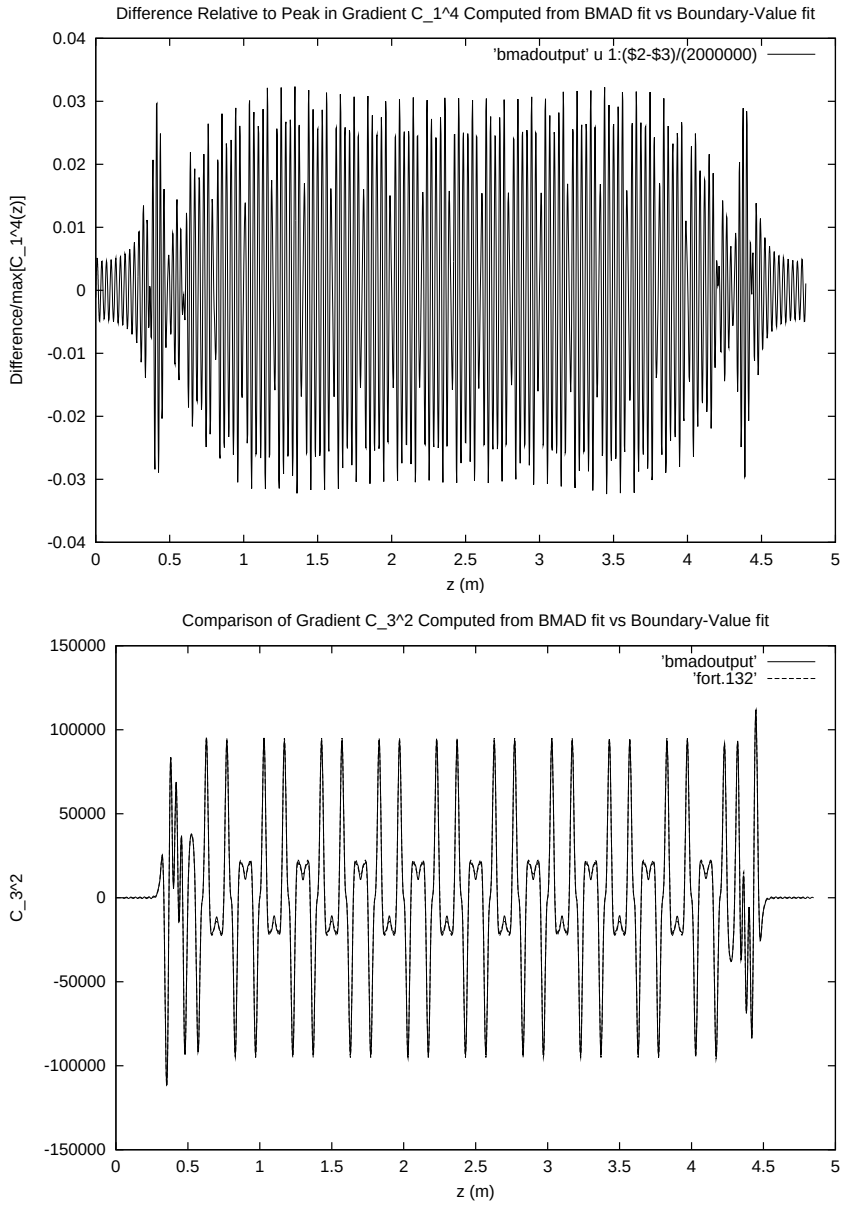

Figure E.4: Comparison of on-axis gradient functions for the field of the prototype ILC wiggler computed using (E.9) versus fitting to an elliptical cylinder as in Section 3.3.2. (Upper) The relative difference between the compared values of $C^4_{1,s}$. (Lower) The function $C^2_{3,s}$. Solid lines denote values obtained using (E.9), while dotted lines denote values computed by fitting to an elliptical cylinder.

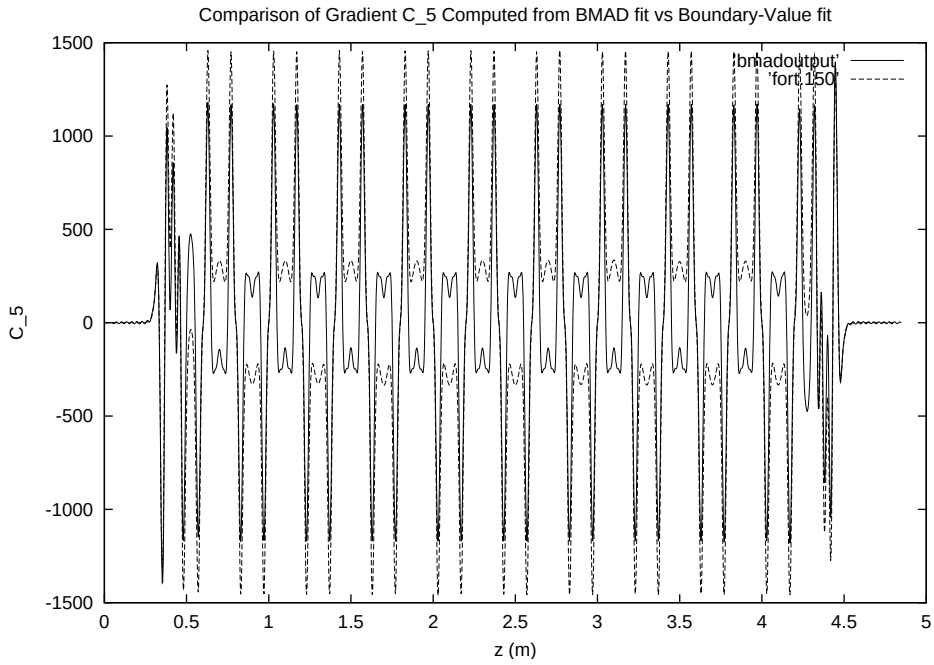

Figure E.5: Comparison of on-axis gradient functions for the field of the prototype ILC wiggler computed using (E.9) versus fitting to an elliptical cylinder as in Section 3.3.2. Here is illustrated a comparision for the function $C_{5,s}$.

Appendix F

Separability of Laplace and Helmholtz Equations

In the following appendix, we classify those coordinate systems in which the equation

$$(\nabla^2 + \omega^2)\Psi = 0 \tag{F.1}$$

can be solved by separation of variables, treating the Laplace equation $\omega = 0$ as a special case. The following treatment presents key results briefly and without proof. For details, see [75] or [76].

Consider some set of orthogonal curvilinear coordinates (u, v, w) on $\mathbb{R}^3$, such that the line element $ds^2 = dx^2+dy^2+dz^2$ can be written $ds^2 = Fdu^2+Gdv^2+Hdw^2$. We will be interested in solutions to (F.1) of the form $\Psi(u, v, w) = U(u)V(v)W(w)$. More generally, we say that a solution is *R-separable* if it takes the form $\Psi(u, v, w) = \exp[R(u, v, w)]U(u)V(v)W(w)$, where the function R is independent of all separation constants. The case $R = 0$ then describes a usual separation of variables. We will see that the set of coordinates for which (F.1) is R-separable is characterized by the symmetries of (F.1). In particular, each separable coordinate system corresponds to a pair of second-order symmetry operators of (F.1). The separated solutions are then simultaneous eigenfunctions of these two operators, and the corresponding eigenvalues are the two separation constants parametrizing the family of separated solutions. In the following section, we provide some necessary definitions

from Lie theory. Applications to the Helmholtz and Laplace equations follow.

F.1 Preliminary Definitions

Let D be some open connected set in $\mathbb{R}^3$. We let $\mathcal{F}$ denote the vector space of all complex-valued functions that are real-analytic on D. That is, given a function f in $\mathcal{F}$ and a point $\mathbf{r}$ in D, f may be represented as a Taylor series about $\mathbf{r}$ in the three variables (x, y, z), converging in some ball containing $\mathbf{r}$. We are interested in the partial differential operator $Q = \nabla^2 + \omega^2$ appearing in (F.1). Note that Q is a linear operator on $\mathcal{F}$. The set of all solutions to $Q\Psi = 0$ therefore forms a subspace $\mathcal{F}_0$ of $\mathcal{F}$, called the *solution space* of (F.1). Thus, $\mathcal{F}_0 = \mathrm{Ker}(Q)$ is the null space of the linear operator Q.

Definition A linear operator of the form $L = B_x\partial_x + B_y\partial_y + B_z\partial_z + C$, with each B_i a real analytic function in $\mathcal{F}$, is a *symmetry operator* for (F.1) provided

$$[L, Q] = RQ \tag{F.2}$$

for some function $R \in \mathcal{F}$, where R may vary with L. All first-order differential operators that commute with Q are symmetry operators. The key feature of a symmetry operator L is that it maps solutions of (F.1) into solutions, $\Psi \in \mathcal{F}_0 \Rightarrow L\Psi \in \mathcal{F}_0$. The set $\mathcal{G}$ of symmetry operators forms a vector space, which becomes a Lie algebra if we introduce the bracket product $[,]$ given by the usual commutator. That is, any linear combination of symmetry operators is again a symmetry operator, and the commutator of any two symmetry operators is again a symmetry operator.

The first-order differential operators L defined above may be extended to con-

struct a representation for a local Lie group G, the *symmetry group* of (F.1). That is, G is the connected Lie group which has $\mathcal{G}$ as its Lie algebra. The following sections will investigate the symmetry group of (F.1). For the purposes of separation of variables, we will be interested in second-order symmetries. We may treat such higher-order symmetries as follows.

Definition Given the Lie algebra $\mathcal{G}$, we may construct its *universal enveloping algebra*, denoted $U(\mathcal{G})$. Let $\{L_1, L_2, ..., L_n\}$ be a basis for $\mathcal{G}$. Then $U(\mathcal{G})$ is the algebra of polynomials in the variables $(L_1, L_2, ..., L_n)$, where the associative product is given by operator composition. We require that $AB - BA = [A, B]$ for any elements A, B in $\mathcal{G}$. A basis for $U(\mathcal{G})$ is the set of monomials of the form $\{L_1^{p_1} L_2^{p_2} ... L_n^{p_n} : p_i \in \mathbb{Z}\}$ such that p_i are positive integers. For the Lie algebra of symmetry operators, $U(\mathcal{G})$ can be identified with the space of differential operators on $\mathcal{F}$ obtained by composing the first-order differential operators in $\mathcal{G}$. Furthermore, the commutator may be extended to apply to all elements in $U(\mathcal{G})$. Note that the commutator $[A, B]$ of a differential operator A of order p with a differential operator B of order q is an operator of order $p + q - 1$.

Definition A second-order operator $S = \sum_{i,j=1}^{3} A_{ij}\partial_i\partial_j + \sum_{i=1}^{3} B_i\partial_i + C$ is a *symmetry operator* for (F.1) provided

$$[S, Q] = UQ \tag{F.3}$$

where $U = H_1\partial_x + H_2\partial_y + H_3\partial_z + J$ for some $H_j, J \in \mathcal{F}$. The set of second-order symmetry operators forms a vector space, which we denote $\mathcal{S}$. A differential equation is called *class I* if the set of all second-order symmetries $\mathcal{S}$ is contained in $U(\mathcal{G})$. Both

the Helmholtz and Laplace equations are class I. That is, all second-order symmetries of (F.1) can be expressed as quadratic polynomials in the first-order symmetries in $\mathcal{G}$.

Definition The group G can be represented as a set of linear operators on the space of second-order symmetries $\mathcal{S}$ as follows. Let $g \in G$ be an element of the symmetry group of (F.1). Let $T(g)$ denote a representation of g on the space of analytic functions $\mathcal{F}$, and let $T(g)^{-1}$ denote its inverse. The group element g then defines a linear operator $\hat{g}$ on the space $\mathcal{S}$ which acts as follows. Given $S \in \mathcal{S}$,

$$\hat{g}S = T(g)ST(g)^{-1}. \tag{F.4}$$

It follows that $\hat{g}S$ is a second-order symmetry operator. Such a representation of the group G is called the *adjoint representation*. Note that the action of G decomposes $\mathcal{S}$ into orbits of equivalent subspaces. We say that S lies on the same orbit as S' if $S = c(\hat{g}S')$ for some nonzero $c \in \mathbb{R}$ and some $g \in G$. [76]

F.2 Application to the Helmholtz Equation

The symmetry algebra $\mathcal{G}$ of the Helmholtz equation (F.1) for $\omega \neq 0$ is 6-dimensional, with a basis given by

$$P_1 = \partial_x, \qquad P_2 = \partial_y, \qquad P_3 = \partial_z, \tag{F.5a}$$

$$J_1 = z\partial_y - y\partial_z, \qquad J_2 = x\partial_z - z\partial_x, \qquad J_3 = y\partial_x - x\partial_y, \tag{F.5b}$$

with commutation relations

$$[P_i, P_j] = 0, \qquad [J_i, P_j] = \sum_{k=1}^{3} \epsilon_{ijk} P_k, \qquad [J_i, J_j] = \sum_{k=1}^{3} \epsilon_{ijk} J_k, \tag{F.6}$$

where ϵ_{ijk} is the Levi-Civita tensor. Thus, $\mathcal{G}$ is isomorphic to the Lie algebra $\mathcal{E}(3)$ of the Euclidean group $E(3)$. In terms of these operators, the Helmholtz equation may be written:

$$(P_1^2 + P_2^2 + P_3^2)\Psi = -\omega^2\Psi. \tag{F.7}$$

The symmetry group $E(3)$ can be represented as a group of transformations on Euclidean three-space $\mathbb{R}^3$. The Euclidean group $E(3)$ is the set of isometries of the Euclidean metric as follows. Given two points $\mathbf{x}_1$ and $\mathbf{x}_2$ in $\mathbb{R}^3$, each element $g \in E(3)$ has the property $\langle g\mathbf{x}_1, g\mathbf{x}_2\rangle = \langle \mathbf{x}_1, \mathbf{x}_2\rangle$, where $\langle , \rangle$ denotes the vector dot product. The group $E(3)$ is not connected. The component of $E(3)$ which contains the identity is the subgroup $E^+(3)$ of isometries preserving orientation, also called *rigid motions*. The rigid motions consist of the translation group T, generated by the three P_i, and the rotation group $SO(3)$, generated by the three J_i. The action of $E^+(3)$ on $\mathbb{R}^3$ is given for $\mathbf{x} = (x, y, z)$ by the affine transformation

$$g\mathbf{x} = A\mathbf{x} + \mathbf{a}, \tag{F.8}$$

where A is a rotation matrix in $SO(3)$ so that $A^tA = E$ and $det(A) = +1$. Thus g corresponds to a rotation about the origin followed by a translation $\mathbf{a}$. The group $SO(3)$ may be parametrized by the Euler angles $0 \le \phi < 2\pi$, $0 \le \theta \le \pi$, $0 \le \psi < 2\pi$, such that

$$A = \begin{pmatrix} \cos\phi & \sin\phi & 0 \\ -\sin\phi & \cos\phi & 0 \\ 0 & 0 & 1 \end{pmatrix} \begin{pmatrix} 1 & 0 & 0 \\ 0 & \cos\theta & \sin\theta \\ 0 & -\sin\theta & \cos\theta \end{pmatrix} \begin{pmatrix} \cos\psi & \sin\psi & 0 \\ -\sin\psi & \cos\psi & 0 \\ 0 & 0 & 1 \end{pmatrix}. \tag{F.9}$$

The local representation T of $E(3)$ on the space of real-analytic functions $\mathcal{F}$ is given by

$$T(g)\Psi(\mathbf{x}) = T\left[\exp(\phi J_3)\exp(\theta J_1)\exp(\psi J_3)\exp(\mathbf{a}\cdot\mathbf{P})\right]\Psi(\mathbf{x}) = \Psi(g\mathbf{x}), \tag{F.10}$$

where $g\mathbf{x}$ is given by (F.8).

F.2.1 Separation of Variables

Consider the set of purely second-order symmetry operators in the enveloping algebra $U(\mathcal{G})$, which we denote by $\mathcal{S}^{(2)}$. These are polynomials of the form $P_l P_m$, $J_l J_m$, and $P_l J_m$. These form a vector space spanned by the 21 operators [1]

$$\{J_l,J_m\}, \qquad \{J_l,P_m\}, \qquad \{P_l,P_m\}, \tag{F.11}$$

where the notation $\{\cdot,\cdot\}$ denotes the anticommutator, such that $\{A,B\} = AB+BA$. We seek a representation of $\mathcal{S}^{(2)}$ on the solution space $\mathcal{F}_0$ of the Helmholtz equation. As differential operators on the space $\mathcal{F}_0$, the elements of $\mathcal{S}^{(2)}$ obey the identities

$$\mathbf{J}\cdot\mathbf{P} = J_1P_1 + J_2P_2 + J_3P_3 = 0, \tag{F.12}$$

$$\mathbf{P}\cdot\mathbf{P} = P_1^2 + P_2^2 + P_3^2 = -\omega^2, \tag{F.13}$$

as required by (F.1). The space of distinct second-order operators on $\mathcal{F}_0$ therefore has dimension 19.

Miller [76] makes the following claims:

1) Each separable coordinate system is associated with a two-dimensional subspace of $U(\mathcal{G})$ spanned by commuting operators S_1, $S_2 \in \mathcal{S}^{(2)}$.

2) The separated solutions $\Psi_{kl} = U(u)V(v)W(w)$ are characterized by the eigenvalue equations

$$Q\Psi_{kl} = 0, \qquad S_1\Psi_{kl} = k^2\Psi_{kl}, \qquad S_2\Psi_{kl} = l^2\Psi_{kl}, \tag{F.14}$$

[1] This count disagrees with that appearing in [76]. Note that $\{J_j,J_k\} = \{J_k,J_j\}$, etc. by construction.

where the k, l are separation constants.

3) The symmetry group $G = E(3)$ acts via the adjoint representation on the set of all two-dimensional subspaces of commuting operators in $\mathcal{S}^{(2)}$, and decomposes this set into orbits of equivalent subspaces. Separable coordinates associated with equivalent subspaces are considered equivalent, since one can obtain any such coordinate system from any other using a symmetry transformation in $E(3)$.

It can be shown using (F.5) that the separable coordinate systems for the Helmholtz equation fall into exactly 11 distinct equivalence classes. This relationship is illustrated in Table (F.1). The coordinate surfaces are orthogonal families of confocal *quadratic surfaces* of the form

$$\frac{x^2}{a_1+\lambda} + \frac{y^2}{a_2+\lambda} + \frac{z^2}{a_3+\lambda} = 1 \tag{F.15}$$

for constants a_i, together with their degenerate forms. These are ellipsoids, hyperboloids, paraboloids, spheres, and planes.

Table F.1: Separable Coordinates for the Helmholtz Equation

Commuting operators S_1, S_2	Separable coordinates	Solutions
1. P_2^2, P_3^2	Cartesian x, y, z	Exponentials
2. J_3^2, P_3^2	Cylindrical $x = r\cos\phi$ $y = r\sin\phi$, $z = z$	Bessel functions
3. $\{J_3, P_2\}$, P_3^2	Parabolic cylindrical $x = (\xi^2 - \eta^2)/2$ $y = \xi\eta$, $z = z$	Parabolic cylinder functions
4. $J_3^2 + d^2P_1^2$, P_3^2	Elliptic cylindrical $x = d\cosh u\cos v$ $y = d\sinh u\sin v$, $z = z$	Mathieu functions
5. $\mathbf{J}\cdot\mathbf{J}$, J_3^2	Spherical $x = \rho\sin\theta\cos\phi$ $y = \rho\sin\theta\sin\phi$, $z = \rho\cos\theta$	Spherical harmonics
6. $\mathbf{J}\cdot\mathbf{J} - a^2(P_1^2 + P_2^2)$, J_3^2	Prolate spheroidal $x = a\sinh\eta\sin\alpha\cos\phi$ $y = a\sinh\eta\sin\alpha\sin\phi$ $z = a\cosh\eta\cos\alpha$	Spheroidal wave functions Ps_n^m
7. $\mathbf{J}\cdot\mathbf{J} + a^2(P_1^2 + P_2^2)$, J_3^2	Oblate spheroidal $x = a\cosh\eta\sin\alpha\cos\phi$ $y = a\cosh\eta\sin\alpha\sin\phi$ $z = a\sinh\eta\cos\alpha$	Spheroidal wave functions
8. $\{J_1, P_2\} - \{J_2, P_1\}$, J_3^2	Parabolic $x = \xi\eta\cos\phi$ $y = \xi\eta\sin\phi$ $z = (\xi^2 - \eta^2)/2$	Confluent hypergeometric functions
9. $J_3^2 - c^2P_3^2 +$ $c(\{J_2, P_1\} + \{J_1, P_2\})$, $c(P_2^2 - P_1^2) +$ $\{J_2, P_1\} - \{J_1, P_2\}$	Paraboloidal $x = 2c\cosh\alpha\cos\beta\sinh\gamma$ $y = 2c\sinh\alpha\sin\beta\cosh\gamma$ $z = c(\cosh 2\alpha + \cos 2\beta$ $-\cosh 2\gamma)/2$	Whittaker-Hill solutions gc_n, gs_n

Table F.1: Separable Coordinates for the Helmholtz Equation (Cont.)

Commuting operators S_1, S_2	Separable coordinates	Solutions
10. $P_1^2 + aP_2^2 +$	Ellipsoidal	Ellipsoidal
$(a+1)P_3^2 + \mathbf{J}\cdot\mathbf{J}$,	$x = \left(\frac{(\mu-a)(\nu-a)(\rho-a)}{a(a-1)}\right)^{1/2}$	wave functions
$J_2^2 + a(J_1^2 + P_3^2)$	$y = \left(\frac{(\mu-1)(\nu-1)(\rho-1)}{1-a}\right)^{1/2}$	el_n^m
	$z = (\mu\nu\rho/a)^{1/2}$	
11. $\mathbf{J}\cdot\mathbf{J}$, $J_1^2 + bJ_2^2$	Conical	Lamé
	$x = r\left(\frac{(b\mu-1)(b\nu-1)}{1-b}\right)^{1/2}$	polynomials
	$y = r\left(\frac{b(\mu-1)(\nu-1)}{b-1}\right)^{1/2}$	
	$z = r(b\mu\nu)^{1/2}$	

F.3 Application to the Laplace Equation

The symmetry algebra $\mathcal{G}$ of the Laplace equation is 10-dimensional with basis

$$P_1 = \partial_x, \qquad P_2 = \partial_y, \qquad P_3 = \partial_z; \tag{F.16a}$$

$$J_1 = z\partial_y - y\partial_z, \qquad J_2 = x\partial_z - z\partial_x, \qquad J_3 = y\partial_x - x\partial_y; \tag{F.16b}$$

$$D = -(\frac{1}{2} + \mathbf{x}\cdot\partial); \tag{F.16c}$$

$$K_1 = x + (x^2 - y^2 - z^2)\partial_x + 2xz\partial_z + 2xy\partial_y, \tag{F.16d}$$

$$K_2 = y + (y^2 - x^2 - z^2)\partial_y + 2yz\partial_z + 2yx\partial_x, \tag{F.16e}$$

$$K_3 = z + (z^2 - x^2 - y^2)\partial_z + 2zx\partial_x + 2zy\partial_y. \tag{F.16f}$$

In terms of these operators, the Laplace equation may be written as

$$(P_1^2 + P_2^2 + P_3^2)\Psi = 0. \tag{F.17}$$

Note that $\mathcal{G}$ contains the symmetry algebra of the Helmholtz equation, $\mathcal{E}(3)$, as a subalgebra. The symmetry group for the Laplace equation is significantly richer. The structure of $\mathcal{G}$ is clarified as follows. We introduce a new basis by defining the operators

$$L_i^+ = \frac{1}{2}(P_i + K_i), \tag{F.18a}$$

$$L_i^- = \frac{1}{2}(P_i - K_i), \tag{F.18b}$$

for $i = 1, 2, 3$. The set of basis elements may then be organized in the following 5×5 matrix Γ:

$$\Gamma = \begin{pmatrix} 0 & L_1^+ & L_2^+ & L_3^+ & D \\ -L_1^+ & 0 & -J_3 & J_2 & L_1^- \\ -L_2^+ & J_3 & 0 & -J_1 & L_2^- \\ -L_3^+ & -J_2 & J_1 & 0 & L_3^- \\ D & L_1^- & L_2^- & L_3^- & 0 \end{pmatrix}. \tag{F.19}$$

The commutation relations may then be written:

$$[\Gamma_{a5}, \Gamma_{b5}] = \Gamma_{ab}, \tag{F.20a}$$

$$[\Gamma_{a5}, \Gamma_{cd}] = -\delta_{ad}\Gamma_{c5} + \delta_{ac}\Gamma_{d5}, \tag{F.20b}$$

$$[\Gamma_{ab}, \Gamma_{cd}] = \delta_{bc}\Gamma_{ad} + \delta_{ad}\Gamma_{bc} + \delta_{ca}\Gamma_{db} + \delta_{db}\Gamma_{ca}. \tag{F.20c}$$

It follows that the symmetry algebra $\mathcal{G}$ is isomorphic to $so(4,1)$. If we define the matrix G by $G = diag(1,1,1,1,-1)$, then $so(4,1)$ is the set of 5×5 matrices a such that $aG + Ga^t = 0$. In particular $so(4,1)$ is the Lie algebra of the *conformal group*. The conformal group $SO(4,1)$ is the group of real 5×5 matrices such that

$$AGA^t = G. \tag{F.21}$$

Note that $SO(4,1)$ is not connected. The identity component consists of those matrices A satisfying (F.23) such that $\det A = 1$ and $A_{55} \geq 1$.

We wish to identify how the conformal group $SO(4,1)$ acts on $\mathbb{R}^3$. First, we have the subgroup $E^+(3)$ of rigid motions generated by the P_i, J_i, whose elements act on $\mathbb{R}^3$ to produce translations and rotations. In addition, two new types of symmetry operators appear. The operator D is a generator of *dilations* such that

$$\exp(\lambda D)\mathbf{x} = \exp(-\lambda)\mathbf{x} = (e^{-\lambda}x, e^{-\lambda}y, e^{-\lambda}z). \tag{F.22}$$

That is, D generates a change of scale. The three K_i generate *conformal transformations* of the form

$$\exp(\mathbf{a}\cdot\mathbf{K})\mathbf{x} = \frac{\mathbf{x} - \mathbf{a}|\mathbf{x}|^2}{1 - 2\mathbf{a}\cdot\mathbf{x} + |\mathbf{a}|^2|\mathbf{x}|^2}. \tag{F.23}$$

Clearly $\mathbf{a} = 0$ corresponds to the identity transformation. Consider a conformal transformation with $\mathbf{a} = a\hat{\mathbf{z}}$ for some $a \neq 0$. It is straightforward to check that

such a transformation leaves the origin invariant, and the origin is its only fixed point. Furthermore, a sphere of radius R is mapped to a new sphere of radius R^* and center $\mathbf{r}^*$ given by:

$$R^* = \frac{R}{1-(aR)^2}, \qquad \mathbf{r}^* = \frac{\mathbf{a}R^2}{1-(aR)^2}. \tag{F.24}$$

Figure F.1 illustrates the behavior of the mapping. Note that the unit ball is mapped into the half-space $z > -a/(1+a^2)$, while all points outside the unit ball are mapped to the half-space $z < -a/(1+a^2)$. The point at infinity is mapped to $\mathbf{x} = -\mathbf{a}/a^2$. The transformation is real-analytic at all points except $\mathbf{x} = \mathbf{a}/a^2$, where it is singular. The transformation is conformal in that it preserves *angles*. This can be seen by noting that the Jacobian matrix J satisfies

$$J^t J = \frac{1}{(1-2\mathbf{a}\cdot\mathbf{x}+a^2|\mathbf{x}|^2)^2} I. \tag{F.25}$$

We show how (F.23) is related to a conformal transformation of the same name in complex analysis as follows. Consider the plane $y = 0$. Note that each point $\mathbf{x} = (x, 0, z)$ in the plane $y = 0$ is mapped under (F.23) to a point $(x', 0, z')$ in the same plane. We consider the action of (F.23) on this plane. Let $u = z + ix$. Then it can be shown that $z' + ix' = f(u)$, where the function f on $\mathbb{C}$ is given by

$$f(u) = \frac{u}{1-au}. \tag{F.26}$$

Then f is a conformal transformation of the complex plane minus the point $u = 1/a$.

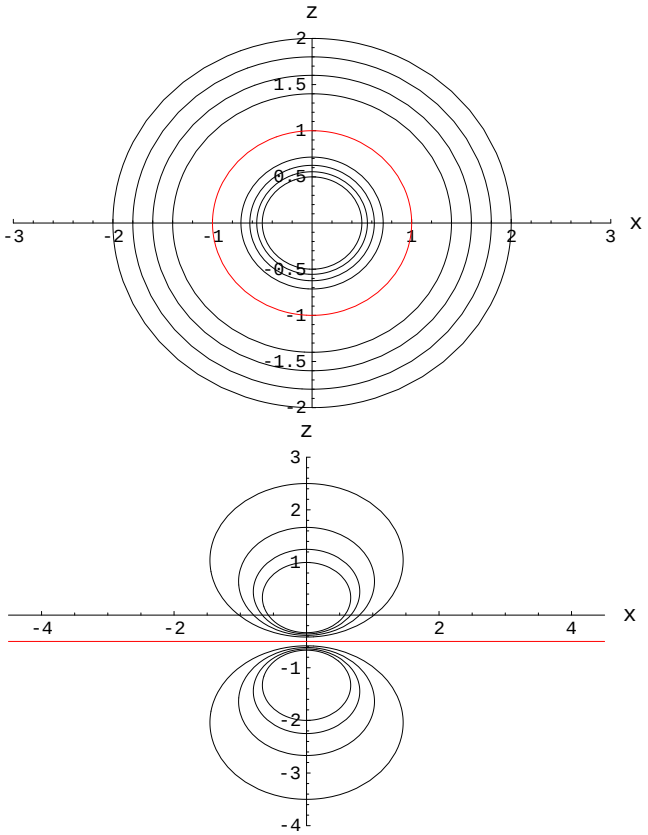

Figure F.1: A conformal transformation of three-space with $\mathbf{a} = 1\hat{\mathbf{z}}$. Illustrated is a cross-section in the plane $y = 0$. The sphere $R = a$ (red) in the upper figure is mapped to the plane $z = -a/(1 + a^2)$ in the lower figure. As a transformation of the plane, (F.23) is the Möbius transformation (F.26). The point $u = 1/a$ (pole) appearing at the top of the northern hemisphere in the upper figure, is mapped to the point at infinity in the lower figure. Conversely, the point at infinity in the upper figure is mapped to $u' = -1/a$ in the lower figure (inverse pole). Points interior to the circle $R = a$ in the upper figure are mapped to points above the red line in the lower figure. Action on $\mathbb{R}^3$ is determined by noting that each figure is symmetric under rotations about the z-axis.

The local representation of $SO(4,1)$ on $\mathcal{F}$ is given by

$$T(g)\Psi(\mathbf{x}) = \Psi(\mathbf{x}g) \quad \text{for all } g \text{ in } E^+(3), \tag{F.27}$$

$$T(\exp(\lambda D))\Psi(\mathbf{x}) = \exp(-\lambda/2)\Psi(\exp(-\lambda)\mathbf{x}), \tag{F.28}$$

$$T(\exp(\mathbf{a}\cdot\mathbf{K})\Psi(\mathbf{x}) = (1-2\mathbf{a}\cdot\mathbf{x}+|\mathbf{a}|^2|\mathbf{x}|^2)^{1/2}\Psi(\exp(\mathbf{a}\cdot\mathbf{K})\mathbf{x}). \tag{F.29}$$

We have summarized the action of $SO(4,1)$ on the real-analytic functions $\mathcal{F}$. However, in addition to the identity component of $SO(4,1)$, the Laplace equation has two additional *discrete* symmetries not possessed by the Helmholtz equation. The first corresponds to inversion I with respect to the unit sphere $\mathbf{x} \to \mathbf{x}/x^2$. The discrete symmetry I acts on a real-analytic function in $\mathcal{F}$ as follows:

$$I\Psi(\mathbf{x}) = \frac{1}{|\mathbf{x}|}\Psi\left(\frac{\mathbf{x}}{x^2}\right), \tag{F.30}$$

where I is known as a *Kelvin transformation*. If Ψ is a solution to the Laplace equation on the domain D, then $I\Psi$ is a solution to the Laplace equation on the transformed domain D^*, obtained by inverting D with respect to the unit sphere. The second discrete symmetry R corresponds to a reflection $\mathbf{x} \to (-x_1, x_2, x_3)$, and acts on an analytic function in $\mathcal{F}$ as

$$R\Psi(\mathbf{x}) = \Psi(-x_1, x_2, x_3), \tag{F.31}$$

where R is known as a *parity transformation*. It is clear that the Laplace equation is invariant under parity transformations. Note that $I^2 = R^2 = E$, the identity. We will consider the symmetry group of the Laplace equation to be the identity component of $SO(4,1)$, augmented by the discrete symmetries I and R described above.

F.3.1 Separation of Variables

The claims 1)-3) of Section F.2.1 again hold for the Laplace equation. In particular, each separable coordinate system is associated with a two-dimensional subspace of second-order symmetry operators. Two coordinate systems are equivalent if one can be obtained from the other under the action of an element in the symmetry group of the Laplace equation.

The Laplace equation is separable in each of the 11 coordinate systems of Table F.1. In addition, 6 new coordinate systems appear in which the Laplace equation is R-separable. These are given in Table F.2. The coordinate surfaces are orthogonal families of confocal *cyclides*. A cyclide is a surface of the form

$$a(x^2 + y^2 + z^2) + P(x, y, z) = 0 \tag{F.32}$$

where a is constant and P is a polynomial of degree 2. If $a = 0$, the cyclide reduces to a quadratic surface.

The only widely-used system in Table F.2 is the system of *toroidal coordinates* (system number 17). A surface of constant ξ is a torus-like (toroidal) surface satisfying

$$x^2 + y^2 + z^2 + 1 = 2\sqrt{x^2 + y^2}\coth(\xi), \tag{F.33}$$

whose surface is parametrized by the two angles $\phi \in [-\pi, \pi]$ and $\psi \in [-\pi, \pi]$.

Table F.2: Additional R-Separable Coordinates for the Laplace Equation

Commuting operators S_1, S_2	Separable coordinates
12. $(a+1)L_2^{+2}+(b+1)L_1^{+2}$ $+(a+b)L_3^{+2}+J_3^2+bJ_2^2+aJ_1^2$, $aL_2^{+2}+bL_1^{+2}+abL_3^{+2}$	$x=R^{-1}\left(\frac{(\mu-a)(\nu-a)(\rho-a)}{(b-a)(a-1)a}\right)^{1/2}$ $y=R^{-1}\left[\frac{(\mu-b)(\nu-b)(\rho-b)}{(a-b)(b-1)b}\right]^{1/2}$ $z=R^{-1}\left[\frac{(\mu-1)(\nu-1)(\rho-1)}{(a-1)(b-1)}\right]^{1/2}$ $R=1+\left(\frac{\mu\nu\rho}{ab}\right)^{1/2}$
13. $2\alpha J_3^2+(\alpha+1)(L_2^{+2}-L_2^{-2})+\beta\{L_2^+,L_2^-\}$ $+\alpha(L_1^{+2}-L_1^{-2})-\beta\{L_1^+,L_1^-\}$, $\alpha(L_2^{+2}-L_2^{-2})+\beta\{L_2^+,L_2^-\}$ $+(\alpha^2+\beta^2)J_3^2$	$x=R^{-1}\left[\frac{(\mu-1)(\nu-1)(\rho-1)}{(a-1)(b-1)}\right]^{1/2}$ $y=R^{-1}\left[-\frac{\mu\nu\rho}{ab}\right]^{1/2}$ $z=R^{-1}$ $R=2\mathcal{R}e\left[-\frac{i(\mu-a)(\nu-a)(\rho-a)}{(a-b)(a-1)a}\right]^{1/2}$,
14. J_3^2, $L_3^{+2}-aL_3^{-2}$	$x=R^{-1}\cos\phi$ $y=R^{-1}\sin\phi$ $z=R^{-1}\left[\frac{(\mu-a)(a-\rho)}{a(a-1)}\right]^{1/2}$ $R=\left[\frac{(\mu-a)(a-\rho)}{a(a-1)}\right]^{1/2}-\left[\frac{(\mu-1)(1-\rho)}{a-1}\right]^{1/2}$
15. J_3^2, $-aD^2-L_3^{-2}$	$x=R^{-1}\cos\phi$ $y=R^{-1}\sin\phi$ $z=R^{-1}\left[\frac{(\mu-a)(a-\rho)}{a(a-1)}\right]^{1/2}$ $R=\left(\frac{\mu\rho}{a}\right)^{1/2}+\left[\frac{(\mu-1)(\rho-1)}{(a-1)}\right]^{1/2}$
16. J_3^2, $\alpha(L_3^{+2}-L_3^{-2})+\beta\{L_3^+,L_3^-\}$	$x=R^{-1}\cos\phi$ $y=R^{-1}\sin\phi$ $z=R^{-1}\left(-\frac{\mu\rho}{ab}\right)^{1/2}$ $R=2\mathcal{R}e\left[\frac{i(\rho-a)(\mu-a)}{a(a-b)}\right]^{1/2}$
17. J_3^2, L_3^{+2}	$x=R^{-1}\sinh\xi\cos\phi$ $y=R^{-1}\sinh\xi\sin\phi$ $z=R^{-1}\cos\psi$ $R=\cosh\xi+\sin\psi$

Appendix G

The Dirac Monopole

G.1 Basic Formulation

A brief treatment of the Dirac monopole is given in Jackson [7]. We supplement these results with a more detailed treatment. For discussion of the Dirac quantization condition and related results, we refer the reader to [51],[52],[7]. In the present section, we show that the Dirac monopole may be constructed as a chain of ideal magnetic dipoles, aligned along a simple smooth curve, whose magnetic moments point along the tangent to the curve at each point.

We begin by constructing an analogy with the electrostatic case. Given a static charge distribution ρ, suppose $\mathbf{F}$ is a vector field satisfying $\nabla \cdot \mathbf{F} = \rho$ and $\nabla \times \mathbf{F} = 0$ on all space, and vanishing at infinity. Then there exists a scalar function ϕ such that $\mathbf{F} = -\nabla\phi$, and therefore $\nabla^2\phi = -\rho$. Suppose that the charge density ρ is piecewise continuous on $\mathbb{R}^3$. In free space, the solution is given by

$$\phi(\mathbf{r}) = \frac{1}{4\pi} \int_{\mathbb{R}^3} \frac{\rho(\mathbf{r}')}{|\mathbf{r} - \mathbf{r}'|} d^3\mathbf{r}', \tag{G.1}$$

provided that 1) ρ is Hölder continuous at the point $\mathbf{r}$, and 2) ρ falls off sufficiently rapidly at infinity [92]. Suppose, in fact, that ρ is smooth and nonzero in some volume V that can be contained in a sphere of radius R surrounding the point $\mathbf{r}_d$, and that ρ vanishes outside V. For $\mathbf{r}'$ in the volume V we write $\mathbf{r}' = \mathbf{r}_d + \eta$. For

points $\mathbf{r}$ outside the sphere $|\mathbf{r}| = R$, we then write

$$\Phi(\mathbf{r}) = \frac{1}{4\pi} \int_{\mathcal{V}} \frac{\rho(\mathbf{r}_d + \eta)}{|\mathbf{r} - \mathbf{r}_d - \eta|} d^3\eta, \tag{G.2}$$

where $\mathcal{V}$ is the volume corresponding to V in the coordinates η. Performing a Taylor series in the variables η_k about $\eta = 0$ we obtain

$$\frac{1}{|(\mathbf{r} - \mathbf{r}_d) - \eta|} = \frac{1}{|\mathbf{r} - \mathbf{r}_d|} \left(1 + \frac{\eta \cdot (\mathbf{r} - \mathbf{r}_d)}{|\mathbf{r} - \mathbf{r}_d|^2} + \frac{\{3[\eta \cdot (\mathbf{r} - \mathbf{r}_d)]^2 - \eta^2 |\mathbf{r} - \mathbf{r}_d|^2\}}{2|\mathbf{r} - \mathbf{r}_d|^4} + O\left(\frac{\eta^3}{|\mathbf{r} - \mathbf{r}_d|^3} \right) \right), \tag{G.3}$$

which is guaranteed to converge since $|\mathbf{r} - \mathbf{r}_d| > R \geq \eta$. The multipole expansion of Φ with respect to the point $\mathbf{r}_d$ is then given by integrating this series term-by-term

$$\Phi(\mathbf{r}) = \frac{1}{4\pi} \left(\frac{q}{|\mathbf{r} - \mathbf{r}_d|} + \frac{\mathbf{p}_d \cdot (\mathbf{r} - \mathbf{r}_d)}{|\mathbf{r} - \mathbf{r}_d|^3} + \frac{1}{2} \sum_{i,j} Q_{ij} \frac{(x - x_d)_i (x - x_d)_j}{|\mathbf{r} - \mathbf{r}_d|^5} + O\left(\frac{1}{|\mathbf{r} - \mathbf{r}_d|} \right) \right). \tag{G.4}$$

Here we have employed the moments relative to $\mathbf{r}_d$:

$$q = \int_V \rho(\mathbf{r}') dV', \tag{G.5}$$

$$\mathbf{p}_d = \int_V (\mathbf{r}' - \mathbf{r}_d) \rho(\mathbf{r}') dV', \tag{G.6}$$

$$Q_{ij} = \int_V \{3(x' - x_d)_i (x' - x_d)_j - |\mathbf{r}' - \mathbf{r}_d|^2 \delta_{ij}\} \rho(\mathbf{r}') dV', \text{ etc.} \tag{G.7}$$

In particular, the dipole contribution is given for $\mathbf{r} \neq \mathbf{r}_d$ by

$$\Phi_d(\mathbf{r}) = \frac{1}{4\pi} \frac{\mathbf{p}_d \cdot (\mathbf{r} - \mathbf{r}_d)}{|\mathbf{r} - \mathbf{r}_d|^3}, \tag{G.8}$$

where

$$\mathbf{p}_d = \int_V (\mathbf{r}' - \mathbf{r}_d) \rho(\mathbf{r}') dV'. \tag{G.9}$$

It is well-known that the field of an ideal dipole may be constructed as the net field of two electric charges q (monopoles) in the limit that their relative displacement $d\mathbf{r}$ goes to zero, such that the product $qd\mathbf{r} = \mathbf{p}$ remains constant. Conversely, we show that the field of an electric monopole may be constructed by a limiting process from a distribution of electric dipoles. Consider a chain of N such electric dipoles with dipole moments $d\mathbf{p}_i$, all of equal magnitude. Assume that these dipoles lie at equidistant intervals of length Δs along a smooth curve L with endpoints at $\mathbf{r}_A$ and $\mathbf{r}_B$, such that each dipole moment points along the direction of the tangent vector at the location of the dipole. We then have $\mathbf{p}_i = qd\mathbf{r}_i$. The net potential of such a chain takes the form of a Riemann sum, which converges in the limit $|d\mathbf{r}| \to 0$ to the path integral

$$\Phi(\mathbf{r}) = \frac{1}{4\pi} \sum_{i=1}^{N} \frac{d\mathbf{p}_i \cdot (\mathbf{r} - \mathbf{r_i})}{|\mathbf{r} - \mathbf{r_i}|^3} \to \frac{q}{4\pi} \int_L \frac{(\mathbf{r} - \mathbf{r}') \cdot d\mathbf{r}'}{|\mathbf{r} - \mathbf{r}'|^3}. \tag{G.10}$$

Here L is a piecewise smooth curve with endpoints at $\mathbf{r}' = \mathbf{r}_A$ and $\mathbf{r}' = \mathbf{r}_B$. Hence,

$$\Phi(\mathbf{r}) = \frac{q}{4\pi} \int_L \nabla' \left(\frac{1}{|\mathbf{r} - \mathbf{r}'|} \right) \cdot d\mathbf{r}' = \frac{q}{4\pi} \left(\frac{1}{|\mathbf{r} - \mathbf{r}_B|} - \frac{1}{|\mathbf{r} - \mathbf{r}_A|} \right). \tag{G.11}$$

That is, a string of electric dipoles is equivalent to a pair of electric charges, one located at each end of the string. Note that the integral is independent of the path L. If the path is chosen such that $|\mathbf{r}_B| \to \infty$, then we recover the potential of a point charge (monopole) of strength q:

$$\Phi_m(\mathbf{r}) = -\frac{q}{4\pi} \frac{1}{|\mathbf{r} - \mathbf{r}_A|}, \tag{G.12}$$

with corresponding field

$$\mathbf{F}_m(\mathbf{r}) = -\nabla \Phi_m(\mathbf{r}) = \frac{q}{4\pi} \frac{\mathbf{r} - \mathbf{r}_A}{|\mathbf{r} - \mathbf{r}_A|^3}. \tag{G.13}$$

We now wish to construct a vector potential $\mathbf{A}_m$ for the field (G.13), such that $\mathbf{F}_m = -\nabla\Phi_m = \nabla \times \mathbf{A}_m$. Given a current distribution $\mathbf{J}$, suppose $\mathbf{F}$ satisfies $\nabla\times\mathbf{F} = \mathbf{J}$ and $\nabla\cdot\mathbf{F} = 0$. Then there exists some $\mathbf{A}$ such that $\mathbf{F} = \nabla\times(\nabla\times\mathbf{A}) = \mathbf{J}$. In the Coulomb gauge, we have that $\nabla\cdot\mathbf{A} = 0$ and $\nabla\times(\nabla\times\mathbf{A}) = \nabla(\nabla\cdot\mathbf{A}) - \nabla^2\mathbf{A}$, hence $\nabla^2\mathbf{A} = -\mathbf{J}$. The solution is now given by

$$\mathbf{A}(\mathbf{r}) = \frac{1}{4\pi}\int_{\mathbb{R}^3}\frac{\mathbf{J}(\mathbf{r}')}{|\mathbf{r}-\mathbf{r}'|}dV', \tag{G.14}$$

where each component of $\mathbf{J}$ must satisfy the same conditions as ρ in (G.1). By construction, $\nabla\cdot\mathbf{A} = 0$. (This can be verified as follows. First, note that by charge continuity we have

$$\frac{\partial\rho}{\partial t} + \nabla\cdot\mathbf{J} = 0. \tag{G.15}$$

In the magnetostatic case the time derivative vanishes, and therefore $\nabla\cdot\mathbf{J} = 0$. We also know that

$$\begin{aligned}\nabla\cdot\left(\frac{\mathbf{J}(\mathbf{r}')}{|\mathbf{r}-\mathbf{r}'|}\right) &= \mathbf{J}(\mathbf{r}')\cdot\nabla\left(\frac{1}{|\mathbf{r}-\mathbf{r}'|}\right) \\ &= -\mathbf{J}(\mathbf{r}')\cdot\nabla'\left(\frac{1}{|\mathbf{r}-\mathbf{r}'|}\right) = -\nabla'\cdot\left(\frac{\mathbf{J}(\mathbf{r}')}{|\mathbf{r}-\mathbf{r}'|}\right) + \frac{\nabla'\cdot\mathbf{J}(\mathbf{r})}{|\mathbf{r}-\mathbf{r}'|}.\end{aligned} \tag{G.16}$$

We may then evaluate the divergence of (G.14) as follows. Consider first the integral (G.14) to be evaluated on a ball B of radius R, surrounding the point $\mathbf{r}$. From the above result we have

$$\begin{aligned}\nabla\cdot\int_B\frac{\mathbf{J}(\mathbf{r}')}{|\mathbf{r}-\mathbf{r}'|}dV' &= -\int_B\nabla'\cdot\left(\frac{\mathbf{J}(\mathbf{r}')}{|\mathbf{r}-\mathbf{r}'|}\right)dV' + \int_B\frac{\nabla'\cdot\mathbf{J}(\mathbf{r}')}{|\mathbf{r}-\mathbf{r}'|}dV' \\ &= -\int_S\frac{\mathbf{n}(\mathbf{r}')\cdot\mathbf{J}(\mathbf{r}')}{|\mathbf{r}-\mathbf{r}'|}dS' \le \max_S(\mathbf{n}\cdot\mathbf{J})4\pi R.\end{aligned} \tag{G.17}$$

If we assume that $\mathbf{J}$ falls off faster than $1/R$, the integral vanishes as $R\to\infty$ and $\nabla\cdot\mathbf{A} = 0$, as claimed.)

We now suppose that $\mathbf{J}$ vanishes outside some bounded region V. The multipole expansion of $\mathbf{A}$ outside of V with respect to the point $\mathbf{r}_d$ is given by using the series (G.3) and integrating term-by-term

$$\mathbf{A}(\mathbf{r}) = \frac{1}{4\pi}\left(\frac{q_m}{|\mathbf{r}-\mathbf{r}_d|} + \frac{\mathbf{m}_d \times (\mathbf{r}-\mathbf{r}_d)}{|\mathbf{r}-\mathbf{r}_d|^3} + O\left(|\mathbf{r}-\mathbf{r}_d|^{-3}\right)\right), \tag{G.18}$$

where

$$q_m = \int_V \mathbf{J}(\mathbf{r}')dV', \tag{G.19}$$

$$\mathbf{m}_d = \frac{1}{2}\int_V (\mathbf{r}'-\mathbf{r}_d) \times \mathbf{J}(\mathbf{r}')dV'. \tag{G.20}$$

It can then be shown that $q_m = 0$. Let $x_i = x, y$, or z. Since $\nabla \cdot \mathbf{J} = 0$ we have

$$\nabla' \cdot (x_i'\mathbf{J}) = \mathbf{J} \cdot \nabla' {x_i}' + x_i'(\nabla \cdot \mathbf{J}) = \mathbf{J} \cdot \mathbf{e}_i. \tag{G.21}$$

Suppose we integrate over a volume Ω such that $V \subset \Omega$. Thus, for each unit vector $\mathbf{e}_i$ we have

$$\mathbf{e}_i \cdot \int_V \mathbf{J}(\mathbf{r}')dV' = \mathbf{e}_i \cdot \int_\Omega \mathbf{J}(\mathbf{r}')dV' = \int_\Omega \nabla' \cdot [x_i \mathbf{J}(\mathbf{r}')]dV' = \int_{\partial\Omega} x_i(\mathbf{n}(\mathbf{r}') \cdot \mathbf{J}(\mathbf{r}'))dS' = 0, \tag{G.22}$$

since $\mathbf{J}$ vanishes outside the volume V.

The vanishing of the monopole term illustrates that no bounded distribution of current $\mathbf{J}$ can produce the field of a magnetic monopole. The dipole term is given by

$$\mathbf{A}_d(\mathbf{r}) = \frac{1}{4\pi}\frac{\mathbf{m}_d \times (\mathbf{r}-\mathbf{r}_d)}{|\mathbf{r}-\mathbf{r}_d|^3} \tag{G.23}$$

where

$$\mathbf{m}_d = \frac{1}{2}\int_V (\mathbf{r}'-\mathbf{r}_d) \times \mathbf{J}(\mathbf{r}')dV'. \tag{G.24}$$

We claim that the dipole fields $\mathbf{F} = -\nabla\Phi_d$ and $\mathbf{F} = \nabla \times \mathbf{A}_d$ are identical in the case when $\mathbf{m}_d = \mathbf{p}_d$. For all points $\mathbf{r} \neq \mathbf{r}_d$, it can be shown that

$$\mathbf{F} = -\nabla\Phi_d = \frac{1}{4\pi}\left(\frac{(3\mathbf{p}_d \cdot \mathbf{r} - \mathbf{r}_d)(\mathbf{r} - \mathbf{r}_d)}{|\mathbf{r} - \mathbf{r}_d|^5} - \frac{\mathbf{p}_d}{|\mathbf{r} - \mathbf{r}_d|^3}\right), \tag{G.25}$$

$$\mathbf{F} = -\nabla \times \mathbf{A}_d = \frac{1}{4\pi}\left(\frac{(3\mathbf{m}_d \cdot \mathbf{r} - \mathbf{r}_d)(\mathbf{r} - \mathbf{r}_d)}{|\mathbf{r} - \mathbf{r}_d|^5} - \frac{\mathbf{m}_d}{|\mathbf{r} - \mathbf{r}_d|^3}\right). \tag{G.26}$$

It follows that

$$-\nabla\Phi_d = \nabla \times \mathbf{A}_d \tag{G.27}$$

when $\mathbf{m}_d = \mathbf{p}_d$ and $\mathbf{r} \neq \mathbf{r}_d$.

Recall that we constructed a scalar potential for the field of a monopole source using a chain of electric dipoles. It follows from (G.27) that we may construct a vector potential for the same field using a chain of magnetic dipoles. We define a string in a form analogous to the electrostatic case. As before, let L denote a curve with one end at $\mathbf{r}_A$ and extending to infinity. Let $\mathbf{F}_i$ denote the field given by (G.25) due to the ith dipole of the chain. Then, for all points away from the curve L, the field is given by the sum

$$\mathbf{F}_m = \sum_{i=1}^{N} \mathbf{F}_i = -\nabla \frac{1}{4\pi} \sum_{i=1}^{N} \frac{d\mathbf{p}_i \cdot (\mathbf{r} - \mathbf{r_i})}{|\mathbf{r} - \mathbf{r_i}|^3} = \nabla \times \frac{1}{4\pi} \sum_{i=1}^{N} \frac{d\mathbf{m}_i \times (\mathbf{r} - \mathbf{r_i})}{|\mathbf{r} - \mathbf{r_i}|^3}. \tag{G.28}$$

The vector potential for the dipole chain can be written in the limit $d\mathbf{r} \to 0$ by the path integral

$$\mathbf{A}(\mathbf{r}) = \frac{1}{4\pi} \sum_{i=1}^{N} \frac{d\mathbf{m}_i \times (\mathbf{r} - \mathbf{r_i})}{|\mathbf{r} - \mathbf{r_i}|^3} \to \frac{g}{4\pi} \int_L \frac{d\mathbf{r}' \times (\mathbf{r} - \mathbf{r}')}{|\mathbf{r} - \mathbf{r}'|^3}, \tag{G.29}$$

where we let $d\mathbf{m}_i = g d\mathbf{r}$ define the magnetic charge g. Unlike the case of the scalar potential this integral will, in general, depend on the path chosen L.

The vector potential of a Dirac monopole of charge g at a fixed location $\mathbf{r}_A \in \mathbb{R}^3$ is given by the line integral

$$\boxed{\mathbf{A}_m(\mathbf{r}) = -\frac{g}{4\pi}\int_L d\mathbf{r}' \times \nabla\left(\frac{1}{|\mathbf{r}-\mathbf{r}'|}\right)} \tag{G.30}$$

where the integral is taken along a directed path L beginning at the point $\mathbf{r}_A$ and extending to infinity. Such a potential has the desired property:

$$\mathbf{F}_m = -\nabla\Phi_m = \nabla \times \mathbf{A}_m \tag{G.31}$$

at all points away from the curve L. Furthermore,

$$\nabla \cdot \mathbf{A}_m = 0. \tag{G.32}$$

These properties may be verified directly as follows. Consider the integrand of (G.30) for a fixed value of $\mathbf{r}'$ along the path L. Let $\hat{\mathbf{t}}$ denote the tangent vector to L at $\mathbf{r}'$. Writing $d\mathbf{r}' = \hat{\mathbf{t}}ds$ we evaluate the curl of the integrand. Using the identity $\nabla \times (\mathbf{A} \times \mathbf{B}) = (\mathbf{B}\cdot\nabla)\mathbf{A} - (\mathbf{A}\cdot\nabla)\mathbf{B} - \mathbf{B}(\nabla\cdot\mathbf{A}) + \mathbf{A}(\nabla\cdot\mathbf{B})$, we find that

$$\nabla \times \left[\hat{\mathbf{t}} \times \nabla\left(\frac{1}{|\mathbf{r}-\mathbf{r}'|}\right)\right] = \hat{\mathbf{t}}\nabla^2\left(\frac{1}{|\mathbf{r}-\mathbf{r}'|}\right) - (\hat{\mathbf{t}}\cdot\nabla)\nabla\left(\frac{1}{|\mathbf{r}-\mathbf{r}'|}\right). \tag{G.33}$$

Noting that $\nabla^2\left(\frac{1}{|\mathbf{r}-\mathbf{r}'|}\right) = 0$ for $\mathbf{r} \neq \mathbf{r}'$, we have that the curl is given by the integral

$$\begin{aligned}\nabla \times \mathbf{A}_m &= \int_L -(d\mathbf{r}'\cdot\nabla)\nabla\left(\frac{1}{|\mathbf{r}-\mathbf{r}'|}\right) \\ &= \int_L (d\mathbf{r}'\cdot\nabla')\nabla\left(\frac{1}{|\mathbf{r}-\mathbf{r}'|}\right) = -\nabla\left(\frac{1}{|\mathbf{r}-\mathbf{r}_A|}\right) = \mathbf{F}_m,\end{aligned} \tag{G.34}$$

provided that $\mathbf{r} \notin L$. Similarly, using the identity $\nabla\cdot(\mathbf{A}\times\mathbf{B}) = \mathbf{B}\cdot(\nabla\times\mathbf{B}) - \mathbf{A}\cdot(\nabla\times\mathbf{B})$, we find that

$$\nabla\cdot\left[\hat{\mathbf{t}}\times\nabla\left(\frac{1}{|\mathbf{r}-\mathbf{r}'|}\right)\right] = -\hat{\mathbf{t}}\cdot\left[\nabla\times\nabla\left(\frac{1}{|\mathbf{r}-\mathbf{r}'|}\right)\right] = 0, \tag{G.35}$$

provided $\mathbf{r} \neq \mathbf{r}'$. Since the integrand vanishes everywhere along the path, it follows that $\nabla \cdot \mathbf{A} = 0$.

G.2 Properties of the Dirac String

We refer to the path L appearing in (G.30) as the *Dirac string*. In the present section, we will demonstrate several properties of the monopole potential (G.30) as they relate to the Dirac string.

Why is such an artifice necessary? The field $\mathbf{F}_m$ of a monopole is smooth on all of space except the location of the source $\mathbf{r}_A$. Furthermore, the field is curl-free and divergence-free on all space except at $\mathbf{r}_A$. However, *there exists no vector potential* $\mathbf{A}$ *such that* $\mathbf{F}_m = \nabla \times \mathbf{A}$ *on all of* $\mathbb{R}^3 \setminus \{\mathbf{r}_A\}$. To prove this statement, suppose that such a vector potential does exist. We surround the point $\mathbf{r}_A$ by a sphere S. We know from the divergence theorem that there will be a net flux through the sphere due to the enclosed magnetic source:

$$\int_S \mathbf{F}_m \cdot \mathbf{n} dS = \int_B \nabla \cdot \mathbf{F}_m dV = \int_B \rho_m dV = g, \tag{G.36}$$

where g is the magnetic charge of the monopole. However, if $\mathbf{F} = \nabla \times \mathbf{A}$ at all points on S, then we also have that

$$\int_S \mathbf{F}_m \cdot \mathbf{n} dS = \int_S (\nabla \times \mathbf{A}) \cdot \mathbf{n} dS. \tag{G.37}$$

Since S is a closed surface, it follows from Stokes' theorem that the integral (G.37) must vanish, contradicting (G.36). Thus, no such vector potential exists. (This is possible because the region $\mathbb{R}^3 \setminus \{\mathbf{r}_A\}$ is not simply-connected.) It follows from the

above argument that on any sphere surrounding a monopole there is at least one point where the identity $\mathbf{F}_m = \nabla \times \mathbf{A}$ fails. The (connected) set of smallest measure on which this identity can fail is therefore a single curve, originating at the point $\mathbf{r}_A$ and extending to infinity. This is the Dirac string.

We now show that the vector potential of (G.30) is, in fact, singular for all points $\mathbf{r} \in L$ on the Dirac string. To demonstrate this, consider a modified version of the previous argument. Let $\mathbf{r}_0$ be a point on the string, and let $\hat{\mathbf{t}}$ be the unit tangent vector to L at $\mathbf{r}_0$. We surround the string by a small circle of radius ϵ, whose center lies at the point $\mathbf{r}_0$. For simplicity, we assume that the circle lies in the plane orthogonal to the string. Let S_ϵ be a surface enclosing the monopole source, which is closed except for a small hole whose boundary is the circle surrounding the string (Fig. G.1). Note $\mathbf{A}_m$ is well-behaved on this surface. Using Stokes' theorem we note that line integral of $\mathbf{A}_m$ over the circle is given by

$$\oint_C \mathbf{A}_m(\mathbf{r}) \cdot d\mathbf{r} = \int_{S_\epsilon} (\nabla \times \mathbf{A}_m) \cdot \mathbf{n} dS = \int_{S_\epsilon} \mathbf{F}_m(\mathbf{r}) \cdot \mathbf{n} dS. \tag{G.38}$$

In the limit as $\epsilon \to 0$, this integral must approach that of a closed surface (G.36). We therefore have the key identity:

$$\boxed{\lim_{\epsilon \to 0} \oint_C \mathbf{A}_m(\mathbf{r}) \cdot d\mathbf{r} = g}. \tag{G.39}$$

Consider cylindrical coordinates in a neighborhood of $\mathbf{r}_0$. We let $d\mathbf{r} = \epsilon \hat{\phi} d\phi$, such that A_ϕ denotes that component of $\mathbf{A}$ encircling the string. Note that we may write

$$\lim_{\epsilon \to 0} \oint_C \mathbf{A}_m(\mathbf{r}) \cdot d\mathbf{r} = \lim_{\epsilon \to 0} \left[\epsilon \int_0^{2\pi} A_\phi(\mathbf{r}_0 + \epsilon \hat{\rho}) d\phi \right] = g. \tag{G.40}$$

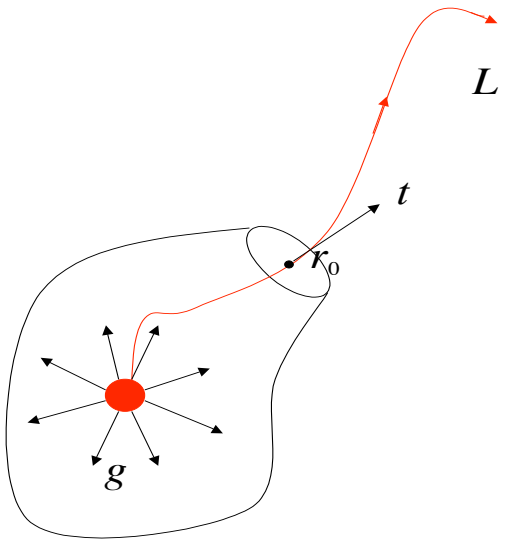

Figure G.1: A monopole of strength g together with its Dirac string.

This is only possible if

$$\lim_{\epsilon \to 0} \int_0^{2\pi} A_\phi(\mathbf{r}_0 + \epsilon \hat{\rho}) d\phi = \pm\infty \tag{G.41}$$

where the sign is determined by the sign of the enclosed charge. We conclude: *The component of* $\mathbf{A}_m$ *encircling the Dirac string diverges as the string is approached from any direction.* This can also be seen directly from the integral (G.30). The integrand appearing in the vector potential (G.30) becomes singular as $1/|\mathbf{r} - \mathbf{r}'|$ for all points near $\mathbf{r} = \mathbf{r}'$. We therefore expect that this line integral will diverge when $\mathbf{r} \in L$.

G.3 Gauge Transformations

In the present section we demonstrate that a change in the Dirac string is equivalent to a change of gauge in the vector potential (G.30), and we study these

gauge transformations in detail.

Consider a Dirac monopole at location $\mathbf{r}_A$. Let L_1 and L_2 be two strings, each with one end at $\mathbf{r}_A$. We wish to show that deforming the string $L_1 \to L_2$ amounts to a change of gauge

$$\mathbf{A}_{L_2} = \mathbf{A}_{L_1} + \nabla f \tag{G.42}$$

for some harmonic function f, on all space excluding the two strings, $\mathbb{R}^3 \setminus \{L_1 \cup L_2\}$. First assume that the string L_2 is obtained by deforming L_1 locally. That is, if we parametrize each string by arc length along the curve from the end $\mathbf{r}_A$, then $L_1(\lambda) = L_2(\lambda + l)$ for all λ sufficiently large, where l is a constant. The strings coincide at all points beyond some value λ_p. (The general case may be obtained by a limiting process as $\lambda_p \to \infty$.) We then have from (G.30) that

$$\begin{aligned}\mathbf{A}_{L_2}(\mathbf{r}) - \mathbf{A}_{L_1}(\mathbf{r}) &= -\frac{g}{4\pi}\left[\int_{L_2} d\mathbf{r}' \times \nabla\left(\frac{1}{|\mathbf{r}-\mathbf{r}'|}\right) - \int_{L_1} d\mathbf{r}' \times \nabla\left(\frac{1}{|\mathbf{r}-\mathbf{r}'|}\right)\right] \\ &= -\frac{g}{4\pi}\oint_C d\mathbf{r}' \times \nabla\left(\frac{1}{|\mathbf{r}-\mathbf{r}'|}\right)\end{aligned} \tag{G.43}$$

where C is the closed path along the curve $L_2 - L_1$. We now establish that

$$\oint_C d\mathbf{r}' \times \nabla\left(\frac{1}{|\mathbf{r}-\mathbf{r}'|}\right) = \nabla \int_S \mathbf{n} \cdot \nabla'\left(\frac{1}{|\mathbf{r}-\mathbf{r}'|}\right) dS' \tag{G.44}$$

where S is any smooth surface with C as its boundary. Throughout, let $\phi(\mathbf{r}) = \frac{1}{|\mathbf{r}-\mathbf{r}'|}$. Let $\mathbf{a}$ be any constant vector, and define $\mathbf{V} = \nabla\phi \times \mathbf{a}$. By the product rule $\mathbf{A} \cdot (\mathbf{B} \times \mathbf{C}) = \mathbf{C} \cdot (\mathbf{A} \times \mathbf{B})$ we have

$$\mathbf{V} \cdot d\mathbf{r}' = d\mathbf{r}' \cdot (\nabla\phi \times \mathbf{a}) = \mathbf{a} \cdot (d\mathbf{r}' \times \nabla\phi). \tag{G.45}$$

Thus

$$\oint_C \mathbf{V} \cdot d\mathbf{r}' = \mathbf{a} \cdot \oint_C d\mathbf{r}' \times \nabla\phi. \tag{G.46}$$

Also, noting $\nabla \times (\mathbf{A} \times \mathbf{B}) = (\mathbf{B} \cdot \nabla)\mathbf{A} - (\mathbf{A} \cdot \nabla)\mathbf{B} - \mathbf{B}(\nabla \cdot \mathbf{A}) + \mathbf{A}(\nabla \cdot \mathbf{B})$ we have that

$$\nabla \times \mathbf{V} = \nabla \times (\nabla\phi \times \mathbf{a}) = (\mathbf{a} \cdot \nabla)\nabla\phi - \mathbf{a}(\nabla^2\phi). \tag{G.47}$$

Noting that $\nabla^2\phi = 0$ for $\mathbf{r} \neq \mathbf{r}'$, we have $\nabla \times \mathbf{V} = (\mathbf{a} \cdot \nabla)\nabla\phi$. Similarly, $\nabla' \times \mathbf{V} = (\mathbf{a} \cdot \nabla')\nabla\phi$. Since derivatives of ϕ with respect to primed and unprimed coordinates commute, we have $\nabla' \times \mathbf{V} = (\mathbf{a} \cdot \nabla)\nabla'\phi$. Hence, using the fact that the normal $\mathbf{n}(\mathbf{r}')$ is independent of the coordinates $\mathbf{r}$,

$$(\nabla' \times \mathbf{V}) \cdot \mathbf{n} = [(\mathbf{a} \cdot \nabla)\nabla'\phi] \cdot \mathbf{n} = \mathbf{a} \cdot \nabla(\mathbf{n} \cdot \nabla'\phi). \tag{G.48}$$

It follows from Stokes' theorem

$$\oint_C \mathbf{V} \cdot d\mathbf{r}' = \int_S (\nabla' \times \mathbf{V}) \cdot \mathbf{n} dS' \tag{G.49}$$

and applying (G.46) and (G.48) that

$$\mathbf{a} \cdot \oint_C d\mathbf{r}' \times \nabla\phi = \mathbf{a} \cdot \nabla \int_S (\mathbf{n} \cdot \nabla'\phi) dS. \tag{G.50}$$

As this result holds for any constant vector $\mathbf{a}$, the result (G.44) is established. We have therefore shown that

$$\mathbf{A}_{L_2} = \mathbf{A}_{L_1} + \frac{g}{4\pi}\nabla\Omega, \tag{G.51}$$

where the gauge function Ω is given by

$$\Omega(\mathbf{r}) = -\int_S \mathbf{n} \cdot \nabla' \left(\frac{1}{|\mathbf{r} - \mathbf{r}'|} \right) dS'. \tag{G.52}$$

Note that

$$\mathbf{n} \cdot \nabla' \left(\frac{1}{|\mathbf{r} - \mathbf{r}'|} \right) = \mathbf{n} \cdot \left(\frac{\mathbf{r} - \mathbf{r}'}{|\mathbf{r} - \mathbf{r}'|^3} \right) = -\frac{\mathbf{n} \cdot \mathcal{R}}{|\mathcal{R}|^3} \tag{G.53}$$

where $\mathcal{R} = \mathbf{r}' - \mathbf{r}$ is a vector pointing from the evaluation point to the surface at $\mathbf{r}'$. Thus, we may write

$$\Omega(\mathbf{r}) = \int_S \frac{\hat{\mathcal{R}} \cdot \mathbf{n}}{\mathcal{R}^2} dS'. \tag{G.54}$$

By definition, $\Omega(\mathbf{r})$ is the solid angle subtended at the point $\mathbf{r}$ by the surface S. We may therefore interpret Ω as the surface area of the projection of the surface S onto the unit sphere surrounding $\mathbf{r}$.

G.3.1 A Choice of Gauge

One particularly simple choice of Dirac string forms the foundation of Section (5.3.2). The Dirac string, which we denote $\mathcal{D}$, is taken to be a straight line that extends from the point $\mathbf{r}_A$ to infinity in the direction of $\mathbf{m}$ [19]. That is, $\mathcal{D} = \{\mathbf{r}_A + \lambda\mathbf{m} : 0 \leq \lambda < \infty\}$. Due to its importance, we evaluate the vector potential in the corresponding gauge. We parametrize the path in terms of λ as, $\mathbf{r}' = \mathbf{r}_A + \lambda\mathbf{m}$. Note that $\mathbf{r} - \mathbf{r}' = \mathbf{r} - \mathbf{r}_A - \lambda\mathbf{m}$ and $d\mathbf{r}' = \mathbf{m}d\lambda$. Then we have

$$\mathbf{A}(\mathbf{r}) = \frac{g}{4\pi} \int_0^\infty \frac{\mathbf{m} \times (\mathbf{r} - \mathbf{r}_A - \lambda\mathbf{m})}{|\mathbf{r} - \mathbf{r}_A - \lambda\mathbf{m}|^3} d\lambda. \tag{G.55}$$

Note $\mathbf{m} \times (\mathbf{r} - \mathbf{r}_A - \lambda\mathbf{m}) = \mathbf{m} \times (\mathbf{r} - \mathbf{r}_A)$ and

$$|\mathbf{r} - \mathbf{r}_A - \lambda\mathbf{m}|^3 = [(\mathbf{r} - \mathbf{r}_A)^2 - 2\lambda\mathbf{m} \cdot (\mathbf{r} - \mathbf{r}_A) + \lambda^2]^{-\frac{3}{2}}. \tag{G.56}$$

Hence, the vector potential is given by the integral

$$\begin{aligned} \mathbf{A}(\mathbf{r}) &= \frac{g}{4\pi} \int_0^\infty \frac{\mathbf{m} \times (\mathbf{r} - \mathbf{r}_A)}{[(\mathbf{r} - \mathbf{r}_A)^2 - 2\lambda\mathbf{m} \cdot (\mathbf{r} - \mathbf{r}_A) + \lambda^2]^{3/2}} d\lambda \\ &= \frac{g}{4\pi} \mathbf{m} \times (\mathbf{r} - \mathbf{r}_A) \int_0^\infty \frac{1}{(c + b\lambda + a\lambda^2)^{3/2}} d\lambda, \end{aligned} \tag{G.57}$$

where $a = (\mathbf{r} - \mathbf{r}_A)^2$, $b = -2\mathbf{m} \cdot (\mathbf{r} - \mathbf{r}_A)$, and $c = 1$. Evaluating integrals of this form using the identity

$$\int_0^\infty \frac{d\lambda}{(a + b\lambda + c\lambda^2)^{3/2}} = \frac{2}{\sqrt{a}} \frac{1}{(2\sqrt{a} + b)}, \tag{G.58}$$

we obtain the result

$$\boxed{\mathbf{A}(\mathbf{r}) = \frac{\mathbf{m} \times (\mathbf{r} - \mathbf{r}_A)}{4\pi |\mathbf{r} - \mathbf{r}_A| (|\mathbf{r} - \mathbf{r}_A| - \mathbf{m} \cdot (\mathbf{r} - \mathbf{r}_A))}} \tag{G.59}$$

at each evaluation point $\mathbf{r}$. The unit vector $\mathbf{m}$ points in the direction of the Dirac string.

We investigate the behavior of (G.59) in a neighborhood of the string $\mathcal{D}$. Given a point $\mathbf{r}_0$ on the string, we let $\boldsymbol{\epsilon}$ denote the displacement of $\mathbf{r}$ relative to $\mathbf{r}_0$. We may write $\mathbf{r} = \mathbf{r}_A + \lambda \mathbf{m} + \boldsymbol{\epsilon}$. It follows that $\mathbf{m} \times (\mathbf{r} - \mathbf{r}_A) = \mathbf{m} \times \boldsymbol{\epsilon}$ and $\mathbf{m} \cdot (\mathbf{r} - \mathbf{r}_A) = \lambda + \mathbf{m} \cdot \boldsymbol{\epsilon}$. The distance to the source point is therefore given by:

$$|\mathbf{r} - \mathbf{r}_A| = \sqrt{\lambda^2 + 2\lambda \mathbf{m} \cdot \boldsymbol{\epsilon} + \boldsymbol{\epsilon}^2} = \lambda + \mathbf{m} \cdot \boldsymbol{\epsilon} + \frac{\boldsymbol{\epsilon}^2}{2\lambda} - \frac{(\mathbf{m} \cdot \boldsymbol{\epsilon})^2}{2\lambda} + O(\epsilon^3). \tag{G.60}$$

We have, to leading order in $\epsilon = |\boldsymbol{\epsilon}|$, that

$$\mathbf{A}(\boldsymbol{\epsilon}) = \frac{g}{4\pi} \frac{1}{\lambda} \frac{\mathbf{m} \times \boldsymbol{\epsilon}}{\epsilon^2/2\lambda - (\mathbf{m} \cdot \boldsymbol{\epsilon})^2/2\lambda} = \frac{g}{2\pi} \frac{\mathbf{m} \times \boldsymbol{\epsilon}}{|\mathbf{m} \times \boldsymbol{\epsilon}|^2}. \tag{G.61}$$

In cylindrical coordinates defined by $\mathbf{m} = \hat{\mathbf{z}}$ with origin at $\mathbf{r}_0$, we have $\boldsymbol{\epsilon} = \rho \hat{\boldsymbol{\rho}} + z\hat{\mathbf{z}}$. In these coordinates, we find that

$$\mathbf{A}(\boldsymbol{\epsilon}) = \frac{g}{2\pi\rho} \hat{\boldsymbol{\phi}} \tag{G.62}$$

where ρ is the distance from the string. In a neighborhood of the string, the dominant component of $\mathbf{A}$ is therefore the component encircling the string, which diverges

as $1/\rho$. Furthermore, the line integral around the string is given by

$$\lim_{\epsilon \to 0} \oint_C \mathbf{A}_m(\mathbf{r}) \cdot d\mathbf{r} = \int_0^{2\pi} \frac{g}{2\pi} d\phi = g, \tag{G.63}$$

as expected from (G.39).

G.3.2 Transformations of the Ray Gauge

We now apply these results to the gauge introduced in Section (G.2.1). Consider the rays $L_1 = \{\mathbf{r}_A + \lambda \mathbf{m}_1 : 0 \leq \lambda < \infty\}$ and $L_2 = \{\mathbf{r}_A + \lambda \mathbf{m}_2 : 0 \leq \lambda < \infty\}$, defining two Dirac strings as in Section (G.2.1). In the present section, we investigate the gauge function (G.52) associated with the change of gauge $\mathbf{A}_{L_1} \to \mathbf{A}_{L_2}$.

Consider the plane spanned by the vectors $\mathbf{m}_1$ and $\mathbf{m}_2$. Let P denote that segment of the plane that lies in the wedge defined by the interior angle between the two rays. The surface P then inherits an orientation from the boundary $L_2 - L_1$ given by the constant normal $\mathbf{n} = \mathbf{m}_2 \times \mathbf{m}_1$. The gauge function (G.52) is then the solid angle subtended by P at the point $\mathbf{r}$, which we evaluate as follows.

We evaluate Ω in coordinates such that the surface P defines the plane $z = 0$ and $\mathbf{n} = \hat{\mathbf{z}}$. Furthermore, we choose the x-axis to coincide with the ray L_2, so that the source $\mathbf{r}_A$ lies at the origin. Let α denote the interior angle between the two rays. In these coordinates we may represent a point on the surface P in polar coordinates as $\mathbf{r}' = \rho \cos\phi \hat{\mathbf{x}} + \rho \sin\phi \hat{\mathbf{y}}$, with $0 \leq \phi < \infty$. Similarly, we write $\mathbf{r} = x\hat{\mathbf{x}} + y\hat{\mathbf{y}} + z\hat{\mathbf{z}}$

so that $\mathcal{R}^2 = \rho^2 - 2\rho(x\cos\phi + y\sin\phi) + r^2$, where $r^2 = x^2 + y^2 + z^2$. Then

$$\begin{aligned}\Omega(\mathbf{r}) &= \int_P \frac{\hat{\mathcal{R}}\cdot\mathbf{n}}{\mathcal{R}^2} dS' \\ &= \int_0^\alpha \int_0^\infty \frac{-z}{\left[\rho^2 - 2(x\cos\phi + y\sin\phi)\rho + x^2 + y^2 + z^2\right]^{3/2}} \rho d\rho d\phi \\ &= \int_0^\alpha \frac{-z}{r - x\cos\phi - y\sin\phi} d\phi = -2\frac{z}{|z|}\arctan\left(\frac{-y + (r+x)t}{|z|}\right)\Bigg|_{t=0}^{t=\tan\alpha/2}. \end{aligned} \quad \text{(G.64)}$$

Let $\kappa = \tan\alpha/2$. We have in these coordinates the result:

$$\Omega(\mathbf{r}) = 2\left(\arctan\left(\frac{y - (r+x)\kappa}{z}\right) - \arctan\left(\frac{y}{z}\right)\right). \quad \text{(G.65)}$$

It can be shown by direct calculation that $\nabla^2\Omega = 0$ at all points where the second derivatives are defined. This is the case for all points away from the plane $z = 0$. What happens in the plane of the strings, $z = 0$? Note that

$$\lim_{u\to+\infty} \arctan(u) = \frac{\pi}{2} \qquad \lim_{u\to-\infty} \arctan(u) = -\frac{\pi}{2}. \quad \text{(G.66)}$$

The arguments of the arctan appearing in (G.65) diverge, but their sign is determined by where the limits are taken. Define $f_1(x,y) = y - (\sqrt{x^2+y^2} + x)\kappa$ and $f_2(x,y) = y$. Then the limit from above is given by

$$\lim_{z^+\to 0} \Omega(\mathbf{r}) = \operatorname{sgn}(f_1)\pi - \operatorname{sgn}(f_2)\pi. \quad \text{(G.67)}$$

In the regions outside the wedge, $\operatorname{sgn}(f_1) = \operatorname{sgn}(f_2)$ and therefore the limit vanishes. Inside the wedge, $\operatorname{sgn}(f_1) = -1$ and $\operatorname{sgn}(f_2) = +1$. Therefore $\lim_{z^+\to 0}\Omega = -2\pi$. The limit from below is given by

$$\lim_{z^-\to 0} \Omega(\mathbf{r}) = -\operatorname{sgn}(f_1)\pi + \operatorname{sgn}(f_2)\pi. \quad \text{(G.68)}$$

Outside the wedge, Ω is continuous across the plane $z = 0$. Inside the wedge, there is a jump discontinuity of magnitude 4π, corresponding to a reversal of sign in crossing from one side of the wedge to the other.

As a final result, we consider the geometric interpretation of Ω. The gauge function Ω is given by the solid angle subtended by the wedge P at the evaluation point $\mathbf{r}$. Surrounding $\mathbf{r}$ by a unit sphere, we project P onto the sphere as follows. Consider the ray L_1 originating at the source point $\mathbf{r}_A$. The segment of the line connecting the center $\mathbf{r}$ and the point $\mathbf{r}_A$ intersects the sphere at a single point $\mathbf{r}'_A$, representing the projection of $\mathbf{r}_A$ onto the sphere. We then construct a ray parallel to L_1 with endpoint at the center of the sphere $\mathbf{r}$. This ray likewise intersects the sphere at a single point $\mathbf{e}_1$. The projection of L_1 onto the sphere is then that segment of the great circle, lying in the plane defined by L_1 and $\mathbf{r}$, that connects points $\mathbf{r}'_A$ and $\mathbf{e}_1$. A similar construction applies for L_2, and for each ray originating at $\mathbf{r}_A$ contained in the wedge P. The projection is therefore a spherical triangle with vertices $\mathbf{r}'_A$, $\mathbf{e}_1$, $\mathbf{e}_2$ (Fig G.2). The gauge function Ω is given by the associated spherical area.

The area of a spherical triangle with interior angles A, B, and C is given by $\triangle ABC = (A + B + C - \pi)R^2 = ER^2$, where R is the radius of the sphere and E is the angle excess. Given three sides a, b, c, the angle excess E of a spherical triangle is given by [53]

$$\tan\frac{E}{4} = \sqrt{\tan\frac{1}{2}d\tan\frac{1}{2}(d-a)\tan\frac{1}{2}(d-b)\tan\frac{1}{2}(d-c)} \tag{G.69}$$

where $d = (a + b + c)/2$. This can be applied as follows. As before, we let α be the

interior angle between the two rays L_1 and L_2. Let θ_1 and θ_2 be the angles of L_1 and L_2, respectively, with respect to the radial segment. In this case the sides of the triangle are given by $a = \alpha$, $b = \pi - \theta_1$, and $c = \pi - \theta_2$. It follows that

$$\Omega = \pm 4 \arctan\left(\sqrt{\frac{\tan\frac{1}{2}(s+\theta_1)\tan\frac{1}{2}(s+\theta_2)}{\tan\frac{1}{2}s\tan\frac{1}{2}(s-\alpha)}}\right) \tag{G.70}$$

where $s = (\alpha - \theta_1 - \theta_2)/2$. The sign is chosen by the orientation of P. Namely, the $+$ sign is chosen if $\mathbf{n}$ points "away from" $\mathbf{r}$ (that is $(\mathbf{r}' - \mathbf{r}) \cdot \mathbf{n} > 0$ for all $\mathbf{r}' \in P$), while the $-$ sign is chosen if $\mathbf{n}$ points "toward" $\mathbf{r}$ (that is $(\mathbf{r}' - \mathbf{r}) \cdot \mathbf{n} < 0$ for all $\mathbf{r}' \in P$).

In the limit as $\mathbf{r}$ passes through the plane of the wedge, we have the following. Outside the wedge, note that either $\theta_2 = \theta_1 + \alpha$ or $\theta_1 = \theta_2 + \alpha$. Thus, $s = -\theta_1$ or $s = -\theta_2$. In either case, $\Omega = 0$. Inside the wedge, note that $\alpha = \theta_1 + \theta_2$ so that $s = 0$ and $\Omega = \pm 2\pi$, as expected.

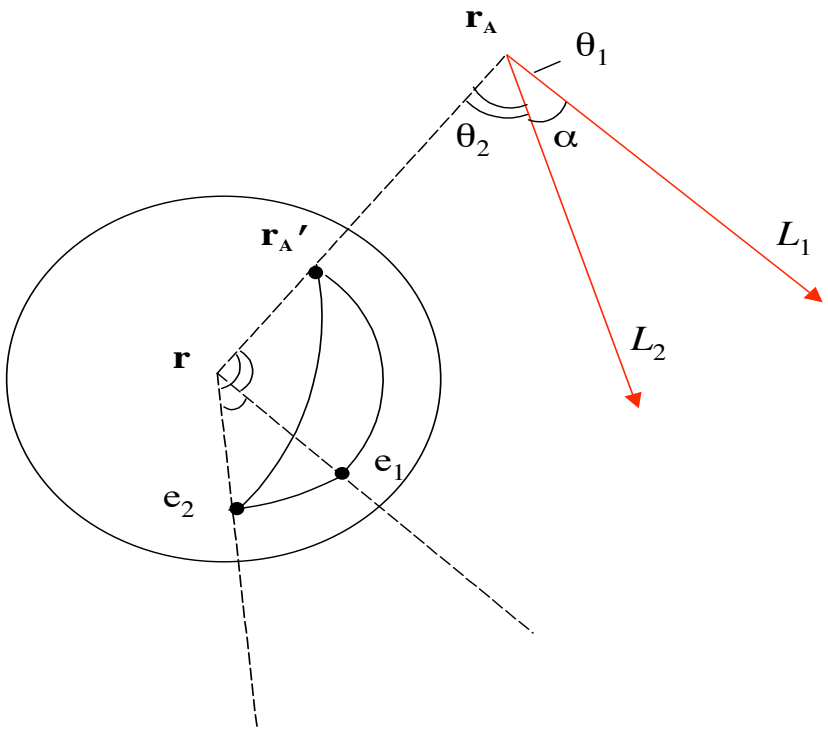

Figure G.2: Geometrical interpretation of the gauge function Ω as a spherical area. (See equation (G.70).)

Appendix H

Potential Theory

H.1 Background

Poisson's equation is an example of a class of partial differential equations known as elliptic PDE's. A general linear partial differential equation of second order in the N variables $x = (x_1, x_2, ..., x_N)$ takes the form

$$Lu = \sum_{i,k=1}^{N} a_{ik} \frac{\partial^2 u}{\partial x_i \partial x_k} + \sum_{i=1}^{N} b_i \frac{\partial u}{\partial x_i} + cu = f, \tag{H.1}$$

where the solution u is assumed to be twice continuously differentiable on some open set $\Omega \subset \mathbb{R}^N$. That is, $u \in C^2(\Omega)$. Similarly, we assume the coefficients a_{ik}, b_i, and c are continuously differentiable functions of x on the domain Ω. Finally, f is assumed to be continuous on Ω. The existence of solutions and their important properties are determined by the second-order part of the linear operator,

$$L_0 = \sum_{i,k=1}^{N} a_{ik}(x) \frac{\partial^2}{\partial x_i \partial x_k}, \tag{H.2}$$

referred to as the *principal* part of L. At a given point $x \in \Omega$, the coefficients of the second-order terms $a_{ik}(x)$ define a quadratic form (the characteristic form of L) given by $Q(\lambda) = \sum_{i,k=1}^{N} a_{ik}\lambda_i\lambda_k = (\lambda, A\lambda)$ for all $\lambda \in \mathbb{R}^N$, where A is the matrix with entries $A_{ij} = a_{ij}$. Note that A may be taken to be symmetric because only the symmetric part of a_{ij} contributes to (H.1). A quadratic form of this type can always be transformed by a similarity transformation employing a real orthogonal

matrix, $\lambda = S\eta$, into the normal form $Q(\eta) = \sum_{i=1}^{N} \kappa_i \eta_i^2$, where the coefficients κ_i take on only the values +1,-1, or 0. We let p be the number of coefficients κ_i taking on positive values, let q be the number of κ_i taking on negative values, and let s be the number of vanishing κ_i. These correspond to the number of positive, negative, and zero eigenvalues of the matrix $A(x)$, respectively. The important feature is that these numbers are invariant under general coordinate transformations of the independent variables appearing in the differential equation.

The equation (H.1) is elliptic at a point x provided all values κ_i are +1 or all values are -1; that is, $A(x)$ is positive definite or negative definite. Similarly, the equation is parabolic at a point x provided one or more of the κ_i vanish; that is, $A(x)$ is a singular matrix. The equation is hyperbolic at x provided all values of the κ_i have the same sign except one, which takes the opposite sign. Finally, when there is more than one nonvanishing κ_i of each sign, the equation is ultrahyperbolic. In this Appendix, we focus on the properties of elliptic equations.

The operator L is elliptic in a domain $R \subseteq \Omega$ if (H.1) is elliptic at each point of R. In the special case that the coefficients are constant, it is possible to reduce the differential equation to normal form over the entire domain Ω. By a linear change of the independent variables and a change in the dependent variable, a general elliptic equation with constant coefficients can be reduced the normal form

$$\nabla^2 v(x) + cv(x) = g(x) \tag{H.3}$$

for $x \in \Omega$, where c is a constant. In particular, for $c = 0$ the expression reduces to Poisson's equation with a source term $g(x)$.

The corresponding homogeneous equation $\nabla^2 v = 0$ is the familiar Laplace equation. A function $v \in C^2(\Omega)$ satisfying the Laplace equation is said to be *harmonic* on Ω. Harmonic functions have a number of well-known special properties, which we summarize here.

Mean-Value Property: Let h be a harmonic function on Ω. For any spherical ball $B(x,r)$ of radius r contained completely within Ω with center at a point x, such that $\overline{B(x,r)} \subset \Omega$, we have

$$h(x) = \frac{1}{vol\{B\}} \int_{B(x,r)} h(y)dy, \tag{H.4}$$

$$h(x) = \frac{1}{area\{S\}} \int_{S(x,r)} h(y)dS. \tag{H.5}$$

Here dy denotes the N-dimensional volume measure on $\mathbb{R}^N$, and dS denotes the $(N-1)$ dimensional measure on the surface of the ball. Similarly, $vol\{B\}$ and $area\{S\}$ are the volume of the ball in $\mathbb{R}^N$ and the surface area of its spherical boundary, respectively. Conversely, suppose $h \in C(\Omega)$ is continuous. If the mean-value property (H.4) or (H.5) holds for every $B(x,r)$ contained in Ω, then h is harmonic on Ω.

Extremum Property: Suppose h is harmonic on Ω, and let $x \in \Omega$. If Ω is connected and h attains an extremum at x, then h is constant. Otherwise, h attains its extrema on the boundary of Ω, and $\min_{\partial\Omega} h \leq h \leq \max_{\partial\Omega} h$.

Regularity Property: If h is harmonic on Ω, then $h \in C^\infty(\Omega)$ and all partial derivatives of h are also harmonic on Ω.

Analyticity Property: If h is harmonic on Ω, then h is real-analytic on Ω. In addition, h can be expanded as a series of harmonic polynomials. That is, for

each $x_0 \in \Omega$ there is a ball of nonzero radius $r > 0$ and a unique sequence $\{H_j\}$ of harmonic polynomials such that

$$h(x_0 + x) = \sum_{j=0}^{\infty} H_j(x), \tag{H.6}$$

where each H_j is homogeneous of degree j. In particular, if h is harmonic on some ball $B(x_0, r)$ of radius r about x_0, then the series (H.6) converges absolutely and locally uniformly on all of $B(x_0, r)$.

Harmonic Polynomials: Let $\mathcal{P}_d$ denote the vector space of all real-valued homogeneous polynomials of degree d on $\mathbb{R}^3$. We note that the set of polynomials in $\mathcal{P}_d$ which are also harmonic forms a finite-dimensional subspace of dimension $2d + 1$, which we denote $\mathcal{H}_d$. Let $\mathcal{Q}_d$ denote the set of all polynomials of the form $Q(x, y, z) = (x^2 + y^2 + z^2)P(x, y, z)$ where $P \in \mathcal{P}_{d-2}$. If we introduce the inner product on $\mathcal{P}_d$,

$$\langle P, Q \rangle = \int_S PQ dS \tag{H.7}$$

by integrating over the surface of the unit sphere S in $\mathbb{R}^3$, then the space of homogeneous polynomials may be written as the orthogonal direct sum $\mathcal{P}_d = \mathcal{H}_d \oplus \mathcal{Q}_d$. (For proofs of the above claims, see [93].)

The properties summarized above will be used repeatedly throughout the body of this dissertation.

H.2 Representation in Terms of Surface Data

Given any linear elliptic differential equation $Lu = f$, a central role is played by the set of fundamental solutions for L. A *fundamental solution* for L, which we

denote as $\mathcal{E}$, is a regular distribution satisfying

$$L\mathcal{E}(x) = \delta(x), \tag{H.8}$$

where $\delta(x)$ is the Dirac-delta distribution centered at the origin $x = 0$ in $\mathbb{R}^N$. We will consider only the case in which L contains derivatives of even order, as in (H.3).

A word of clarification is warranted. Let $C_0^\infty(\Omega)$ denote the space of infinitely differentiable functions ϕ which have compact support contained in Ω. (That is, the closure of the set of points for which $\phi \neq 0$ is compact and contained within Ω.) Then (H.8) is equivalent to

$$\begin{aligned} L\mathcal{E}(x) &= 0, \qquad x \neq 0 && \text{(H.9)} \\ (L\mathcal{E}, \phi) &= \int_\Omega \mathcal{E}(L\phi)dx = \phi(0), && \text{(H.10)} \end{aligned}$$

for all test functions $\phi \in C_0^\infty(\Omega)$. Here dx denotes the volume measure on $\mathbb{R}^N$. We note that the function

$$\mathcal{E}_N(x) = \begin{cases} \frac{1}{2\pi}\log||x|| & \text{if } N = 2 \\ -\frac{1}{(N-2)\omega_N}\frac{1}{||x||^{N-2}} & \text{if } N \geq 3 \end{cases} \tag{H.11}$$

is a fundamental solution for the Laplace operator in $\mathbb{R}^N$, where the constant $\omega_N = 2\pi^{N/2}/\Gamma(N/2)$ is the volume of the unit sphere in $\mathbb{R}^N$. In $\mathbb{R}^3$, this is the familiar expression for the potential of a point charge at the origin

$$\mathcal{E}_3(\mathbf{x}) = -\frac{1}{4\pi}\frac{1}{|\mathbf{x}|^2}, \tag{H.12}$$

where we denote vectors in $\mathbb{R}^3$ by boldface. The significance of the fundamental solutions is that they allow the general solution of the PDE to be constructed, at

least formally, for a general domain. A particular solution for the inhomogeneous equation $Lu = f$ is given by

$$u(x) = (\mathcal{E} \star f)(x) = \int_{\mathbb{R}^N} \mathcal{E}(x-y) f(y) dy, \tag{H.13}$$

provided the convolution is defined. This follows from the fact that

$$L(\mathcal{E} \star f) = (L\mathcal{E}) \star f = \delta \star f = f. \tag{H.14}$$

Note that for any u, $v \in C^2(\Omega) \cup C^1(\bar{\Omega})$ we have

$$\nabla \cdot (u\nabla v - v\nabla u) = u\nabla^2 v - v\nabla^2 u. \tag{H.15}$$

Integrating over the domain $\Omega \subset \mathbb{R}^N$ produces Green's integral identity,

$$\int_\Omega (u\nabla^2 v - v\nabla^2 u) dx = \int_{\partial\Omega} \left(u\frac{\partial v}{\partial n} - v\frac{\partial u}{\partial n} \right) dS, \tag{H.16}$$

where here n is a unit vector denoting the direction of the exterior normal to the boundary $\partial\Omega$, and we introduce the normal derivative

$$\frac{\partial}{\partial n} = n \cdot \partial. \tag{H.17}$$

We can now set $v(x') = \mathcal{E}_N(x - x')$ from (H.12), provided we omit from the domain some small ball B_ϵ of radius $\epsilon > 0$ about the point x where $\mathcal{E}_N(x - x')$ is singular. Then v is smooth on $\Omega_\epsilon = \Omega \setminus B_\epsilon$ and (H.16) applies to this domain. In particular, $\nabla^2 v = 0$ and

$$\begin{aligned} -\int_\Omega \mathcal{E}(x-x')\nabla^2 u(x') dx' = \int_{\partial\Omega} \left(u(x')\frac{\partial \mathcal{E}(x-x')}{\partial n} - \mathcal{E}(x-x')\frac{\partial u}{\partial n} \right) dS' \\ - \frac{1}{4\pi\epsilon^2} \int_{|x-x'|=\epsilon} \left(u(x') + \epsilon\frac{\partial u}{\partial n} \right) dS'. \end{aligned} \tag{H.18}$$

Taking the limit at $\epsilon \to 0$, we obtain the following result.

Green's Representation Theorem 1. *Let $u \in C^2(\Omega) \cap C^1(\overline{\Omega})$. Then for any $x \in \Omega$ we have*

$$u = Z\nabla^2 u + V \left.\frac{\partial u}{\partial n}\right|_{\partial\Omega} + W\, u|_{\partial\Omega} \tag{H.19}$$

where the following three integrals,

$$Z\psi(x) = \int_\Omega \psi(y)\mathcal{E}_n(x-y)dy, \tag{H.20}$$

$$V\psi(x) = -\int_{\partial\Omega} \psi(y)\mathcal{E}_n(x-y)dS(y), \tag{H.21}$$

$$W\psi(x) = \int_{\partial\Omega} \psi(y)\frac{\partial \mathcal{E}_n}{\partial n_y}(x-y)dS(y), \tag{H.22}$$

are referred to as the volume potential, the single-layer potential, and the double-layer potential corresponding to a density ψ.

The theorem states that a general function can be reconstructed as a sum of these three types of potentials. Within the domain Ω, the *volume potential* satisfies the Poisson equation $\nabla^2(Z\psi) = \psi$. The volume potential appearing in (H.19) is the potential due to a charge distribution $\psi = \nabla^2 u$ within Ω. Both the single-layer and double-layer potentials are harmonic functions at all points in Ω. The *single-layer* potential in (H.19) represents the potential due to a monopole distribution of density $\psi = -\partial u/\partial n$ on the surface $\partial\Omega$. Finally, the *double-layer* potential in (H.19) is the potential due to a distribution of dipoles on the surface $\partial\Omega$, the direction of which at any point coincides with the exterior normal, with dipole moment $\psi = u$.

In the particular case that u is a harmonic function, the first term of (H.19) vanishes. We then see that u can be represented entirely in terms of its values on the surface of the domain Ω. Exactly how this is to be accomplished in practice depends

on the boundary-values available. In the case that u is taken to be a scalar electric or magnetic potential, we may have the values of the potential itself available on the bounding surface. In this case, we wish to represent the solution in the interior in terms of a single-layer potential alone, leading to the inner *Dirichlet* problem. More likely, we may have values of the electric or magnetic field available on the surface, and we wish to represent the solution in the interior in term of a double-layer potential alone, leading to the inner *Neumann* problem. We focus here on the latter case.

In particular, consider the Neumann problem for the Poisson equation

$$\nabla^2 u = f \text{ on } \Omega, \tag{H.23a}$$

$$\left.\frac{\partial u}{\partial n}\right|_{\partial\Omega} = \phi \text{ on } \partial\Omega, \tag{H.23b}$$

with $\Omega \subset \mathbb{R}^N$. Under fairly general conditions on the bounding surface, it is possible to construct a Green's function for (H.23) as follows. Let $G : \bar{\Omega} \times \bar{\Omega} \to \mathbb{R}$ be a fundamental solution of the Laplace operator satisfying

$$\frac{\partial G(x,y)}{\partial n} = \alpha, \tag{H.24a}$$

$$G(x,y) - \mathcal{E}_N(x-y) = v_y(x), \tag{H.24b}$$

where α is a constant and v_y is harmonic in x for all $y \in \Omega$. Then G is a Green's function for the inner Neumann problem (H.23) on Ω. By construction, G is a fundamental solution in the variable $x-y$. Applying Green's representation theorem (H.19) then allows us to write a given $u \in C^2(\Omega) \cap C^1(\overline{\Omega})$ in the form

$$u(x) = \int_\Omega G(x,y)\nabla^2 u(y)dy + \int_{\partial\Omega}\left[u(y)\frac{\partial G(x,y)}{\partial n_y} - G(x,y)\frac{\partial u}{\partial n}(y)\right]dS(y). \tag{H.25}$$

Any solution of $\nabla^2 u = f$ may therefore be written by using (H.24) together with (H.25) to find that

$$u(x) = \alpha \langle u \rangle_{\partial\Omega} + \int_\Omega G(x,y) f(y) dy - \int_{\partial\Omega} G(x,y) \frac{\partial u}{\partial n}(y) dS(y), \tag{H.26}$$

where $\langle u \rangle_{\partial\Omega}$ denotes the integral of u over the boundary $\partial\Omega$. In the case of the Laplace equation, the source term f vanishes, and we again obtain a representation of the solution in terms of surface data alone. Namely,

$$u(x) = \alpha \langle u \rangle_{\partial\Omega} - \int_{\partial\Omega} G(x,y) \frac{\partial u}{\partial n}(y) dS(y). \tag{H.27}$$

It can be shown that a solution to the source-free Neumann problem exists for continuous boundary data if and only if the boundary data satisfies the condition

$$\int_{\partial\Omega} \frac{\partial u}{\partial n}(y) dS(y) = 0. \tag{H.28}$$

If this is satisfied, the solution is unique up to a constant. For this reason, we may choose u such that its integral over the boundary vanishes. That is, if $\phi(x) = \partial u(x)/\partial n$ satisfies (H.28), then the unique solution of (H.23) with $\langle u \rangle_{\partial\Omega} = 0$ is found from (H.27) to be

$$u(x) = -\int_{\partial\Omega} G(x,y) \phi(y) dS(y). \tag{H.29}$$

Note that while the fundamental solutions appearing in (H.19) depend only on the dimension of the space, the Green's function G depends strongly on the geometry of the domain Ω. In the context of magnetic fields, (H.29) allows one to express source-free fields of the form $\mathbf{B} = \nabla u$ in terms of their normal component $\mathbf{n} \cdot \mathbf{B} = \partial u/\partial n$ on the boundary. We have thus eliminated the need for potential data

on the surface, at the cost of introducing a geometry-dependent integration kernel. (An alternative approach, utilizing both field and potential data, is discussed in Chapter 5.)

H.3 Smoothing Property of Elliptic PDE's

Many of the properties of harmonic functions described in Section H.1 also apply to solutions of more general elliptic PDE's. As this class of PDE's includes the Poisson and Helmholtz equations, critical to the electromagnetic modeling of beamline elements, we wish to consider this more general case. In particular, a general feature of elliptic PDE's is the *smoothness* of their interior solutions. In this section, we present the primary results which describe the smoothness of these solutions and place corresponding bounds on their derivatives. In particular, we will see that (unlike the derivative operator discussed in Appendix A) the inverse of an elliptic operator is often a continuous linear transformation.

H.3.1 Interior Estimates

We consider differential operators L of the form appearing in (H.1). In addition, we assume for simplicity that the coefficients a_{ik}, b_i, c are constant. (Such is the case for the Poisson and Helmholtz equations.) The form of the fundamental solution for such a differential operator L may be used to study the local properties of the solution at interior points, and to provide various interior estimates.

This technique may be used, for example, to show that the following claims

are equivalent [96]:

1) L is an elliptic operator.

2) There exists a fundamental solution for L which is analytic except at the origin.

3) All solutions of the homogeneous equation $Lu = 0$ are analytic in Ω.

To see that 2) implies 3), we note that the behavior near a point $x_0 \in \Omega$ of any solution u of $Lu = 0$ can be written in terms of the fundamental solution $\mathcal{E}$ as follows. Let $\phi \in C_0^\infty(\Omega)$ be a smooth test function such that $\phi = 1$ on some neighborhood B_ϵ of x_0. By construction, ϕ vanishes outside some larger compact domain K such that $B_\epsilon \subset K \subset \Omega$. Now consider the function $u\phi$. Clearly $u\phi = u$ in B_ϵ, and $u\phi = 0$ outside K. If we define $f = L(u\phi)$, then the convolution given in (H.13) is well-defined, since each derivative of $u\phi$ (and therefore the function f) mush vanish outside the compact domain K. The equation $L(u\phi) = f$ therefore has the solution

$$u\phi = \mathcal{E} \star f = \mathcal{E} \star L(u\phi). \tag{H.30}$$

However, in the neighborhood B_ϵ surrounding x_0 we know $u\phi = u$, so that for $x \in B_\epsilon$ we have the integral representation

$$u(x) = \int_K \mathcal{E}(x - x')L(u\phi)|_{x'}\, dx'. \tag{H.31}$$

If follows from (H.31) that if the fundamental solution $\mathcal{E}(x)$ is analytic for all $x \neq 0$, then u is analytic at the point $x_0 \in \Omega$. In particular, this construction makes *no* assumptions about the geometry of the domain Ω or the values of u on the boundary.

In addition, if the equation $Lu = 0$ is brought to the normal form $\nabla^2 u + cu = 0$ on Ω, then for any sphere S contained in Ω we have a mean-value property analogous

to the mean-value property for harmonic functions. In particular, [94] gives the mean-value relationship

$$u(x)\frac{\sin R\sqrt{c}}{R\sqrt{c}} = \frac{1}{4\pi R^2}\int_{S(x,R)} u(y)dS(y), \tag{H.32}$$

where R is the radius of a sphere centered at the point x.

As a final example, we consider interior estimates for Laplace equation. Suppose $L = \nabla^2$, so that u is harmonic. Let $x \in \Omega$ and let d denote the distance of x to the boundary $\partial\Omega$. (That is, d is the radius of the largest ball $B(x,d)$ centered at x such that $B(x,d) \subseteq \Omega$.) We let

$$D^\alpha = \frac{\partial^{|\alpha|}}{\partial^{\alpha_1} x_1 \partial^{\alpha_2} x_2 \ldots \partial^{\alpha_N} x_N} \tag{H.33}$$

denote a mixed partial derivative of order $|\alpha| = \alpha_1 + \alpha_2 + \cdots \alpha_N$. Then the value of this derivative is bounded by

$$|D^\alpha u(x)| \leq \left(\frac{n|\alpha|}{d}\right)^{|\alpha|} \max_{\bar{\Omega}} |u(x)|. \tag{H.34}$$

Thus, we see that high-order derivatives of harmonic functions decay quickly as we move away from the boundary toward the interior.

H.3.2 Global Estimates

Rather than presenting theorems for a general elliptic operator L, we describe the results in the setting $L = \nabla^2$. Those features specific to the Laplacian operator will be stated explicitly. The following results may be found in [96], [97], [37].

H.3.2.1 Formulation in Sobolev spaces

We first define the appropriate spaces of functions. Let Ω be a bounded open region in $\mathbb{R}^3$ with a smooth boundary, and let m be a nonnegative integer. Recall that $C^m(\Omega)$ denotes the vector space of real-valued functions on Ω possessing continuous partial derivatives through order m. We define a norm $||\cdot||_m$ given by

$$||u||_m^2 = \sum_{|\alpha|\leq m} ||D^\alpha u||^2 = \int_\Omega \sum_{|\alpha|\leq m} |D^\alpha u|^2 dx, \tag{H.35}$$

where $||\cdot||$ denotes the usual norm on the space $L_2(\Omega)$, and the sum is taken over all multi-indices α defined in (H.33). Let $C^{m,*}(\Omega)$ denote the space of functions $u \in C^m(\Omega)$ for which the above norm is finite. That is, those functions have square-integrable derivatives through order m on Ω. The *Sobolev space* $H^m(\Omega)$ is the completion of the space $C^{m,*}(\Omega)$ with respect to the norm (H.35). (A similar technique may be used to define the spaces $H^m(\partial\Omega)$ on the boundary, where the integrals in (H.35) become integrals over the surface $\partial\Omega$.)

The completion of $C^{m,*}(\Omega)$ requires the introduction of functions which may not be differentiable in the usual pointwise sense. We say that a function $u \in L_2(\Omega)$ possesses a *weak derivative* $D^\alpha u$ in $L_2(\Omega)$ if there is some function $v \in L_2(\Omega)$ such that

$$\int v\phi dx = (-1)^{|\alpha|} \int u D^\alpha \phi dx \tag{H.36}$$

for every test function $\phi \in C_0^\infty(\Omega)$. (That is, v is the derivative of u in the sense of distributions.) The Sobolev space $H^m(\Omega)$ is then the set of functions $u \in L_2(\Omega)$ possessing weak derivatives $D^\alpha u \in L_2(\Omega)$ through order m. We note that $H^m(\Omega)$ is a subspace of the usual $L_2(\Omega)$ space for $m = 0, 1, 2, \cdots$. In fact, we have $L_2(\Omega) =$

$H^0(\Omega) \supset H^1(\Omega) \supset H^2(\Omega) \cdots$. In addition, functions appearing in the Sobolev space $H^m(\Omega)$ are contained in the usual $C^k(\Omega)$ spaces for m sufficiently large. Indeed, for any piecewise-smooth domain $\Omega \subset \mathbb{R}^n$,

$$H^s(\Omega) \subset C_b^k(\Omega) \qquad \text{for } s > n/2 + k, \tag{H.37}$$

where $C_b^k(\Omega)$ denotes the subset of functions in $C^k(\Omega)$ that are also *bounded* with bounded derivatives through order k.

To use these spaces in discussing boundary-value problems, we must first define the restriction of a function $u \in H^m(\Omega)$ to the boundary $\partial\Omega$, $m \geq 1$. While the boundary values of u may not be defined in the usual pointwise sense, we note that the space of smooth functions $C^\infty(\bar{\Omega})$ is *dense* in $H^m(\Omega)$. Thus, we may construct a sequence $\{u_k\}$ of functions in $C^\infty(\bar{\Omega})$ such that $u_k \to u$ with respect to (H.35). Each of these functions has a pointwise restriction to the boundary $u_k|_{\partial\Omega} \in C^\infty(\partial\Omega)$. It can be shown that this sequence converges in the space $H^{m-1}(\partial\Omega)$ to a unique limit $u|_{\partial\Omega}$, called the *trace* of u on $\partial\Omega$. Note that $u|_{\partial\Omega}$ is independent of the sequence $\{u_k\}$ used to represent u. The trace $u|_{\partial\Omega}$ of all functions $u \in H^m(\Omega)$ in fact defines a smaller space $H^{m-1/2}(\partial\Omega) \subseteq H^{m-1}(\partial\Omega)$ of functions on the boundary, with norm given by:

$$||u||_{m-1/2} = \inf \left\{ ||w||_m \text{ such that } w \in H^m(\Omega), w = u \text{ on } \partial\Omega \right\}. \tag{H.38}$$

A norm equivalent to (H.38) can be written explicitly as

$$||u||_{m-1/2}^2 = ||u||_{m-1}^2 + \sum_{|\alpha|=m-1} \int_{\partial\Omega} \int_{\partial\Omega} \frac{|D^\alpha u(x) - D^\alpha u(x')|^2}{|x - x'|^3} dS dS', \tag{H.39}$$

where, in expression (H.39) only, $||\cdot||_{m-1}$ denotes the norm as defined on $H^{m-1}(\partial\Omega)$. For more about these spaces and associated theorems, we refer the reader to [96].

H.3.2.2 Elliptic Problems in Bounded Domains

The theory of elliptic boundary-value problems on smooth, bounded domains involves demonstrating that the linear operator appearing in the PDE is well-behaved when considered as a mapping between the appropriate function spaces. By well-behaved, we mean that such operators are *Fredholm*. A Fredholm operator $\mathcal{U}$, from a Banach space X into a Banach space Y, is a bounded linear transformation such that

- The kernel of $\mathcal{U}$ is finite-dimensional.
- The range of $\mathcal{U}$ is closed.
- The complement of the range of $\mathcal{U}$ is finite-dimensional.

In many cases, inverse operators can then be constructed by considering appropriate subspaces of the domain and range. As a result, the inverse of a differential operator L becomes an *integral* operator whose kernel is given by the Green's function for the domain Ω.

Consider, for example, the Dirichlet boundary-value problem given by

$$\nabla^2 u = f \text{ on } \Omega, \tag{H.40a}$$

$$u|_{\partial\Omega} = \phi \text{ on } \partial\Omega. \tag{H.40b}$$

We may associate with this problem the linear transformation

$$\mathcal{U}_D : H^m(\Omega) \to H^{m-2}(\Omega) \times H^{m-1/2}(\partial\Omega) \tag{H.41}$$

which takes

$$u \mapsto \left(\nabla^2 u, u|_{\partial\Omega}\right). \tag{H.42}$$

Then the following statements hold [96]:

1) For any $m \geq 2$, the operator $\mathcal{U}_D$ is a continuous (bounded) linear transformation with a continuous (bounded) inverse. In particular, $\mathcal{U}_D$ is an isomorphism.

2) The relation $u \in H^m(\Omega)$ is equivalent to the set of conditions $\nabla^2 u = f \in H^{m-2}(\Omega)$ and $u|_{\partial\Omega} = \phi \in H^{m-1/2}(\partial\Omega)$. If the boundary $\partial\Omega$ and the data f and ϕ are analytic, then the solution u is analytic on $\bar{\Omega}$.

3) As a consequence of 1) above, we have the so-called *Schauder* estimate

$$||u||_m \leq C\left(||\nabla^2 u||_{m-2} + ||u|_{\partial\Omega}||_{m-1/2}\right) \tag{H.43}$$

where the constant $C > 0$ depends only on the geometry of the domain. As a result, the global behavior and size of the derivatives of a solution u is determined by the behavior of the source f and the boundary-value data ϕ.

Similarly, consider the Neumann problem given by

$$\nabla^2 u = f \text{ on } \Omega, \tag{H.44a}$$

$$\left.\frac{\partial u}{\partial n}\right|_{\partial\Omega} = \phi \text{ on } \partial\Omega. \tag{H.44b}$$

We associate with this problem the linear transformation

$$\mathcal{U}_N : H^m(\Omega) \to H^{m-2}(\Omega) \times H^{m-3/2}(\partial\Omega) \tag{H.45}$$

which takes

$$u \mapsto \left(\nabla^2 u, \left. \frac{\partial u}{\partial n} \right|_{\partial\Omega} \right). \tag{H.46}$$

We then have the following [96]:

1) For any $m \geq 2$, the operator $\mathcal{U}_N$ is a Fredholm operator.

2) The relation $u \in H^m(\Omega)$ is equivalent to the set of conditions $\nabla^2 u = f \in H^{m-2}(\Omega)$ and $\partial u/\partial n|_{\partial\Omega} = \phi \in H^{m-3/2}(\partial\Omega)$. If the boundary $\partial\Omega$ and the data f and ϕ are analytic, then the solution u is analytic on $\bar{\Omega}$.

3) For all $m \geq 2$, we have the Schauder estimate

$$||u||_m \leq C \left(||\nabla^2 u||_{m-2} + \left\| \left. \frac{\partial u}{\partial n} \right|_{\partial\Omega} \right\|_{m-3/2} + ||u||_0 \right) \tag{H.47}$$

where the constant $C > 0$ depends only on the geometry of the domain.

In general, the operator $\mathcal{U}_N$ is not invertible. This follows since any constant function $u = c$ for $c \in \mathbb{R}$ is a solution for the data $\nabla^2 u = 0$, $\partial u/\partial n = 0$. We see in fact that the kernel of $\mathcal{U}_N$ is the one-dimensional subspace of $H^m(\Omega)$ containing the constant functions. The image of $\mathcal{U}_N$ consists of the pairs (f, ϕ) satisfying the compatibility condition

$$\int_\Omega f(x)dx - \int_{\partial\Omega} \phi(x)dS = 0. \tag{H.48}$$

An invertible operator $\hat{\mathcal{U}}$ may therefore be constructed by considering the subspaces

$$\mathcal{D} = \left\{ u \in H^m(\Omega) \,\middle|\, \int_\Omega u = 0 \right\} \tag{H.49}$$

$$\mathcal{R} = \left\{ (f, \phi) \in H^{m-2}(\Omega) \times H^{m-3/2}(\partial\Omega) \,\middle|\, \int_\Omega f(x)dx - \int_{\partial\Omega} \phi(x)dS = 0 \right\}. \tag{H.50}$$

The operator $\hat{\mathcal{U}} : \mathcal{D} \to \mathcal{R}$ defined as in (H.44) is then an isomorphism; $\hat{\mathcal{U}}$ is a continuous linear operator with continuous inverse.

H.3.2.3 Generalization to Cylinder Domains

Treatment of Unbounded Domains

The study of elliptic boundary-value problems on unbounded domains introduces a number of subtleties. For example, consider the Dirichlet problem for the Laplace equation in the strip $[0, \alpha] \times \mathbb{R}$, where we desire $u(x, 0) = 0$ and $u(x, \alpha) = 0$ on the two lines bounding the domain. Note than an infinite number of solutions to this boundary-value problem exist of the form

$$u_n(x, y) = e^{n\pi x/\alpha} \sin\left(\frac{n\pi y}{\alpha}\right) \tag{H.51}$$

for $n = 1, 2, \cdots$. Furthermore, these solutions grow without bound as $x \to \infty$. Interior values of u_n can be significantly greater than values appearing on the boundary! Note that this is not a violation of the extremum property of harmonic functions, since u_n has no local maxima or minima in the interior of the strip, and no global maximum or minimum.

These issues appear due to the fact that the closure of an unbounded domain in $\mathbb{R}^N$ is not *compact*. To avoid this problem, we may introduce the one-point compactification of $\mathbb{R}^N$, denoted $\mathbb{R}^N \cup \{\infty\}$, by including a "point at infinity." The set $\mathbb{R}^N \cup \{\infty\}$ can then be made into a differentiable manifold. A neighborhood containing the point at infinity may be covered by a coordinate patch with coordinates $\mathbf{r}^* = \mathbf{r}/r^2$, obtained by inverting with respect to the unit sphere. In particular, the point at infinity is then mapped to the origin in the coordinates $\mathbf{r}^*$. A function h is said to be "harmonic at infinity" if its Kelvin transform

$$h^*(\mathbf{r}) = \frac{1}{r^{N-2}} h\left(\frac{\mathbf{r}}{r^2}\right) \tag{H.52}$$

is harmonic at $\mathbf{r} = 0$. (For the significance of the Kelvin transform and its relationship to inversion with respect to the unit sphere, see Section F.3.) Note that this is equivalent to the condition that

$$h(\mathbf{r}) = O\left(\frac{1}{r^{N-2}}\right) \qquad \text{as } r \to \infty. \tag{H.53}$$

The condition (H.53) then allows one to define the usual Dirichlet and Neumann problems in unbounded domains. Similar asymptotic conditions may be constructed for other elliptic boundary-value problems (eg., Sommerfeld radiation conditions for the Helmholtz equation).

In the case of unbounded domains, the global estimates of the previous section also fail. However, the results of Section H.3.2.1 may be modified by restricting consideration to functions with a specified rate of growth. This can be done by introducing an appropriate weight into the norms appearing in the relevant function spaces. In the following section we apply this idea to the cylindrical domains of Chapters 2-4 by introducing the spaces H^m_β. While standard treatments (eg., [34]) use exponential weights of the form $e^{\beta z}$, we prefer more recent treatments involving polynomial weights due to the clear physical relevance of the resulting spaces. We follow [37], [38].

Application to Cylinders

Consider an infinite domain of uniform cross-section, given by $\Pi = \{(\mathbf{r}, z) : \mathbf{r} \in \Omega, z \in \mathbb{R}\}$ where Ω is a domain in $\mathbb{R}^2$ with compact closure $\bar{\Omega}$ and smooth boundary $\partial\Omega$. We let z denote the coordinate along the axis of the cylinder. For all $\beta \in \mathbb{R}$, we introduce the weighted space $H^m_\beta(\Pi)$ consisting of those functions u for which

the norm

$$||u||_{m,\beta} = ||(1+z^2)^{\beta/2}u||_m \tag{H.54}$$

is finite, where $||\cdot||_m$ denotes the norm in $H^m(\Pi)$ given in (H.35). (More precisely, we consider the completion of the space $C_0^\infty(\Pi)$ with respect to (H.54).)

Continuous functions in $H^m_\beta(\Pi)$ must decay asymptotically faster than some power of z to ensure convergence of the integral appearing in (H.54). To clarify this point, consider the integral

$$\int_{-\infty}^{\infty} \frac{1}{(1+z^2)^a} dz = \frac{\sqrt{\pi}\Gamma(a-1/2)}{\Gamma(a)}, \tag{H.55}$$

for real $a > 1/2$. The integral (H.55) converges to the rhs if and only if $a > 1/2$; otherwise, the integral diverges. It follows that a function of the form $g_a = (1+z^2)^{-a/2}$ lies in $L_2(\Pi)$ if and only if $a > 1/2$. This illustrates the necessary asymptotic behavior of functions in $L_2(\Pi)$. In particular, for a continuous function v to lie in $L_2(\Pi)$ it is sufficient that

$$v = O\left(\frac{1}{|z|^a}\right) \qquad \text{for } a > 1/2. \tag{H.56}$$

In addition, we see that

$$||g_a||^2_{0,\beta} = ||(1+z^2)^{\beta/2}g_a||^2_0 = \int_{-\infty}^{\infty} \frac{|g_a|^2}{(1+z^2)^{-\beta}} dz. \tag{H.57}$$

It follows that $g_a \in H^0_\beta(\Pi)$ if and only if $a > \beta + 1/2$. More generally, for a continuous function v to lie in $H^0_\beta(\Pi)$ it is sufficient that

$$v = O\left(\frac{1}{|z|^a}\right) \qquad \text{for } a > \beta + 1/2. \tag{H.58}$$

A treatment of boundary-value problems for Poisson's equation with general weights $\beta \in \mathbb{R}$ can be found in [37],[38]. We will consider only the simplest physically relevant

cases below. Consider an electric or magnetic field $\mathbf{F}$ in a source-free cylindrical region Π. We know that far outside the magnetic element in the fringe-field region the field and the corresponding scalar potential ψ, related by $\mathbf{F} = \nabla\psi$, are dominated by the lowest-lying spherical multipole moment. In particular, if the *monopole* moment is nonvanishing then

$$\psi \sim O\left(\frac{1}{|z|}\right) \qquad \text{as } z \to \infty \tag{H.59}$$

$$F_w \sim O\left(\frac{1}{z^2}\right) \qquad \text{as } z \to \infty \tag{H.60}$$

for each component $w = x, y, z$. For general magnetic fields, for which there is no monopole moment, the power of z appearing in the denominator of (H.59,H.60) is increased by 1. It follows that for realistic data, $\psi \in H_0^0(\Pi) = L_2(\Pi)$ and $F_w \in H_1^0(\Pi)$.

For the Dirichlet problem it is then sufficient to consider the case of weights with $\beta = 0$. We associate with this problem the operator

$$\mathcal{U}_D : H_0^m(\Pi) \to H_0^m(\Pi) \times H_0^{m-1/2}(\partial\Pi) \tag{H.61}$$

which takes

$$u \mapsto \left(\nabla^2 u, u|_{\partial\Pi}\right). \tag{H.62}$$

This operator is then an isomorphism. The claims 1)-3) of Section H.3.2.2 hold as described in the case of bounded domains, with the estimate

$$||u||_{m,0} \leq C\left(||\nabla^2 u||_{m-2,0} + ||\ u|_{m-1/2,0}\ ||\right) \tag{H.63}$$

where the constant $C > 0$ depends only on the geometry of the cylinder.

The theory of the Neumann problem in cylinder domains with polynomial weights appears to be incompletely developed at the time of writing of this dissertation. We describe the relevant results found in Theorem 6.3, Corollary 6.5 of [37] as we presently understand them. We wish to study the operator corresponding to the Neumann problem, which takes

$$u \mapsto \left(\nabla^2 u, \left. \frac{\partial u}{\partial n} \right|_{\partial \Pi} \right), \tag{H.64}$$

as defined on the appropriate function spaces. To ensure the appropriate asymptotic behavior (H.60) of the boundary data, consider the case of weights with $\beta = 1$. Suppose $(f, \phi) \in H_1^{m-2}(\Pi) \times H_1^{m-3/2}(\partial\Pi)$. Then there is a solution $u \in H_{-1}^m(\Pi)$ with $\nabla u \in L_2(\Pi)$ if and only if

$$\int_\Pi f(x)dx - \int_{\partial\Pi} \phi(x)dS = 0. \tag{H.65}$$

This solution is unique up to a constant. Futhermore, this solution may be written in the form

$$u = \hat{u} + U \tag{H.66}$$

where $\hat{u} \in H_1^m(\Pi)$ and

$$||\hat{u}||_{m,1} + ||(1+z^2)^{1/2}\partial_z^2 U||_{m-1,1} + ||\partial_z U||_{0,0} + ||(1+z^2)^{-1/2} U||_{0,0} \tag{H.67}$$

$$\leq C \left(||f||_{m-2,1} + ||\phi||_{m-3/2,1} \right). \tag{H.68}$$

H.4 Relationship between Green and Helmholtz Theorems

We now discuss the relationship between Green's theorem and the Helmholtz theorem. In this section, vectors in $\mathbb{R}^3$ are denoted in boldface, such that $\mathbf{x} = (x, y, z)$

in Cartesian coordinates.

For the subspace Im(grad) of vector fields which can be written as gradients, the Helmholtz theorem (5.3), (5.21-5.22) of Chapter 5 is equivalent to Green's representation theorem (H.19). This can be seen as follows. Let $\mathbf{F}$ lie in Im(grad) such that $\mathbf{F} = \nabla u$. It then follows that $\nabla^2 u = \nabla \cdot \mathbf{F}$ and $\partial u/\partial n = \mathbf{n} \cdot \mathbf{F}$. Recall the notation $\mathcal{E}(\mathbf{r}, \mathbf{r}') = -\frac{1}{4\pi|\mathbf{r}-\mathbf{r}'|}$. Using Green's representation theorem,

$$\begin{aligned} u(\mathbf{r}) &= \int_\Omega \mathcal{E}(\mathbf{r}, \mathbf{r}') \nabla'^2 u dV' + \int_{\partial\Omega} \left(u \frac{\partial \mathcal{E}(\mathbf{r}, \mathbf{r}')}{\partial n} - \mathcal{E}(\mathbf{r}, \mathbf{r}') \frac{\partial u}{\partial n} \right) dS' \\ &= -\frac{1}{4\pi} \int_\Omega \frac{\nabla' \cdot \mathbf{F}}{|\mathbf{r} - \mathbf{r}'|} dV' + \int_{\partial\Omega} \left(u \frac{\partial \mathcal{E}(\mathbf{r}, \mathbf{r}')}{\partial n} + \frac{\mathbf{n} \cdot \mathbf{F}}{4\pi|\mathbf{r} - \mathbf{r}'|} \right) dS' \end{aligned} \quad \text{(H.69)}$$

we see that

$$\mathbf{F} = \nabla u(\mathbf{r}) = \nabla \Phi + \nabla \int_{\partial\Omega} u \frac{\partial \mathcal{E}(\mathbf{r}, \mathbf{r}')}{\partial n} dS' \quad \text{(H.70)}$$

where Φ is given by (5.22). We now establish that

$$\nabla \int_{\partial\Omega} u \frac{\partial \mathcal{E}(\mathbf{r}, \mathbf{r}')}{\partial n} dS' = \nabla \times \int_{\partial\Omega} \mathcal{E}(\mathbf{r}, \mathbf{r}') \left(\mathbf{n} \times \nabla' u \right) dS'. \quad \text{(H.71)}$$

First consider the corollary to Stokes' theorem given by

$$\int_{\partial\Omega} (\mathbf{n} \times \nabla \phi) dS = 0 \quad \text{(H.72)}$$

for any smooth ϕ where $\partial\Omega$ is a closed, piecewise smooth surface. This is proven as follows. Given any constant vector $\mathbf{a} \in \mathbb{R}^3$, let $\mathbf{V} = \phi \mathbf{a}$. Note that $\nabla \times \mathbf{V} = \nabla \times (\phi \mathbf{a}) = \nabla \phi \times \mathbf{a}$. Furthermore, using the identity $\mathbf{A} \cdot (\mathbf{B} \times \mathbf{C}) = \mathbf{C} \cdot (\mathbf{A} \times \mathbf{B})$ we have $\mathbf{n} \cdot (\nabla \phi \times \mathbf{a}) = \mathbf{a} \cdot (\mathbf{n} \times \nabla \phi)$ for the normal $\mathbf{n}$ at each point and

$$\mathbf{a} \cdot \int_{\partial\Omega} (\mathbf{n} \times \nabla \phi) dS = \int_{\partial\Omega} \mathbf{n} \cdot (\nabla \times \mathbf{V}) dS = 0, \quad \text{(H.73)}$$

where the last integral vanishes by applying Stokes' theorem to a closed surface. Since this holds for any vector $\mathbf{a} \in \mathbb{R}^3$, (H.72) must hold as a vector identity. Now let $\phi(\mathbf{r}') = u(\mathbf{r}')\mathcal{E}(\mathbf{r}, \mathbf{r}')$. Noting $\nabla'\phi = \mathcal{E}\nabla' u + u\nabla'\mathcal{E}$ we apply (H.72) to find

$$\int_{\partial\Omega} \mathcal{E}(\mathbf{r}, \mathbf{r}')(\mathbf{n} \times \nabla' u) dS' = -\int_{\partial\Omega} u(\mathbf{n} \times \nabla'\mathcal{E}(\mathbf{r}, \mathbf{r}'))dS'. \tag{H.74}$$

This identity was used in Section 5.3.2.2. We must now take the curl of (H.74). Using the identity $\nabla \times (\mathbf{A} \times \mathbf{B}) = (\mathbf{B} \cdot \nabla)\mathbf{A} - (\mathbf{A} \cdot \nabla)\mathbf{B} - \mathbf{B}(\nabla \cdot \mathbf{A}) + \mathbf{A}(\nabla \cdot \mathbf{B})$, note that $\nabla \times [\mathbf{n}(\mathbf{r}') \times \nabla'\mathcal{E}] = -(\mathbf{n} \cdot \nabla)\nabla'\mathcal{E} - \mathbf{n}(\nabla'^2\mathcal{E})$. Derivatives of $\mathcal{E}$ with respect to primed and unprimed coordinates commute. Furthermore, since $\nabla'^2\mathcal{E} = 0$ for all $\mathbf{r} \neq \mathbf{r}'$, we have $\nabla \times [\mathbf{n}(\mathbf{r}') \times \nabla'\mathcal{E}] = -(\mathbf{n} \cdot \nabla)\nabla'\mathcal{E} = -(\mathbf{n} \cdot \nabla')\nabla\mathcal{E} = -\nabla(\mathbf{n} \cdot \nabla'\mathcal{E}) = -\nabla\frac{\partial\mathcal{E}}{\partial n}$. Therefore

$$\begin{aligned} \nabla \times \int_{\partial\Omega} \mathcal{E}(\mathbf{r}, \mathbf{r}') \, (\mathbf{n} \times \nabla' u) \, dS' &= -\nabla \times \int_{\partial\Omega} u(\mathbf{n} \times \nabla'\mathcal{E}(\mathbf{r}, \mathbf{r}'))dS' \\ &= \nabla \int_{\partial\Omega} u\frac{\partial\mathcal{E}(\mathbf{r}, \mathbf{r}')}{\partial n}dS'. \end{aligned} \tag{H.75}$$

Finally, since $\mathbf{F} = \nabla u$, it follows that $\nabla \times \mathbf{F} = 0$. The expression (5.21) of Chapter 5 therefore becomes

$$\mathbf{A}(\mathbf{r}) = -\frac{1}{4\pi}\int_{\partial\Omega} \frac{\mathbf{n}(\mathbf{r}') \times \mathbf{F}(\mathbf{r}')}{|\mathbf{r} - \mathbf{r}'|}dS' = \int_{\partial\Omega} \mathcal{E}(\mathbf{r}, \mathbf{r}') \, (\mathbf{n} \times \nabla' u) \, dS', \tag{H.76}$$

and by (H.71),

$$\nabla \times \mathbf{A} = \nabla \int_{\partial\Omega} u\frac{\partial\mathcal{E}(\mathbf{r}, \mathbf{r}')}{\partial n}dS'. \tag{H.77}$$

Comparing with (H.70) we have shown that

$$\mathbf{F} = \nabla\Phi + \nabla \times \mathbf{A}, \tag{H.78}$$

which is the Helmholtz theorem. □

Appendix I

Mathematica 5.2 Notebook: Calculation of On-Axis Gradients Using a Rectangular Cylinder

In the following notebook, we illustrate the calculation of the lowest-lying on-axis gradients for the monopole-pair test field. These are computed using field values on the surface of a rectangular cylinder of transverse dimension 7 cm x 4 cm.

We check the fit to a dipole field using the rectangular cylinder. Throughout, we will utilize the known Fourier transforms of the field B and scalar potential ψ. In this notebook, we compute only the on-axis gradient functions.

```
d = 5;

g = 50;

a = Sqrt[x^2 + (y - d)^2 + z^2]
```

$$\sqrt{x^2 + (-5 + y)^2 + z^2}$$

```
b = Sqrt[x^2 + (y + d)^2 + z^2]
```

$$\sqrt{x^2 + (5 + y)^2 + z^2}$$

```
a3 = a^3;

b3 = b^3;

Bx = g * x * (-1 / a3 + 1 / b3);

By = g * ((d - y) / a3 + (d + y) / b3);

Bz = g * z * (-1 / a3 + 1 / b3);

ψ = g * (1 / a - 1 / b);

Normal[Series[ψ /. {x → λ * X, y → λ * Y}, {λ, 0, 4}]] /. λ → 1
```

$$\frac{31\,250\,Y^3}{\left(25 + z^2\right)^{7/2}} - \frac{750\,X^2\,Y}{\left(25 + z^2\right)^{5/2}} - \frac{750\,Y^3}{\left(25 + z^2\right)^{5/2}} + \frac{500\,Y}{\left(25 + z^2\right)^{3/2}}$$

We must Fourier transform the surface field values in z. Fortunately, we have exact expressions for this.

```
a1 = Sqrt[x^2 + (y - d)^2];

a2 = Sqrt[x^2 + (y + d)^2];

Bxtilde = -g * (2 / Sqrt[2 * π]) * Abs[k] * x *
  (BesselK[1, a1 * Abs[k]] / a1 - BesselK[1, a2 * Abs[k]] / a2)
```

$$-50\sqrt{\frac{2}{\pi}}\;x\,\text{Abs}[k]\left(\frac{\text{BesselK}\left[1, \sqrt{x^2 + (-5 + y)^2}\;\text{Abs}[k]\right]}{\sqrt{x^2 + (-5 + y)^2}} - \frac{\text{BesselK}\left[1, \sqrt{x^2 + (5 + y)^2}\;\text{Abs}[k]\right]}{\sqrt{x^2 + (5 + y)^2}}\right)$$

```
Bytilde = -g * (2 / Sqrt[2 * π]) * Abs[k] *
  ((y - d) * BesselK[1, a1 * Abs[k]] / a1 - (y + d) * BesselK[1, a2 * Abs[k]] / a2)
```

$$-50\sqrt{\frac{2}{\pi}}\,\text{Abs}[k]\left(\frac{(-5+y)\,\text{BesselK}\left[1,\sqrt{x^2+(-5+y)^2}\,\text{Abs}[k]\right]}{\sqrt{x^2+(-5+y)^2}}-\frac{(5+y)\,\text{BesselK}\left[1,\sqrt{x^2+(5+y)^2}\,\text{Abs}[k]\right]}{\sqrt{x^2+(5+y)^2}}\right)$$

Now we define the basis functions for our Fourier series. We take the width of the rectangular cylinder to be s=7.

```
s = 7;
```

```
cnx = Cos[(x + s) * n * π / (2 * s)]
```

$$\text{Cos}\left[\frac{1}{14}\,n\pi\,(7+x)\right]$$

We take the height of the rectangular cylinder to be d=4, just under the monopole source.

```
dn = 4;
```

```
cny = Cos[(y + dn) * n * π / (2 * dn)]
```

$$\text{Cos}\left[\frac{1}{8}\,n\pi\,(4+y)\right]$$

Now we define the surface values. Here they are evaluated after the Fourier transform in z.

```
Byplus = Bytilde /. y → dn
```

$$-50\sqrt{\frac{2}{\pi}}\,\text{Abs}[k]\left(-\frac{\text{BesselK}\left[1,\sqrt{1+x^2}\,\text{Abs}[k]\right]}{\sqrt{1+x^2}}-\frac{9\,\text{BesselK}\left[1,\sqrt{81+x^2}\,\text{Abs}[k]\right]}{\sqrt{81+x^2}}\right)$$

```
Byminus = Bytilde /. y → -dn
```

$$-50\sqrt{\frac{2}{\pi}}\,\text{Abs}[k]\left(-\frac{\text{BesselK}\left[1,\sqrt{1+x^2}\,\text{Abs}[k]\right]}{\sqrt{1+x^2}}-\frac{9\,\text{BesselK}\left[1,\sqrt{81+x^2}\,\text{Abs}[k]\right]}{\sqrt{81+x^2}}\right)$$

```
Bxplus = Bxtilde /. x → s
```

$$-350\sqrt{\frac{2}{\pi}}\,\text{Abs}[k]\left(\frac{\text{BesselK}\left[1,\sqrt{49+(-5+y)^2}\,\text{Abs}[k]\right]}{\sqrt{49+(-5+y)^2}}-\frac{\text{BesselK}\left[1,\sqrt{49+(5+y)^2}\,\text{Abs}[k]\right]}{\sqrt{49+(5+y)^2}}\right)$$

```
Bxminus = Bxtilde /. x → -s
```

$$350\sqrt{\frac{2}{\pi}}\,\text{Abs}[k]\left(\frac{\text{BesselK}\left[1,\sqrt{49+(-5+y)^2}\,\text{Abs}[k]\right]}{\sqrt{49+(-5+y)^2}}-\frac{\text{BesselK}\left[1,\sqrt{49+(5+y)^2}\,\text{Abs}[k]\right]}{\sqrt{49+(5+y)^2}}\right)$$

Next we will evaluate the Fourier coefficients on each surface. To do this numerically, we construct an array of frequency values with spacing δk=0.05 and cutoff 2.

```
ktable = Table[0.01 * j, {j, 1, 300}]

βT = Table[SetAccuracy[
    NIntegrate[(Byplus /. k → ktable[[p]]) * (cnx /. n → 2 * j), {x, -s, s}] /
     s, 16], {j, 1, 20}, {p, 1, 300}];

βB = Table[
   -SetAccuracy[NIntegrate[(Byminus /. k → ktable[[p]]) * (cnx /. n → 2 * j),
       {x, -s, s}] / s, 16], {j, 1, 20}, {p, 1, 300}];

βR = Table[SetAccuracy[
    NIntegrate[(Bxplus /. k → ktable[[p]]) * (cny /. n → 2 * j - 1),
      {y, -dn, dn}] / dn, 16], {j, 1, 20}, {p, 1, 300}];

βL = Table[-SetAccuracy[
     NIntegrate[(Bxminus /. k → ktable[[p]]) * (cny /. n → 2 * j - 1),
       {y, -dn, dn}] / dn, 16], {j, 1, 20}, {p, 1, 300}];

βT0 = Table[
   SetAccuracy[NIntegrate[Byplus /. k → ktable[[p]], {x, -s, s}] / (2 * s),
    16], {p, 1, 300}];

βB0 =
  Table[SetAccuracy[-NIntegrate[Byminus /. k → ktable[[p]], {x, -s, s}] /
     (2 * s), 16], {p, 1, 300}];

βR0 =
  Table[SetAccuracy[NIntegrate[Bxplus /. k → ktable[[p]], {y, -dn, dn}] /
     (2 * dn), 16], {p, 1, 300}];

βL0 =
 Table[SetAccuracy[NIntegrate[Bxminus /. k → ktable[[p]], {y, -dn, dn}] /
    (2 * dn), 16], {p, 1, 300}]
```

Now we define the interior solution corresponding to each face. First, we define $\lambda_n$and $\tau_n$as follows. Note that for λ_n we require only even values of n, since βnT and βnB are nonzero only for even values of n. Similarly, for τ_n we require only odd values of n, since βnR and βnL are nonzero only for odd values of n.

```
λn = Table[SetAccuracy[n * π / (2 * s) /. n → 2 * j, 16], {j, 1, 20}]
```

```
{0.448798950512828, 0.897597901025655,
 1.346396851538483, 1.795195802051310, 2.243994752564138,
 2.692793703076966, 3.141592653589793, 3.590391604102621,
 4.039190554615448, 4.487989505128276, 4.936788455641104,
 5.385587406153931, 5.834386356666759, 6.283185307179586,
 6.731984257692414, 7.180783208205242, 7.629582158718069,
 8.078381109230897, 8.527180059743725, 8.975979010256552}
```

```
τn = Table[SetAccuracy[n * π / (2 * dn) /. n → 2 * j - 1, 16], {j, 1, 20}]
```

```
{0.392699081698724, 1.178097245096172,
 1.963495408493621, 2.748893571891069, 3.534291735288517,
 4.319689898685966, 5.105088062083414, 5.890486225480862,
 6.675884388878311, 7.461282552275759, 8.246680715673207,
 9.032078879070656, 9.817477042468104, 10.602875205865552,
 11.388273369263000, 12.173671532660449, 12.959069696057897,
 13.744467859455345, 14.529866022852794, 15.315264186250242}
```

```
<< NumericalMath`ListIntegrate`
```

```
dk = 0.01;
```

We wish to compute values on a grid in x,y, and z. We define such a grid as follows.

```
dz = 1;
```

```
ztable = Table[dz * (j - 1) - 30, {j, 1, 61}]
```

```
{-30, -29, -28, -27, -26, -25, -24, -23, -22, -21, -20, -19,
 -18, -17, -16, -15, -14, -13, -12, -11, -10, -9, -8, -7, -6, -5,
 -4, -3, -2, -1, 0, 1, 2, 3, 4, 5, 6, 7, 8, 9, 10, 11, 12, 13, 14,
 15, 16, 17, 18, 19, 20, 21, 22, 23, 24, 25, 26, 27, 28, 29, 30}
```

Since ψ is symmetric in z, we know that only the cosine Fourier integral contributes, and ψNeumann should be symmetric in k. Thus, we need compute only the inverse Fourier cosine integral. We'll use 2x the integral over the half-range (0,kmax) where kmax is 2. We first define an array storing the expressions for the integrand at each value of k in 'ktable'.

```
splus = Table[
   λn[[j]] + Sqrt[ktable[[p]]^2 + λn[[j]]^2], {j, 1, 20}, {p, 1, 300}];
```

```
sminus = Table[
   λn[[j]] - Sqrt[ktable[[p]]^2 + λn[[j]]^2], {j, 1, 20}, {p, 1, 300}];
```

```
qplus = Table[
   τn[[j]] + Sqrt[ktable[[p]]^2 + τn[[j]]^2], {j, 1, 20}, {p, 1, 300}];
```

```
qminus = Table[
   τn[[j]] - Sqrt[ktable[[p]]^2 + τn[[j]]^2], {j, 1, 20}, {p, 1, 300}];
```

```
fn = Table[Sqrt[ktable[[p]]^2 + λn[[j]]^2], {j, 1, 20}, {p, 1, 300}];
```

```
gn = Table[Sqrt[ktable[[p]]^2 + τn[[j]]^2], {j, 1, 20}, {p, 1, 300}];
```

```
r =.
```

```
δrn =
 Piecewise[{{1, (FractionalPart[n / 2] == 0 && FractionalPart[r / 2] ≠ 0) ||
     (FractionalPart[n / 2] ≠ 0 && FractionalPart[r / 2] == 0)}}, 0]
```

$$\left\{ 1 \quad \left(\text{FractionalPart}\left[\frac{n}{2}\right] == 0 \;\&\&\; \text{FractionalPart}\left[\frac{r}{2}\right] \neq 0\right) \;||\; \left(\text{FractionalPart}\left[\frac{n}{2}\right]\right.$$

```
coef = (-1) ^ (IntegerPart[r / 2]) / (r ! * 2 ^ r);
```

We first check the terms contributing to the top face ψT. Note that the n=0 term must be included, and it is added separately in each case. For this purpose, we define $(\delta\text{rn} - 1)^n$ for the n=0 case as follows

```
δcoefr0 =
 Piecewise[{{1, FractionalPart[r / 2] == 0}, {0, FractionalPart[r / 2] ≠ 0}}]
```

$$\begin{cases} 1 & \text{FractionalPart}\left[\frac{r}{2}\right] == 0 \end{cases}$$

```
CrcTtable = Table[coef * Sum[(splus[[j, p]] ^ r + sminus[[j, p]] ^ r) *
         (-1) ^ (IntegerPart[n / 2]) / fn[[j, p]] * (δrn - 1) ^ n *
         βT[[j, p]] / (2 * Sinh[dn * fn[[j, p]]]) /. n → 2 * j, {j, 1, 20}] +
     (coef * (Abs[k] ^ r + (-Abs[k]) ^ r) / Abs[k] * δcoefr0 *
        βT0[[p]] / (2 * Sinh[dn * Abs[k]]) /.
       {k → ktable[[p]], n → 0}), {p, 1, 300}, {r, 1, 10}];

C0cT = Table[Sum[(-1) ^ (IntegerPart[n / 2]) / fn[[j, p]] *
         βT[[j, p]] / (2 * Sinh[dn * fn[[j, p]]]) /. {r → 0, n → 2 * j},
       {j, 1, 20}] + βT0[[p]] / (2 * Abs[k] * Sinh[dn * Abs[k]]) /.
     {k → ktable[[p]], r → 0, n → 0}, {p, 1, 300}];

CrsTtable = Table[coef *
      Sum[(splus[[j, p]] ^ r - sminus[[j, p]] ^ r) * (-1) ^ (IntegerPart[n / 2]) /
          fn[[j, p]] * δrn * βT[[j, p]] / (2 * Cosh[dn * fn[[j, p]]]) /. n → 2 * j,
        {j, 1, 20}] + (coef * (Abs[k] ^ r - (-Abs[k]) ^ r) / Abs[k] *
         δrn * βT0[[p]] / (2 * Cosh[dn * Abs[k]]) /.
        {k → ktable[[p]], n → 0}), {p, 1, 300}, {r, 1, 10}];

δrn =
 Piecewise[{{1, (FractionalPart[n / 2] == 0 && FractionalPart[r / 2] ≠ 0) ||
      (FractionalPart[n / 2] ≠ 0 && FractionalPart[r / 2] == 0)}}, 0]

θlm = Piecewise[{{1, FractionalPart[(l + m) / 2] ≠ 0},
   {0, FractionalPart[(l + m) / 2] == 0}}, 0]

δnlm = Piecewise[
  {{θlm, FractionalPart[n / 2] == 0}, {1 - θlm, FractionalPart[n / 2] ≠ 0}}, 0]

CrcBtable = Table[coef * Sum[(splus[[j, p]] ^ r + sminus[[j, p]] ^ r) *
         (-1) ^ (IntegerPart[n / 2]) / fn[[j, p]] * (δrn - 1) ^ n *
         βB[[j, p]] / (2 * Sinh[dn * fn[[j, p]]]) /. n → 2 * j, {j, 1, 20}] +
     (coef * (Abs[k] ^ r + (-Abs[k]) ^ r) / Abs[k] * δcoefr0 *
        βB0[[p]] / (2 * Sinh[dn * Abs[k]]) /.
       {k → ktable[[p]], n → 0}), {p, 1, 300}, {r, 1, 10}];

C0cB = Table[Sum[(-1) ^ (IntegerPart[n / 2]) / fn[[j, p]] *
         βB[[j, p]] / (2 * Sinh[dn * fn[[j, p]]]) /. {r → 0, n → 2 * j},
       {j, 1, 20}] + βB0[[p]] / (2 * Abs[k] * Sinh[dn * Abs[k]]) /.
     {k → ktable[[p]], r → 0, n → 0}, {p, 1, 300}];

CrsBtable = Table[-coef *
      Sum[(splus[[j, p]] ^ r - sminus[[j, p]] ^ r) * (-1) ^ (IntegerPart[n / 2]) /
          fn[[j, p]] * δrn * βB[[j, p]] / (2 * Cosh[dn * fn[[j, p]]]) /. n → 2 * j,
        {j, 1, 20}] + (-coef * (Abs[k] ^ r - (-Abs[k]) ^ r) / Abs[k] *
         δrn * βB0[[p]] / (2 * Cosh[dn * Abs[k]]) /.
        {k → ktable[[p]], n → 0}), {p, 1, 300}, {r, 1, 10}];
```

Now we consider the right and left sides of the box. First, the right side.

```
coefnew = 1 / (2 ^ r * r!);

CrcLtable =
  Table[coefnew * Sum[((-1) ^ r * qplus[[j, p]] ^ r + qminus[[j, p]] ^ r) *
       (-1) ^ (IntegerPart[n / 2]) / gn[[j, p]] *
       βL[[j, p]] * (1 - θlm /. {l → n, m → 0}) *
       ((1 - θlm /. {l → 0, m → r}) / (2 * Sinh[s * gn[[j, p]]]) +
         (θlm /. {l → 0, m → r}) / (2 * Cosh[s * gn[[j, p]]])) /.
      n → 2 * j - 1, {j, 1, 20}], {p, 1, 300}, {r, 1, 10}];

C0cL = Table[0, {p, 1, 300}];
```

```
CrsLtable =
  Table[coefnew * Sum[(-(-1)^r * qplus[[j, p]]^r + qminus[[j, p]]^r) *
      (-1)^(IntegerPart[n / 2]) / gn[[j, p]] *
      βL[[j, p]] * (θlm /. {l → n, m → 0}) *
      (-(θlm /. {l → 0, m → r}) / (2 * Sinh[s * gn[[j, p]]]) -
        (1 - θlm /. {l → 0, m → r}) / (2 * Cosh[s * gn[[j, p]]])) /.
    n → 2 * j - 1, {j, 1, 20}], {p, 1, 300}, {r, 1, 10}];

CrcRtable =
  Table[coefnew * Sum[((-1)^r * qplus[[j, p]]^r + qminus[[j, p]]^r) *
      (-1)^(IntegerPart[n / 2]) / gn[[j, p]] *
      βR[[j, p]] * (1 - θlm /. {l → n, m → 0}) *
      ((1 - θlm /. {l → 0, m → r}) / (2 * Sinh[s * gn[[j, p]]]) -
        (θlm /. {l → 0, m → r}) / (2 * Cosh[s * gn[[j, p]]])) /.
    n → 2 * j - 1, {j, 1, 20}], {p, 1, 300}, {r, 1, 10}];

C0cR = Table[0, {p, 1, 300}];

CrsRtable =
  Table[coefnew * Sum[(-(-1)^r * qplus[[j, p]]^r + qminus[[j, p]]^r) *
      (-1)^(IntegerPart[n / 2]) / gn[[j, p]] * (θlm /. {l → n, m → 0}) *
      βR[[j, p]] * (-(θlm /. {l → 0, m → r}) / (2 * Sinh[s * gn[[j, p]]]) +
        (1 - θlm /. {l → 0, m → r}) / (2 * Cosh[s * gn[[j, p]]])) /.
    n → 2 * j - 1, {j, 1, 20}], {p, 1, 300}, {r, 1, 10}];
```

We now check the full on-axis gradients against their known values. To do this, we must invert the Fourier integral.

```
Crstable = Table[CrsTtable[[p, m]] + CrsBtable[[p, m]] +
    CrsRtable[[p, m]] + CrsLtable[[p, m]], {p, 1, 300}, {m, 1, 10}];
```

We first compute the gradient m=1 as follows.

```
Crs1Cos =
  Table[Crstable[[p, 1]] * Cos[k * z] /. k → ktable[[p]], {p, 1, 300}];

Crs1 = Table[SetAccuracy[(2 / Sqrt[2 * π]) *
    ListIntegrate[Crs1Cos /. {z → ztable[[l]]}, dk], 16], {l, 1, 61}];

Crctable = Table[CrcTtable[[p, m]] + CrcBtable[[p, m]] +
    CrcRtable[[p, m]] + CrcLtable[[p, m]], {p, 1, 300}, {m, 1, 10}];

Crc1Cos =
  Table[Crctable[[p, 1]] * Cos[k * z] /. k → ktable[[p]], {p, 1, 300}];

Crc1 = Table[SetAccuracy[(2 / Sqrt[2 * π]) *
    ListIntegrate[Crc1Cos /. {z → ztable[[l]]}, dk], 16], {l, 1, 61}];
```

Now we compute the gradients m=3, 5.

```
Crs3Cos =
  Table[Crstable[[p, 3]] * Cos[k * z] /. k → ktable[[p]], {p, 1, 300}];

Crs3 = Table[SetAccuracy[(2 / Sqrt[2 * π]) *
    ListIntegrate[Crs3Cos /. {z → ztable[[l]]}, dk], 16], {l, 1, 61}];

Crs5Cos =
  Table[Crstable[[p, 5]] * Cos[k * z] /. k → ktable[[p]], {p, 1, 300}];

Crs5 = Table[SetAccuracy[(2 / Sqrt[2 * π]) *
    ListIntegrate[Crs5Cos /. {z → ztable[[l]]}, dk], 16], {l, 1, 61}];
```

Finally, the fourth derivative of the gradient m = 1 is computed as :

```
Crs1d4Cos =
  Table[Crstable[[p, 1]] * k^4 * Cos[k * z] /. k → ktable[[p]], {p, 1, 300}];
Crs1d4 = Table[SetAccuracy[(2 / Sqrt[2 * π]) *
     ListIntegrate[Crs1d4Cos /. {z → ztable[[l]]}, dk], 16], {l, 1, 61}];
```

However, we have not included the k=0 contribution. This was done to avoid division by zero. As a result, we treat the k=0 solution separately below.

```
βTk0 = Table[SetAccuracy[
    NIntegrate[(Limit[Byplus, k → 0]) * (cnx /. n → 2 * j), {x, -s, s}] / s,
    16], {j, 1, 20}];

βBk0 =
  Table[-SetAccuracy[NIntegrate[(Limit[Byminus, k → 0]) * (cnx /. n → 2 * j),
       {x, -s, s}] / s, 16], {j, 1, 20}];

βRk0 = Table[
   SetAccuracy[NIntegrate[(Limit[Bxplus, k → 0]) * (cny /. n → 2 * j - 1),
      {y, -dn, dn}] / dn, 16], {j, 1, 20}];

βLk0 = Table[
   -SetAccuracy[NIntegrate[(Limit[Bxminus, k → 0]) * (cny /. n → 2 * j - 1),
       {y, -dn, dn}] / dn, 16], {j, 1, 20}];

βT0k0 =
  SetAccuracy[NIntegrate[Limit[Byplus, k → 0], {x, -s, s}] / (2 * s), 16];

βB0k0 =
  SetAccuracy[-NIntegrate[Limit[Byminus, k → 0], {x, -s, s}] / (2 * s), 16];

βR0k0 = SetAccuracy[
   NIntegrate[Limit[Bxplus, k → 0], {y, -dn, dn}] / (2 * dn), 16];

βL0k0 = SetAccuracy[
   NIntegrate[Limit[Bxminus, k → 0], {y, -dn, dn}] / (2 * dn), 16];

CrsTk0 =
  Table[coef * Sum[(2 * λn[[j]]) ^ r * (-1) ^ (IntegerPart[n / 2]) / λn[[j]] *
       δrn * βTk0[[j]] / (2 * Cosh[dn * λn[[j]]]) /. n → 2 * j, {j, 1, 20}] +
    (coef * (2 * Abs[k] ^ (r - 1)) * δrn * βT0k0 / 2 /. {k → 0, n → 0}), {r, 1, 5}];

CrsBk0 =
  Table[-coef * Sum[(2 * λn[[j]]) ^ r * (-1) ^ (IntegerPart[n / 2]) / λn[[j]] *
       δrn * βBk0[[j]] / (2 * Cosh[dn * λn[[j]]]) /. n → 2 * j, {j, 1, 20}] +
    (-coef * (2 * Abs[k] ^ (r - 1)) * δrn * βB0k0 / (2) /. {k → 0, n → 0}), {r,
    1, 5}];

coefnew = 1 / (2 ^ r * r!);

CrsLk0 = Table[
   coefnew * Sum[(-(-1) ^ r * (2 * τn[[j]]) ^ r) * (-1) ^ (IntegerPart[n / 2]) /
       τn[[j]] * βLk0[[j]] * (Θlm /. {l → n, m → 0}) *
      (-(Θlm /. {l → 0, m → r}) / (2 * Sinh[s * τn[[j]]]) -
        (1 - Θlm /. {l → 0, m → r}) / (2 * Cosh[s * τn[[j]]])) /.
     n → 2 * j - 1, {j, 1, 20}], {r, 1, 5}];

CrsRk0 = Table[coefnew * Sum[(-(-1) ^ r * (2 * τn[[j]]) ^ r) *
      (-1) ^ (IntegerPart[n / 2]) / τn[[j]] * (Θlm /. {l → n, m → 0}) *
      βRk0[[j]] * (-(Θlm /. {l → 0, m → r}) / (2 * Sinh[s * τn[[j]]]) +
        (1 - Θlm /. {l → 0, m → r}) / (2 * Cosh[s * τn[[j]]])) /.
     n → 2 * j - 1, {j, 1, 20}], {r, 1, 5}];

Crsk0 =
  Table[CrsTk0[[m]] + CrsBk0[[m]] + CrsRk0[[m]] + CrsLk0[[m]], {m, 1, 5}];
```

We now compute the gradient m=1, including the k=0 term.

```
Crs1Cosk0 = Table[0, {p, 1, 301}];

Crs1Cosk0[[1]] = Crsk0[[1]]

15.9576912160572

Do[Crs1Cosk0[[p + 1]] = Crs1Cos[[p]], {p, 1, 300}]

Crs1k0 = Table[SetAccuracy[(2 / Sqrt[2 * π]) * ListIntegrate[
      (Crs1Cosk0 /. z → ztable[[l]]), dk, 3], 16], {l, 1, 61}];
```

Now we compute the gradient m=3.

```
Crs3Cosk0 = Table[0, {p, 1, 301}];

Crs3Cosk0[[1]] = Crsk0[[3]]

-0.212769216214094

Do[Crs3Cosk0[[p + 1]] = Crs3Cos[[p]], {p, 1, 300}]

Crs3k0 = Table[SetAccuracy[(2 / Sqrt[2 * π]) *
     ListIntegrate[Crs3Cosk0 /. {z → ztable[[l]]}, dk], 16], {l, 1, 61}];
```

Now we compute the gradient m=5.

```
Crs5Cosk0 = Table[0, {p, 1, 301}];

Crs5Cosk0[[1]] = Crsk0[[5]]

0.0051064611891382

Do[Crs5Cosk0[[p + 1]] = Crs5Cos[[p]], {p, 1, 300}]

Crs5k0 = Table[SetAccuracy[(2 / Sqrt[2 * π]) *
     ListIntegrate[Crs5Cosk0 /. {z → ztable[[l]]}, dk], 16], {l, 1, 61}];
```

Finally, the derivative C_1^4.

```
Crs1d4Cosk0 = Table[0, {p, 1, 301}];

Do[Crs1d4Cosk0[[p + 1]] = Crs1d4Cos[[p]], {p, 1, 300}]

Crs1d4k0 = Table[SetAccuracy[(2 / Sqrt[2 * π]) *
     ListIntegrate[(Crs1d4Cosk0 /. z → ztable[[l]]), dk], 16], {l, 1, 61}];

Crs1values = Table[{ztable[[l]], Crs1k0[[l]]}, {l, 1, 61}];
```

```
grad1computed = ListPlot[Crs1values]
```

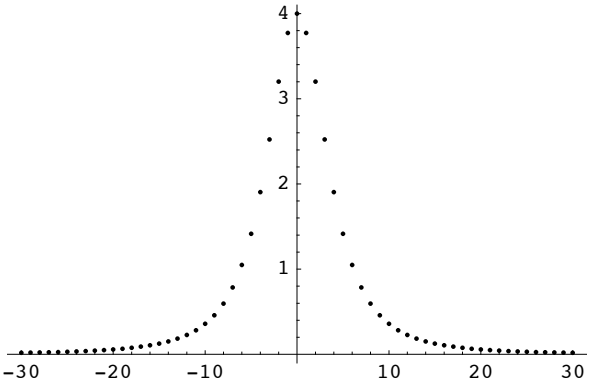

- Graphics -

```
Crs3values = Table[{ztable[[l]], Crs3k0[[l]]}, {l, 1, 61}];

grad3computed = ListPlot[Crs3values]
```

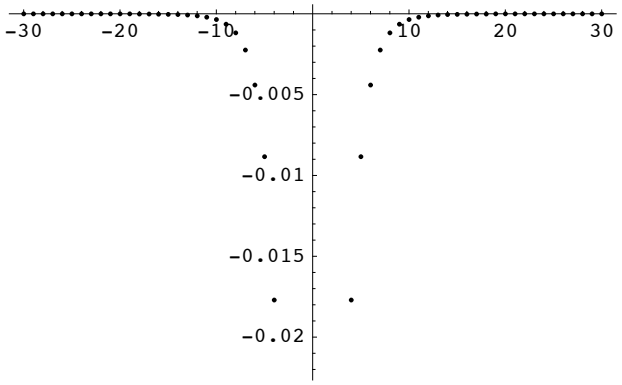

- Graphics -

```
Crs5values = Table[{ztable[[l]], Crs5k0[[l]]}, {l, 1, 61}];
```

```
grad5computed = ListPlot[Crs5values, PlotRange → {0, 0.00314}]
```

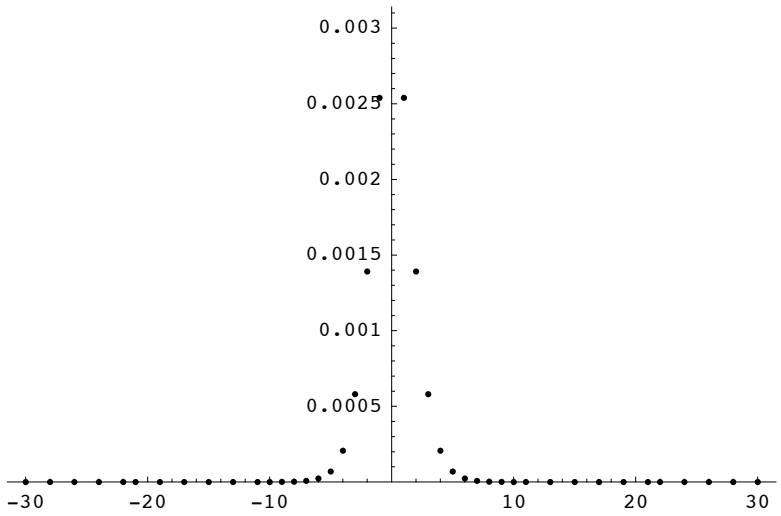

- Graphics -

```
Crs1d4values = Table[{ztable[[l]], Crs1d4k0[[l]]}, {l, 1, 61}];

grad1d4computed = ListPlot[Crs1d4values]
```

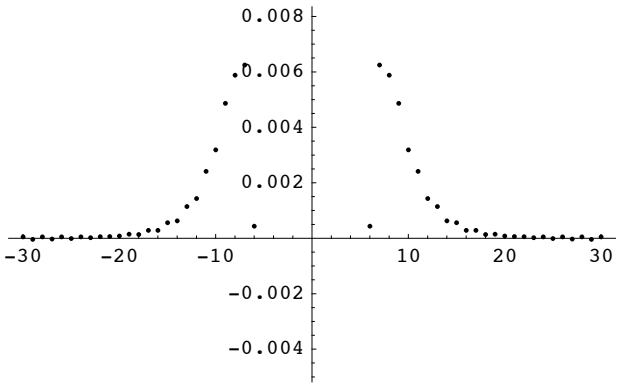

- Graphics -

```
beta = d / Sqrt[z ^ 2 + d ^ 2];

Crsexact = (-1) ^ ((n - 1) / 2) * (g / d ^ (n + 1)) *
    (2 * n) ! / (2 ^ (2 * n - 2) * (n !) ^ 2) * beta ^ (2 n + 1);

C1sexact = Crsexact /. n → 1
```

$$\frac{500}{\left(25 + z^2\right)^{3/2}}$$

```
C3sexact = Crsexact /. n → 3
```

$$-\frac{15\,625}{2\left(25 + z^2\right)^{7/2}}$$

C5sexact = Crsexact /. n → 5

$$\frac{4\,921\,875}{32\,\left(25 + z^2\right)^{11/2}}$$

C1d4exact = D[Crsexact /. n → 1, {z, 4}]

$$500\left(\frac{945\,z^4}{\left(25 + z^2\right)^{11/2}} - \frac{630\,z^2}{\left(25 + z^2\right)^{9/2}} + \frac{45}{\left(25 + z^2\right)^{7/2}}\right)$$

grad1exact = Plot[C1sexact, {z, -30, 30}]

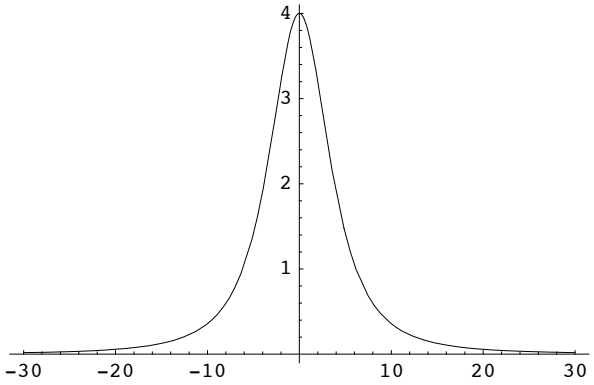

- Graphics **-**

grad3exact = Plot[C3sexact, {z, -30, 30}]

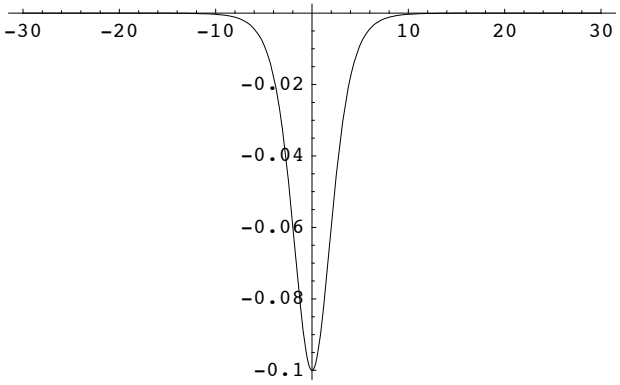

- Graphics **-**

```
grad5exact = Plot[C5sexact, {z, -30, 30}, PlotRange → {0, 0.00314}]
```

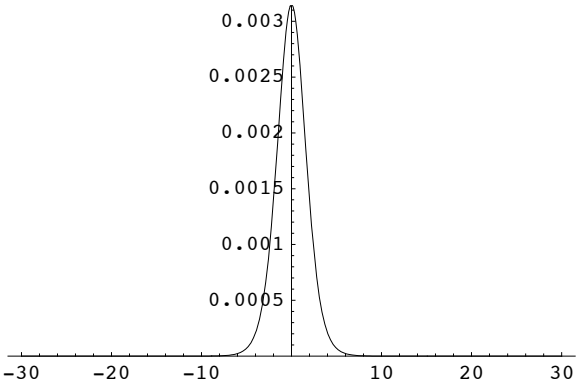


```
- Graphics -
```

```
grad1d4exact = Plot[C1d4exact, {z, -30, 30}, PlotRange -> {-0.15, 0.3}]
```

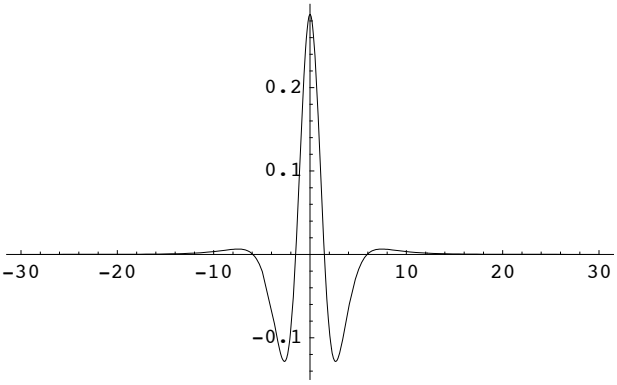


```
- Graphics -
```

Here is a comparison of the computed on - axis gradient functions with the corresponding exact expressions.

Show[grad1exact, grad1computed]

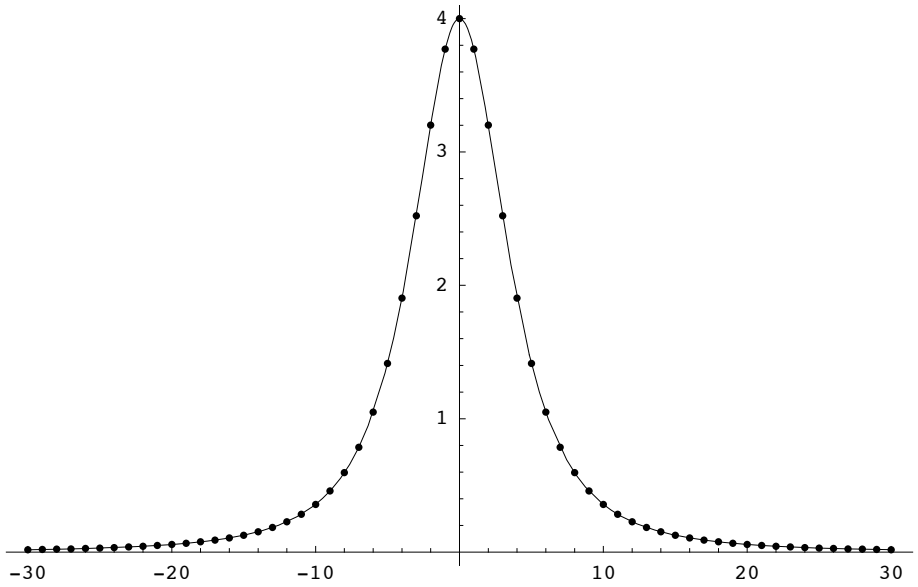

- Graphics -

Show[grad3exact, grad3computed]

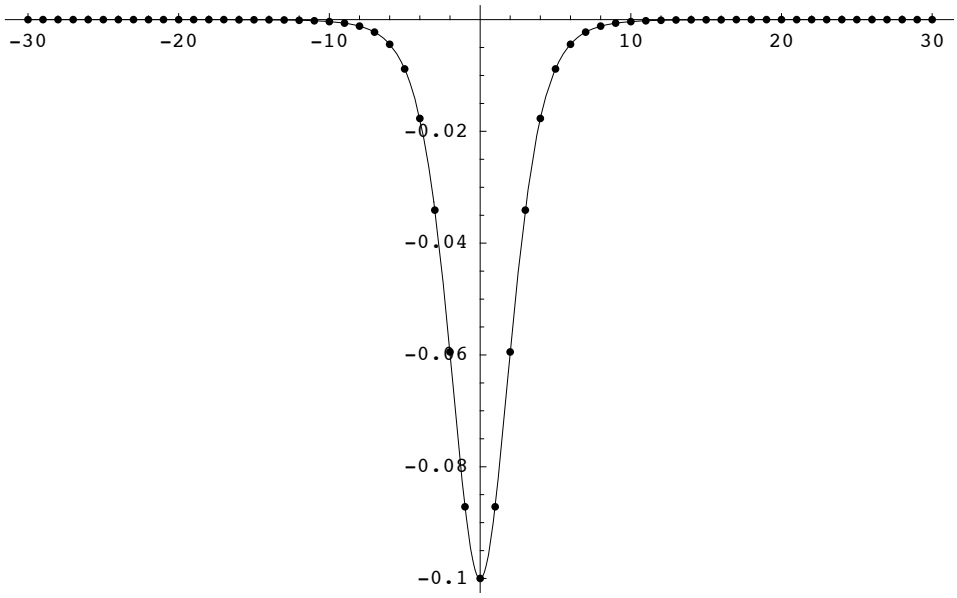

- Graphics -

```
Show[grad5exact, grad5computed]
```

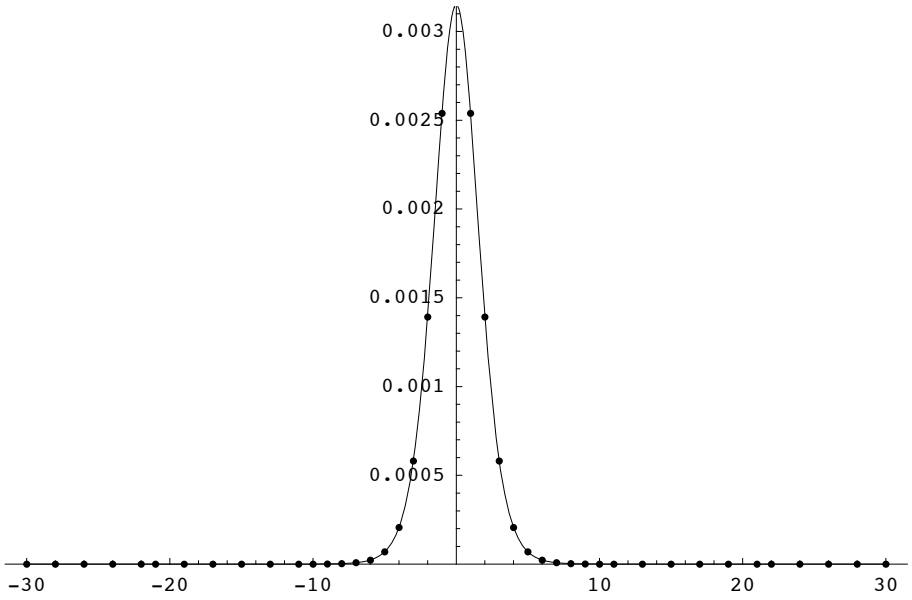


```
- Graphics -
```

```
Show[grad1d4exact, grad1d4computed]
```

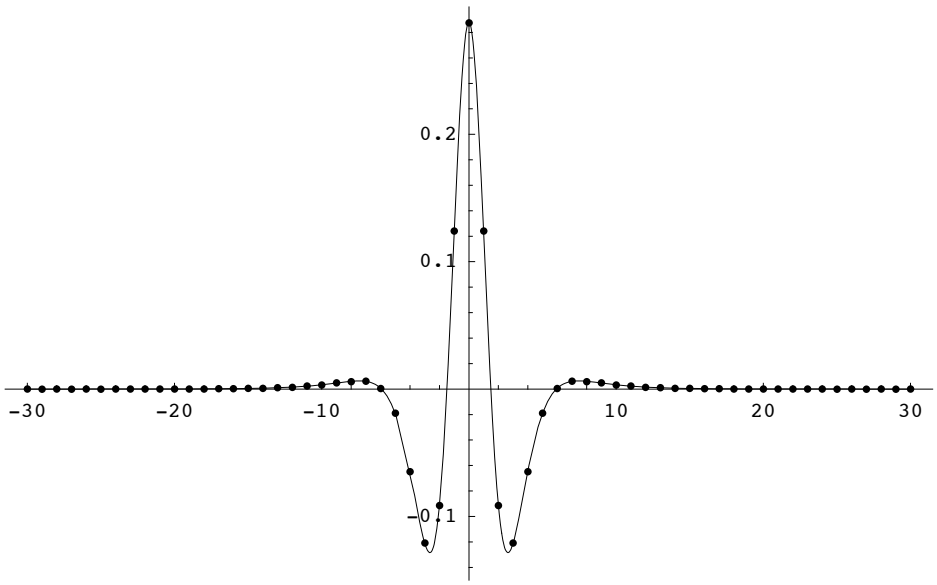


```
- Graphics -
```

Below are illustrations of the the resulting error.

```
errorC1 = Table[{ztable[[l]],
    (Crs1k0[[l]] - C1sexact) / 4 /. z → ztable[[l]]}, {l, 1, 61}];

errorC3 = Table[{ztable[[l]],
    (Crs3k0[[l]] - C3sexact) / 0.1 /. z → ztable[[l]]}, {l, 1, 61}];

errorC5 = Table[{ztable[[l]],
    (Crs5k0[[l]] - C5sexact) / 0.003 /. z → ztable[[l]]}, {l, 1, 61}];

errorC1d4 = Table[{ztable[[l]],
    (Crs1d4k0[[l]] - C1d4exact) / 0.3 /. z → ztable[[l]]}, {l, 1, 61}];

ListPlot[errorC1, PlotJoined → True]
```

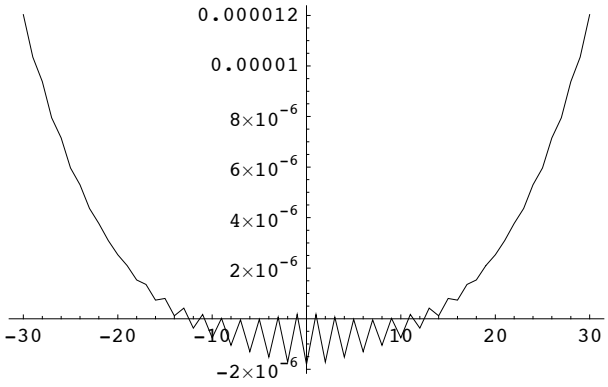


```
- Graphics -
```

```
ListPlot[errorC3, PlotJoined → True]
```

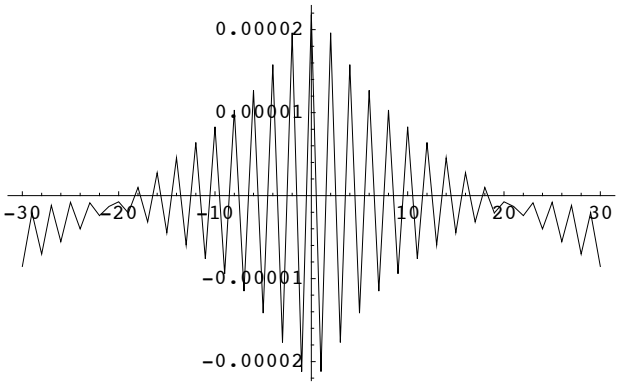


```
- Graphics -
```

```
ListPlot[errorC5, PlotJoined → True]
```

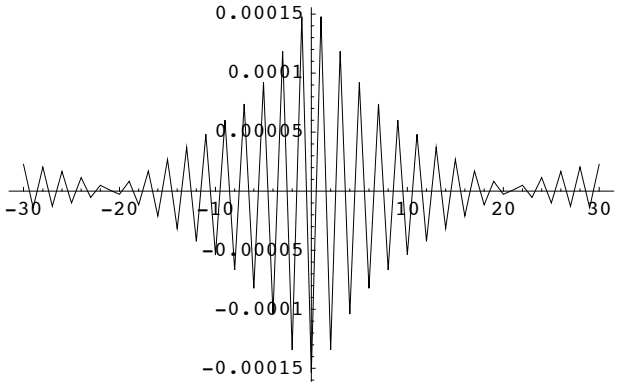


```
- Graphics -
```

```
ListPlot[errorC1d4, PlotRange → {-0.00144, 0.00144}, PlotJoined → True]
```

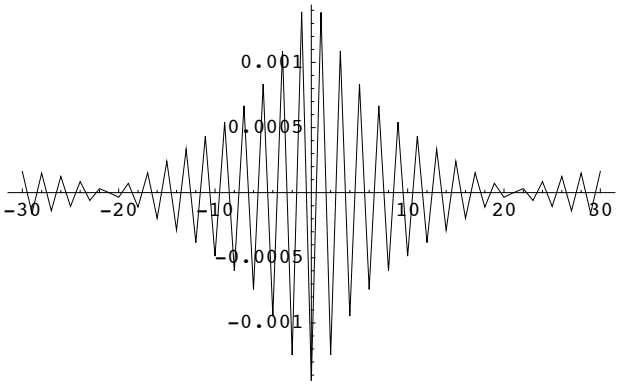


```
- Graphics -
```

Bibliography

[1] A. Katok and B. Hasselblatt, *Introduction to the Modern Theory of Dynamical Systems* (Cambridge University Press, Cambridge, UK, 1995).

[2] S. Y. Lee, *Accelerator Physics* (World Scientific Publishing Co. Pte. Ltd., River Edge, NJ, 1999).

[3] See lhc.web.cern.ch/lhc/general/acphy.htm.

[4] A. J. Dragt, *Lie Methods for Nonlinear Dynamics with Applications to Accelerator Physics* (University of Maryland, College Park, Physics Department Report, 2007.)

[5] A. J. Dragt, in *Physics of High-Energy Particle Accelerators*, AIP Conf. Proc. No. 87, edited by M. M. R. A. Carrigan and F. R. Huson (AIP, New York, New York, 1982), pp. 147-313.

[6] E. Ott, *Chaos in Dynamical Systems* (Cambridge University Press, Cambridge, UK, 2002).

[7] J. D. Jackson, *Classical Electrodynamics* 3rd Ed. (Wiley & Sons, Inc., New York, 1999).

[8] M. Venturini, *Lie Methods, Exact Map Computation, and the Problem of Dispersion in Space Charge Dominated Beams*, Ph. D. Thesis, University of Maryland at College Park, MD (1998).

[9] A. J. Dragt and J. M. Finn, "Lie series and invariant functions for analytic symplectic maps," J. Math. Phys. **17**, 2215 (1976).

[10] F. B. Hildebrand, *Introduction to Numerical Analysis* 2nd Ed. (McGraw-Hill, Inc., New York, 1974).

[11] G. Strang and G. Fix, *An Analysis of the Finite Element Method* (Prentice-Hall, Inc., Eaglewood Cliffs, NJ, 1973).

[12] D. Braess, *Finite Elements: Theory, Fast Solvers, and Applications to Solid Mechanics* (Cambridge University Press, Cambridge, UK, 1997).

[13] J. A. Akin, *Finite Element Analysis with Error Estimators* (Elsevier Butterworth-Heinemann, Oxford, 2005).

[14] L. Gaul, M. Kogl, and M. Wagner, *Boundary Element Methods for Engineers and Scientists* (Springer-Verlag Berlin, Heidelberg, 2003).

[15] J. T. Katsikadelis, *Boundary Elements: Theory and Applications* (Elsevier Science Ltd., Oxford, UK, 2002).

[16] M. Venturini and A. Dragt, "Accurate computation of transfer maps from magnetic field data," Nucl. Inst. and Meth. A **427**, 387 (1999).

[17] R.M.G.M. Trines, et. al., "Modeling the fields of magneto-optical devices, including fringe fields and higher order multipole contributions, with applications to charged particle optics," Phys. Rev. ST Accel. Beams **4**, 062401 (2001).

[18] D. Abell, "Numerical computation of high-order transfer maps in rf cavities," Phys. Rev. ST Accel. Beams **9**, 042001 (2006).

[19] A. Dragt, T. Stasevich, P. Walstrom, "Computation of charged-particle transfer maps for general fields and geometries using electromagnetic boundary-value data," *Proceedings of the 2001 Particle Accelerator Conference, Chicago, Illinois, 2001*, **3**, 1776 (IEEE, Piscataway, NJ, 2001).

[20] N.W. McLachlan, *Theory and Application of Mathieu Functions* (Dover Publications, Inc., New York, 1964).

[21] A. Erdélyi ed., *Higher Transcendental Functions vol. III* (McGraw-Hill Book Company, Inc., New York, 1955).

[22] Abramowitz and Stegun, *Handbook of Mathematical Functions* (Dover Publications, Inc., New York, 1970).

[23] A. Jeffrey, *Handbook of Mathematical Formulas and Integrals* (Academic Press, New York, 1995).

[24] G. B. Arfken and H. J. Weber, *Mathematical Methods for Physicists* 5th Ed., (Harcourt/Academic Press, New York, New York, 2001).

[25] D. Frenkel and R. Portugal, "Algebraic methods to compute Mathieu functions," J. Phys. A: Math. Gen. **34**, 3541(2001).

[26] M. Aunola, "The discretized harmonic oscillator: Mathieu functions and a new class of generalized Hermite polynomials," J. Math. Phys. **44**, 1913 (2003).

[27] A. Rey et al., "Ultracold atoms confined in an optical lattice plus parabolic potential: a closed-form approach," Phys. Rev. A **72**, 033616 (2005).

[28] T. M. Dunster, "Uniform asymptotic approximation of Mathieu functions," Methods and Applications of Analysis **1** (2), 143 (1994).

[29] T. Kato, *Perturbation Theory for Linear Operators* (Springer-Verlag New York Inc., 1966).

[30] S. Y. Lee and A. Riabko, "Envelope hamiltonian of an intense charged-particle beam in periodic solenoidal fields," Phys. Rev. E. **51**, 1609 (1995).

[31] A. Erdélyi, "On certain expansions of the solutions of Mathieu's differential equation," Proc. Camb. Phil. Soc. **38**, 28-33 (1942).

[32] S. Zhang and J. Jin, *Computation of Special Functions* (John Wiley & Sons, Inc., New York, 1996).

[33] P. L. Walstrom, "Reconstructing interior wiggler fields from surface field data with a Fourier series/integral approach," (private communication).

[34] S. Nazarov and B. Plamenevsky, *Elliptic Problems in Domains with Piecewise Smooth Boundaries* (Walter de Gruyter and Co., Berlin, 1994).

[35] P. Grisvard, *Elliptic Problems in Nonsmooth Domains (Monographs and Studies in Mathematics **24*** (Pitman Publishing, Boston, 1985).

[36] V. A. Kozlov, V. G. Maz'ya, J. Rossmann, *Elliptic Boundary Value Problems in Domains with Point Singularities* (AMS, Providence, RI, 1997).

[37] G. Thater, "The Neumann problem, cylindrical outlets and Sobolev spaces," Math. Meth. Appl. Sci., **25**, 875-894 (2002).

[38] G. Thater, "Neumann problem in domains with outlets of bounded diameter," Acta Applicandae Mathematicae, **73**, 251-274 (2002)

[39] E. Ludmirsky, "Helical Siberian Snakes," (IEEE, Piscataway, NJ, 1996).

[40] J. Takano et. al., "Helical dipole partial Siberian snake for the AGS," J. of Instrumentation, **11**, 11002 (2006).

[41] H. V. Helmholtz, "Uber Integrale der hydromechanischen Gleichung, welche den Wirbelbewegungen entsprechen," J. Reine Angew. Math., **55**, No. 25 (1858).

[42] P.L. Walstrom, "Soft-edged magnet models for higher-order beam-optics map codes," Nucl. Inst. and Meth. **A519**, 216 (2004).

[43] S. Manikonda and M. Berz, "Multipole expansion solution of the Laplace equation using surface data," Nucl. Inst. and Meth. A558, 175 (2006).

[44] S. Manikonda and M. Berz, "An accurate high-order method to solve the Helmholtz boundary value problem for the 3D Laplace equation," IJPAM **23**, 365 (2005).

[45] G. Schwarz, *Hodge Decomposition: A Method for Solving Boundary Value Problems* (Springer-Verlag, Berlin, 1995).

[46] J. Cantarella, D. DeTurck, and H. Gluck, "Vector calculus and the topology of domains in 3-space," The American Mathematical Monthly, **109**, 409 (May 2002).

[47] A. Bossovit, "Magnetostatic problems in multiply connected regions: some properties of the curl operator," IEEE Proceedings A, **135**, 179 (1988).

[48] B. L. Beers and A. Dragt, "New theorems about spherical harmonic expansions and SU(2)," J. Math. Phys., **11**, No. 8 (1970).

[49] B. L. Beers, "Harmonic analysis of analytic functions on hyperspheres," J. Math. Phys. **13**, No. 7 (1972).

[50] A. H. Stroud, *Approximate Calculation of Multiple Integrals* (Prentice-Hall, Englewood Cliffs, NJ, 1971).

[51] P. A. M. Dirac, Proc. R. Soc. London **A133**, 60 (1931); Phys. Rev. **74**, 817 (1948).

[52] A. S. Goldhaber and W. P. Trower, "Resource Letter MM-1: Magnetic Monopoles," Am. J. Phys. **58**, 429 (1990).

[53] J. Shibli, *Plane and Spherical Trigonometry* (Ginn and Company, New York, 1949).

[54] D. Sagan, D. Rubin, E. Forest, "A magnetic field model for wigglers and undulators," Proceedings PAC 2003, 1023 (2003).

[55] J. Urban and G. Dugan, "CESR-c wiggler studies in the context of the International Linear Collider Damping Rings," Proceedings PAC 2005, 1880 (2005).

[56] C. Steier et. al., "Measuring and optimizing the momentum aperture in a particle accelerator," Phys. Rev. E, **65**, 056506 (2002).

[57] A. Chao, M. Tigner ed., *Handbook of Accelerator Physics and Engineering* (World Scientific Publishing Company, 1999).

[58] R. Davidson, *Physics of Nonneutral Plasmas* (Addison-Wesley Publishing Co., Redwood City, CA, 1990).

[59] A. J. Lichtenberg and M. A. Lieberman, *Regular and Stochastic Motion* (Springer-Verlag New York, Inc., 1983).

[60] J. Safranek et. al., "Nonlinear dynamics in a SPEAR wiggler," Phys. Rev. ST Accel. Beams, **5**, 010701 (2002).

[61] P. Emma and T. Raubenhemier, "Systematic approach to damping ring design," Phys. Rev. ST Accel. Beams, **4**, 021001 (2001).

[62] N. Phinney, N. Toge, and N. Walker eds., *International Linear Collider Reference Design Report, Volume 3: Accelerator*, International Committe for Future Accelerators (2007). http://www.linearcollider.org/

[63] A. Wolski, J. Gao, and S. Guiducci eds., "Configuration studies and recommendations for the ILC damping rings," Lawrence Berkeley National Laboratory Paper, LBNL-59449 (2006). http://repositories.cdlib.org/lbnl/LBNL-59449/

[64] H. S. Dumas and J. Laskar, "Global dynamics and long-time stability in Hamiltonian systems via numerical frequency analysis," Phys. Rev. Lett. **70**, 2975 (1993).

[65] F. Gournaris, "Top quark physics, luminosity spectrum and the beam energy spectrometer at the International Linear Collider," University College London, London (2006).

[66] R. L. Stratonovich, *Topics in the Theory of Random Noise* vol. 1,2, (Gordon & Breach, New York, 1963).

[67] G. Bachman and L. Narici, *Functional Analysis* (Dover Publications, Inc., Mineola, NY, 2000).

[68] F. Riesz and B. Sz.-Nagy, *Functional Analysis* (Frederick Ungar Pub. Co., New York, 1955).

[69] M. H. Protter and C. B. Morrey, *A First Course in Real Analysis* 2nd Ed. (Springer-Verlag New York, Inc., 1991).

[70] E. W. Cheney, *Introduction to Approximation Theory* (E. W. Cheney, 1982).

[71] R. W. Hamming, *Numerical Methods for Scientists and Engineers* 2nd ed. (McGraw-Hill, Inc., New York, 1973).

[72] K. Knight, *Mathematical Statistics* (Chapman & Hall/CRC, New York, 2000).

[73] M. Bôcher, *Die Reihenentwickelungen der Potentialtheorie* (Leipzig, 1894).

[74] P. Morse and H. Feshbach, *Methods of Theoretical Physics*, vol. 1 & 2 (McGraw-Hill Book Company, Inc., New York, 1953).

[75] C. P. Boyer, E. G. Kalnins, W. Miller, "Symmetry and the separation of variables for the Helmholtz and Laplace equations," Nagoya Math. J. **60**, 35 (1976).

[76] W. Miller, *Symmetry and Separation of Variables* (Addison-Wesley Publishing Company, Inc., Providence, Rhode Island, 1977).

[77] P. Davis and P. Rabinowitz, *Methods of Numerical Integration* 2nd Ed. (Academic Press, Inc., Orlando, FL, 1984).

[78] L.N.G. Filon, "On a quadrature formula for trigonometric integrals," Proc. Roy. Soc. Edinburgh, **49**, 38 (1929).

[79] B. Einarsson, "Numerical calculation of Fourier integrals with cubic splines," BIT **8**, 279 (1968).

[80] T. Havie, "Remarks on an expansion for integrals of rapidly oscillating functions," BIT **13**, 16 (1973).

[81] R. Piessens and F. Poleunis, "A numerical method for the integration of oscillatory functions," BIT **11**, 317 (1971).

[82] P. Dierckx and R. Piessens, "Calculation of Fourier coefficients of discrete functions with cubic splines," J. Comp. and Applied Math. **3**, No. 3 (1977).

[83] C. de Boor, *A Practical Guide to Splines, Revised Ed.* (Springer-Verlag New York, Inc., 2001).

[84] C. K. Chui, *Multivariate Splines* (Society for Industrial and Applied Mathematics, Philadelphia, 1988).

[85] W. Gautschi, "Attenuation factors in practical Fourier analysis," Numer. Math. **18**, 373 (1972).

[86] E. Neumann, "Moments and Fourier transforms of B-splines," J. Comp. and Applied Math., **7**, No. 1 (1981).

[87] John Tukey, "The estimation of (power) spectra and related quantities," appearing in R. E. Langer ed., *On Numerical Approximation* (University of Wisconsin Press, Madison, WI, 1959).

[88] J. W. Cooley and J. W. Tukey, "An algorithm for the machine calculation of complex Fourier series," Math. Comput., **19**, No. 90, 297 (1965).

[89] E. O. Brigham, *The Fast Fourier Transform* (Prentice-Hall, Inc., Englewood Cliffs, NJ, 1974).

[90] B. P. Lathi, *Signal Processing and Linear Systems* (Berkeley-Cambridge Press, Carmichael, CA, 1998).

[91] W. Press et al., *Numerical Recipes in Fortran 77* Vol. 1 (Cambridge University Press, Cambridge, UK, 1992).

[92] O. D. Kellog, *Foundations of Potential Theory* (Dover Publications, Inc., New York, 1953).

[93] D. H. Armitage and S. J. Gardiner, *Classical Potential Theory* (Springer-Verlag, London, 2001).

[94] R. Courant and D. Hilbert, *Methods of Mathematical Physics*, 1,2, (Interscience Publishers, Inc., New York, 1962).

[95] R. Cade, "A Class of Physically Relevant Insoluble Dirichlet Problems," IMA J. Appl. Math. **29** (3), 281 (1982).

[96] Y. V. Egorov and M. A. Shubin, *Foundations of the Classical Theory of Partial Differential Equations* (Springer-Verlag Berlin, Heidelberg, 1998).

[97] M. Renardy and R. Rogers, *An Introduction to Partial Differential Equations* 2nd Ed. (Springer-Verlag New York, Inc., 2004).